PREMIXED SYNGAS COMBUSTION: MODELING AND APPLICATION TO A SWIRL-STABILIZED COMBUSTOR

BY

FAHAD MOHAMMED MAJHOUD ALZAHRANI

A Thesis Presented to the
DEANSHIP OF GRADUATE STUDIES

KING FAHD UNIVERSITY OF PETROLEUM & MINERALS

DHAHRAN, SAUDI ARABIA

In Partial Fulfillment of the
Requirements for the Degree of

MASTER OF SCIENCE

In

MECHANICAL ENGINEERING

MAY 2014

KING FAHD UNIVERSITY OF PETROLEUM & MINERALS
DHAHRAN 31261, SAUDI ARABIA

DEANSHIP OF GRADUATE STUDIES

This thesis, written by **FAHAD MOHAMMED MAJHOUD ALZAHRANI** under the direction of his thesis adviser and approved by his thesis committee, has been presented to and accepted by the Dean of Graduate Studies, in partial fulfillment of the requirements for the degree of **MASTER OF SCIENCE IN MECHANICAL ENGINEERING**.

Thesis Committee

Med Habib
Dr. Mohamed A. Habib (Adviser)

Dr. Esmail M.A. Mokheimer (Co-adviser)

Dr. Rached Ben-Mansour (Member)

Dr. Ahmed F. Ghoniem (Member)

MAntar
Dr. Mohamed A. Antar (Member)

Dr. Zuhair M. Gasem
Department Chairman

Dr. Salam A. Zummo
Dean of Graduate Studies

2/11/14
Date

بسم الله الرحمن الرحيم

Dedication

To

My Beloved Parents

Azza Saleh Alghamdi

&

Mohammed Majhoud Alzahrani

My Brothers

Bandar, Khalid & Abdullah

My Sisters

Noura, Nada & Najla

ACKNOWLEDGMENTS

All thankfulness, first and foremost, to Almighty Allah, most Gracious, who in His limitless mercy has guided me into the completion of this MS thesis. My Peace and Blessings be upon His Prophet Muhammad, peace be upon him. I am so much thankful to my mother, father, brothers, and sisters for their continuous moral support throughout my life.

I would like to thank my advisor, Prof. Mohamed Habib, and co-advisor, Prof. Esmail Mokheimer, for their guidance, help, and patience during my course of work. Their flexibility and trust they have given me were source for motivation behind my hard work. Prof. Habib's long experience in combustion and turbulence modeling helped me a lot in my research. When I faced difficulties in my simulations, a small tip from him lead to a successful run. I am so grateful for that. Prof. Esmail gave me many important advices that helped me manage my work in a better way. During my stay at MIT, he was very generous to help me in completing the requirements for readmission. I am so much thankful for his modesty.

I would like also to acknowledge the support and guidance of Dr. Rached Ben-Mansour in the CFD modeling part of my work. His expertise was tremendous and invaluable for me. He also allowed me to use his high performance computer

in order to perform my simulations. The runs would not have been completed in time without it. So, I would like to thank him very much for that.

Also, I would like to express my gratitude to Prof. Mohamed Antar for the amount of knowledge and understanding he has given me. I have been his student in the undergraduate level and in the graduate level and he always has shown an enthusiasm which transferred to me. In addition, I am really thankful for the combustion course I took with him in the graduate level. It provided help and understanding in my research.

My heartfelt thanks to Prof. Ahmed Ghoniem for taking me into his Reacting Gas Dynamics laboratory at MIT and for giving me the opportunity to work under his supervision. He expanded my vision and cleared the research objectives of this thesis. He motivated me just by sitting and talking about the kind of work I was supposed to do. Therefore, I would like to express my sincere appreciation for everything he has given me.

My deepest gratitude to Dr. Konstantina Vogiatzaki for her continuous support and guidance throughout my work during my stay at MIT. She dedicated many precious times in order to help me and explain me things that I did not understand. Therefore, I am really thankful for her. I am also so much thankful to my friend and colleague Mr. Sofiene Tamallah, who is currently a PhD student at MIT. He has been a great team player. He also helped me a lot and made my life easier when it came to programming. He always followed the saying ”Do not reinvent the wheel”. So, I would like to thank him for that.

All the thanks to my dear friend and colleague Mr. Yinka Sanusi, who is currently a PhD student at KFUPM. He has been a wonderful team player. He was a motivation and guidance for me, technically and academically. I always took his opinion at difficult times, and his wisdom always worked.

I also would like to acknowledge the financial and administrative support of the Ministry of Higher Education, King Fahd University of Petroleum and Minerals, and the Center for Clean Water and Clean Energy at MIT and KFUPM through MIT-KFUPM Project # R12-CE-10. Part of this work would not have been done without my visit to MIT. Their support for this visit allowed me to gain and transfer some of the invaluable knowledge from MIT to KFUPM. So, thank you very much for that.

TABLE OF CONTENTS

ACKNOWLEDGEMENTS v

LIST OF TABLES xi

LIST OF FIGURES xii

LIST OF ABBREVIATIONS xix

THESIS ABSTRACT (ENGLISH) xxiii

THESIS ABSTRACT (ARABIC) xxvi

CHAPTER 1 INTRODUCTION 1

1.1 Syngas Production Processes 4
1.2 Syngas Oxidation Chemistry 5
1.3 Thesis Objectives 8

CHAPTER 2 LITERATURE REVIEW 9

2.1 Syngas Reaction Mechanisms 9
2.2 Premixed Syngas Laminar Flame Characteristics 19
  2.2.1 Adiabatic Flame Temperature 20
  2.2.2 Laminar Flame Speed 26
  2.2.3 Laminar Flame Thickness 31
  2.2.4 Flame Ignition and Extinction 38
  2.2.5 Flame Stretch 41

2.2.6 Flammability Limits 43
2.2.7 Emissions 46
2.3 Combustion of Syngas in Swirl-Stabilized Burners 50
2.4 Combustion Modeling Techniques 55
2.4.1 Fundamental Modeling Techniques: CANTERA 56
2.4.2 CFD Modeling Techniques: ANSYS FLUENT 56

CHAPTER 3 DETAILED-CHEMISTRY ANALYSIS OF LPM SYNGAS LAMINAR FLAMES 57

3.1 Mathematical Models 58
3.1.1 Modeling of Adiabatic Flame Temperature 58
3.1.2 Modeling of Laminar Flame Speed 59
3.1.3 Modeling of NO Emissions 61
3.1.4 Chemistry Model 62
3.2 Results and Discussion 63
3.2.1 Adiabatic Flame Temperature 63
3.2.2 Laminar Flame Speed 66
3.2.3 NO Emissions 69

CHAPTER 4 COMPARISON OF SYNGAS REACTION MECHANISMS FOR CFD APPLICATIONS 73

4.1 Mathematical Models 74
4.2 Experimental Data for Laminar Flame Speed 75
4.3 Results and Discussion 76
4.3.1 Adiabatic Flame Temperature 76
4.3.2 Laminar Flame Speed 82
4.3.3 NO Emissions 93

CHAPTER 5 SIMULATION OF LPM SYNGAS COMBUSTION IN A SWIRL-STABILIZED COMBUSTOR 100

5.1 Geometry Description and Boundary Conditions 101

5.2 Mathematical Models 103
5.2.1 Continuity Equation 104
5.2.2 Momentum Equation 104
5.2.3 Energy Equation 106
5.2.4 Radiation Equation 107
5.2.5 Species Equation 108
5.3 Computational Details and Solution Methods 109
5.4 Models Validation 110
5.4.1 Choosing a Turbulence Model 113
5.4.2 Models Validation and Chemistry Model Selection 118
5.5 Results and Discussion 125
5.5.1 Influence of Swirl Number 125
5.5.2 Influence of H_2/CO Ratio 139
5.5.3 Influence of Equivalence Ratio 150

CHAPTER 6 CONCLUSIONS **162**

APPENDICES **165**

APPENDIX A SYNGAS REACTION MECHANISMS **166**

APPENDIX B CANTERA CODES **195**

B.1 Adiabatic Flame Temperature 195
B.2 Laminar Flame Speed 198
B.3 NO Emissions 202

REFERENCES **209**

VITAE **223**

LIST OF TABLES

1.1 Historical terminology for various types of syngas 3

2.1 Summary of most kinetic models used for syngas oxidation 16
2.2 Ignition delay times at stoichiometric conditions 40

3.1 Parameters and their corresponding values used in the parametric study 58

4.1 Mechanisms tested for syngas oxidation 74

5.1 Cases used in the parametric study of LPM syngas combustion in the swirl-stabilized combustor 103

A.1 GRI reaction mechanism 166
A.2 C1 reaction mechanism 180
A.3 NI reaction mechanism 184
A.4 PO reaction mechanism 187
A.5 DA reaction mechanism 189
A.6 BO reaction mechanism 191
A.7 SL reaction mechanism 193
A.8 JL reaction mechanism 194
A.9 WO reaction mechanism 194

LIST OF FIGURES

1.1 Integrated gasification combined cycle 2
1.2 Gasification process and major reactions 5

2.1 Comparison between GRI-Mech. 3.0 model and C1 model 15
2.2 Adiabatic flame temperatures for CH_4, H_2, CO, and typical syngas fuels burning with air 21
2.3 Adiabatic flame temperature and flame speed as a function of equivalence ratio for different syngas mixtures 23
2.4 Adiabatic flame temperature of syngas flames as a function of equivalence ratio and fuel composition 24
2.5 Effect of dilution on adiabatic flame temperature for a 50/50 H_2/CO mixture at $\phi = 1.0$ 25
2.6 Influence of pressure and preheat temperature on adiabatic flame temperature for typical syngas fuel burning with air 27
2.7 Flame speeds as a function of equivalence ratio for various H_2/CO mixtures 28
2.8 Flame speed response to variable CO_2, H_2O, and N_2 dilution for different syngas mixtures 29
2.9 Laminar flame speed as a function of pressure for a 50/50 H_2/CO fuel mixture at $T_u = 300K$ 31
2.10 Laminar flame speed as a function of pressure for three H_2/CO fuel mixtures at $\phi = 0.6$ and $T_u = 300K$ 32

2.11 Laminar flame speed of different syngas compositions for various preheat temperatures at $p = 1atm$ 33
2.12 Spatial distributions of major and minor species for a 50/50 H_2/CO mixture at varying equivalence ratios 35
2.13 Laminar flame thickness from simulations for a range of H_2/CO fuel mixtures 36
2.14 Pressure dependence of laminar flame thickness from simulations for a 50/50 H_2/CO fuel mixture 36
2.15 Laminar flame thicknesses as a function of preheat temperature from simulations for four H_2/CO fuel-air mixtures 37
2.16 Schematic view of (a) a constant-pressure and (b) a constant-volume closed homogenous reactors 38
2.17 Schematic view of a well/perfectly stirred reactor 39
2.18 Ignition delay times for homogenous and well stirred reactors as a function of temperature for H_2/CO mixtures in air 41
2.19 Ignition and extinction delay times for a well stirred reactor as a function of temperature for H_2/CO mixtures in air 42
2.20 Extinction strain rates as a function of H_2 level in H_2/CO-air flames for two lean mixtures 43
2.21 The lean limit of binary fuel mixtures involving hydrogen as a function of the volumetric concentration of hydrogen in the fuel 46
2.22 Lean flammability limits of H_2/CO mixtures in air at different temperatures 47
2.23 Rich flammability limits of H_2/CO mixtures in air at different temperatures 47
2.24 LIF-measured postflame front NO concentrations as a function of equivalence ratio in syngas-air flames 49
2.25 LIF-measured postflame front NO concentrations as a function of CH_4 addition for different pressures 50

3.1 Freely propagating laminar flame model configuration 59
3.2 Schematic diagram for the well-stirred reactor model 62
3.3 Effect of syngas composition on LPM syngas adiabatic flame temperature for different equivalence ratios 64
3.4 Effect of operating pressure on LPM syngas adiabatic flame temperature for different equivalence ratios 64
3.5 Effect of preheat temperature on LPM syngas adiabatic flame temperature for different equivalence ratios 65
3.6 Effect of syngas composition on LPM syngas adiabatic flame temperature for different equivalence ratios 65
3.7 Effect of syngas composition on LPM syngas laminar flame speed for different equivalence ratios 67
3.8 Effect of operating pressure on LPM syngas laminar flame speed for different equivalence ratios 67
3.9 Effect of preheat temperature on LPM syngas laminar flame speed for different equivalence ratios 68
3.10 Comparable LPM syngas laminar flame speeds at different conditions 68
3.11 Effect of syngas composition on LPM syngas production of thermal NO for different equivalence ratios 70
3.12 Effect of operating pressure on LPM syngas production of thermal NO for different equivalence ratios 70
3.13 Effect of preheat temperature on LPM syngas production of thermal NO for different equivalence ratios 71
3.14 Effect of preheat temperature upon operating pressure of LPM syngas production of thermal NO 71
3.15 Effect of syngas composition upon operating pressure of LPM syngas production of thermal NO 72

4.1 Adiabatic flame temperature of pure H_2 and CO fuels under lean conditions predicted by GRI mechanism 77

4.2 Adiabatic flame temperature of 50/50 H_2/CO fuel under lean conditions predicted by different kinetic models 77
4.3 Adiabatic flame temperature predictions by different kinetic models for varying syngas composition 79
4.4 Adiabatic flame temperature predictions by different kinetic models for varying operating pressure 80
4.5 Adiabatic flame temperature predictions by different kinetic models for varying preheat temperature 81
4.6 Laminar flame speed of pure H_2 and CO fuels under lean conditions predicted by GRI mechanism 82
4.7 Experimental (symbols) and predicted (lines) laminar flame speeds at varying equivalence ratio 84
4.8 Experimental (symbols) and predicted (lines) laminar flame speeds for varying syngas composition 86
4.9 Predicted laminar flame speeds for varying operating pressure . . 89
4.10 Experimental (symbols) and predicted (lines) laminar flame speeds for varying preheat temperature 91
4.11 Laminar flame speed average error between experimental and calculated values for all kinetic models 92
4.12 NO predictions of detailed and reduced kinetic models at varying equivalence ratio 96
4.13 NO predictions of detailed and reduced kinetic models for varying syngas composition 97
4.14 NO predictions of detailed and reduced kinetic models for varying operating pressure 98
4.15 NO predictions of detailed and reduced kinetic models for varying preheat temperature 99

5.1 Two-dimensional view of the swirl-stabilized combustor 102

5.2 Three-dimensional view of the swirl-stabilized combustor along with the boundary conditions 102
5.3 The influence of mesh refinement on (a) the axial velocity and (b) temperature along the centerline of the combustion chamber . . . 111
5.4 Geometry and boundary conditions used for the investigation of the different turbulence models 114
5.5 Temperature distribution predicted by the four turbulence models 116
5.6 Axial distribution of species along the centerline of the combustor predicted by the four turbulence models 117
5.7 Geometry and boundary conditions used for validation 119
5.8 Radial distribution of CO concentration predicted by the Realizable $k - \epsilon$ model, DO model, EDC model and a number of kinetic models 122
5.9 Radial distribution of O_2 concentration predicted by the Realizable $k - \epsilon$ model, DO model, EDC model and a number of kinetic models 123
5.10 Radial distribution of NO concentration predicted by the Realizable $k - \epsilon$ model, DO model, EDC model and a number of kinetic models 124
5.11 Axial velocity contours across a vertical-symmetrical plane for different swirl numbers 126
5.12 Axial velocity profiles across the centerline of combustion chamber for different swirl numbers. 127
5.13 Radial profiles of axial velocity for different swirl numbers 129
5.14 OH contours along a vertical-symmetrical plane across combustion chamber for different swirl numbers 131
5.15 Temperature contours along a vertical-symmetrical plane across combustion chamber for different swirl numbers 132
5.16 Axial profiles of temperature across combustor centerline for different swirl numbers 133
5.17 Comparison between maximum, average and exit temperatures for different swirl numbers 134

5.18 Axial profiles of fuel concentrations in the syngas-air mixture across combustor centerline for different swirl numbers 136
5.19 NO and CO emissions at the exit of the combustor for different swirl numbers 138
5.20 CO_2 emissions at the exit of the combustor for different swirl numbers 138
5.21 Axial velocity contours across a vertical-symmetrical plane for different hydrogen content 140
5.22 Axial velocity profiles along the centerline of the combustor for different hydrogen content 141
5.23 Radial profiles of axial velocity at different cross-sections for different hydrogen content 142
5.24 OH contours along a vertical-symmetrical plane across combustion chamber for different hydrogen content 144
5.25 Temperature contours along a vertical-symmetrical plane across combustion chamber for different hydrogen content 145
5.26 Axial profiles of temperature along the centerline of the combustion chamber for different hydrogen content 146
5.27 Comparison between maximum, average and exit temperatures for different syngas compositions 146
5.28 Axial profiles of fuel concentrations in the syngas-air mixture across combustor centerline for different syngas compositions 148
5.29 NO and CO emissions at the exit of combustor for different syngas compositions 149
5.30 CO_2 emissions at the exit of combustor for different syngas compositions 150
5.31 Axial velocity contours across a vertical-symmetrical plane for different equivalence ratios 151
5.32 Axial velocity profiles across the centerline of combustion chamber for different equivalence ratios 152

5.33 Radial profiles of axial velocity at different cross-sections for different equivalence ratios 153
5.34 OH contours along a vertical-symmetrical plane across combustion chamber for different equivalence ratios 155
5.35 Temperature contours along a vertical-symmetrical plane across combustion chamber for different equivalence ratios 156
5.36 Axial profiles of temperature along the centerline of the combustion chamber for different equivalence ratios 156
5.37 Comparison between maximum, average and exit temperatures for different equivalence ratios 157
5.38 Axial profiles of fuel concentrations in the syngas-air mixture across combustor centerline for different equivalence ratios 159
5.39 NO and CO emissions at the exit of combustor for different equivalence ratios 160
5.40 CO_2 emissions at the exit of combustor for different equivalence ratios 161

LIST OF ABBREVIATIONS

Acronyms

CFD	Computational Fluid Dynamics
HR	Closed Homogenous Reactor
HHV	Higher Heating Value
IGCC	Integrated Gasification Combined Cycle
IRZ	Inner Recirculation Zone
ISRCC	Integrated Solar Reforming Combined Cycle
LBO	Lean Blow Out
LFL	Lean Flammability Limit
LHV	Lower Heating Value
LPM	Lean Premixed Combustion
ORZ	Outer Recirculation Zone
PDF	Probability Density Function
RFL	Rich Flammability Limit

WSR	Well Stirred Reactor

Roman Symbols

A	cross-sectional area, [m^2]
a	absorption coefficient, [-]
c_p	specific heat, [J/kg·K]
D_m	mass diffusion coefficient, [-]
D_T	thermal diffusion coefficient, [-]
h	specific enthalpy, [J/kg·K]
I	radiation intensity, [W/m^2]
k	rate constant, [(mol/m^3)$^{1-(m+n)}$ s^{-1}], turbulent kinetic energy, [J/kg]
$\dot{m}$	mass flow rate, [kg/s]
N	number of species
n	refractive index, [-]
p	static pressure, [Pa]
R	universal gas constant, [8.314 J/mol·K]
r	position vector, [m]
s	direction vector, [m]
Sc_t	turbulent Schmidt number, [-]
s'	scattering direction vector, [m]
S	swirl number, [-]

T	local temperature, [K]
u, v	velocity, [m/s]
W	molecular weight, [g/mol]
$\overline{W}$	mean molecular weight, [g/mol]
x	axial distance, [m]
Y	mass fraction, [-]

Greek Symbols

ϵ	turbulent dissipation rate, [J/kg·s]
λ	thermal conductivity, [W/m·K]
μ	dynamic viscosity, [Pa·s]
μ_t	turbulent viscosity, [Pa·s]
$\dot{\omega}$	rate of reaction, [mol/m^3·s]
ϕ	equivalence ratio, [-]
ρ	density, [kg/m^3]
σ	Stefan-Boltzmann constant, [5.669×10^{-8} W/m^2·K^4]
σ_s	scattering coefficient through the path length s, [-]

Superscripts

0	reference state

Subscripts

b	burned

f	formation
k, m	species
u	unburned

THESIS ABSTRACT

NAME:	Fahad Mohammed Majhoud Alzahrani
TITLE OF STUDY:	Premixed Syngas Combustion: Modeling and Application to a Swirl-Stabilized Combustor
MAJOR FIELD:	Mechanical Engineering
DATE OF DEGREE:	May 11, 2014

The stringent regulations of harmful gases and pollutants, such as nitrogen oxides, lead to the use of alternative fuels in order to lower these emissions. Hydrogen is one of the cleanest fuels. When burnt with oxidizer, it produces water and no other harmful emissions. Thus, it has the potential to become a major contributor to a near-zero emission future. However, currently, technology limitations, mostly associated with storage and transportation, limit its use in a wide range. A very promising alternative is synthetic gas (syngas), which is composed mainly of hydrogen (H_2) and carbon monoxide (CO). Lean premixed (LPM) combustion of syngas can be one of the most promising technologies for increased combustion efficiency and reduced emissions. In this thesis, LPM syngas combustion characteristics have been studied numerically. LPM syngas laminar flames are modeled *in zero- and one-dimensional forms using a detailed chemistry model (GRI-Mech. 3.0) to understand their most important basic properties, namely adiabatic flame temperature, laminar flame speed, and NO emissions. An emphasis has been given to the importance of syngas reaction mechanisms by studying some of the available reduced chemical mechanisms and how accurate they are in predicting the basic properties of LPM syngas laminar flames studied. Finally, LPM syngas combustion in a real geometry lab-scale swirl-stabilized combustor is modeled using computational fluid dynamics (CFD) to study the effect of swirl number, syngas composition, and equivalence ratio on flame characteristics and emissions. The adiabatic flame temperature of syngas was observed to increase with equivalence ratio, operating pressure, and preheat temperature, and decrease with hydrogen volume percent in syngas. The laminar flame speed increased with increasing equivalence ratio, hydrogen content in the syngas and preheat temperature, and decreased with increasing operating pressure. The NO production was also observed to increase with increasing equivalence ratio and preheat temperature. However, it decreased with increasing hydrogen in the syngas mixture. As the operating pressure increased, NO formation decreased at low equivalence ratios, and increased at high equivalence ratio. At very lean conditions, the NO predictions by the GRI-Mech. 3.0 were highly under-predicted by the reduced mechanisms. Different combination of these factors resulted in varying degree of discrepancy by the mechanisms understudy. It can be concluded that there is a need for developing more robust chemical mechanisms that could predict LPM syngas flames proper-*

ties, especially at high preheat temperatures and operating pressures. In addition, experimental data for the effect of pressure on H_2/CO *laminar flame speeds with air* (O_2+N_2) *as the oxidizer is required and will be helpful for validating the developed kinetic models for syngas oxidation at high pressures. For the swirl-stabilized flames, the swirl geometry was found to have a significant effect on the different flame properties. The different strength levels of gases recirculation resulted in different values of flame temperature. The flame was found to be shorter for high swirl numbers. This gave higher residence time of combustion products, which reduced* CO *emissions. On the other hand, the higher capability of hydrogen to ignite and burn increased the flame temperature and* NO_X *levels locally. Increasing* H_2/CO *ratio resulted in higher flame temperatures, shorter flame lengths, and weaker reverse flow associated with the inner recirculation zones. In addition, upstream flame propagation (flashback phenomenon) occurred beyond* $H_2 = 50\%$. *Higher* NO_X *emissions and lower* CO *and* CO_2 *emissions resulted from increasing* H_2/CO *ratio. The equivalence ratio was found to have the most significant influence on flame temperature and emissions. Undesirable levels of* NO *were observed for equivalence ratios beyond* $\phi = 0.6$, *while undesirable levels of* CO *were recorded for equivalence ratios below* $\phi = 0.6$. *Moreover, increasing equivalence ratio caused* CO_2 *emissions to increase.*

THESIS ABSTRACT (ARABIC)

ملخص الرسالة

الاسم الكامل: فهد محمد مجحود الزهراني

عنوان الرسالة: الاحتراق المختلط للغاز الصناعي: محاكاته وتطبيقاته في غرفة احتراق ذات دوامة مستقرة

التخصص: الهندسة الميكانيكية

تاريخ الدرجة العلمية: ١٤٣٥/٠٦/١٢ هـ

أدت اللوائح الصارمة للحد من انتشار الغازات الضارة والملوثة للبيئة مثل أكاسيد النيتروجين، الى البحث عن بدائل للغاز الطبيعي في إنتاج الطاقة الكهربائية. ويعتبر غاز الهيدروجين من أهم الغازات البديلة والصديقة للبيئة لأن بخار الماء هو المنبعث الوحيد عند احتراقه. لذلك، فإن لدى الهيدروجين القدرة على أن يصبح الوقود الأساسي نحو مستقبل خال من التلوث إذا تم التغلب على التحديات التقنية التي تواجه استخدام الهيدروجين، والتي تتعلق بتخزينه ونقله وتكلفة إنتاجه. ومن البدائل الواعدة أيضاً، الغاز الصناعي والذي يتكون بشكل رئيسي من خليط غازي الهيدروجين وأول أكسيد الكربون. الاحتراق المختلط للغاز الصناعي منخفض نسبة التكافؤ (نسبة تكافؤ الوقود للهواء) يعتبر من التقنيات الواعدة التي تزيد كفاءة الاحتراق وتقلل من انبعاثات الغازات الضارة. درست هذه الرسالة خواص الاحتراق المختلط للغاز الصناعي منخفض نسبة التكافؤ عن طريق استخدام وسائل المحاكاة الرياضية. حيث تم محاكاة اللهب المختلط الرقائقي للغاز الصناعي لفهم خصائصه الأساسية والتي تشمل درجة حرارة اللهب القصوى، وسرعة اللهب الرقائقية، وانبعاثات أكسيد النيتروجين عن طريق حل المعادلات الصفرية والأحادية الأبعاد باستخدام نموذج كيميائي معقد (آلية GRI 3.0). كما أكدت على أهمية آليات تفاعل الغاز الصناعي وذلك بعد دراسة بعض نماذجه الكيميائية البسيطة المتوفرة ومدى دقتها في تحديد خصائصه الأساسية.

أخيراً، تم إجراء محاكاة الاحتراق المختلط للغاز الصناعي منخفض نسبة التكافؤ في غرفة احتراق ذات دوامة مستقرة باستخدام ديناميكية الموائع الحسابية (CFD) لدراسة تأثير كلاً من: درجة قوة الدوامة، ومقدار كمية الهيدروجين في الغاز الصناعي، ونسبة تكافؤ الوقود للهواء على خواص اللهب والانبعاثات. وقد لوحظ أن درجة حرارة اللهب القصوى تزيد بازدياد نسبة التكافؤ وارتفاع كلاً من ضغط التشغيل ودرجة حرارة الخليط، وتقل بازدياد كمية الهيدروجين في الغاز الصناعي. أما سرعة اللهب الرقائقية تزيد بازدياد كلاً من نسبة التكافؤ وكمية الهيدروجين وارتفاع درجة حرارة الخليط، وتقل بارتفاع ضغط التشغيل. كما أن انبعاثات أكسيد النيتروجين تزيد بارتفاع درجة حرارة الخليط وارتفاع ضغط التشغيل مع ازدياد نسبة التكافؤ، وتقل بازدياد كمية الهيدروجين في الغاز الصناعي وارتفاع ضغط التشغيل مع انخفاض نسبة التكافؤ. وبمقارنة نتائج آليات التفاعل البسيطة مع آلية التفاعل المعقدة GRI 3.0 يتضح أن هناك بون شاسع وهو ما يدعو إلى تطوير نماذج كيميائية بسيطة قادرة على تحديد خصائص احتراق الغاز الصناعي بشكل دقيق خاصة عند درجات حرارة مرتفعة للخليط وضغط تشغيل مرتفع. كما أن هناك نقص في التجارب المعملية لسرعة اللهب الرقائقية باستخدام الهواء كمؤكسد عند ضغط تشغيل مرتفع، والتي ستساعد في معرفة مدى دقة النماذج المطورة. كما تبين أن الشكل الهندسي لغرفة الاحتراق ذات الدوامة المستقرة له تأثير بالغ على خصائص اللهب المختلفة. وأن اختلاف آليات الاستقرار بسبب إعادة تدوير الغازات الحارة داخل غرفة الاحتراق تؤدي الى تباين درجات حرارة اللهب. وأن ارتفاع درجة قوة الدوامة يؤدي الى تقصير ألسنة اللهب وزيادة الوقت اللازم لبقاء الغازات الحارة داخل غرفة الاحتراق، وكل ذلك يساعد على تقليل انبعاثات أول أكسيد الكربون. من ناحية اخرى، وجد أن قابلية الهيدروجين للاحتراق تزيد من حرارة اللهب ومستويات أكسيد النيتروجين. وأن لنسبة التكافؤ تأثير جوهري على درجة الحرارة والانبعاثات. حيث أن المستويات الغير مرغوب بها من غاز أكسيد النيتروجين أو غاز أول اكسيد الكربون تكون عند نسبة تكافؤ أعلى من ٠,٦ لغاز أكسيد النيتروجين، وأقل من ٠,٦ لغاز أول أكسيد الكربون.

CHAPTER 1

INTRODUCTION

There is an increasing interest in the use of carbon-free fuels containing various amounts of hydrogen in combined cycles, such as integrated gasification combined cycle (IGCC) and integrated solar reforming combined cycle (ISRCC). Similar to a natural gas combined cycle, IGCC and ISRCC use gas and steam turbines to generate electricity, but the gas in this case is a synthetic gas (syngas), which is a gas mixture, composed mainly of hydrogen (H_2) and carbon monoxide (CO). In IGCC technology [1], syngas is produced by gasification process using a gasifier integrated with the combined cycle. Syngas is then used in gas turbines combustors for power generation. The fossil fuel in this case is a solid fuel, such as coal or biomass. In ISRCC on the other hand [2, 3], syngas is generated by steam reforming of natural gas where the renewable energy, i.e. solar energy is integrated with the combined cycle and utilized as an input source of energy for the reforming process. Figure 1.1 shows a simplified schematic representation for IGCC. ISRCC has a similar schematic view with the gasifier replaced by a reformer and the solid

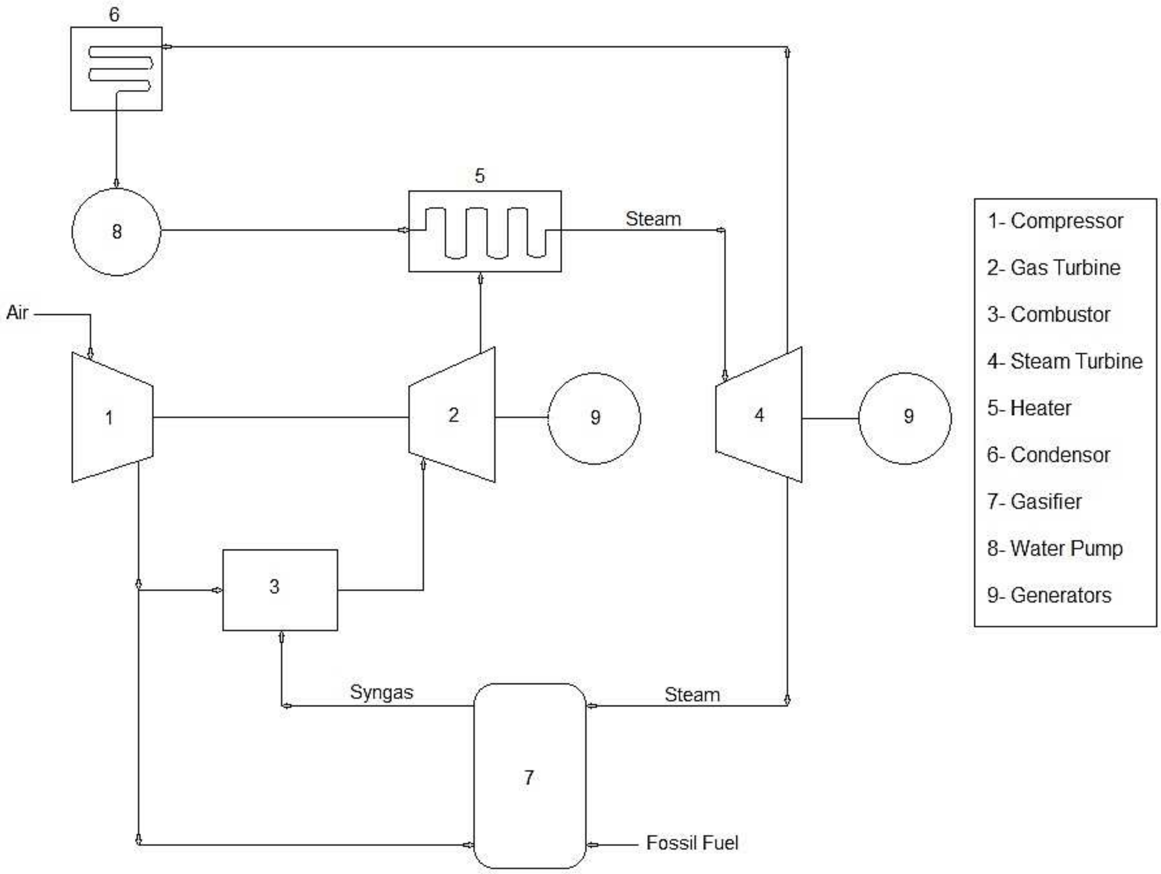

Figure 1.1: Integrated gasification combined cycle that use syngas as a fuel

fuel is replaced by a hydrocarbon fuel.

As a matter of fact, syngas is not a new fuel. It existed even before electricity was discovered where it has been known to the world by other terminologies (see Table 1.1 for historical background) [4]. For example, in the 1800s, Town gas, generated by coal gasification, was used for street lighting and commercial heating besides its use in residential cooking. Nowadays, the interest in syngas for todays applications has been recovered for a number of reasons [5]. First, syngas can be produced from many solid fuel feedstocks. This allows the use of low-cost and renewable fuels, such as biomass. Second, since syngas is a flexible fuel, i.e. can be produced by different methods in various amounts of constituents depending on the type of feedstock used, it can be used by itself for power generation, fuel production, and/or chemical manufacturing. Moreover, the carbon associated with the feedstock can be converted into CO_2 and captured.

Table 1.1: Historical terminology for various types of syngas [4]

Town Gas	Syngas generated from coal and distributed principally for lighting in the later 1800s. Depending on the gasification approach, higher hydrocarbons could be added to create yellow flame for illumination (termed carbureted).
Water Gas	Syngas produced by reacting hot coke with steam, producing nearly equal volumes of CO and hydrogen.
Producer Gas	Syngas produced by reacting humid air with coke, resulting in syngas with significant nitrogen diluent.
Blast Furnace Gas	The product gas from blast furnaces where coke is used to reduce iron oxide to iron. The resulting gas in mostly nitrogen-diluted CO, because air is used to oxidize the coke.

Furthermore, the stringent regulations on harmful gases and pollutants, such as nitrogen oxides (NO_X), carbon dioxide (CO_2), carbon monoxide (CO), unburned hydrocarbons (UHC), and other particulate matters, lead to the use of such a fuel, as well as the development of new methods for lowering these emissions. Lean premixed (LPM) combustion is one of the promising techniques for lowered pollutants. However, operating a combustor under the LPM mode poses many challenges related to flame stability, i.e. blowout and flashback as well as higher CO emissions. In addition, using hydrogen-enriched fuel like syngas in LPM combustion increases the combustor's susceptibility for these dynamic instabilities due to the higher diffusivity and reactivity of hydrogen, resulting in a narrow window of stable and low pollutant emissions operations.

1.1 Syngas Production Processes

Syngas is generated mainly from solid fuel gasification or fossil fuel reforming. Figure 1.2 shows a schematic view of the general process of gasifying solid fuels to produce synthesis gas [5]. The gasification process is an endothermic process and it is carried out by the reaction of the solid fuel, which is a carbon rich fuel, with an oxidizer (air or oxygen) to gasify the fuel, where the heat from carbon oxidation is used to maintain the gasification reactions. In addition, water or steam is added for two main reasons: (1) to control the reaction temperature and (2) to participate in some of the gasification reactions.

On the other hand, fossil fuel reforming, sometimes called steam reforming [6], is the process of producing syngas from hydrocarbon fuels such as natural gas. This is achieved by the reaction of the fossil fuel with steam at high temperatures in a device called a reformer. Typical reforming process is the reaction of methane with steam at high temperatures (700 - 1100 ^oC) with the presence of metal-based catalyst (such as nickel) in the following form,

$$CH_4 + H_2O \rightarrow CO + 3H_2$$

More hydrogen can be produced by the water-gas shift reaction at lower temperatures which yields hydrogen and carbon dioxide,

$$CO + H_2O \rightarrow CO_2 + H_2$$

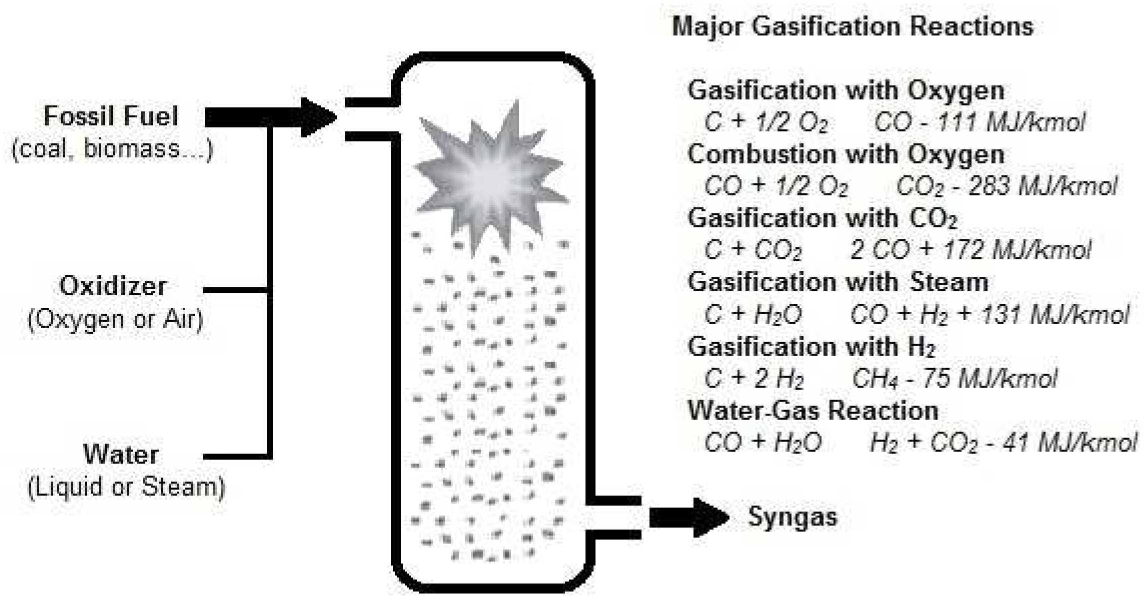

Figure 1.2: Schematic representation of the gasification process and major reactions associated with it

In addition to hydrogen and carbon monoxide, syngas can contain various proportions of carbon dioxide (CO_2), steam (H_2O), nitrogen (N_2), and small amounts of hydrocarbons, typically methane (CH_4). Moreover, impurities in the solid feedstock (contents of sulfur, nitrogen, chlorine, etc.) will produce impurities in the syngas that need to be removed in order to have a clean synthetic fuel.

1.2 Syngas Oxidation Chemistry

One way of understanding syngas combustion and its thermochemistry is through understanding hydrogen combustion behavior since the syngas derived from gasification can contain a considerable amount of hydrogen depending on the type of feedstock used. This will make syngas combustion characteristics very similar to those of hydrogen. The reason for this close similarity in characteristics is because the principal reaction that produces CO_2 for both syngas and hydrogen oxidation is $CO + OH \rightarrow CO_2 + H$. To understand this more clearly, one should know that the driving force of any fuel-oxidizer blend reactions is the generation and chain propagation of free active radicals i.e. initiation and chain reactions. For instance, in the case of carbon monoxide combustion with zero hydrogen content, initiation and chain reactions (reactions C.1 and C.2) are slow in nature. However, adding small quantities of hydrogen or species that contain hydrogen atoms such as water would increase the CO oxidation rate dramatically [7], the oxidation being dominant by reaction C.3. Thus, understanding hydrogen combustion characteristics is very important in determining the desired combustion properties of syngas, such as flammability limits and flame propagation, as it will help in designing a combustion system that is capable of handling syngas fuel. [8].

$$CO + O_2 \rightarrow CO_2 + O \tag{C.1}$$

$$CO + O + M \rightarrow CO_2 + M \tag{C.2}$$

$$CO + OH \rightarrow CO_2 + H \tag{C.3}$$

According to the single step mechanism of the syngas constituents oxidation, the global reactions are,

$$H_2 + 0.5(O_2 + 3.76N_2) \rightarrow H_2O + 0.5(3.76)N_2$$

$$CO + 0.5(O_2 + 3.76N_2) \rightarrow CO_2 + 0.5(3.76)N_2$$

Since syngas is usually a mixture of H_2 and CO with certain volume fraction for each constituent in the mixture, the global reaction becomes,

$$\alpha H_2 + (1-\alpha)CO + 0.5(O_2 + 3.76N_2) \rightarrow \alpha H_2O + (1-\alpha)CO_2 + 0.5(3.76)N_2$$

where α is the volume fraction of hydrogen in the H_2/CO mixture. As mentioned earlier, syngas can have certain amounts of diluents or hydrocarbons. So, in the case of CH_4, for example, the reaction is,

$$\alpha H_2 + \beta CO + (1-\alpha-\beta)CH_4 + [2 - 1.5(\alpha+\beta)](O_2 + 3.76N_2) \rightarrow$$
$$(2-\alpha-2\beta)H_2O + (1-\alpha)CO_2 + [2 - 1.5(\alpha+\beta)](3.76)N_2$$

where α is the volume fraction of hydrogen in the $H_2/CO/CH_4$ mixture and β is the volume fraction of carbon monoxide in the same mixture.

This thesis intends to study syngas combustion properties in the numerical context. A literature review of premixed syngas combustion is given at first. Then, LPM syngas laminar flames are modeled in zero- and one-dimensional forms to understand their most important basic properties. After that, an emphasis is given to the importance of syngas reaction mechanisms by studying some of the available chemical mechanisms and how accurate they are in predicting the basic properties studied. Finally, LPM syngas combustion in a real geometry lab-scale swirl-stabilized combustor is modeled using Computational Fluid Dynamics (CFD).

1.3 Thesis Objectives

The specific objectives of this research are

- To study the effect of equivalence ratio, fuel composition, operating pressure and preheat temperature on the adiabatic flame temperature, laminar flame speed and NO emissions of syngas flames under LPM conditions.
- To evaluate the accuracy of some selected syngas reaction mechanisms for possible use in CFD applications under LPM conditions.
- To perform CFD modeling aiming at providing an insight into the flame characteristics and emissions of LPM syngas combustion in a swirl-stabilized combustor at varying swirl number, fuel composition (H_2/CO ratio) and equivalence ratio.

CHAPTER 2

LITERATURE REVIEW

This chapter presents a literature review intended to revise the work on premixed syngas combustion. The available syngas reaction mechanisms are first reviewed. This is followed by a review on the premixed syngas laminar flame properties. Finally, a review of works performed on syngas combustion in swirl-stabilized burners is presented.

2.1 Syngas Reaction Mechanisms

There has been a number of works on developing different kinetic models for syngas combustion. One of the famous kinetic models for syngas combustion was developed by Davis et al. [9]. The model consisted of 14 species and 30 reactions, which incorporated thermodynamic, kinetic, and species transport data important to high-temperatures oxidation of H_2/CO mixtures. Some important elementary steps rate parameters and three-body efficiencies were subject to optimization in order to improve the models accuracy. The optimized model was tested against available data of laminar flame speeds, ignition delay times, species mole fractions, and extinction strain rates at different operating conditions and fuel compositions. It was clearly shown that discrepancies in the previous model were resolved after performing the systematic optimization. It was believed that the optimized model can predict reliably syngas oxidation for all conditions similar to the ones presented their data in the related paper.

A 12-species, 30-step chemical mechanism was developed by Saxena et al. [10] for syngas combustion. The mechanism was tested for premixed hydrogen flames, hydrogen diffusion-flame extinction, laminar burning velocities of premixed carbon monoxide flames containing different proportions of hydrogen, and for autoignition of hydrogen-carbon monoxide mixtures. The authors achieved reasonable agreement with experiments only after alteration of some hydrogen elementary steps rate parameters as well as increasing some three-body recombination rates. In addition, a hydrogen initiation reaction was removed, and replaced by a carbon monoxide initiation step. The authors believed that these changes made the mechanism more acceptable for use in future studies.

Sun et al. [11] performed experimental study to investigate the effect of operating pressure on the laminar flame speed of different H_2/CO mixtures. Measurements of ignition temperatures and species mole fractions were taken as well. These measurements were used to validate a developed kinetic model for syngas combustion. The model consisted of 13 species and 33 elementary reactions. Furthermore, predictions from Davis mechanism and Li mechanism [12] were compared to the developed model and measurements. It was concluded that the Sun mechanism is the most accurate model among the others.

In another work, Frassoldati et al. [13] revised a 14 species, 34 reaction kinetic model for the oxidation of H_2/CO mixtures, with interest in the interactions with nitrogen species and NO_X formation. This work provided good collection of experimental measurements from literature, which were used to validate the kinetic scheme. In particular, the mechanism was validated for plug flow reactor, stirred reactor, ignition delay times, flame speeds, and ignition in a counter-flow flame and premixed flame. It was reported that the model achieved better agreement with experimental data when the rate parameters for the reactions $CO + OH \Leftrightarrow CO_2 + H$ and $CO + O\ (+M) \Leftrightarrow CO_2\ (+M)$ were changed, the latter change being suggested by ignition delay times and high-pressure data. Furthermore, NO_X model performed better when rate parameters by Skreiberg et al. [14] were implemented for the reaction $HONO + OH = NO_2 + H_2O$. The authors believed that this kinetic model is reliable since it was successfully implemented in a CFD code in another work [15].

Slavinskaya et al. [16] on the other hand developed two syngas reduced mechanisms that can be used in CFD commercial codes; a skeletal mechanism that contained 12 species and 20 irreversible reactions, and a global mechanism that comprised 5 species with 2-step reactions. The skeletal mechanism was validated against laminar flame speed for a wide range of pressures (up to 20 bars) and various equivalence ratios. However, the global mechanism had a restricted range of use, with pressure equals to 20 bars and equivalence ratio range of 0.83 to 1.67 only, as reported by the authors.

Attempts to improve existing global kinetic models for CFD applications have also been carried out. Cuoci et al. [17] improved two simplified kinetic schemes for syngas combustion; a 3-step mechanism by Westbrook and Dryer and another 3-step syngas mechanism by Jones and Lindstedt. The optimization target was a counter-flow diffusion flame, where a non-linear regression technique for the optimization process was implemented. The optimized mechanisms were applied to a turbulent jet diffusion flame, and they showed very good match with experimental data in terms of axial profiles of flame temperature compared to the original mechanisms. The authors suggested that more investigations are needed in order to make sure that the optimization procedure is feasible. However, they believed that this method is promising and could be used for the formulation of new kinetic schemes for different kinds of fuel mixtures.

Another 15 species, 44 reactions kinetic model was developed by Starik et al. [18]. The model was validated against available data on ignition delay times, laminar flame speeds, and species mole fractions. The validations were carried out for a wide range of equivalence ratio, fuel composition, operating pressure and preheat temperature. It reported that determining the basic properties of ignition and combustion depends solely on the fuel composition and equivalence ratio.

A 14 species, 16-step skeletal mechanism and a 9 species, 4-step reduced mechanism were developed by Boivin et al. [19] for syngas oxidation. It is worth mentioning that the reaction rates for the reduced mechanism are dependent upon the reactions rates of the skeletal mechanism. Though this method decreased the number of species and hence the species equations to be solved, the reaction rate calculations can still be expensive, and in fact are not mechanistically predictive i.e. do not use Arrhenius rate parameters to solve for reaction rates of the reduced mechanism. However, both mechanisms predicted experimental measurements for autoignition times and flame velocities closely, with small discrepancies in the reduced mechanism. The authors suggested that more investigation on rate parameters for elementary steps is needed in order to improve the reduced mechanism predictions. Moreover, the reduced mechanism could be used for a wide range of combustion conditions including gas turbine-like conditions, as indicated by the authors.

In a work similar to the work of Boivin et al. [19], Nikolaou et al. [20] developed a 5-step, 8 species syngas reduced mechanism based on a skeletal mechanism with 49 reactions and 17 species, derived from GRI-Mech. 3.0 model [21] using sensitivity analysis. The reduced mechanism aimed to predict mixtures with low hydrogen/methane and high water vapor contents. The steady-state and partial equilibrium approximations the species and reactions were applied for the reduction process. The 5-step reduced mechanism was validated for laminar flame speeds, heat release rates, ignition delay times, and species mole fractions using available experimental data over a wide range of pressures, preheat temperatures, and fuel compositions. In addition, the reduced mechanism was compared to the GRI-Mech. 3.0 model since the latter provided a comprehensive set of detailed elementary reactions that are known to give accurate predictions of the different flame properties. Both mechanisms, skeletal and reduced, had very good predictions when compared to experimental measurements and/or GRI-Mech. 3.0 model.

It is also a common practice to use detailed chemistry models to validate reduced chemical mechanisms in the absence or presence of experimental data. Some of these mechanisms include the GRI-Mech. 3.0 model [21] (originally for methane) and Li et al. [12] mechanism (for syngas). The GRI-Mech. 3.0 mechanism consists of 53 species with 325 elementary reactions, while the Li mechanism, called C1 model, comprises 21 species and 93 multi-step reactions (this is an updated model. The original model consisted of 84 reactions). Both mechanisms give close predictions in terms of adiabatic flame temperature and laminar flame speed calculations, as shown in Figures 1.

Some papers compared a number of kinetic models and reported the different accuracies associated with each of them. Marzouk et al. [22], for example, performed a comparative study of eight finite-rate chemistry kinetics for syngas combustion. The models studied are a global 2-step/5-species Slavinskaya, a global 3-step/5-species Watanabe and Otaka, a global 3-step/5-species Westbrook and Dryer, a 9-step/8-species Edelman and Fortune, a 21-step/10-species Westbrook and Dryer, a 34-step/14-species Frassoldati, a 37-step/14-species model

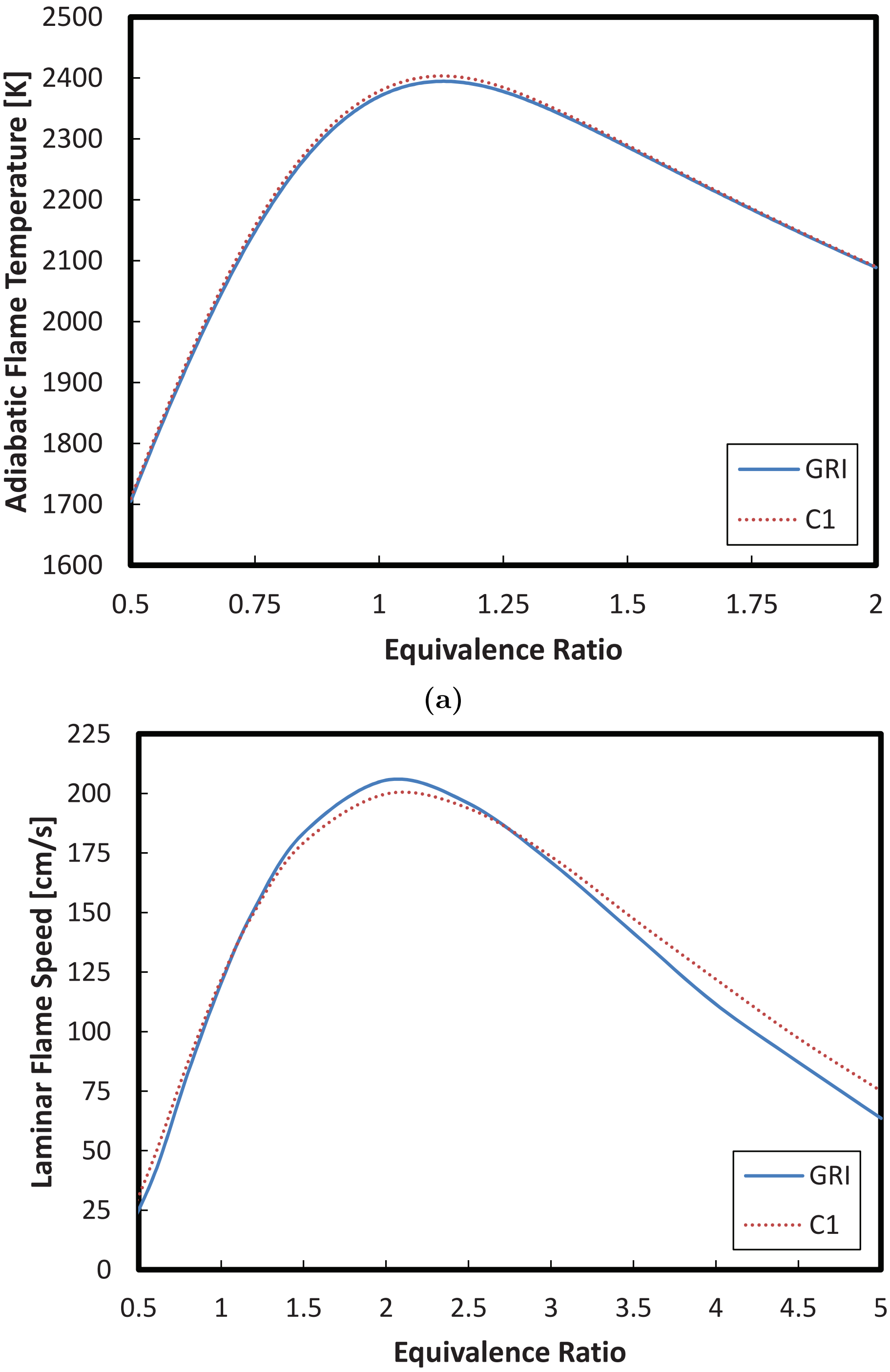

(a)

(b)

Figure 2.1: Comparison between GRI-Mech. 3.0 model and C1 model in terms of (a) adiabatic flame temperature and (b) laminar flame speed of syngas mixture. $H_2/CO = 50/50$, $p = 1atm$, and $T_u = 300K$

from Polytechnic of Milan, which is an extension of the Frassoldatis model, and a 38-step/13-species model which was referred to as UODE. The previous models were used to predict the combustion of a turbulent non-premixed syngas flame diluted with 30% nitrogen. The different flame characteristics were examined for all kinetic models, and accuracy and performance in terms of CPU time were noticed. Furthermore, it was observed that the global mechanism of Westbrook and Dryer was the best to predict the experimental data, and hence it was suggested that it should be used for CFD modeling of turbulent syngas flames.

A summary of all kinetic models previously mentioned in the literature is given in Table 2.1.

Table 2.1: Summary of most kinetic models used for syngas oxidation

Model	Species Number	Steps Number	Reference
GRI-Mech. 3.0	53	325	[21]
Li	21	93	[12]
Nikolaou	17	49	[20]
Starik	15	44	[18]
Polytechnic of Milan	14	37	[22]
Davis	14	30	[9]
Frassoldati	14	34	[13]
Boivin	14	16	[19]
UODE	13	38	[22]
Sun	13	33	[11]
Saxena	12	30	[10]
Westbrook and Dryer	11	21	[22]
Slavinskaya	10	20	[16]
Boivin	9	4	[19]
Fortune and Edelman	8	9	[22]
Nikolaou	8	5	[20]
Westbrook and Dryer	5	3	[17]
Jones and Lindstedt	5	3	[17]
Watanabe and Otaka	5	3	[22]
Slavinskaya	5	2	[16]

Most of the developed mechanisms have been validated against experimental values of laminar flame speed. The use of laminar flame speed for the validation of the chemistry is due to the fact that the flame speed is the controlling parameter of the stabilization locations of the flame [23, 24]. In addition, many turbulent combustion models require the laminar flame speed as an input. So, capturing it by the kinetic model is important. Various researchers have verified the accuracy of isolated kinetic models for syngas and further used it to understand the combustion dynamics at various conditions. Prathap et al. [25] carried out experimental and numerical investigations using Davis et al. mechanism [9] to study the effect of nitrogen and carbon dioxide dilution on the laminar flame speed of syngas, while Yousefian et al. [26] reported using Davis et al. kinetic mechanism [9] that increasing preheat temperature, pressure, and decreasing the level of dilution with N_2 and CO_2, increase the laminar flame speed with the extinction limits extended. Bouvet et al. [27] reported that the mechanism of Li et al. [12] agrees well with the data of McLean et al. [28]. However, it over-predicts the data of Sun et al. [11] at rich-fuel conditions. In another work, Sung et al. [29] reported that laminar flame speeds of $H_2/CO/air$ mixtures are best predicted by Li et al. mechanism [12], while Bouvet et al. [30] reported that the mechanisms of Sun et al. [11] and Li et al. [12] give similar predictions of laminar flame speed for lean premixed syngas flames. Yepes et al. [31] carried out experimental and numerical study of the laminar burning velocity of syngas and air enriched with oxygen using GRI-Mech. 3.0 [21], Davis et al. [9] and Li et al. [12] mechanisms and observed that laminar burning velocity increases with the concentration of the oxygen in the mixture with the GRI-Mech. 3.0, Davis, and Li mechanisms being the best that predict it. Natarajan et al. [32] reported that the measured flame speeds for H_2/CO mixtures with and without CO_2 dilution can be predicted by the Davis mechanism [9] more accurately than the GRI-Mech. 3.0 mechanism [21]. This better agreement is more pronounced at high H_2 content in syngas. Monteiro et al. [33] similarly used Davis et al. [9] and GRI-Mech. 3.0 [21] mechanisms to show that increasing the pressure and decreasing the preheat temperature decreases the laminar burning velocity which compared reasonably with the corresponding experimental values. Fu et al. [34] showed that laminar flame speed predictions for different syngas compositions using Li et al. mechanism [12] match well with its corresponding experimental data.

Beside the laminar flame speed, NO_X emission is also an important parameter of interest in combustion to meet the stringent environmental regulation. The EU for example is committed to reduce its emissions by 20% under the Kyoto Protocol's second period, which runs from 2013 to 2020. Accurate prediction of the NO_X is central to meeting the emission requirement and depends on both the combustion chemistry and NO_X model being implemented. Iyer et al. [35] used the GRI-Mech. 3.0 [21] predictions to show that single-digit NO emissions could be maintained for combustor exit temperatures of less than $1800K$ for a perfectly premixed system. However, 20% decrease in degree of premixing could potentially increase NO emissions by a factor of two. In another work, Chun et al. [36] used the GRI-Mech. 3.0 to show that conditions that can achieve high extinction stretch rates can lead to an increase in the NO_X production. Moreover, Giles et al. [37] used the GRI-Mech. 3.0 to show that CO_2 and H_2O are more effective than N_2 in reducing NO_X in syngas flames. Ding et al. [38] on the other hand used Davis et al. mechanism [9] to show that for different compositions of syngas, higher CO concentration leads to higher NO emissions. In addition, Rortveit et al. [39] showed that measured NO emissions compared well with values calculated using Li et al. kinetic model [12] at lower operating temperatures, but begins to differ as the temperature increased, up to a factor of 2 for the hottest flames.

2.2 Premixed Syngas Laminar Flame Characteristics

It is well-known that understanding laminar flames is essential for understanding the behavior of turbulent flames, since laminar flames are flames with very low or no turbulent intensity. A laminar flame, once affected by turbulence, will change properties, becoming a turbulent flame eventually. Therefore, understanding this kind of transition and interactions between turbulence and laminar flames makes a basis for turbulent combustion study. Despite the fact that combustion characteristics of conventional hydrocarbon fuels e.g. methane have been fairly well studied, the characteristics of alternative fuels, such as syngas, are not fully identified. In the laminar flame context, these characteristics include adiabatic flame temperature, laminar flame speed, laminar flame thickness, flame ignition and extinction, flame stretch, and pollutant emissions, which can be affected by a wide range of mixture composition, equivalence ratio, operating pressure and inlet temperature. Diluents present in the fuel can also affect the previous properties.

2.2.1 Adiabatic Flame Temperature

In flames, cold reactants are converted into hot products at constant pressure. Thus, the adiabatic flame temperature (AFT) can be defined as the maximum, equilibrium temperature of the products without any heat release to or from the ambient at constant pressure. The AFT is one of the most important parameters related to fuel combustion for a number of reasons. First, the flame temperature is responsible for the production of thermal NO_X through the Zeldovich mechanism which dominates beyond $1800K$. In addition, flame propagation and extinction is highly influenced by the flame temperature.

A good starting point to study AFT of syngas is to compare it with different pure gaseous fuels. This comparison can be shown in Figure 2.2 [40] where the AFT of a typical syngas mixture made of 35% H_2, 35% CO, and 30% CO_2 is compared to those of pure fuels, namely CH_4, H_2, and CO. Among the three pure fuels (CH_4, H_2, and CO), CO has the highest AFT for a specific equivalence ratio, whereas CH_4 has the lowest. Moreover, CO AFT is slightly higher than that of H_2 for a given equivalence ratio. This is due to the higher lower heating value of CO (11.4 MJ/m^3) as compared to H_2 (9.8 MJ/m^3). Syngas on the other hand

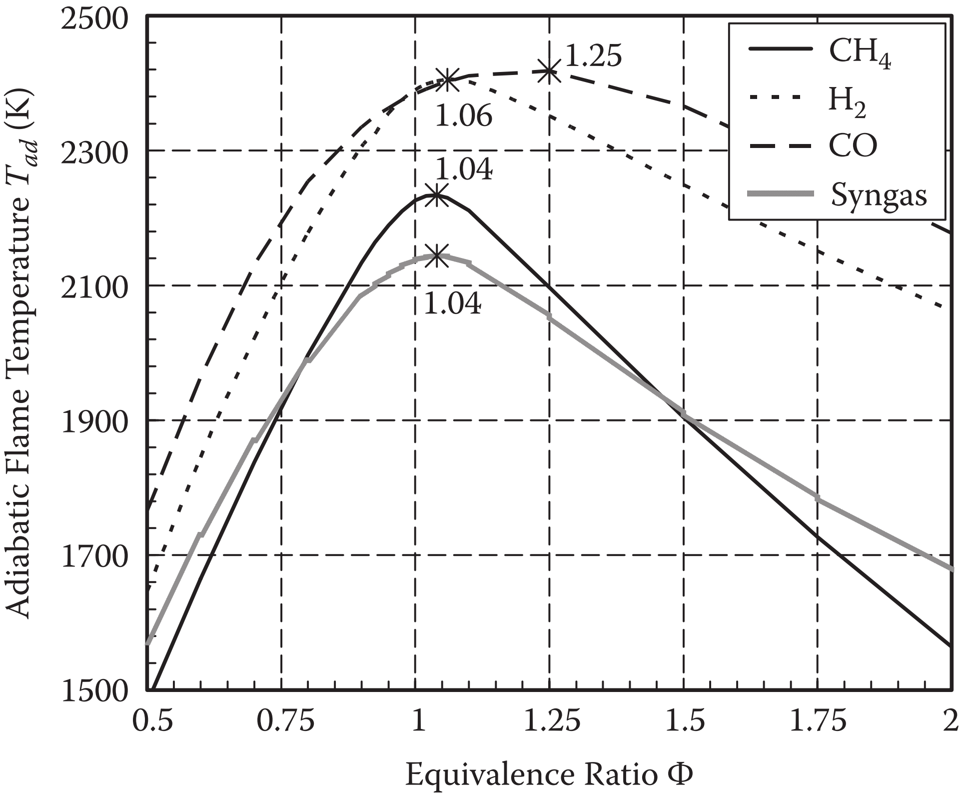

Figure 2.2: Adiabatic flame temperatures for CH_4, H_2, CO, and typical syngas (35% H_2, 35% CO, and 30% CO_2) fuels burning with air at atmospheric pressure and 300K initial temperature [40]

is noticed to have AFT lower than that of all fuels. This is due to the fact that a considerable amount of dilution exists in the syngas i.e. 30% CO_2. The flame temperature of diluted syngas, however, is close to methane flame temperature in this case, with approximately 100 K temperature difference. For all fuels shown, the maximum AFT exists at slightly rich mixtures ($\phi = 1.04$ for CH_4 and diluted syngas, 1.06 for H_2, 1.25 for CO and 1.15 for undiluted syngas).

Effect of H_2/CO Ratio

Syngas different compositions can have an effect on the AFT. This effect is shown in the following two figures. Figure 2.3 [41] shows the AFT and flame speed of three different H_2/CO compositions as a function of equivalence ratio. For all three compositions, the maximum AFT occurs at almost stoichiometric conditions, but not close to the equivalence ratio at which the peak flame speed occurs. More discussion about flame speed will be given later. Though all three compositions show close similarity in temperatures, the AFT tends to increase as the level of CO increases, owing to the higher heating value associated with CO oxidation as mentioned before. Figure 2.4 [42] on the other hand shows the increasing effect of CO level in the range between $\phi = 0.25$ and $\phi = 0.6$, where the AFT increases as CO level increases (or H_2 level decreases) in the syngas.

Effect of Dilution

The presence of diluents such as, carbon dioxide (CO_2), steam (H_2O), nitrogen (N_2), or methane (CH_4) in syngas can influence its combustion characteristics sig-

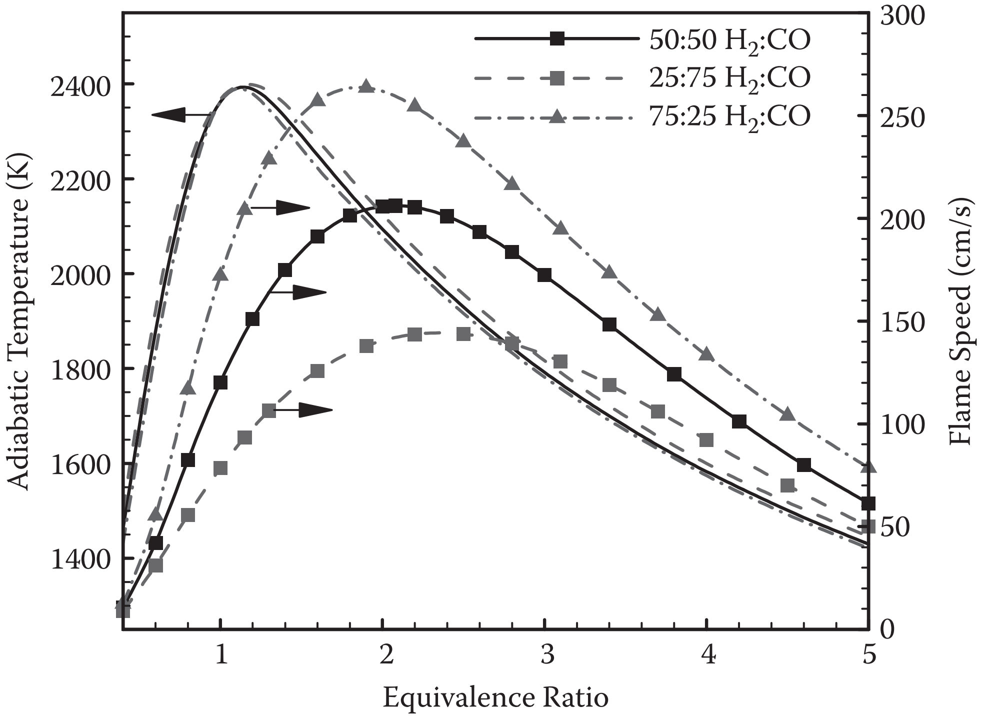

Figure 2.3: Adiabatic flame temperature (lines) and flame speed (symbols and lines) as a function of equivalence ratio for 25:75, 50:50, and 75:25 H_2/CO mixtures [41]

nificantly. Adding a diluent to the fuel mixture will reduce the flame temperature, and consequently the laminar burning velocity. Figure 2.5 [41] shows the effect of N_2, H_2O, and CO_2 dilution on the AFT for a 50/50 H_2/CO mixture at $\phi = 1.0$. It is noticed for the same amount of dilution (%), CO_2 has the highest reduction effect on the AFT when compared to the other diluents, while N_2 has the lowest effect. This can be explained by the heat capacity of the diluents where CO_2 has the highest value and N_2 has the lowest. The mass fractions of the diluents and burned CO_2 is also shown in the figure. Generally, increasing the volume fraction (dilution %) of a specific diluent increases its mass fraction in the mixture. In the case of N_2 and H_2O dilution, burned CO_2 does not change significantly as the percentage of dilution increases; in fact, slight decrease is noticed. For CO_2

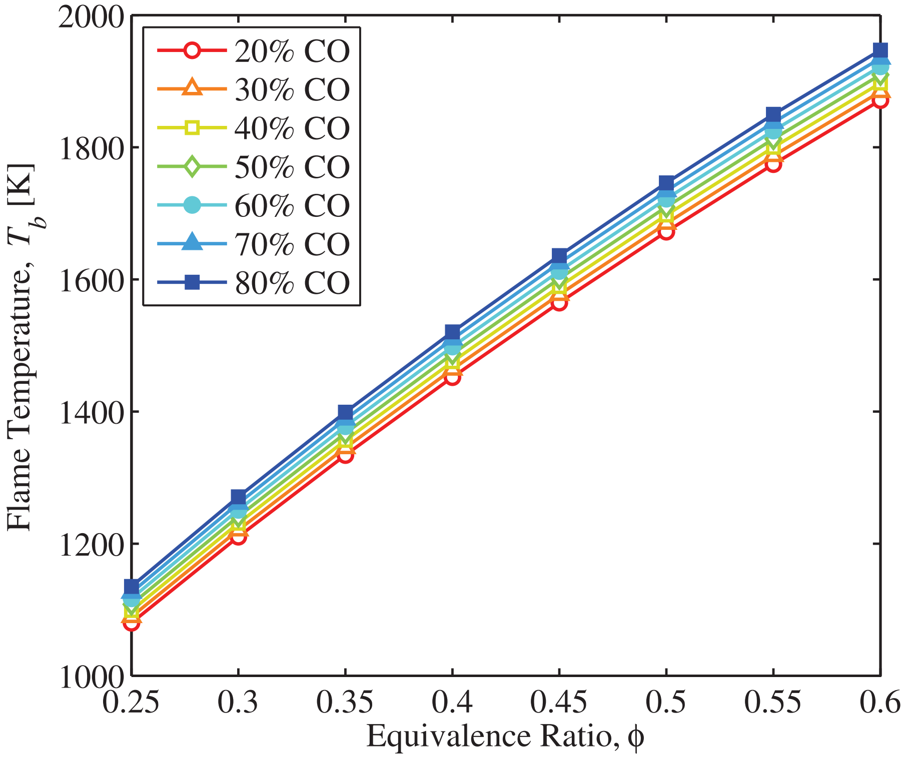

Figure 2.4: Adiabatic flame temperature of syngas flames as a function of equivalence ratio and fuel composition [42]

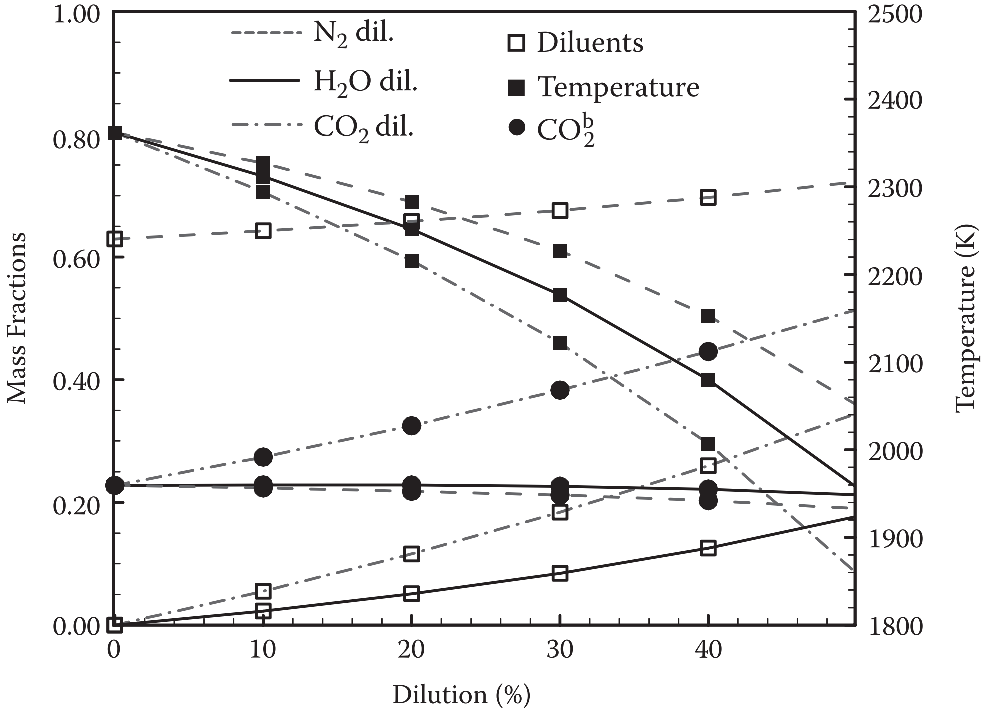

Figure 2.5: Effect of dilution (N_2, H_2O, or CO_2) on adiabatic flame temperature for a 50/50 H_2/CO mixture at $\phi = 1.0$. Superscript b indicates burned [41]

dilution, however, burned CO_2 is noticed to increase as the dilution percentage increases. In summary, while undiluted syngas mixtures would have higher flame temperatures than conventional methane fuels, increasing the dilution level in syngas would result in lowered flame temperatures that are comparable to those of methane (as can be seen from Figure 2.2).

Effect of Pressure and Preheat Temperature

Figure 2.6 [40] shows the impact of pressure and initial reactants temperature on the AFT for three different conditions. For $T_u = 300\ K$, there is no significant influence on the AFT as the pressure increases from 1 to 30 atm. For stoichiometric conditions, however, a small increase in AFT (in the order of 50 K) occurs due to the high-pressure suppression of product dissociation which matters only in high AFT regions i.e. near stoichiometric conditions. Suppression of product dissociation is also responsible for shifting the maximum flame temperature toward stoichiometric equivalence ratio (from $\phi = 1.04$ to $\phi = 1.02$).

The reactants initial temperature is very important in many combustion systems, for instance, due to compression or heat waste recovery. The preheat temperature effects on AFT can be inferred from Figure 2.6 [40]. Increasing the reactants temperature while keeping the pressure, results in increasing the AFT. Considering this case, increasing the initial reactants temperature from 300 K to 700 K results in increasing the AFT by around $300K$ at $\phi = 0.5$ and $\phi = 2$, but only 200 K at $\phi = 1$. This is due to the high temperature product dissociation (near stoichiometric conditions) which reduces the energy required to raise the products temperature, causing lower temperature increase near stoichiometry.

2.2.2 Laminar Flame Speed

The laminar flame speed (LFS) is the main parameter that characterizes flame propagation in premixed combustion. It is defined as the velocity at which a flame propagates towards the unburned gases [43]. Flame speed is important in determining flashback and blow off velocities, relevant to flame stability, since a stationary flame is accomplished when the local flow velocity matches the flame speed. Many factors can influence the LFS such as, H_2/CO ratio, dilution, pressure, and preheat temperature.

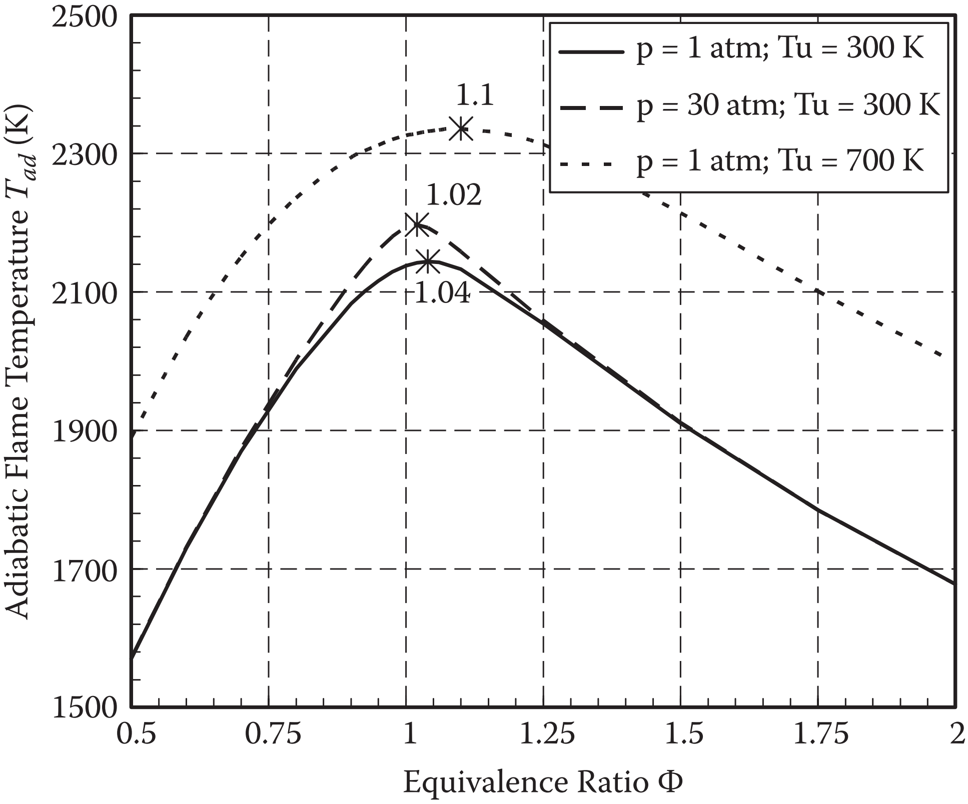

Figure 2.6: Influence of pressure and preheat temperature on adiabatic flame temperature for typical syngas (35% H_2, 35% CO, and 30% CO_2) fuel burning with air [40]

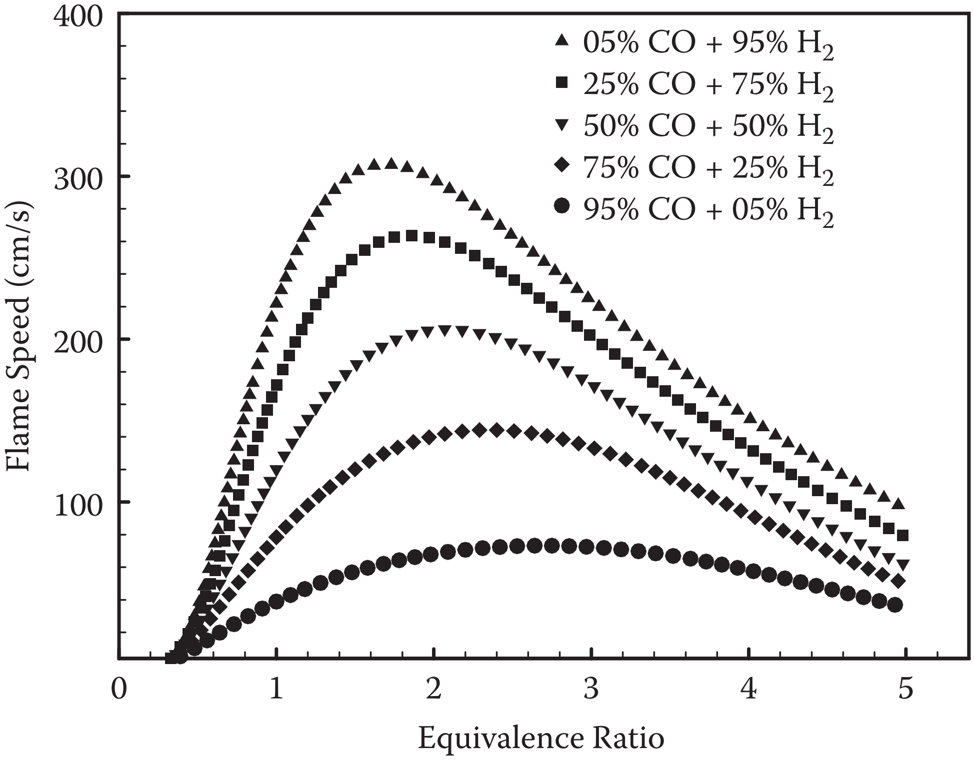

Figure 2.7: Flame speeds as a function of equivalence ratio for various H_2/CO mixtures. $p = 1atm$ and $T_{in} = 300K$ [41]

Effect of H_2/CO Ratio

Figure 2.7 [41] shows the LFS as a function of equivalence ratio for different H_2/CO compositions. For a specific equivalence ratio, the flame speed increases as the H_2 level in the fuel mixture increases. Also, as the level of H_2 content in syngas increases, the peak flame speed shifts toward stoichiometry.

Effect of Dilution

The effect of the different diluents (CO_2, H_2O and N_2) on the LFS is shown in Figure 2.8 [41]. For a given diluent and equivalence ratio, the flame speed decreases as the dilution (%) increases. For a specified dilution percentage and

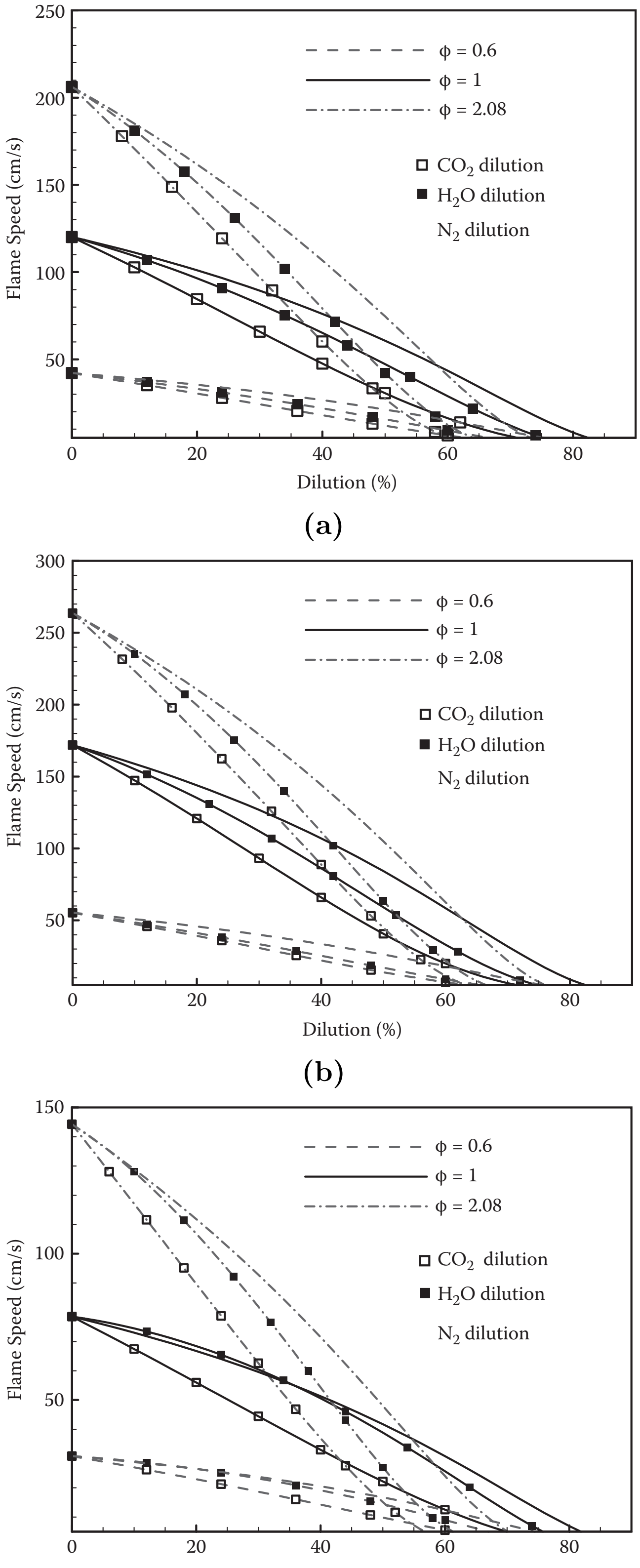

(a)

(b)

(c)

Figure 2.8: Flame speed response to variable CO_2, H_2O, and N_2 dilution for (a) 50:50, (b) 75:25, and (c) 25:75 H_2/CO mixtures at three equivalence ratios [41]

equivalence ratio, however, the flame speed is highly affected by CO_2, followed by H_2O and then N_2. Also, we notice that the effect of dilution increases with the equivalence ratio. This can be noticed from comparing the slopes of the curves.

Effect of Pressure

Pressure has a negative influence on the LFS. Figure 2.9 [40] presents the effect of pressure on the flame speed for a 50/50 H_2/CO fuel mixture at lean, stoichiometric, and rich conditions, with the flame speed normalized by the LFS at 1 atm. The increase in pressure causes the total reaction rate to increase since molecular collision rates increase, which tends to increase the flame speed. On the other hand, more energy is needed to heat the reactants, since their density is increased with pressure. This will cause the thermal diffusivity to decrease, outweighing the increased reaction rate. The net effect of pressure increase is a reduced flame speed. Figure 2.10 [40] indicates that syngas different compositions have a weak effect on the pressure dependency of the LFS. The simulation is for a fuel-lean mixture ($\phi = 0.6$).

Effect of Preheat Temperature

Figure 2.11 [32] presents the LFS as a function of equivalence ratio (from $\phi = 0.55$ to $\phi = 1.05$) for three H_2/CO syngas compositions at $1 atm$ for different preheat temperatures (from $T_u = 300\ K$ to $T_u = 700\ K$). It is clearly shown that the flame speed increases with the preheat temperature, since increasing the reactants initial temperature increases the thermal diffusivity and decreases the unburned

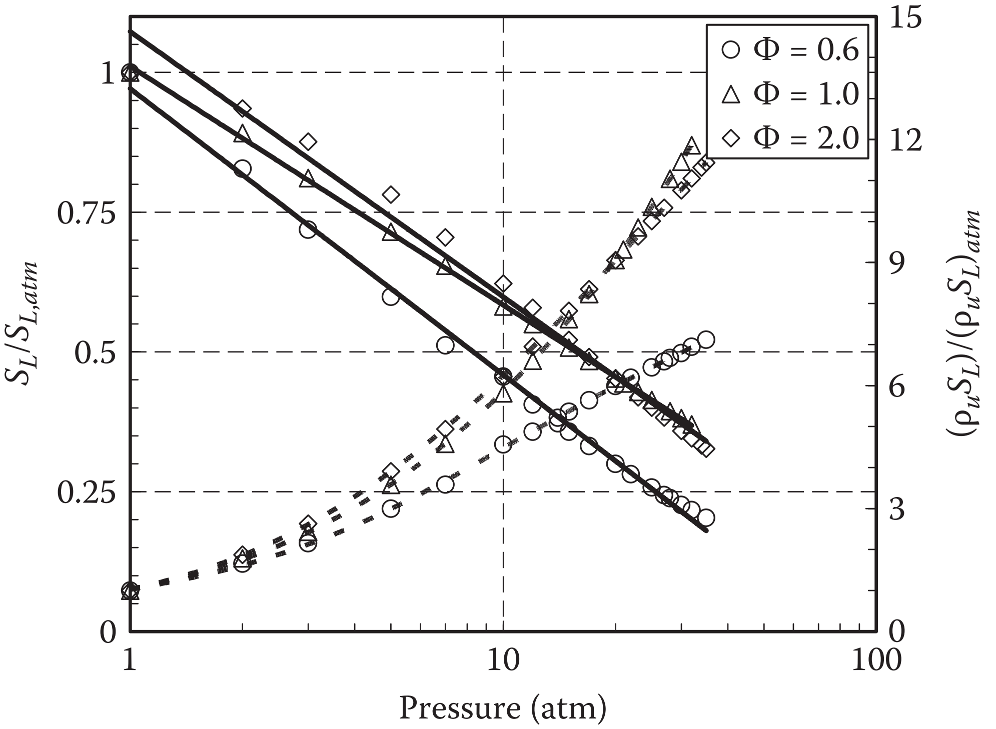

Figure 2.9: Laminar flame speed as a function of pressure for a 50/50 H_2/CO fuel mixture at $T_u = 300K$ (symbols = simulations, lines = curve fits) [40]

mixture density, which all result in increasing the flame speed.

2.2.3 Laminar Flame Thickness

In order to develop an understanding of the premixed syngas laminar flame propagation, it is important to have an idea about the flame structure. Figure 2.12 [41] shows the flame structure of premixed laminar flame (1-D domain) in terms of major and minor species mass fractions and temperature along the position for different equivalence ratios ($\phi = 0.6$, 1.0, and 2.08) of a 50/50 H_2/CO mixture in air. The maximum equivalence ratio corresponds to the peak flame speed.

In lean mixtures, H_2 and CO are completely oxidized to produce CO_2 and H_2O. In rich mixtures, a considerable amount of CO is unburned, with increasing

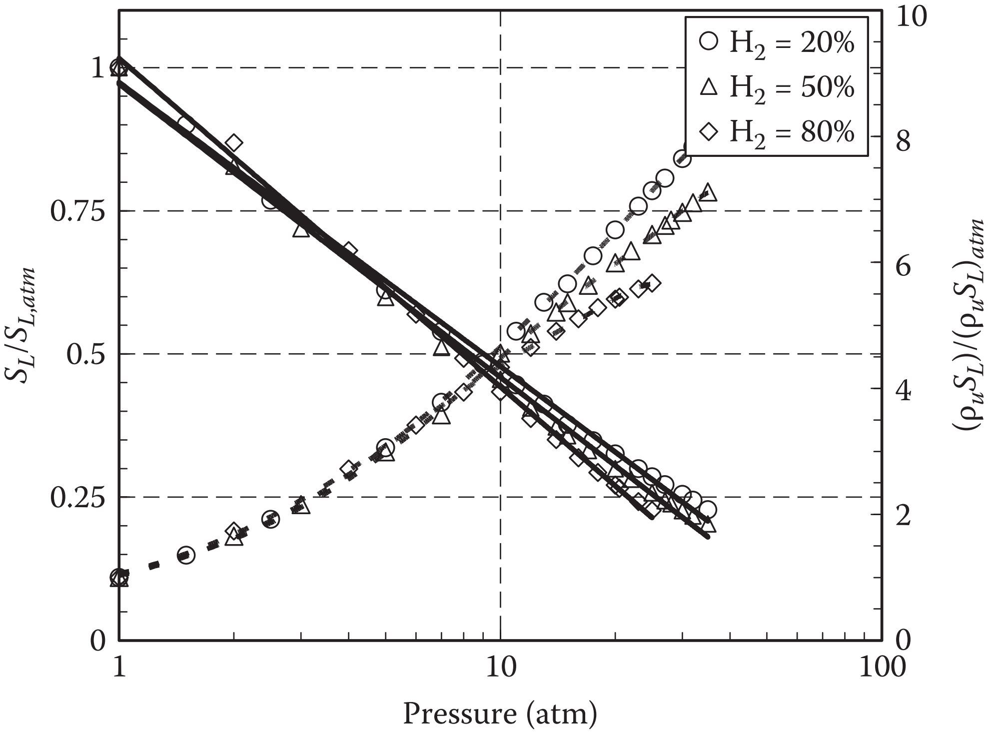

Figure 2.10: Laminar flame speed as a function of pressure for three H_2/CO fuel mixtures at $\phi = 0.6$ and $T_u = 300K$ (symbols = simulations, lines = curve fits) [40]

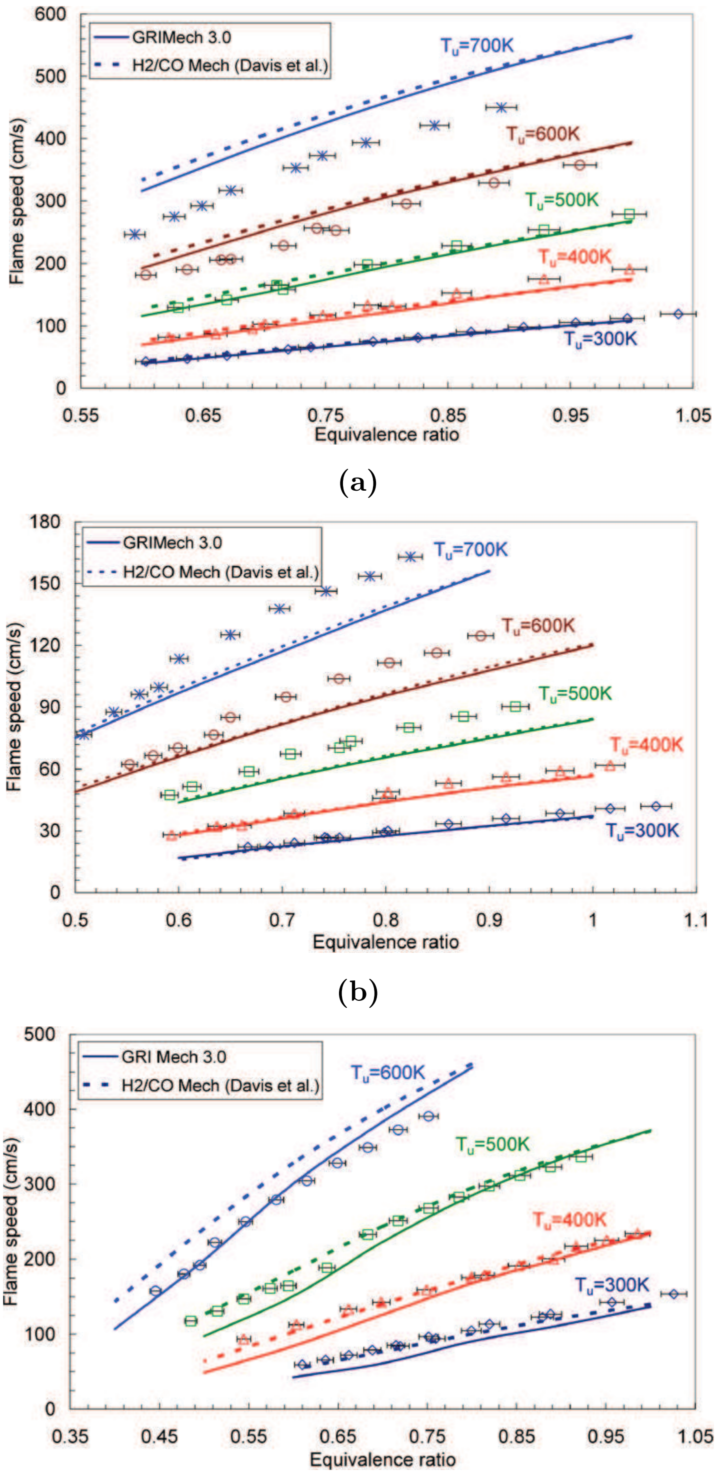

(a)

(b)

(c)

Figure 2.11: Laminar flame speed for fuels with (a) 50/50, (b) 5/95, (c) 95/5 H_2/CO compositions for various preheat temperatures at $p = 1atm$; Bunsen flame measurements (symbols) and PREMIX predictions (lines) [32]

concentration of CO in the burned side due to CO_2 dissociation. Another notable thing is that increasing the equivalence ratio leads to a decrease in the flame thickness, another important parameter for evaluating the flame speed, as can be seen when H_2O_2 concentrations over different equivalence ratios are compared.

The flame thickness can be defined based on temperature [44] as the ratio of the temperature rise to the maximum temperature gradient, that is $\delta_L = \Delta T/\nabla T_{max}$. Figure 2.13 [40] shows the effect of syngas composition and equivalence ratio on the flame thickness. It is clearly shown that increasing the content of H_2 in the fuel mixture, causes the flame thickness to decrease. Moreover, for a fixed H_2 content, the flame thickness decreases as the equivalence ratio increases.

Other influences on the LFT include pressure and preheat temperature. Figure 2.14 [40] shows the impact of pressure on the flame thickness for different equivalence ratios. It is noticed that as pressure increases, the LFT decreases. In addition, the decrease in flame thickness is steep at lower pressures and reduces at elevated pressures, with lean mixtures revealing a greater decline in pressure reliance. Again, for a given pressure, the LFT decreases with increasing the equivalence ratio.

The reactants initial temperature can influence the LFT as well. Figure 2.15 [40] shows that increasing the initial temperature of reactants, causes an increase in the LFT. Despite the fact that increasing the preheat temperature causes the overall reaction rate to increase, the increase in thermal and mass diffusivities dominates, causing the flame thickness to increase, with less dependency for very

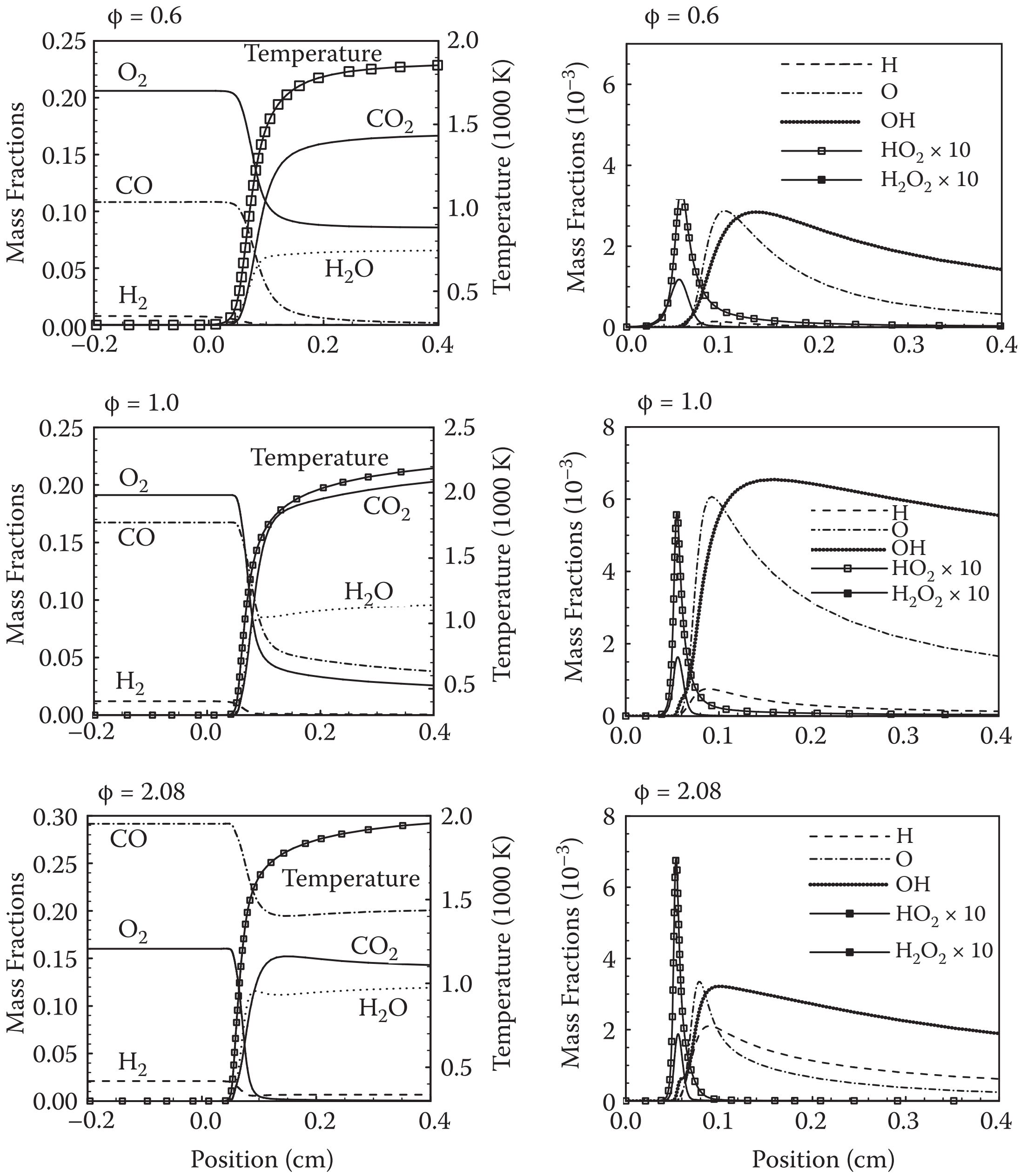

Figure 2.12: Spatial distributions of major and minor species for a 50/50 H_2/CO mixture at $\phi = 0.6$, $\phi = 1.0$ and $\phi = 2.08$ [41]

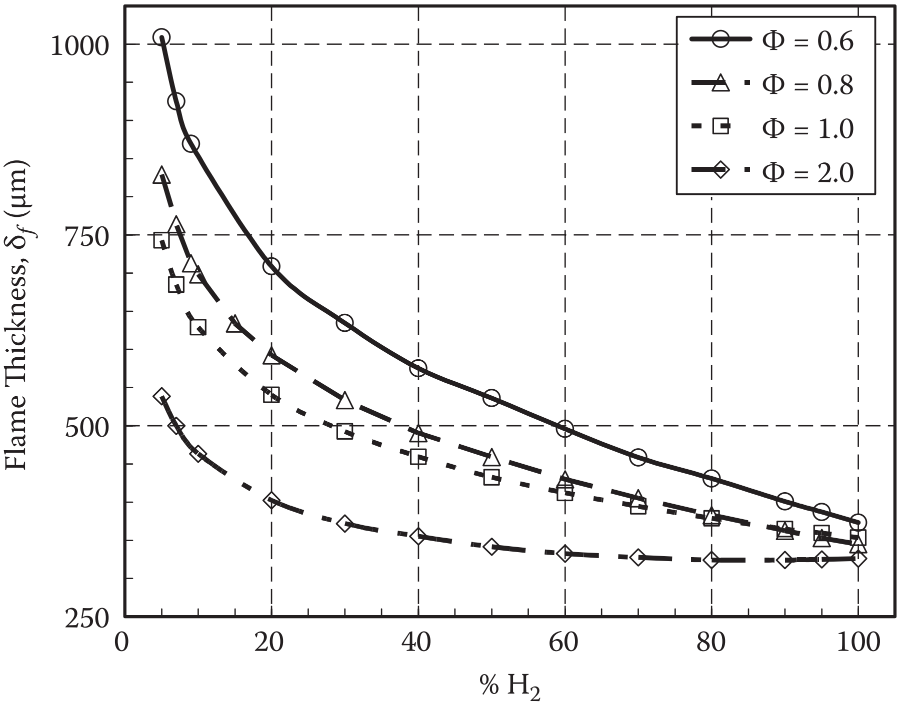

Figure 2.13: Laminar flame thickness from simulations for a range of H_2/CO fuel mixtures at $p = 1atm$ and $T_u = 300K$ [40]

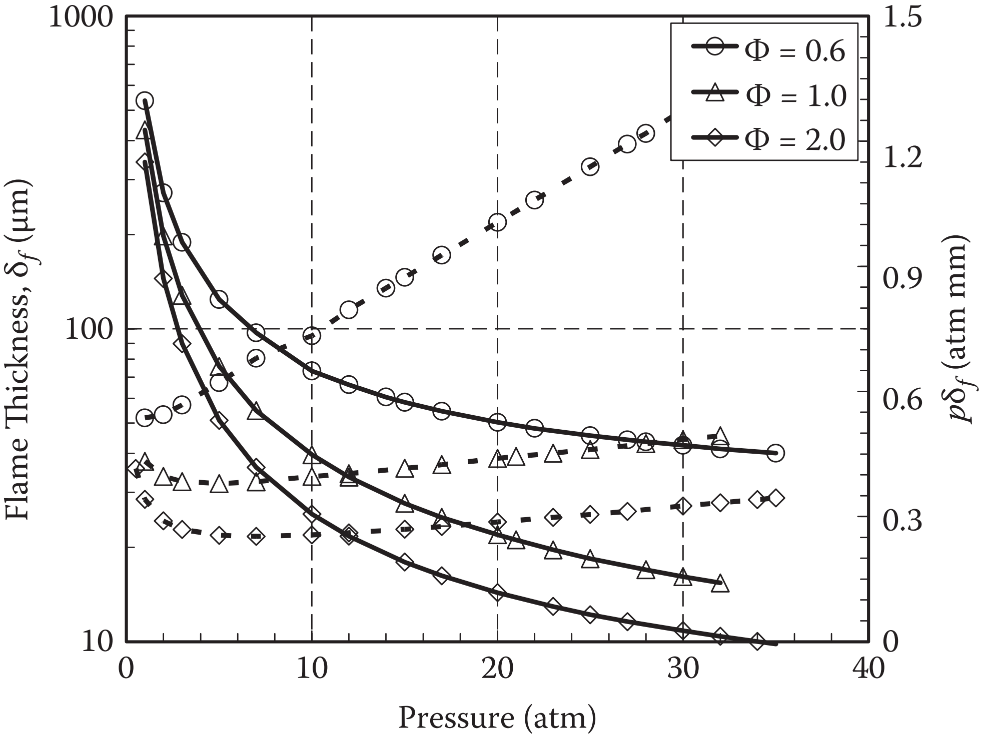

Figure 2.14: Pressure dependence of laminar flame thickness from simulations for a 50/50 H_2/CO fuel mixture at $T_u = 300K$ [40]

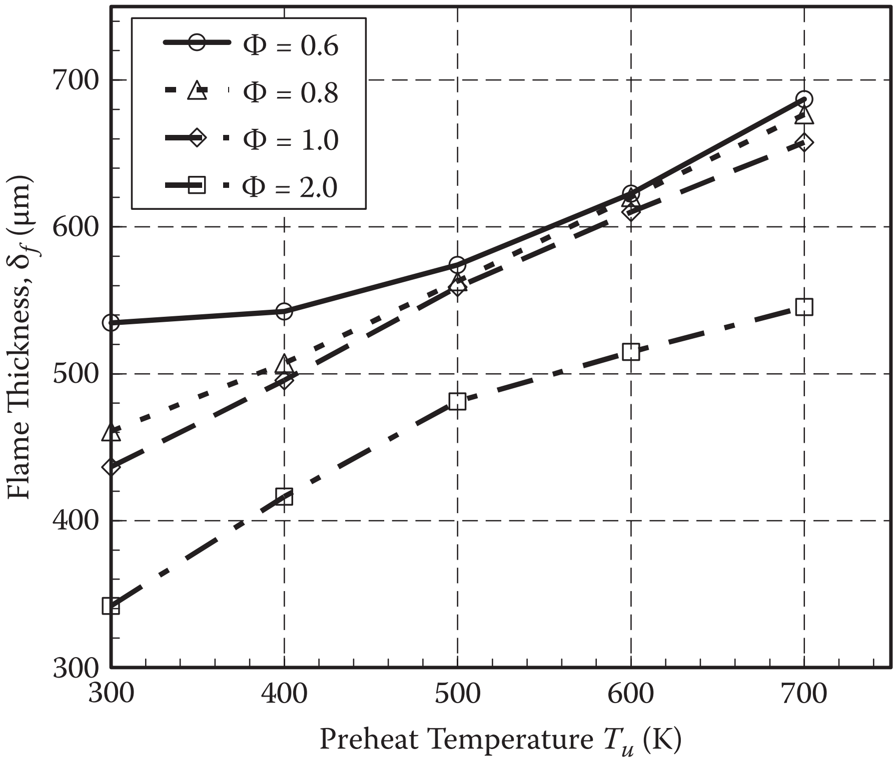

Figure 2.15: Laminar flame thicknesses as a function of preheat temperature from simulations for four H_2/CO fuel-air mixtures at $p = 1atm$ [40]

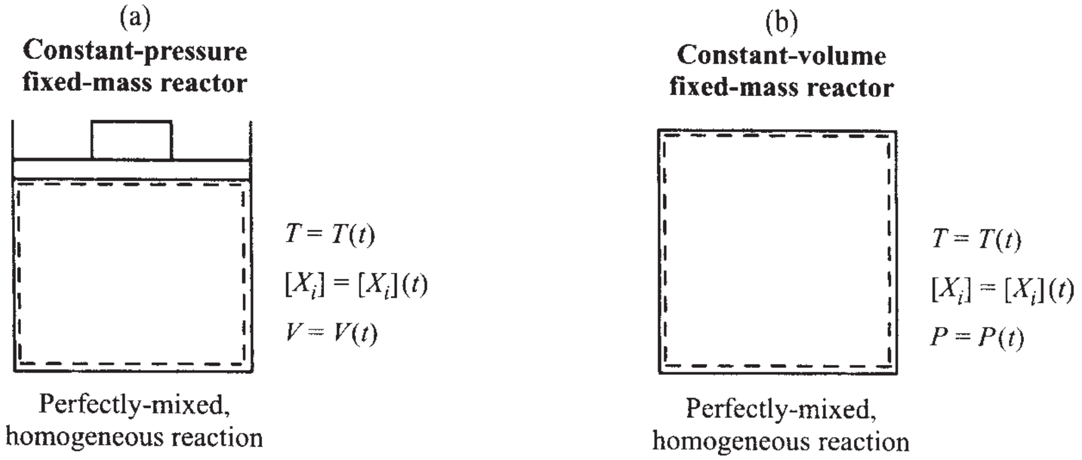

Figure 2.16: Schematic view of (a) a constant-pressure and (b) a constant-volume closed homogenous reactors [43]

lean mixtures, as can be seen from the figure.

2.2.4 Flame Ignition and Extinction

The ignition and extinction properties of syngas differ significantly from conventional hydrocarbons. Two systems, closed homogenous reactor (HR) and well stirred reactor (WSR), are used to determine those characteristics in terms of ignition and extinction time delays. An HR and a WSR characterize two different situations in terms of mixing properties. The HR (Figure 2.16 [43]) is a closed system where the composition and temperature of fuel-air mixture are uniformly distributed in system's space but changes with time. On the other hand, the WSR (Figure 2.17 [43]) is an open system where the composition and temperature of the fuel-air mixture at the inlet differ from their equivalents in the reactor. Thus, a growing pool of products and intermediate species are encountered in the case of a WSR, in which they mix instantly with the reactants mixture.

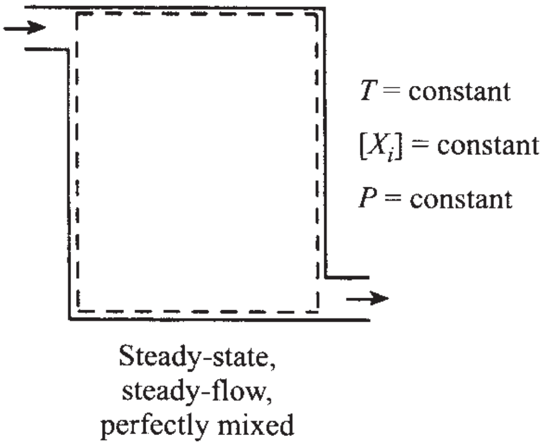

Figure 2.17: Schematic view of a well/perfectly stirred reactor [43]

For a WSR, the ignition time delay is specified as the residence time necessary for the onset of significant heat release when no external source of ignition is used. The extinction time, in contrast, is defined as the residence time required for an already ignited mixture to extinguish inside the WSR. For an HR, the ignition time delay is identified as the time delay prior to a sharp temperature increase due to continuing exothermic chemical reactions.

CHEMKIN (2004) code [45] was used to analyze the ignition and extinction times for syngas with a 50/50 H_2/CO fuel mixture. Table 2.2 compares the resulted ignition time delays for three different cases at stoichiometric conditions, $T = 700\ K$, and $p = 20\ atm$. As can be seen from the table, for both the WSR and HR, the shortest ignition time delays are presented by the H_2/CO mixture. Also, we can notice that methane, hydrogen, and syngas ignition delays are decreasing gradually in the previous order. This indicates that combustion systems containing hydrogen require additional care to ensure that the operation is safe.

Table 2.2: Ignition delay times[a] at stoichiometric conditions (700 K, 20 atm; oxidizer: air) [41]

Reactor	H_2/CO **(50/50)**	H_2	CH_4
Well Stirred Reactor	13.5[b] 18[c]	26[b] 19[c]	29[b]
Homogenous Reactor	50[b]	104[b]	187[b]

[a] Unit: Seconds
[b] Using GRI-Mech. 3.0
[c] Using Li et al. mechanism

Figure 2.18 [41] shows the WSR and HR ignition delay times for syngas as a function of the mixture temperature at 1atm and varying equivalence ratios. At high temperatures, the predicted and measured ignition delay times are reasonably compared, but the model over-predicts the ignition delay at low temperatures. This, probably, can be explained by the pressure sensitivity of the $H_2/CO/O_2$ kinetic mechanism, where most of the experiments were carried out at high pressures.

From Figure 2.18 [41], we can see that as the temperature increases, the ignition delay decreases. Moreover, there are two temperature ranges characterizing the ignition delay times for the two reactors. In the range 650 K to 1000 K, the ignition delay for the HR is about ten times higher than that for the WSR. In the range 1000 K to 2000 K, on the other hand, the ignition delay for the HR is only about twice that for the WSR. The lower times related to the WSR can be explained, mostly, by the perfect mixing of the reactants mixture with the produced intermediate species and products. Another notable thing is that the ignition delay for the HR is highest for lean mixtures, followed by stoichiometric

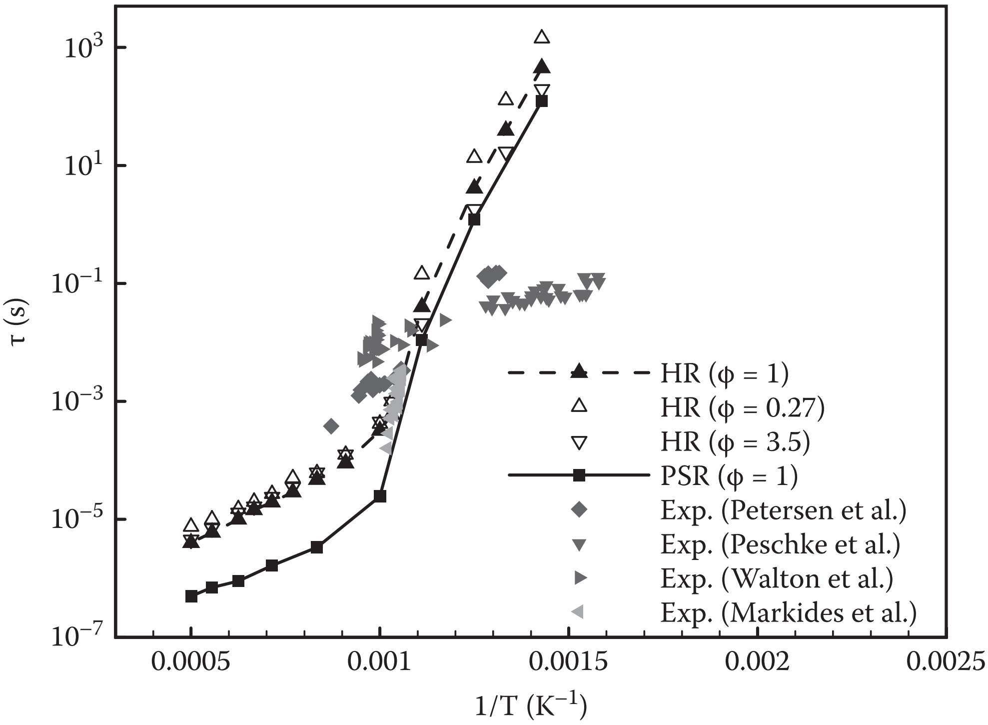

Figure 2.18: Ignition delay times for homogenous and well stirred reactors as a function of temperature for H_2/CO mixtures in air ($1atm$) [41]

conditions and then rich mixtures.

Figure 2.19 [41] represents the ignition and extinction delay times for a WSR as a function of temperature for different syngas fuel mixtures. At high temperatures, ignition and extinction times are comparable, but the latter is much smaller than the former at low temperatures. For fuel-lean and stoichiometric conditions, the extinction times overlap. However, they are much larger for lean mixtures at temperatures lower than about 1000 K.

2.2.5 Flame Stretch

Flame extinction in premixed combustion is caused mainly by flame stretch. The stretch is defined as the fractional rate of change of the flame surface area. It is

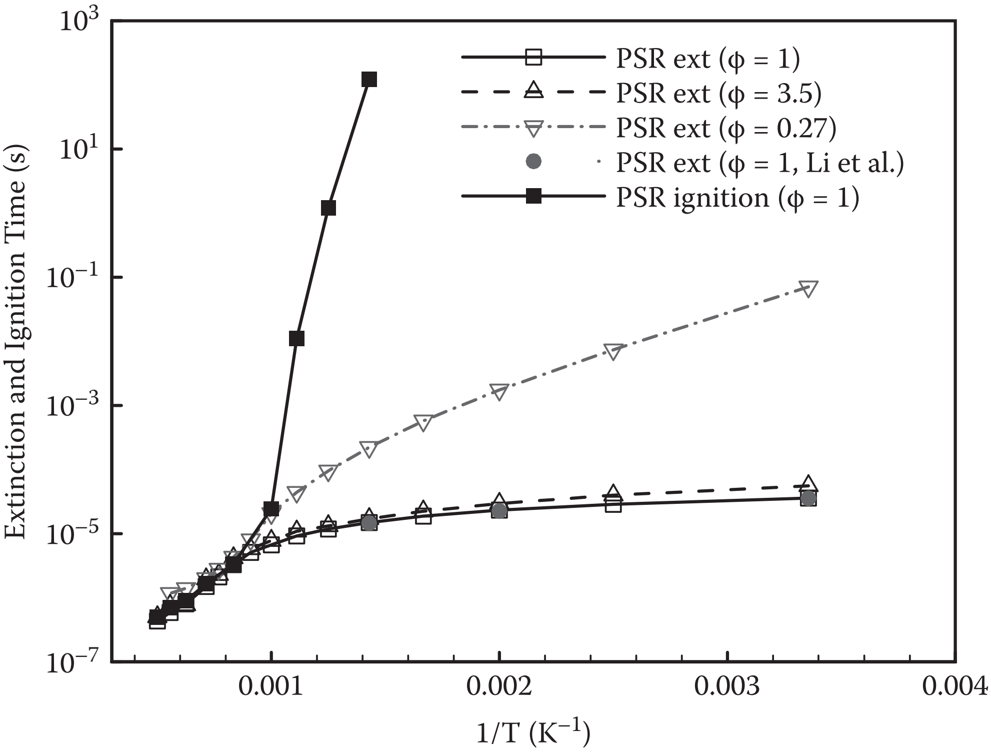

Figure 2.19: Ignition and extinction delay times for a well stirred reactor as a function of temperature for H_2/CO mixtures in air ($1atm$) [41]

primarily due to the tangential strain, i.e. velocity gradients in the incoming flow, and flame curvature [44]. Stretch effects can be characterized by the so-called strain rate (K), which is the maximum gradient of the axial velocity ahead of the minimum velocity before the preheat zone. At sufficiently high strain rates, the flame temperature and heat release rates are significantly decreased, causing the flame to extinguish. The corresponding strain rate is called the extinction strain rate (K_{ext}). The extinction strain rate is a fundamental property of the fuel-air mixture that contributes to flames stability phenomena, like liftoff and blowout. Figure 2.20 [46] shows the variation of the extinction strain rate as a function of syngas composition for two lean mixtures ($\phi = 0.32$ and $\phi = 0.39$). It is clearly shown that the amount of H_2 has a significant effect on K_{ext}. As the percentage

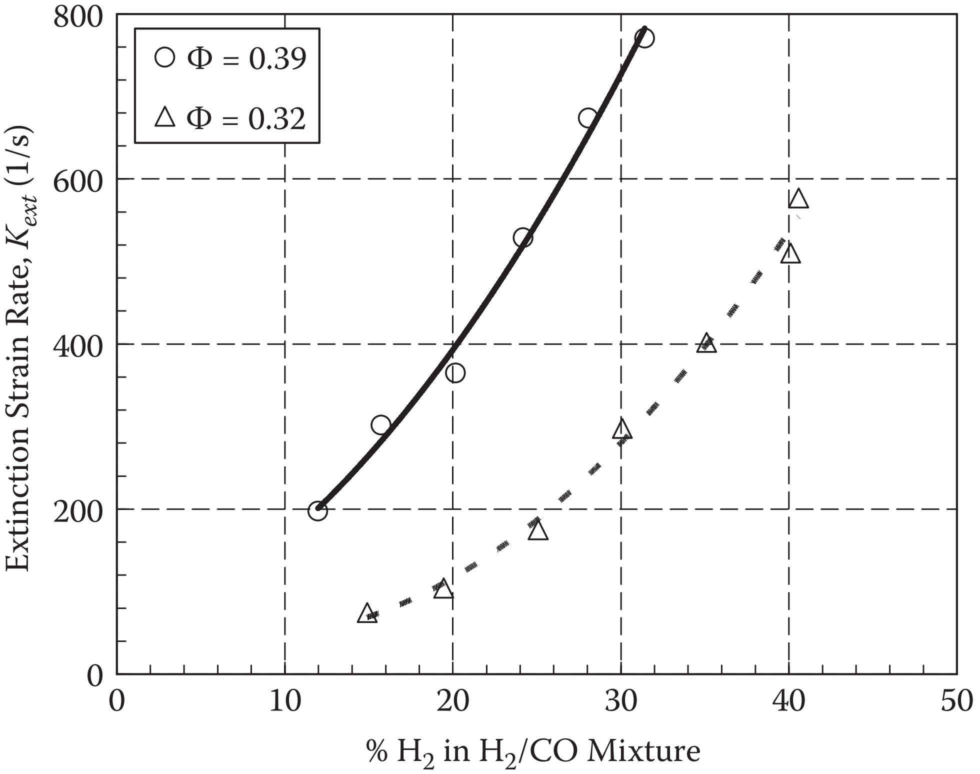

Figure 2.20: Extinction strain rates as a function of H_2 level in H_2/CO-air flames for two lean mixtures at $p = 1atm$ and $T_u = 300K$ (symbols = measurements, lines = curve fits) [46]

of H_2 in fuel mixture increases, the extinction strain rate increases due to the increase in burning rate with H_2. For a given H_2 percentage, the extinction strain rate increases with the equivalence ratio due to the increase in temperature caused by additional fuel energy.

2.2.6 Flammability Limits

Fuel-oxidizer mixtures are flammable only when there is a certain limit of fuel and oxidizer that allows a steady propagation of the flame. The lean flammability limit (LFL) is the leanest mixture ($\phi < 1$) that will allow steady flame propagation and the rich flammability limit (RFL) is the richest mixture ($\phi > 1$). Below the

LFL ($\phi < \phi_{LFL}$) and above the RFL ($\phi > \phi_{RFL}$) the mixture will not ignite and no flame will propagate. This property of the fuel is important since, for instance, environments employing flammable gases can be subjected to leaks of their contents into the environment. Thus, monitors should be designed to detect flammable mixtures in case of such leakages. [43]

Flammability limits are generally represented in percent fuel by volume in the mixture. They are determined experimentally using the so-called tube method. In this method, a premixed flame is initiated at the bottom of a 50 mm diameter and 1.5 m long vertical tube, and it is determined whether or not the flame can propagate the length of the tube. Mixtures that sustain steady flame propagation along the length of the tube are considered flammable. By altering the mixture strength (or equivalence ratio), flammability limits can be ascertained.

In order to study the flammability limits of syngas, it is important to study the flammability limits of its constituents, i.e. hydrogen and carbon monoxide, since syngas flammability limits usually lay between the ranges of pure hydrogen and pure carbon monoxide flammability limits. At normal temperature and pressure, H_2 has a LFL of about 4% by volume in air and a RFL of about 75% by volume in air. CO on the other hand has a LFL of approximately 12.5% by volume in air and a RFL of 74% by volume in air [47]. From the previous limits we see that hydrogen has a wider range of flammability when compared to carbon monoxide. This can be explained by the calorific value, where hydrogen has much higher specific calorific value (about 12 times) than carbon monoxide. When it comes to syngas, which is a mixture of H_2 and CO, its lean and rich flammability limits are expected to be within the lean and rich flammability limits of pure H_2 and CO. In other words, $LFL_{H_2} < LFL_{H_2+CO} < LFL_{CO}$ and $RFL_{H_2} < RFL_{H_2+CO} < RFL_{CO}$. Since the RFLs of hydrogen and carbon monoxide are almost the same, then one can write $RFL_{H_2+CO} \approx RFL_{H_2} \approx RFL_{CO}$.

Syngas flammability limit, as with any other property, is affected by the different fuel compositions and operating conditions. Figure 2.21 [48] shows the lean limit for a number of fuels mixtures containing hydrogen as a function of hydrogen concentration in the fuel at 25 ^oC. For syngas fuel ($H_2 + CO$ mixture), we see that the LFL fuel concentration decreases (lean flammability range increases) as the concentration of hydrogen in the mixture increases, reaching the lean limit of hydrogen for the case of 100% H_2.

The effect of initial temperature on the lower and upper flammability limits of H_2/CO mixture is shown in Figure 2.22 [49] and Figure 2.23 [49]. It can be inferred that for fixed hydrogen content, increasing the initial temperature of the fuel causes the LFL to decrease and the RFL to increase, and hence increasing the flammability range of the mixture. Furthermore, for a fixed initial temperature, increasing the hydrogen content in the H_2/CO mixture, results in a wider range of LFL, with the RFL being almost constant.

The effect of operating pressure on the flammability limits of H_2/CO mixtures has not been well-studied. Coward et al. [50] declared that at atmospheric pressure, a 49/51 H_2/CO mixture had LFL and RFL of 10.4% and 63% in air,

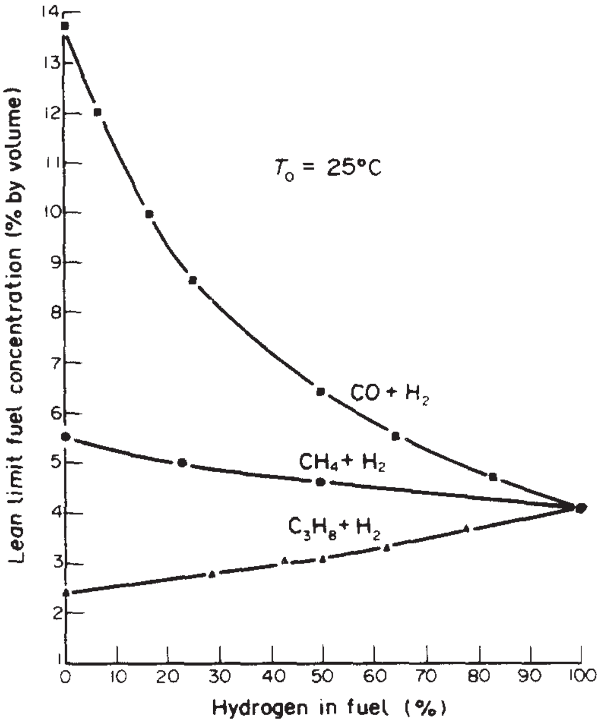

Figure 2.21: The lean limit of binary fuel mixtures involving hydrogen as a function of the volumetric concentration of hydrogen in the fuel at 25^oC [48]

respectively. At 800 *atm*, on the other hand, the limits became 11% and 78% in air, respectively. From this alone one cannot see the real effect of operating pressure and more studies are required to explore the effect of pressure on syngas flammability limits at different fuel compositions.

2.2.7 Emissions

Syngas combustion, as with any other fuel, can produce many gaseous pollutants, such as nitrogen oxides (NO_X), sulfur oxides (SO_2), carbon monoxide (CO), besides other species and particulate matters. However, existing data indicate that emissions from IGCC systems are less than those from conventional hydrocarbon fuels, hence the interest in syngas.

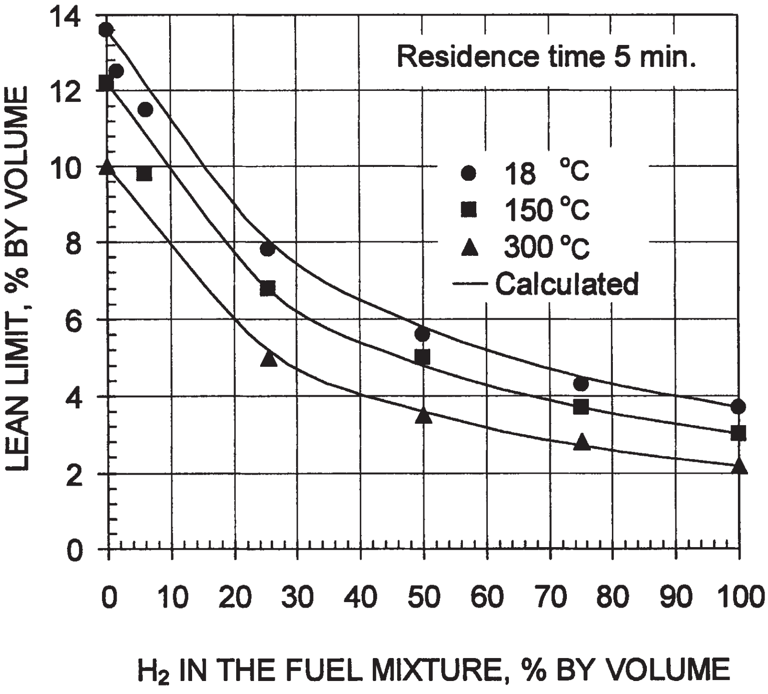

Figure 2.22: Lean flammability limits of H_2/CO mixtures in air at different temperatures [49]

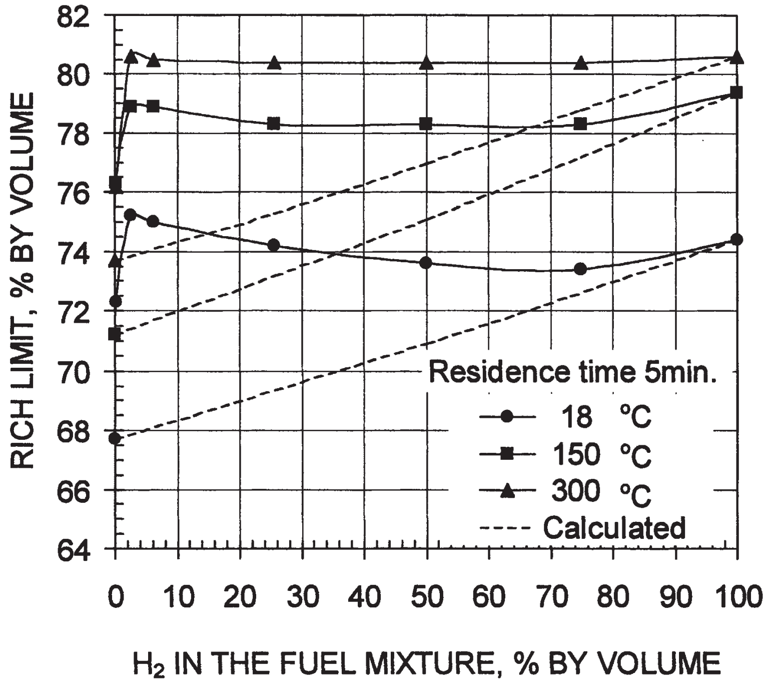

Figure 2.23: Rich flammability limits of H_2/CO mixtures in air at different temperatures [49]

The main NO_X species of concern is NO. Here, we will consider the characteristics of NO since it is produced in larger quantities compared to other NO_X. There are three different mechanisms for NO production: (1) fuel NO formation, (2) thermal NO formation, and (3) prompt NO formation. *Fuel* NO, as the name suggests, results from the oxidation of nitrogen-enriched species that evolved from the fuel during the gasification process of syngas production. These species include, mainly, HCN and NH_3. *Thermal* NO ascends from the oxidation of nitrogen (N_2) in the combustion air during the fuel combustion process. The Zeldovich mechanism [39] explains the fundamental steps in this oxidation process, which is given by reactions N.1, N.2, and N.3. *Prompt* NO results from the reaction of N_2 with fuel fragments, such as CH or NNH radicals, in the early stage of the flame, thus the name *prompt*.

$$O + N_2 \rightarrow NO + N \tag{N.1}$$

$$N + O_2 \rightarrow NO + O \tag{N.2}$$

$$N + OH \rightarrow NO + H \tag{N.3}$$

NO formation depends on the characteristics of the syngas mixture and the operating conditions, i.e. composition, dilution, pressure, and preheat temperature, similar to the other syngas combustion characteristics. Figure 2.24 [51] shows NO concentration (*ppm*) as a function of equivalence ratio for five different pressures for syngas-air mixture (17.5% H_2, 21.2% CO, 12.2% CO_2, and 49.1% N_2) with

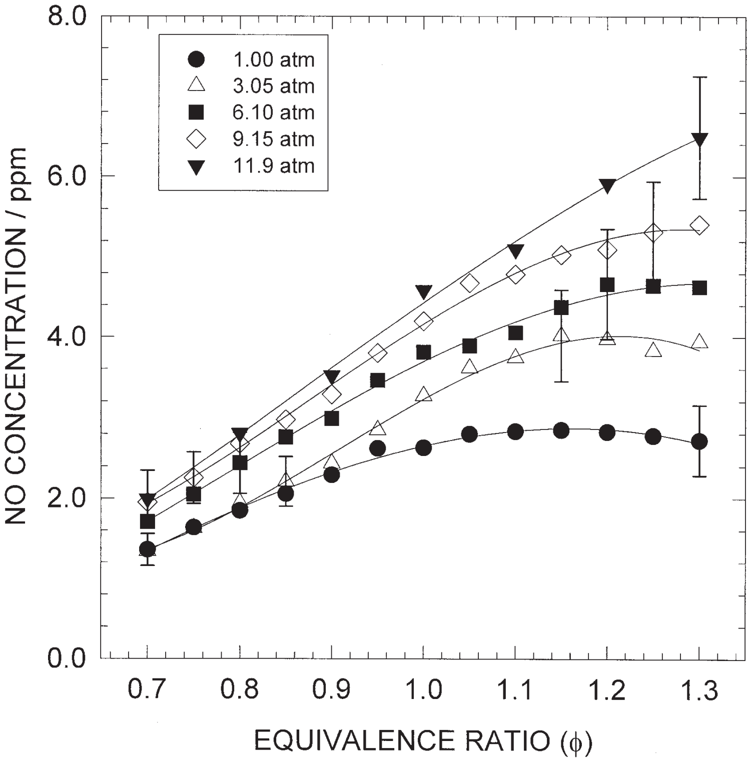

Figure 2.24: LIF-measured postflame front NO concentrations as a function of equivalence ratio in syngas-air flames ($CH_4 = 2.8\%$) for pressures from $1.0 to 11.9 atm$ [51]

2.8% of CH_4 added later. It is clearly shown that NO concentration increases with the equivalence ratio. In addition, for a given equivalence ratio, increasing the pressure causes the NO concentration to increase. Figure 2.25 [51] investigates the effect of hydrocarbon content in syngas mixtures. The figure shows a linear increase in NO concentration as the content of CH_4 in the fuel increases; due to the presence of CH radicals that promote more prompt NO production.

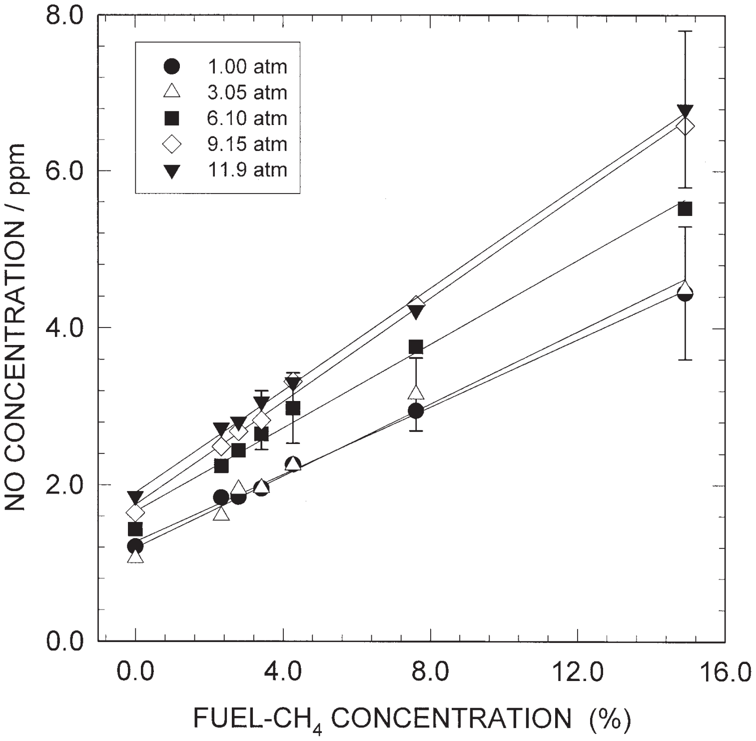

Figure 2.25: LIF-measured postflame front NO concentrations as a function of CH_4 addition for pressures from $1.0to11.9atm$ [51]

2.3 Combustion of Syngas in Swirl-Stabilized Burners

Swirl-stabilized combustion is the preferred mode in many power generation applications. It utilizes the dynamics of swirling motion generated by a swirler, usually along with a sudden expansion in inlet cross-section, to stabilize the flame. Swirl number, S, is the dimensionless parameter that characterizes the degree of swirl for a swirling flow. First proposed by Chigier and Beer [52] and simplified by Sheen et al. [53], it can be defined as the ratio between the axial flux of the tangential momentum to the axial flux of the axial momentum (Eq. 2.1).

$$S = \frac{\int_0^R uwr^2 dr}{R\int_0^R u^2 r dr} \tag{2.1}$$

Experimental investigations of syngas combustion (diffusion and premixed) in this kind of geometry is important and can offer a great insight into the composition effects on the flames characteristics and emissions. In this regard, a number of experimental studies can be found in literature. Sayad et al. [54] studied the effect of syngas and syngas/methane fuel variability and N_2 dilution on the lean blowout (LBO) limits at different swirl numbers. The results indicated that for a given fuel composition, increasing the swirl number decreased the LBO equivalence ratio. For a fixed swirl number, on the other hand, increasing hydrogen volume percent in the syngas mixture reduced the LBO equivalence ratio significantly. CH_4 and N_2 addition had an opposite effect on the LBO equivalence ratio. In another work, Syred et al. [55] studied the effect of hydrogen-enriched fuel mixtures on flashback behavior and LBO limits in swirling flows. The fuels tested were pure methane, methane/hydrogen, pure hydrogen, and coke oven gas. The effect of swirl number was studied as well. It was reported that the central recirculation zone broadened for high swirl numbers allowing the flashback to occur earlier at high velocities. However, at low swirl numbers, flashback occurred in the outer boundary layer. The authors highlighted the possibility to run premixed swirl combustors with varying hydrogen fuel mixtures to reduce the susceptibility of flashback while achieving low NO_X emissions. Similarly, Shelil et al. [56] investigated the flashback behavior of hydrogen/methane blends in premixed swirl combustion and determined the flashback limits for different CH_4/H_2 mixtures. They concluded that even though the LBO limits were extended, hydrogen-enriched methane fuels were more prone to flashback behavior. This was postulated to the higher burning velocities of hydrogen. Shao et al. [57] investigated the influence of swirl intensity on syngas diffusion flames and observed the difference between air swirl effects and fuel swirl effects on the flame shape. They concluded that fuel swirl intensity showed much higher influence on the flame structure compared to air swirl intensity, making it a key effect in this kind of geometry. Kutne et al. [58] characterized the combustion behavior of hydrogen rich syngas fuels in swirl-stabilized flames at elevated pressure (10 bars) under varying fuel mixtures and equivalence ratios. They observed the flame to be stable without pulsations with the overall flame shape remained similar under varying conditions investigated. They concluded, however, that the fuel composition and equivalence ratio had clear influence on the flame structure. Kim et al. characterized the combustion behavior and emissions of hydrogen-enriched methane-air mixtures under unconfined [59] and confined [60] conditions for different swirl strengths. They concluded for the unconfined conditions that swirl strength is more dominant than hydrogen content effects in the upstream region of swirl-stabilized combustor. As for the confined conditions, the authors concluded that flame stability was enhanced with hydrogen addition at both low and high swirl intensities. Daniele et al. [61] investigated the LBO limits, emissions, and turbulent flame speed of LPM syngas combustion at gas turbine relevant conditions. It was found that hydrogen addition extended the LBO extinction equivalence ratio, while the NO_X was observed to be highly dependent on the adiabatic flame temperature. The authors concluded that H_2 content played a major role in all parameters investigated. In the work of Scheer et al. [62], effect of hydrogen addition to methane was studied in a premixed, swirl-stabilized combustor for different fuel-air flow rates. It was found that enriching methane with hydrogen reduced CO emissions without affecting the NO_X emissions, with the flame shape changing significantly.

CFD simulation is also an important technique to gain further insight into properties that cannot be achieved by conventional laboratories. Moreover, it is a cheaper and safer way of combustion study. There are several attempts to simulate syngas combustion in swirl-stabilized combustors. Most of these simulations used large eddy simulation (LES) as the modeling technique since LES has the ability to capture the unsteady behavior of hydrogen and hydrogen-containing mixtures combustion. However, numerical investigations of syngas combustion in a gas turbine can combustor using Reynolds averaging (RANS) technique were performed by Ghenai [63], who studied the effect of syngas composition and lower heating value on the flame structure and emissions (CO_2 and NO_X). The $k-\epsilon$ model for turbulence, mixture fraction/probability density function (PDF) model for non-premixed combustion, and P-1 model for radiation were used. The results indicated lower gas temperatures when using syngas as the fuel compared to methane. It was concluded that higher reductions of NO_X and CO_2 could be achieved when firing syngas in the can combustor. Navarro-Martinez et al. [64] performed a study of the interactions between different instabilities and swirling motions in hydrogen annular jet flames. The authors compared different swirl number effects and noticed the changes in the flow structure, the mixing process as well as the combustion process as a whole. In this work, it was apparent that increasing the swirl number caused the inner recirculation zone and the reverse flow associated with it to increase, thus enhancing the mixing during combustion process. Giacomazzi et al. [65] performed an LES analysis of a syngas turbulent premixed dump-combustor at a pressure of 5 bar and equivalence ratio of $\phi = 0.45$ to study the flame structure of a hydrogen jet flame. The geometrical set-up simulated is identical to the one studied experimentally by Daniele et al. [61]. In this study although only qualitative comparison was provided through comparison of the instantaneous temperature contour plots, the importance of the choice of the chemical scheme was highlighted. Two different chemical kinetic models were compared; the reduced mechanism of Chen [66] and the skeletal mechanism of Politecnico di Milano (POLIMI) [13]. The flame structure predicted by the Chen mechanism, which is similar to a flat flame, was far from what was observed in the experiment and the reason for this is the over-prediction of the laminar flame speed. However, when changing to the POLIMI mechanism, the flame showed a more realistic structure which highlights the importance of chemistry for these types of calculations. A more recent work by De et al. [67] conducted a parametric study to investigate the effect of swirl on the flashback behavior of hydrogen-enriched methane flames. It was shown that increasing the swirl strength caused the recirculation zone to be broadened, making the system more susceptible to upstream flame movement due to increased levels of turbulence. Additional work by De et al. [68] was performed to study the effect of hydrogen percentage on upstream flame propagation in a methane-air flame. The different compositions were studied at a fixed equivalence ratio and Reynolds number. It was noticed that increasing the hydrogen content in methane reduced the size and shape of the inner recirculation bubble, leading to upstream flame propagation as a result of the higher diffusivity of hydrogen and higher reactivity. In another recent work, Zheng et al. [69] studied the effect of composition, Reynolds number, equivalence ratio, and operating pressure on LPM syngas flames. They reported that the flame became shorter with increasing hydrogen content in syngas. In addition, larger recirculation zones were observed as the Reynolds number was increased. Moreover, for lower equivalence ratios, lower flame temperatures were observed reducing NO_X formation and flame stability.

2.4 Combustion Modeling Techniques

Combustion modeling has been popular in the past decade. It is more economical and a safer way of combustion study. Fundamental properties of combustion can be modeled using zero- and one-dimensional techniques, while more complex properties representing lab- or real-size combustors can be modeled using Computational Fluid Dynamics (CFD).

2.4.1 Fundamental Modeling Techniques: CANTERA

CANTERA is an object-oriented software used in the field of combustion modeling. It represents a collection of data and subroutines written in different programming languages, such as FORTRAN, C++, PYTHON, and MATLAB. They are used to solve problems related to the physics of combustion such as chemical kinetics, equilibrium, and species transport. The different problems that can be solved using Cantera include adiabatic flame temperature, flame speed, species concentrations and mole fractions at equilibrium and as a function of time, as well as reacting vessels and many other problems. The advantage of Cantera is that it solves the governing equations in simplified forms, i.e. zero- and one-dimensional, describing such a complex phenomenon like combustion in a more fundamental way [70].

2.4.2 CFD Modeling Techniques: ANSYS FLUENT

ANSYS FLUENT is a CFD software that has the capability of modeling combustion phenomenon by solving the different conservation equations of continuity, momentum, energy, and species. Turbulence, radiation, and chemistry can be modeled by ANSYS FLUENT as well.

CHAPTER 3

DETAILED-CHEMISTRY ANALYSIS OF LPM SYNGAS LAMINAR FLAMES

The current chapter presents a parametric study performed, using CANTERA, to investigate the effect of equivalence ratio, fuel composition, operating pressure, and initial reactants temperature on the foremost basic properties of LPM syngas laminar flames. These properties include:

1. Adiabatic flame temperature
2. Laminar flame speed
3. NO emissions

Table 3.1 indicates the different parameters used in the study and their corresponding values.

Table 3.1: Parameters and their corresponding values used in the parametric study

H_2/CO ($volume$ %)	p (atm)	T_{in} (K)	ϕ
05/95	1	300	0.5
25/75	10	400	0.6
50/50	20	500	0.7
75/25	30	600	0.8
95/05	40	700	0.9

3.1 Mathematical Models

The method CANTERA uses to solve for different properties is through solving the conservation equations of mass, species, momentum, and energy. The mathematical models used in the current calculation are described in this section.

3.1.1 Modeling of Adiabatic Flame Temperature

The adiabatic flame temperature is modeled using the equilibrium state (Eq. 3.1) of the fuel-air mixture, burning adiabatically at constant pressure.

$$H_R(T, p) = H_P(T_{ad}, p) \tag{3.1}$$

The equilibrium state of a gas mixture holding two properties fixed at their initial state - in our case enthalpy and pressure - is calculated based on a solver for chemical equilibrium that uses the element potential method. This method is a non-stoichiometric method that reduces the problem to set of nonlinear algebraic equations, where the number of equations is equal to the number of elements, and not species (see [71] for more details).

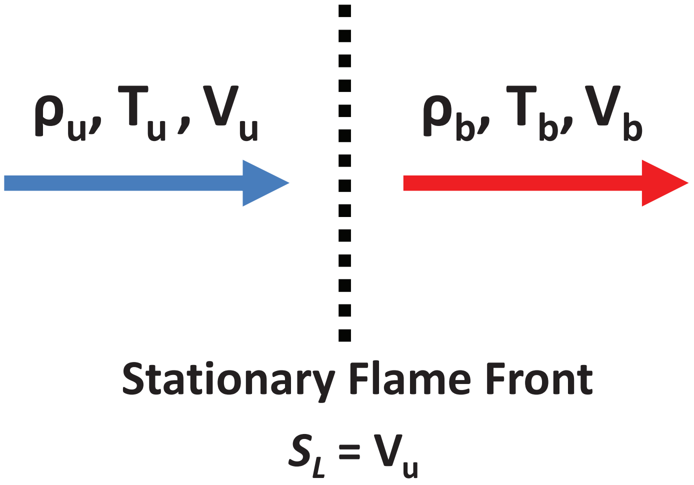

Figure 3.1: Freely propagating laminar flame model configuration (u = unburned, b = burned)

3.1.2 Modeling of Laminar Flame Speed

The laminar flame speed calculations are conducted using the freely propagating laminar flame model [45]. In this model, the flame is modeled as one-dimensional with the flame speed defined as the inlet velocity (unburned gas mixture velocity that moves toward the flame) that allows the flame to stay in a fixed (stationary) position (Figure 3.1).

Eq. 3.2 to 3.7 present the governing equations describing the reacting flow in this case, along with the boundary conditions [45].

Continuity Equation

$$\dot{m} = \rho u A \tag{3.2}$$

$\dot{m}$ is the mass flow rate, ρ is the mixture density, u is the flow velocity, and A is the cross-sectional area.

Energy Equation

$$\dot{m}\frac{dT}{dx} - \frac{1}{c_p}\frac{d}{dx}\left(\lambda A \frac{dT}{dx}\right) + \frac{A}{c_p}\sum_{k=1}^{N} \rho Y_k u_k c_{p_k}\frac{dT}{dx} + \frac{A}{c_p}\sum_{k=1}^{N} \dot{\omega}_k h_k W_k = 0 \qquad (3.3)$$

T is the temperature of the mixture, x is the axial distance, c_p is the specific heat of the mixture, λ is the thermal conductivity of the mixture, Y_k is the mass fraction of the k^{th} species, u_k is the velocity of the k^{th} species, c_{p_k} is the specific heat of the k^{th} species, $\dot{\omega}_k$ is the rate of creation or destruction of the k^{th} species, h_k is the specific enthalpy of the k^{th} species, and W_k is the molecular weight of the k^{th} species.

Species Conservation Equation

$$\dot{m}\frac{dY_k}{dx} + \frac{d}{dx}\left(\rho A Y_k u_k\right) - A\dot{\omega}_k W_k = 0 \qquad (3.4)$$

Equation of State

$$\rho = \frac{p\overline{W}}{RT} \qquad (3.5)$$

p is the static pressure, $\overline{W}$ is the mean molecular weight of the mixture, and R is the universal gas constant which equals to 8.314 $J/mol{\cdot}K$.

Boundary Conditions

At the cold boundary

$$T_u = T_{burner}, \qquad Y_k + \left(\frac{\rho A Y_k u_k}{\dot{m}}\right) = 1 \qquad (3.6)$$

T_u is the temperature of the unburned reactants.

At the hot boundary

$$\frac{dY_k}{dx} = 0, \qquad \frac{dT}{dx} = 0 \tag{3.7}$$

An additional interior boundary condition is required to fix the location of the flame through specifying the temperature at one point

The mass flow rate ($\dot{m}$) is an Eigen-value of the problem that is being solved for. On the other hand, the rate constant (k) used in the calculation of the reaction rate ($\dot{\omega}$) is modeled using the Arrhenius form (Eq. 3.8).

$$k = AT^n exp\left(\frac{-E_a}{RT}\right) \tag{3.8}$$

where A is the pre-exponential factor, n is the temperature exponent, and E_a is the activation energy.

3.1.3 Modeling of NO Emissions

NO concentrations are calculated using the well-stirred reactor (WSR) model (Figure 3.2) [43]. The equations describing the model in this case is a set of coupled nonlinear algebraic equations.

Species Equation

$$\dot{\omega}_k W_k \not{V} + \dot{m}\left(Y_{k_{in}} - Y_{k_{out}}\right) = 0 \tag{3.9}$$

$\not{V}$ is the reactor's volume.

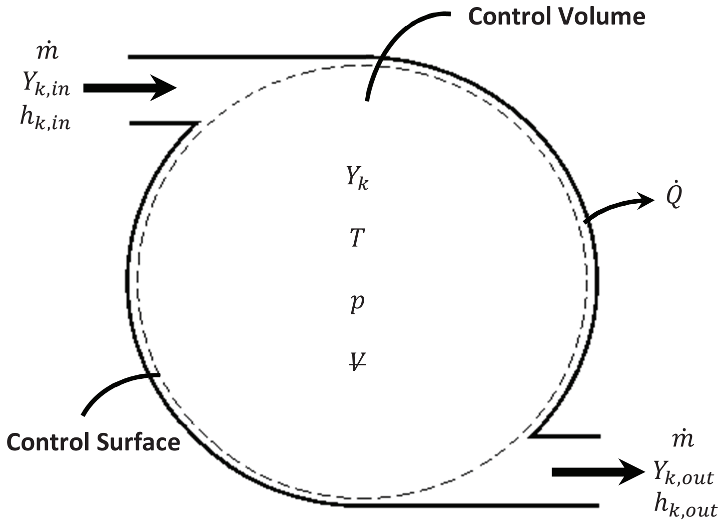

Figure 3.2: Schematic diagram for the well-stirred reactor model

Energy Equation

$$\dot{Q} = \dot{m}\left(\sum_{k=1}^{N} Y_{k_{out}} h_k(T) - \sum_{k=1}^{N} Y_{k_{in}} h_k(T_{in})\right) \tag{3.10}$$

$$h_k(T) = h^0_{f_k} + \int_{T_{ref}}^{T} c_{p_k} dT \tag{3.11}$$

$\dot{Q}$ is the rate of heat transfer through the reactor's wall and $h^0_{f_k}$ is the specific enthalpy of formation for the k^{th} species.

3.1.4 Chemistry Model

In the present study, the GRI Mech. 3.0 [21] model for chemistry was used for reaction rate calculations. This model comprises 53 species and 325 elementary reactions. In addition, it incorporates the detailed chemistry required for NO_X production. See Appendix A for details of the elementary reactions of the GRI Mech. 3.0.

3.2 Results and Discussion

3.2.1 Adiabatic Flame Temperature

Figure 3.3 shows the AFT as a function of equivalence ratio at varying hydrogen composition. It can be observed that increasing the equivalence ratio increases the AFT for all compositions. This is due to the decrease in the amount of air which serves as a sink in the combustion process and thus causing the effective flame temperature to increase. However, it increases with increasing the concentration of carbon monoxide. This can be attributed to the heating value of the fuel which is higher for carbon monoxide (about 13 $kJ/kmol$) than hydrogen (10 $kJ/kmol$).

Increasing the operating pressure increases the rate of reaction which in turns increases the flame temperature. However, this increase is not significant at very lean conditions as seen from Figure 3.4. This on the other hand becomes visible toward stoichiometric conditions. This is due to the effect of products dissociation which is suppressed at higher pressures, allowing the energy that is supposed to be used for dissociation at lower pressures, to increase the AFT. This effect is only obvious at high temperature regions i.e. stoichiometric regions.

Increasing the preheat temperature increases the AFT due to the increased available energy that raises the products temperature. Figure 3.5 shows that for a fixed composition, increasing the preheat temperature increases the AFT. Similar profiles are noticed for all compositions. Figure 3.6 shows a similar trend at higher inlet temperature (700 K) and operating pressure (40 atm), which is a typical condition for gas turbine combustors.

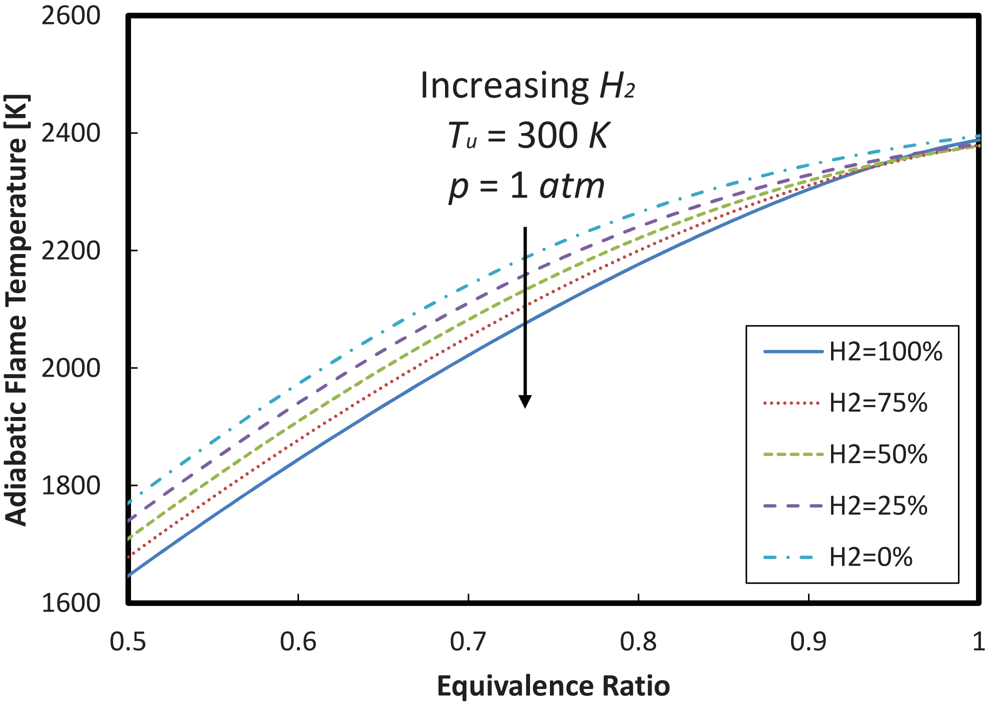

Figure 3.3: Effect of syngas composition on LPM syngas adiabatic flame temperature for different equivalence ratios. $T_u = 300K$ and $p = 1atm$

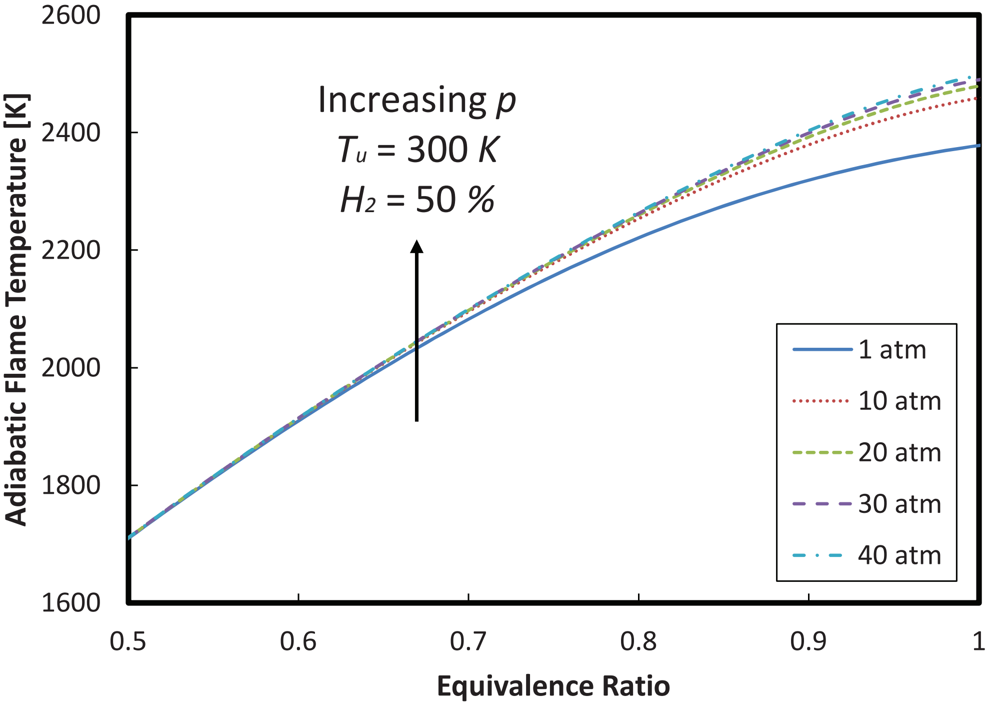

Figure 3.4: Effect of operating pressure on LPM syngas adiabatic flame temperature for different equivalence ratios. $T_u = 300K$ and $H_2 = 50\%$

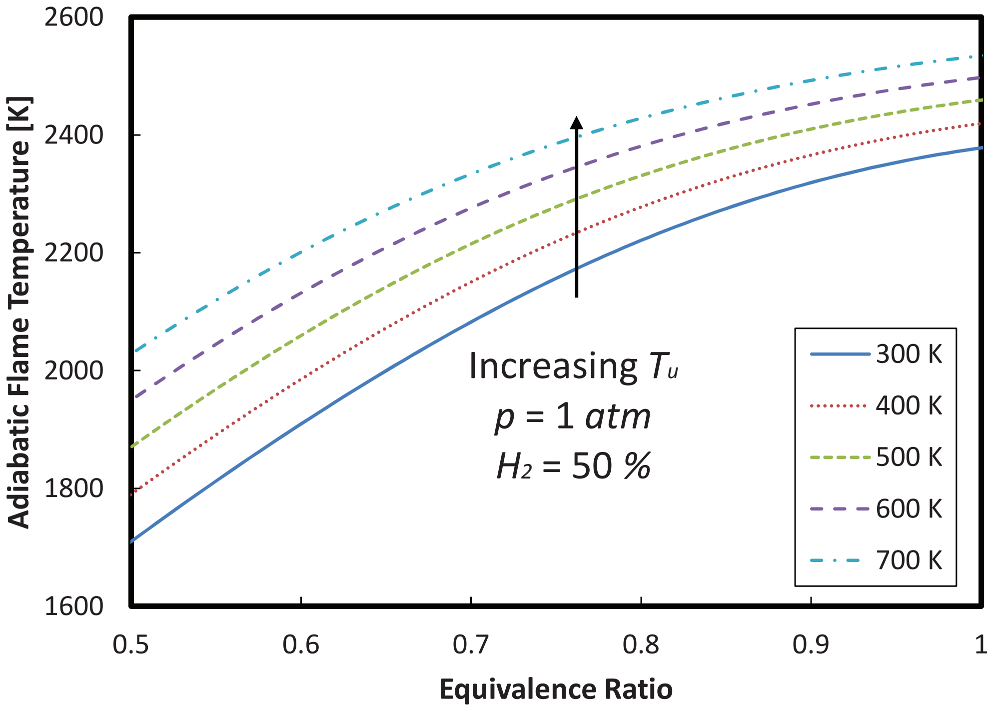

Figure 3.5: Effect of preheat temperature on LPM syngas adiabatic flame temperature for different equivalence ratios. $p = 1atm$ and $H_2 = 50\%$

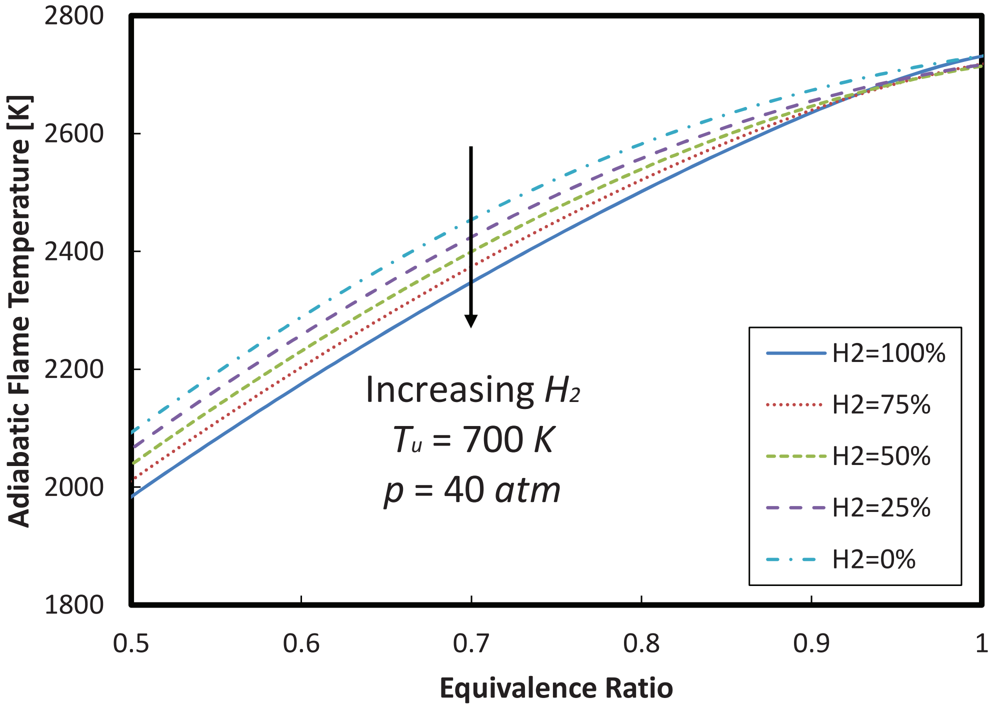

Figure 3.6: Effect of syngas composition on LPM syngas adiabatic flame temperature for different equivalence ratios. $T_u = 700K$ and $p = 40atm$

3.2.2 Laminar Flame Speed

Increasing the equivalence ratio increases the LFS in the lean region due to the increase in the flame temperature that results from burning more fuel.l The LFS increases with increasing volume percent of hydrogen that results from hydrogen high diffusivity and reactivity compared to carbon monoxide as observed in Figure 3.7.

Conversely, the flame speed decreases with increasing the pressure (see Figure 3.8). While increasing the pressure will increase the reaction rate which tends to increase the flame speed, the high density resulted from increasing the pressure will cause the energy required to raise the temperature to outweigh the benefit for increasing the reaction rate which leads to significant reduction in the flame speed. For a given pressure, increasing the temperature generally increases the LFS at all conditions (Figure 3.9).

At very lean mixtures ($\phi = 0.5$), the flame speed is strongly dominated by the preheat temperature, which justifies that even mixtures with 5% hydrogen content at 700 K has higher flame speed than that of 95% hydrogen at 300 K. As the mixture approaches stoichiometry conditions, the effect of increasing hydrogen content becomes more significant than the preheat temperature, which makes the flame speed higher than those at higher preheat temperatures. This increase becomes more significant with slight increase in the preheat temperature (95% hydrogen at 400 K in Figure 3.10).

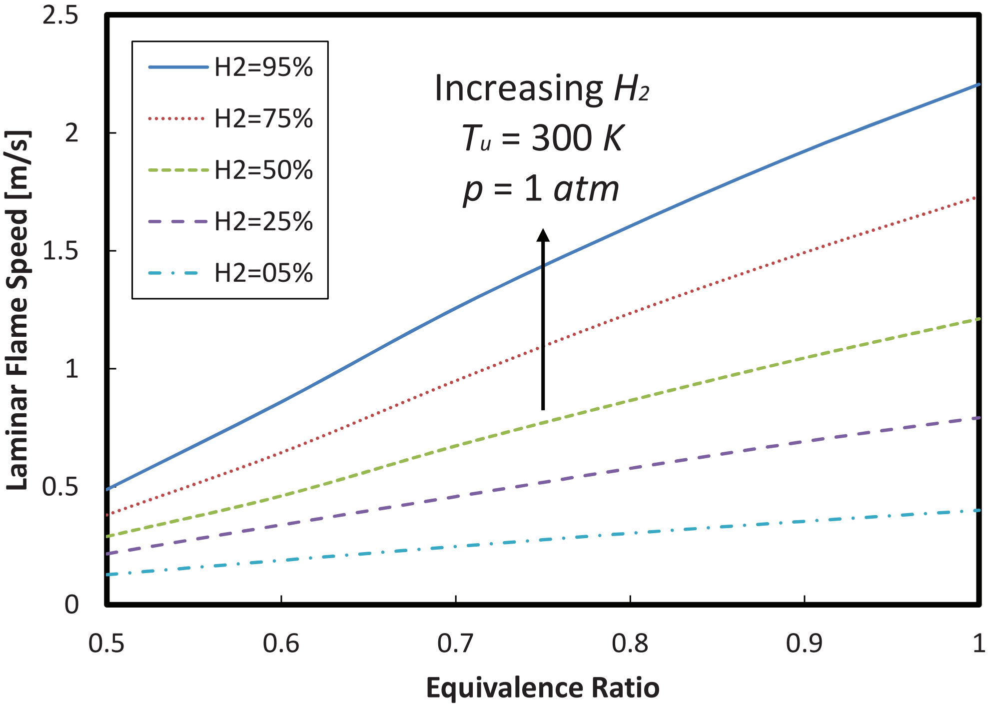

Figure 3.7: Effect of syngas composition on LPM syngas laminar flame speed for different equivalence ratios. $T_u = 300K$ and $p = 1atm$

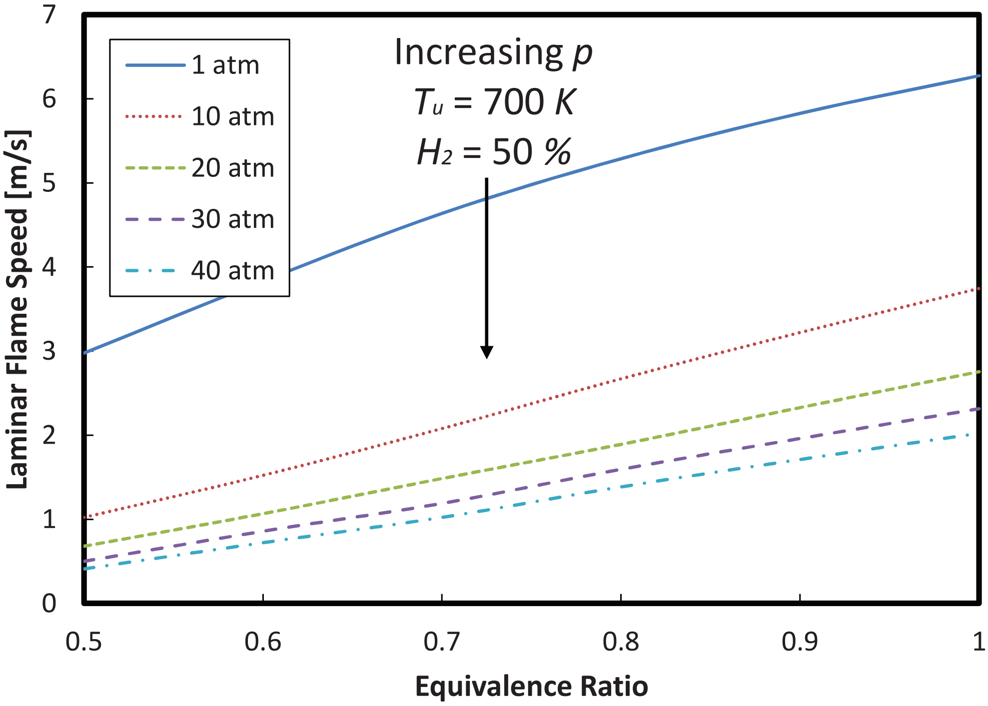

Figure 3.8: Effect of operating pressure on LPM syngas laminar flame speed for different equivalence ratios. $T_u = 700K$ and $H_2 = 50\%$

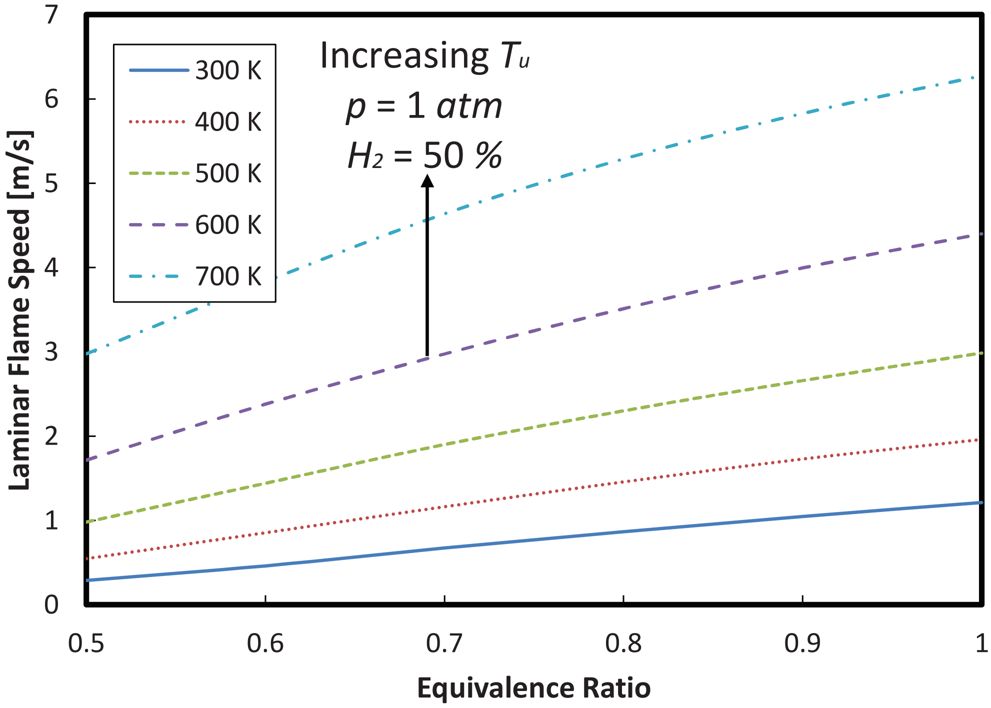

Figure 3.9: Effect of preheat temperature on LPM syngas laminar flame speed for different equivalence ratios. $p = 1atm$ and $H_2 = 50\%$

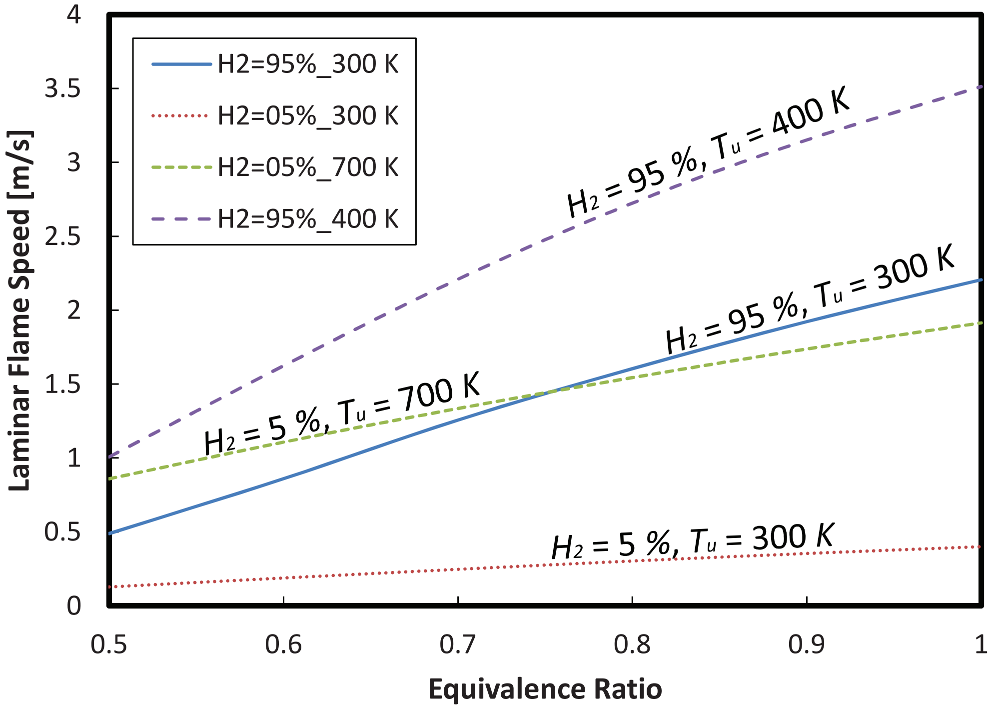

Figure 3.10: Comparable LPM syngas laminar flame speeds at different conditions. $p = 1atm$

3.2.3 NO Emissions

From Figure 3.11, at very low equivalence ratio, thermal NO production is almost similar for all fuel compositions. However, increasing the equivalence ratio increases the AFT beyond 1800 K (as observed in Figure 3.3) which causes the rate of production of NO to increase as explained by the Zeldovich mechanism. Similarly, Figure 3.12 shows that the pressure increase favors the production of thermal NO due to the increase in the reaction rate which causes the flame temperature to increase.

In the same way, increasing the preheat temperature increase the AFT which increases the NO production at all equivalence ratios as shown in Figure 3.13. Simultaneous increase in temperature and pressure increases NO mole fraction as observed in Figure 3.14. This increase is drastic at higher pressure level. NO mole fraction however decreases with increasing hydrogen content in the fuel (Figure 3.15), which is consistent with the reduction of AFT for increasing hydrogen concentration as observed in Figure 3.3.

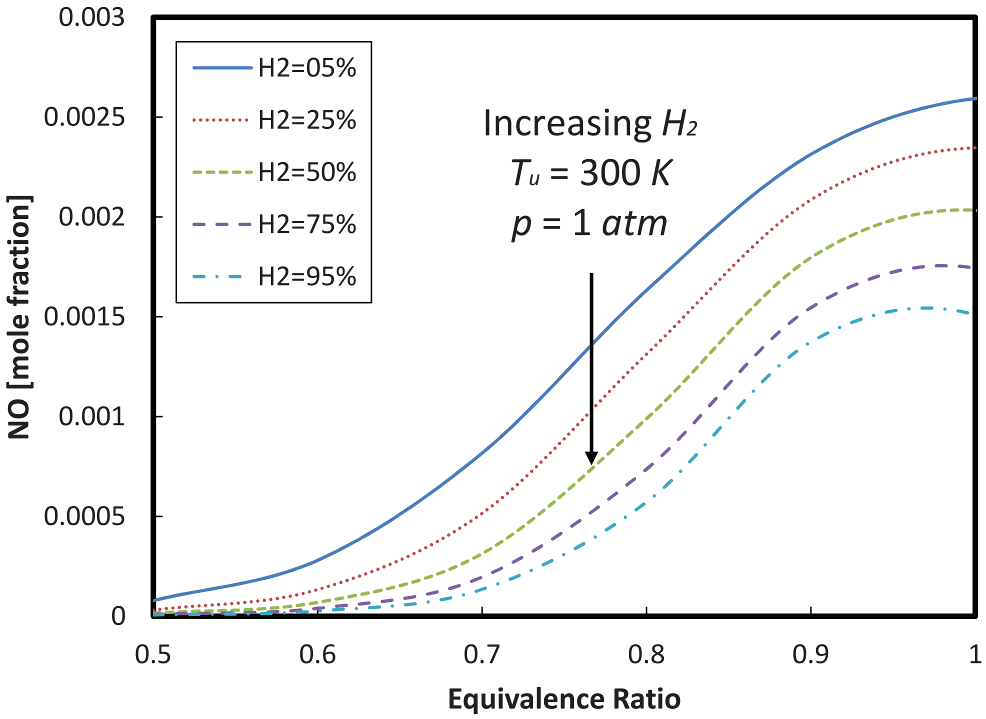

Figure 3.11: Effect of syngas composition on LPM syngas production of thermal NO for different equivalence ratios. $T_u = 300K$ and $p = 1atm$

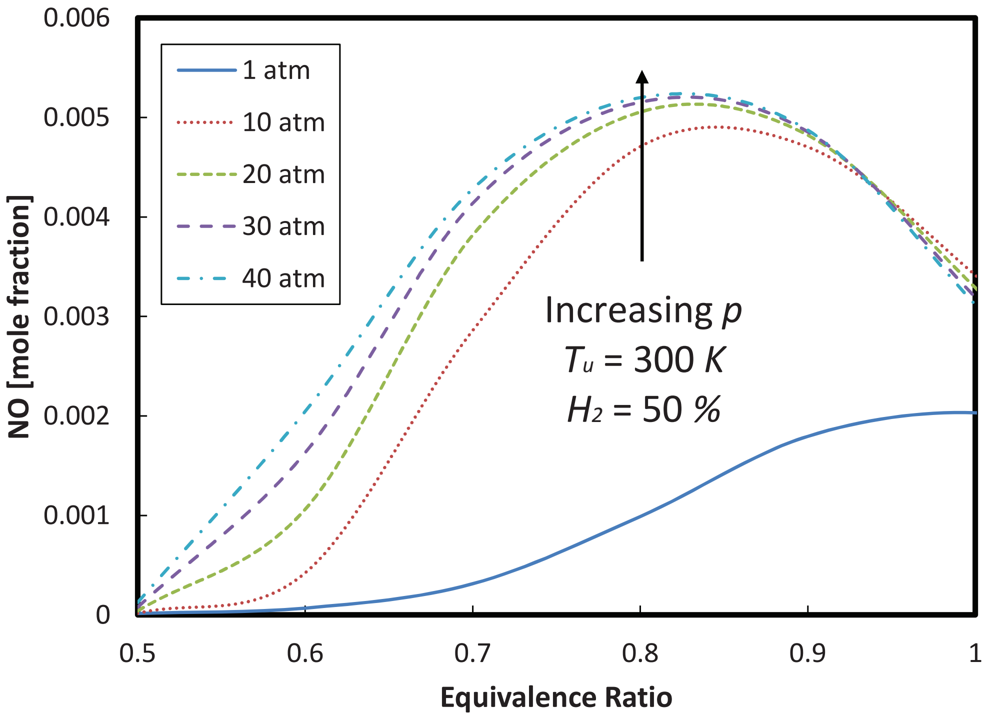

Figure 3.12: Effect of operating pressure on LPM syngas production of thermal NO for different equivalence ratios. $T_u = 300K$ and $H_2 = 50\%$

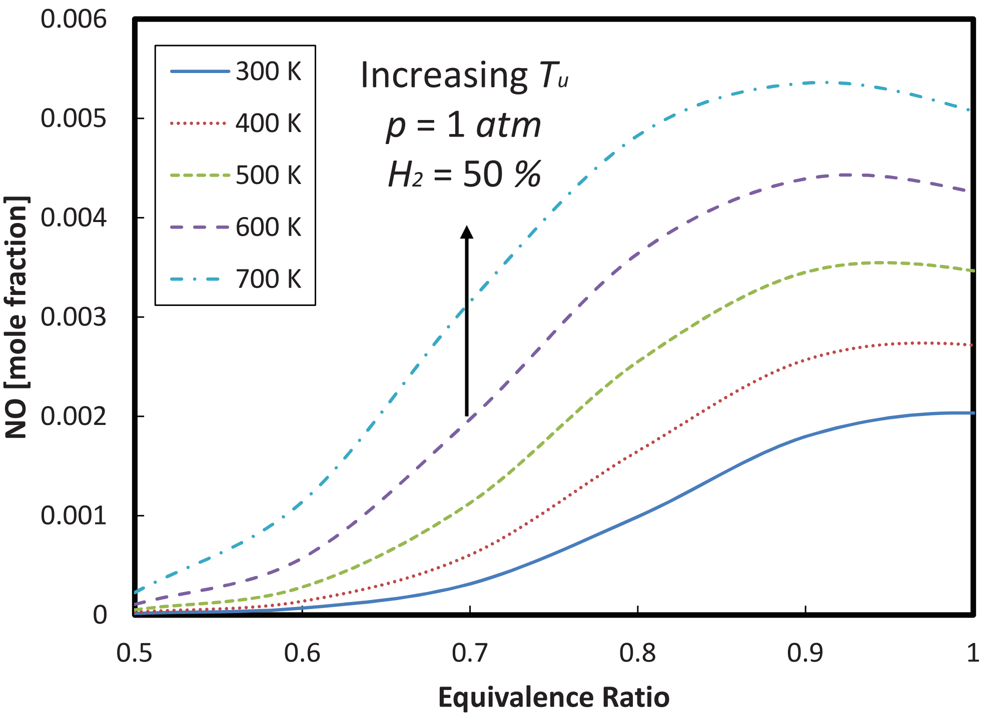

Figure 3.13: Effect of preheat temperature on LPM syngas production of thermal NO for different equivalence ratios. $p = 1atm$ and $H_2 = 50\%$

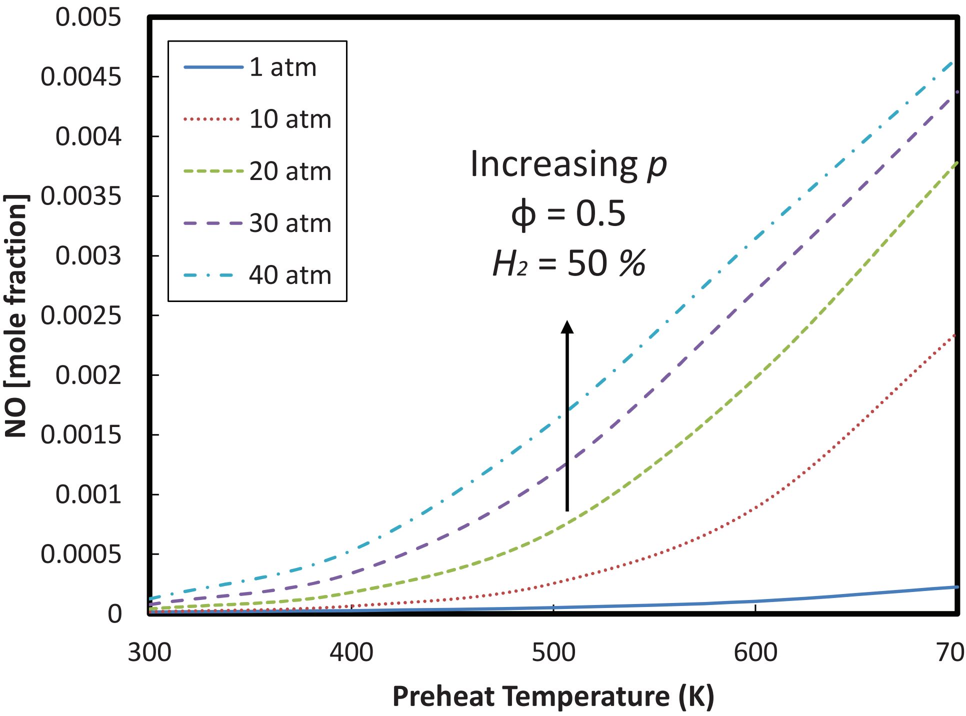

Figure 3.14: Effect of preheat temperature upon operating pressure of LPM syngas production of thermal NO. ϕ=0.5 and $H_2 = 50\%$

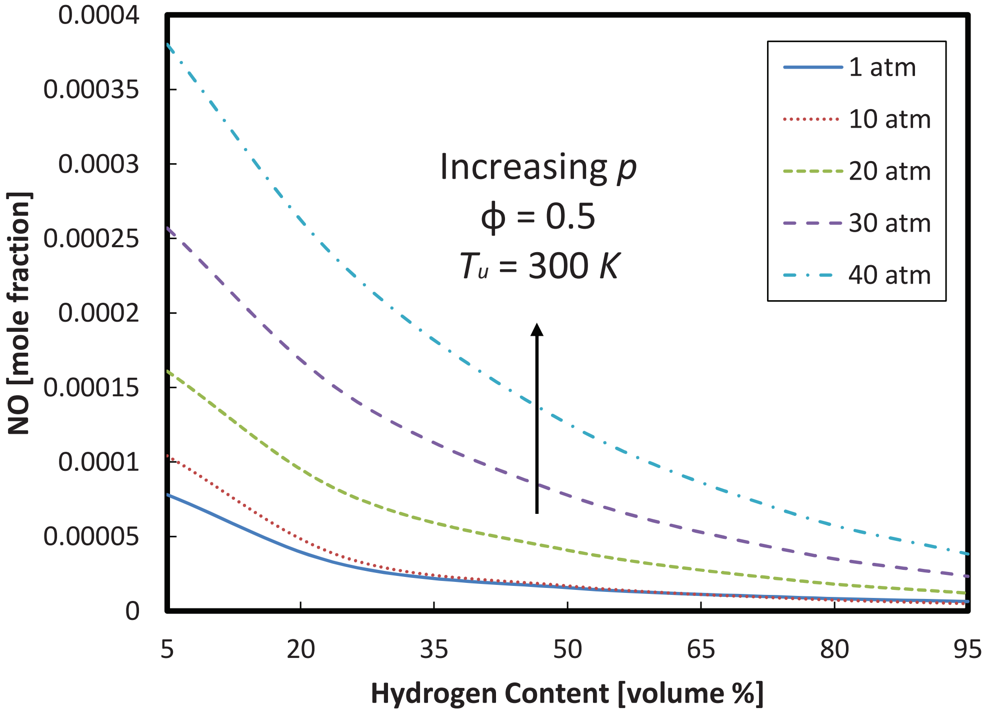

Figure 3.15: Effect of syngas composition upon operating pressure of LPM syngas production of thermal NO. ϕ=0.5 and $T_u = 300K$

CHAPTER 4

COMPARISON OF SYNGAS REACTION MECHANISMS FOR CFD APPLICATIONS

Most of the developed chemical mechanisms were tested under specific operating conditions and without a detailed analysis of a range of mechanisms. Thus, the objective of this chapter is to perform a sensitivity analysis of a range of the most commonly used syngas chemical mechanisms (Table 4.1 & Appendix A) under lean premixed conditions. The grouping of mechanisms was based on the number of elementary reactions, where a mechanism with more than 50 steps is classified as a detailed mechanism, less than 5 steps as a global mechanism, and in between this range as a reduced mechanism. The basis for the comparison is the laminar flame speed. In addition, since the flame temperature is responsible for thermal NO_X as well as it highly influences the flame propagation and extinction, the adiabatic flame temperature was also compared. The ability of the selected mechanisms to predict NO_X formation that depicts the emission characteristics in lean premixed syngas flames was studied as well.

Table 4.1: Mechanisms tested for syngas oxidation

Model	**Acronym**	**Species Number**	**Steps Number**
		Detailed	
GRI-Mech. 3.0	GRI	53	325
Li	C1	21	93
		Reduced	
Nikolaou	NI	17	49
Polytechnic of Milan	PO	14	37
Davis	DA	14	30
Boivin	BO	14	24
Slavinskaya	SL	10	20
		Global	
Jones and Lindstedt	JL	5	3
Watanabe and Otaka	WO	5	3

4.1 Mathematical Models

The mathematical models used in the current calculation are previously described in Section 3.1.

4.2 Experimental Data for Laminar Flame Speed

In order to evaluate the accuracy of the different chemical mechanisms, experimental data for laminar flame speed for varying equivalence ratio at 50/50 H_2/CO were obtained from Bunkute et al. [72]. In addition, laminar flame speed data for varying equivalence ratio at 5/95 H_2/CO as well as for varying H_2 content in syngas at equivalence ratio of $\phi = 0.6$ and $\phi = 0.8$ were obtained from Bouvet et al. [27]. The experimental data [27, 72] were earlier validated against similar experimental results of Hassan et al. [73], Sun et al. [11], Mclean et al. [28], Burke et al. [74], and Prathap et al. [25]. Similarly, the laminar flame speed at different preheat temperatures were obtained from Natarajan et al. [32], which were also validated against the work of Hassan et al. [73], Sun et al. [11], and Mclean et al. [28]. It is worth mentioning that there is lack of experimental data on the effect of pressure on H_2/CO mixtures using air as the oxidizer. For this reason, the GRI mechanism was used as a reference for comparison in the case of variable operating pressure. However, since the selected experimental data were consistent with previous experimental studies, they served as the basis for this work.

4.3 Results and Discussion

4.3.1 Adiabatic Flame Temperature

The calculated AFT for lean premixed syngas flames is given in Figure 4.1 to 4.5. Figure 4.1 shows the AFT of pure H_2 and pure CO gases under lean conditions using the GRI mechanism. In general, it can be observed that by increasing the equivalence ratio the AFT increases due to the presence of more fuel corresponding to more energy, i.e. lower heating value (LHV), available in the fuel-air mixture. Also, the AFT of pure CO is higher than that of H_2. This is related to the higher heating value of pure CO (11.4 MJ/m^3) as compared to pure H_2 (9.8 MJ/m^3). The difference in their AFT, however, decreases as the equivalence ratio increases. This decrease is due to energy consumption for the dissociation of the products at higher temperatures in the CO combustion.

Figure 4.2 shows the effect of equivalence ratio on the predicted AFT, by different models at 50/50 H_2/CO syngas composition. It can be observed that increasing the equivalence ratio increases the amount of fuel in the fuel-air mixture thereby increasing the AFT. At very lean conditions, the AFT of all mechanisms is essentially similar; this trend continues as the mixture approaches stoichiometry except for JL and WO global mechanisms. The over-prediction of the AFT by the global mechanisms is attributed to the absence of intermediary species present in reduced and detailed mechanism which are formed from the dissociation of the parent compound, consuming energy. These over-predictions are however within 10% accuracy range of the GRI mechanism.

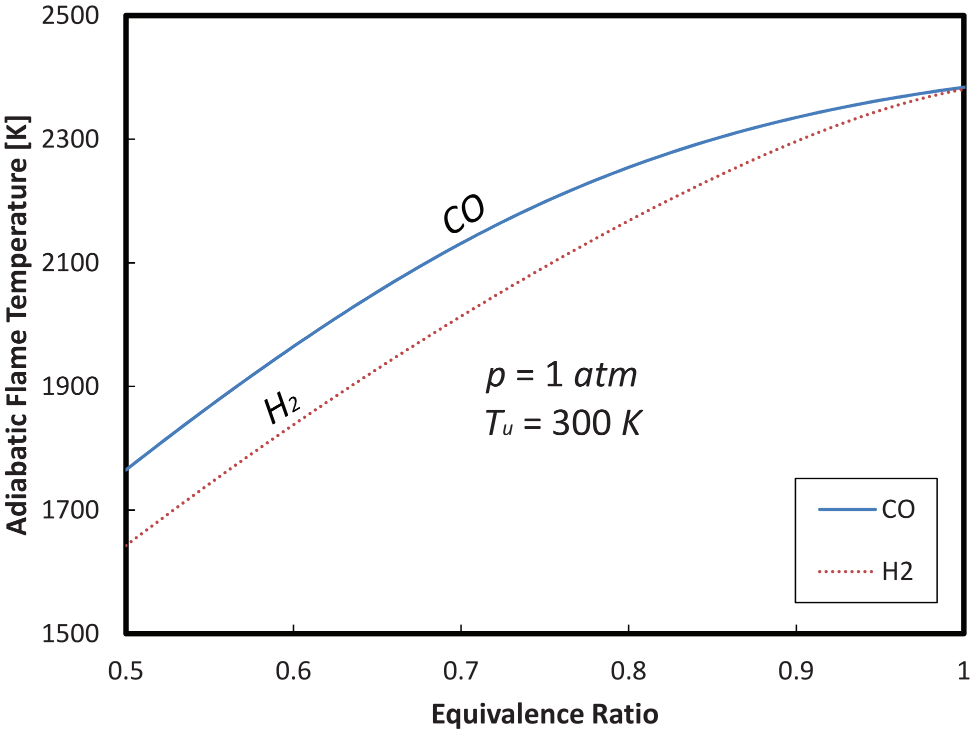

Figure 4.1: Adiabatic flame temperature of pure H_2 and CO fuels under lean conditions predicted by GRI mechanism. $T_u = 300K$ and $p = 1atm$

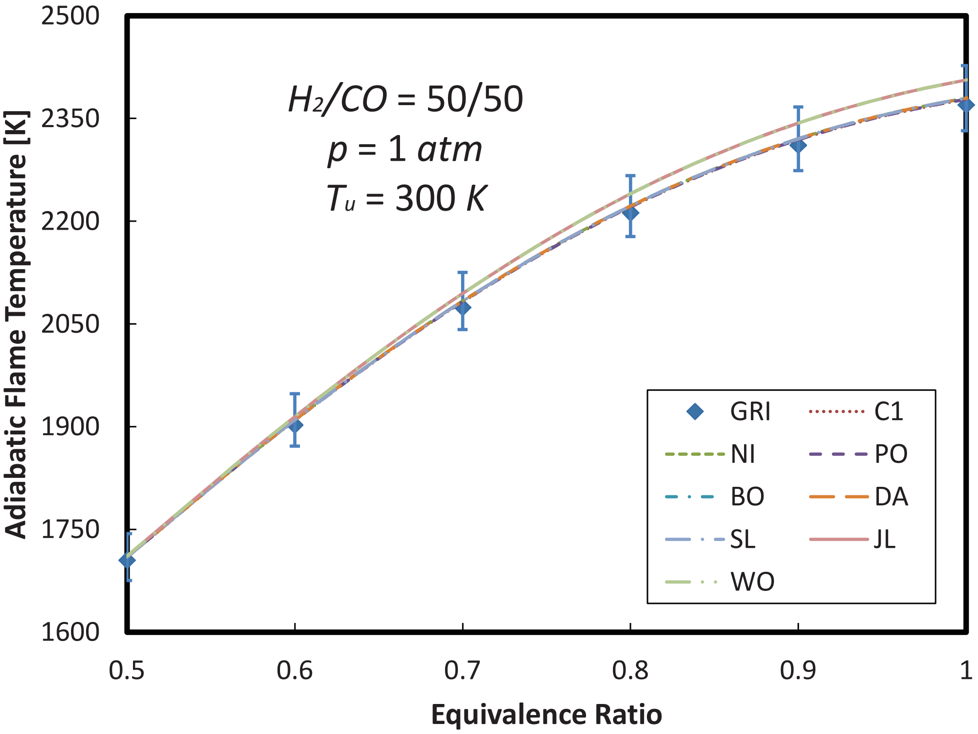

Figure 4.2: Adiabatic flame temperature of 50/50 H_2/CO fuel under lean conditions predicted by different kinetic models. $p = 1atm$ and $T_u = 300K$

Moreover, the effect of increasing H_2 content in syngas at $\phi = 0.5$ and $\phi = 0.9$ is presented in Figure 4.3. Increasing the hydrogen content (on volume basis) in the syngas results in a decrease in the AFT. This is due to lower heating value of H_2 gas as compared to CO. At $\phi = 0.9$ there is a significant over-prediction by the global mechanisms compared to GRI base case. These observed discrepancies increase as the H_2 content increases and is attributed to the dominant effect of H_2 in the syngas reaction.

The predictions of AFT by all kinetic models understudy for different operating pressures are shown in Figure 4.4 for two different equivalence ratios. At $\phi = 0.5$ (Figure 4.4a) all predictions are basically the same where there is no impact of pressure on the AFT. However, at a higher equivalence ratio ($\phi = 0.9$, Figure 4.4b) an increase in the AFT is visible at lower pressures which decreases for higher pressures. There is over-prediction by the global mechanisms i.e. JL and WO, due to the absence of elementary species as mentioned above. However, this over-prediction is within 10% prediction range of the GRI.

Figure 4.5 on the other hand shows that increasing the syngas preheat temperature increases the AFT due to the reduction in the amount of energy required for fuel ignition, thus enhancing the amount of energy release and hence the AFT. At lean conditions (ϕ=0.5), the reduced and global mechanisms are similar to those of the GRI. However, at nearly stoichiometry (ϕ=0.9), the AFT values for the global mechanisms exceeded 10% accuracy range of the GRI by about 2%.

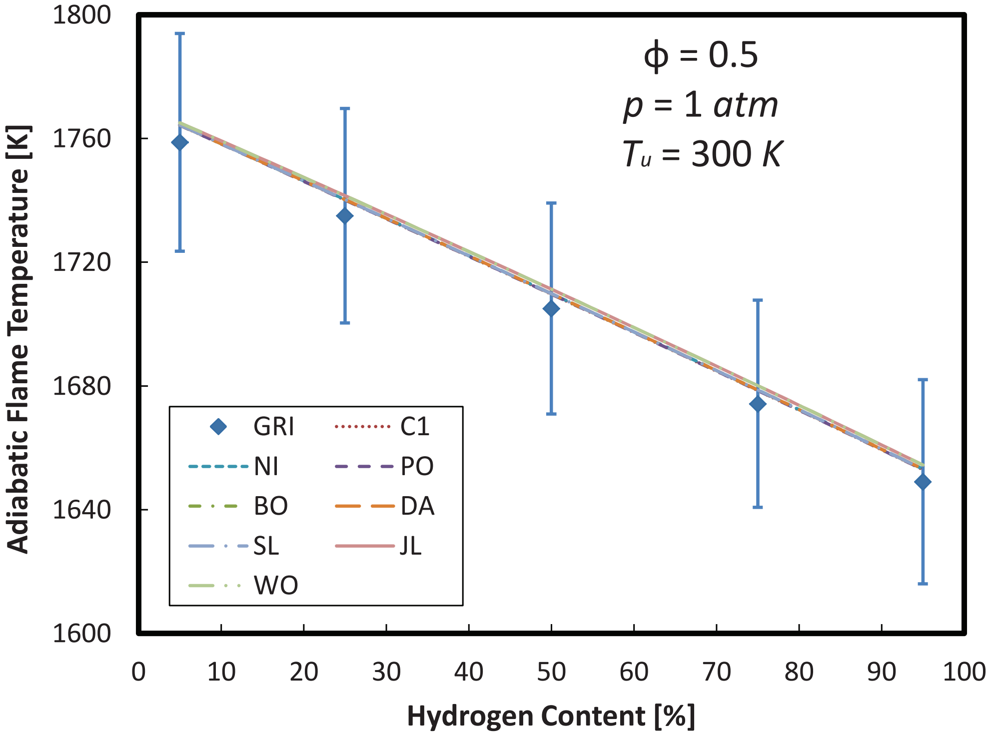

(a)

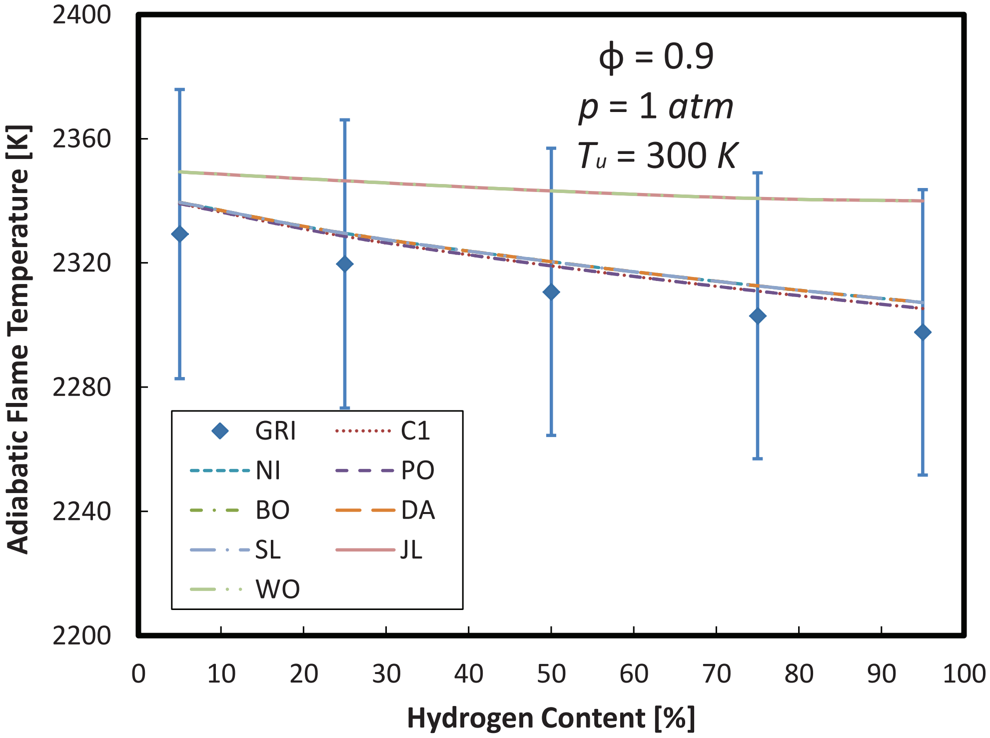

(b)

Figure 4.3: Adiabatic flame temperature predictions by different kinetic models for varying syngas composition at (a) $\phi = 0.5$ and (b) $\phi = 0.9$. $p = 1atm$ and $T_u = 300K$

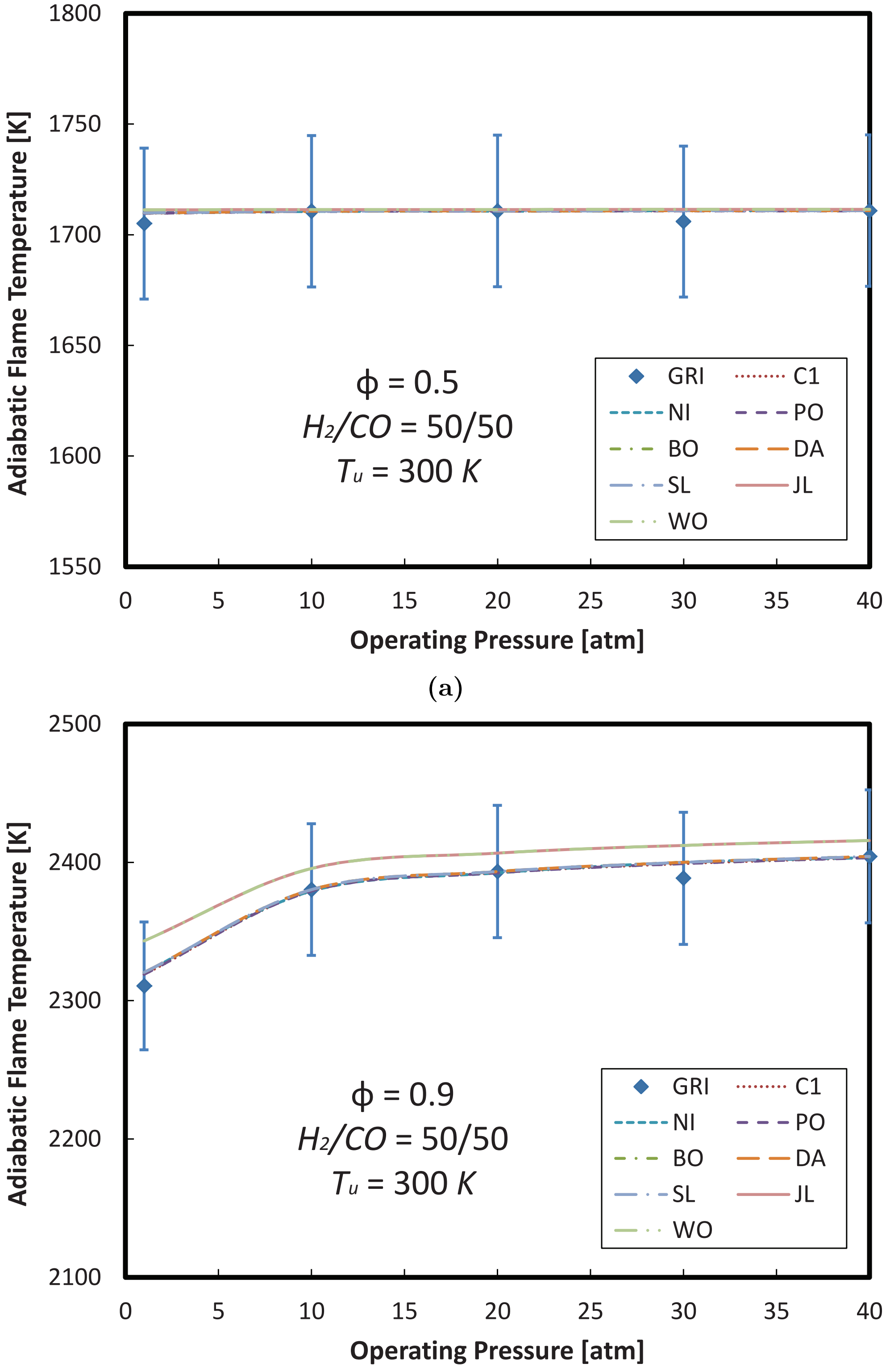

(a)

(b)

Figure 4.4: Adiabatic flame temperature predictions by different kinetic models for varying operating pressure at (a) $\phi = 0.5$ and (b) $\phi = 0.9$. $H_2/CO = 50/50$ and $T_u = 300K$

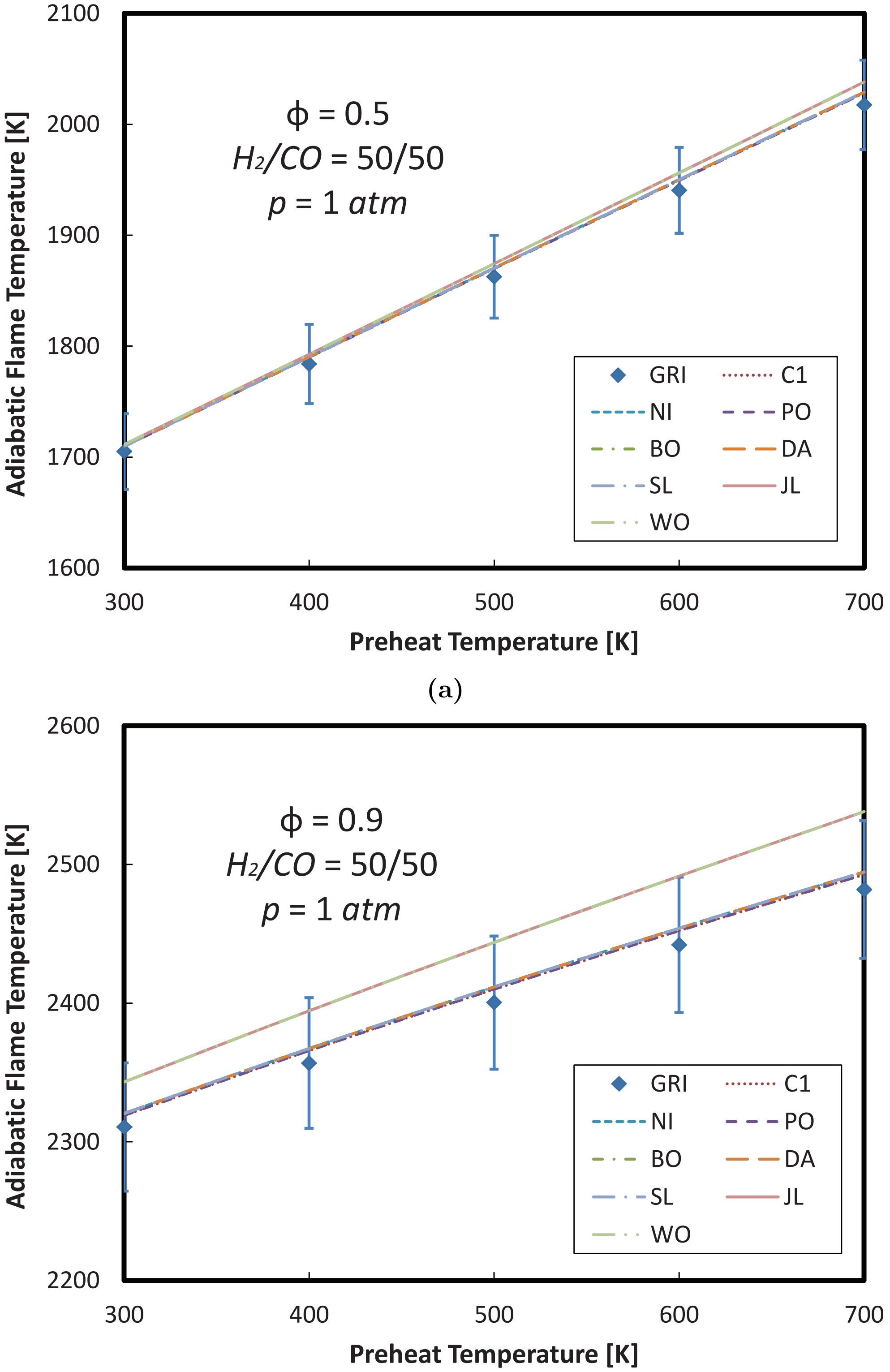

(a)

(b)

Figure 4.5: Adiabatic flame temperature predictions by different kinetic models for varying preheat temperature at (a) $\phi = 0.5$ and (b) $\phi = 0.9$. $H_2/CO = 50/50$ and $p = 1atm$

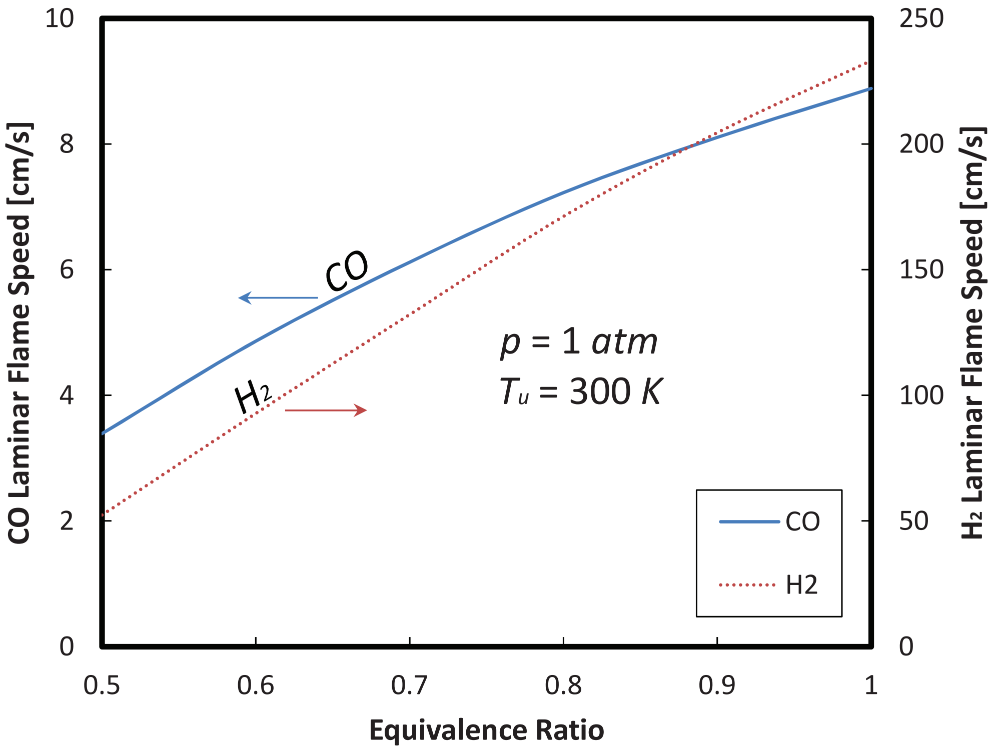

Figure 4.6: Laminar flame speed of pure H_2 and CO fuels under lean conditions predicted by GRI mechanism. $T_u = 300K$ and $p = 1atm$

4.3.2 Laminar Flame Speed

In qualitative terms, the laminar flame speed (LFS) is proportional to the square root of thermal diffusivity and reaction rate and inversely proportional to the square root of fuel density. Figure 4.6 shows the LFS for both pure H_2 and CO under lean premixed conditions. It can be seen that the LFS for H_2 is constantly higher than that of CO. This is due to the fact that the thermal diffusivity and the density of H_2 gas are 7 times higher and 14 times lower, respectively, than that of CO, the combination of which favors higher LFS for hydrogen. However, in both cases of H_2 and CO, LFS increases with the equivalence ratio.

Effect of Equivalence Ratio

The effect of equivalence ratio (ϕ) on the accuracy of the selected mechanisms under lean conditions is presented in Figure 4.7. LFS of representative syngas compositions of 50/50 H_2/CO and 5/95 H_2/CO were computed and compared with experimental results of Bunkute [72] and Bouvet [27], respectively. In general, it can be observed that enriching the fuel (i.e. increasing the equivalence ratio) in the fuel-air mixture increases the LFS. This is attributed to increased LHV of fuel that enhances flame propagation. This trend was followed by all mechanisms understudy. At very lean condition ($\phi = 0.4$, 5/95 H_2/CO), GRI, C1 and SL mechanisms predicted LFS within 10% accuracy, while NI, BO, PO and DA predicted within 5%. This error further decreases as the syngas approaches intermediate equivalence ratio ($\phi = 0.6$) but increases as the mixture approaches stoichiometry. At stoichiometric conditions, SL mechanism predicted LFS within 20% accuracy while other reduced and detailed mechanisms predicted within 25% error. The global mechanisms of JL and WO over-predict and under-predict the LFS, respectively. Figure 4.7a similarly shows that the accuracy of the global mechanisms decreases as the syngas becomes richer with about 60% under-prediction in JL mechanism and more than 170% over-prediction in WO mechanism. These trends are similarly observed at 50/50 H_2/CO (Figure 4.7b) but with larger error in all cases. The large error obtained in the case of the global mechanisms is due to the absence of elementary species and radicals that consume energy for the dissociation and recombination processes.

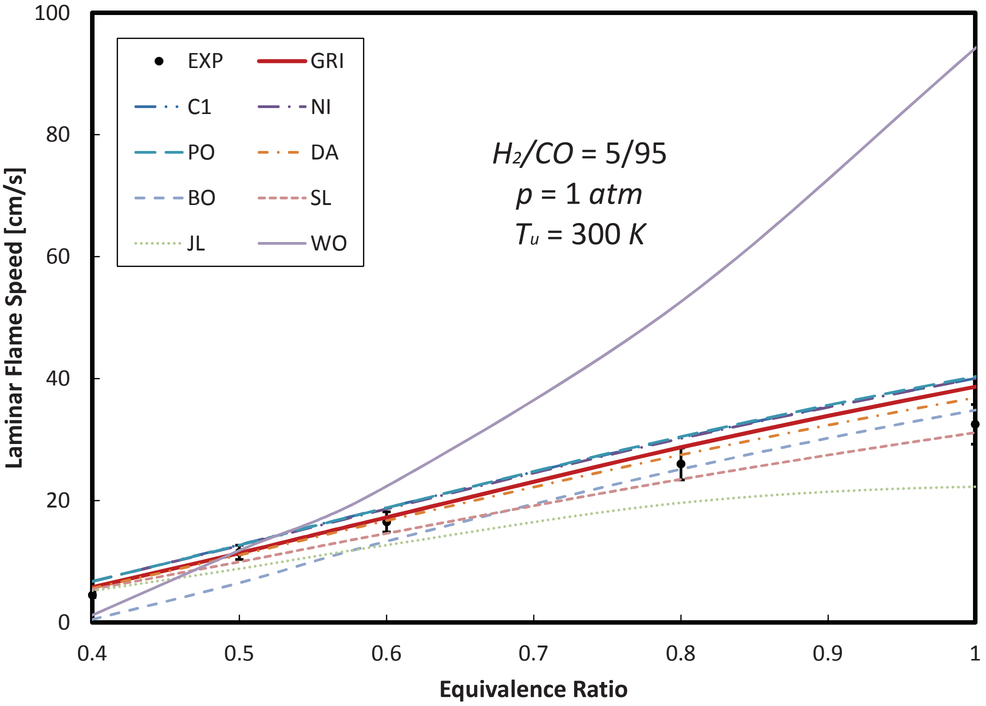

(a)

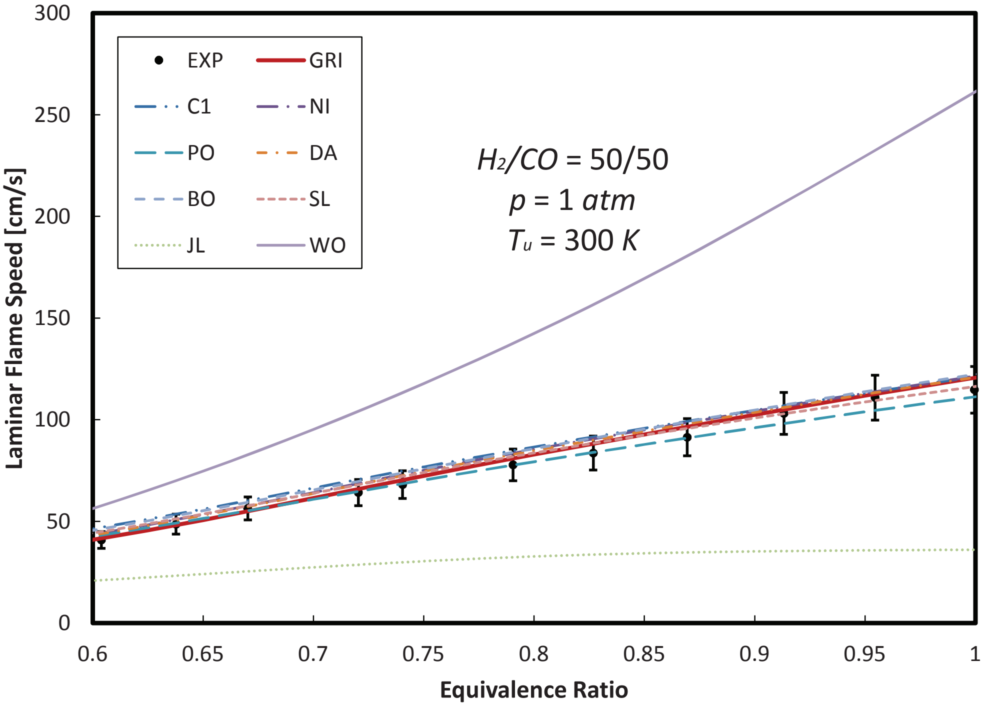

(b)

Figure 4.7: Experimental (symbols) and predicted (lines) laminar flame speeds at varying equivalence ratio for (a) $H_2/CO = 5/95$ (experimental from Bouvet [27]) and (b) $H_2/CO = 50/50$ (experimental from Bunkute [72]). $p = 1atm$ and $T_u = 300K$

Effect of Syngas Composition

The computed LFSs using all chemical mechanisms (detailed, reduced and global) understudy and experimental data (Bouvet [27]) at equivalence ratio of 0.6 and 0.8 are given in Figure 4.8. It can be observed that increasing the hydrogen content in the syngas mixture increases the LFS due to high diffusivity of H_2 gas. The reduced mechanism of SL gave the best prediction with 5% maximum error as compared to DA mechanism with 11% maximum error, GRI and BO mechanisms with 15% maximum error, while other reduced mechanisms of PO, NI, and C1 gave 25% maximum error as presented in Figure 4.7a. It should be noted that this maximum error is observed at low hydrogen content in the syngas which decreases as the hydrogen content of the syngas increases for all reduced and detailed mechanisms. The global mechanism of JL was observed to consistently under-predict the LFS with error of 18% at 5% H_2 content which increases with increasing hydrogen content up to about 50% at 50% H_2 as against WO mechanism whose error decreases from 43% at 5% H_2 to 35% at 50% H_2. It is important to note that the prediction error decreases as the hydrogen content of the syngas increases at $\phi = 0.6$ (Figure 4.8a). However, it increases as the hydrogen content increases at $\phi = 0.8$ (Figure 4.8b). This trend was followed by all mechanisms but with higher error margin in the global mechanisms. For instance, SL mechanism which gave the best prediction has error variation of about 3-13% at $\phi = 0.8$ while WO mechanism which gave the worst prediction had between 35-97% over-prediction at $\phi = 0.8$.

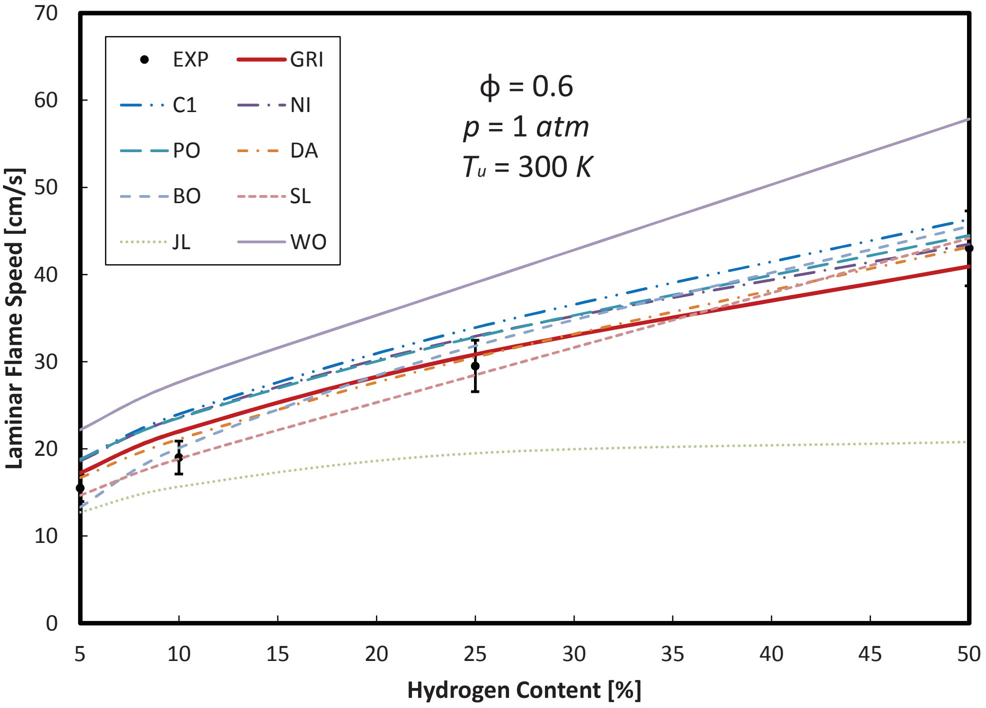

(a)

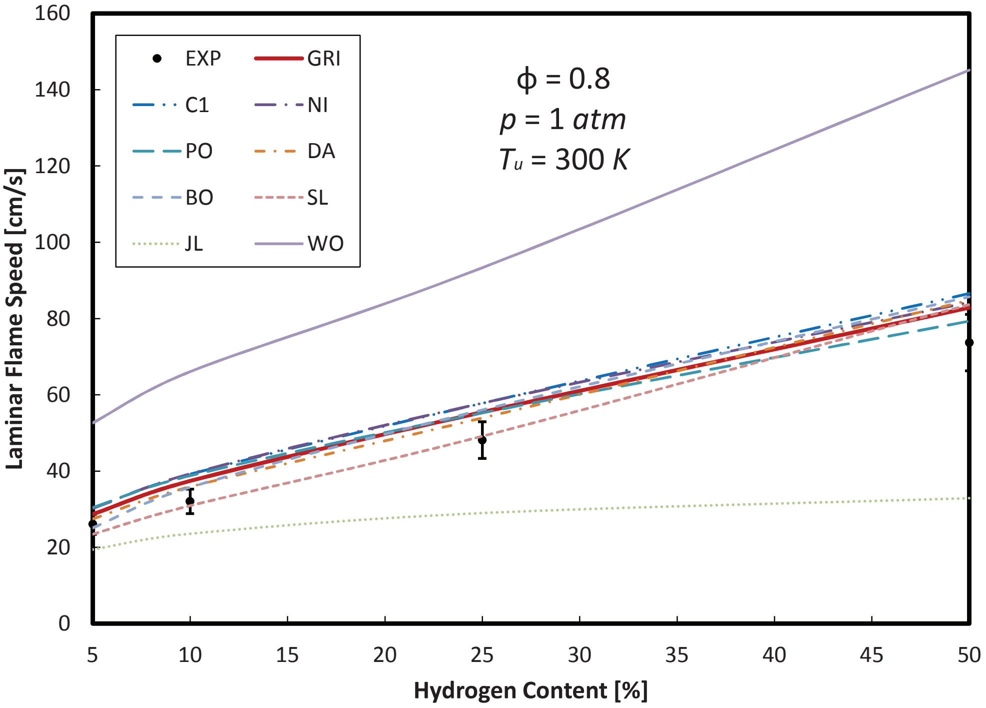

(b)

Figure 4.8: Experimental (symbols) and predicted (lines) laminar flame speeds for varying syngas composition at (a) $\phi = 0.6$ and (b) $\phi = 0.8$. Experimental from Bouvet [27]. $p = 1atm$ and $T_u = 300K$

Effect of Operating Pressure

The effects of pressure in turbulent combustion modeling are also important since reaction pathways are affected by pressure. High pressure combustion simulations must therefore make use of appropriate mechanism to improve the numerical accuracy. Thus, the need to study the effect of pressure on the LFS and the predictability of different mechanisms under varying pressure is imperative. It is however noteworthy to mention that experimental data to validate the effect of pressure are substantially limited. The GRl mechanism was therefore used as the base case in the present study. Figure 4.9 shows the effect of pressure on the LFS at $\phi = 0.6$ and $\phi = 0.8$ for all kinetic models. It can generally be observed that as the pressure increases, the LFS in a 50/50 H_2/CO syngas flame decreases. This is due to the fact that even though the reaction rate increases with pressure which tends to increase the LFS, the increase in the density causes the thermal diffusivity to decrease, outweighing the increase in the reaction rate, reducing the LFS eventually. At higher equivalence ratio ($\phi = 0.8$), the LFS is generally observed to be higher than those at $\phi = 0.6$. This shows that the contribution of the presence of fuel rich zones cannot be overshadowed by the effect of higher pressure. While all reduced mechanisms predicted the LFS within 10% GRl mechanism prediction range at lower pressure (less than 5 atm), there is a significant over-prediction of the GRl mechanism LFS at higher pressures. Under varying condition of pressure, SL mechanism, that had earlier (Section 4.3.2) good predictions of the experimental data, resulted in an average of 76% and 45%

prediction range of the GRI mechanism at $\phi = 0.6$ and $\phi = 0.8$, respectively. In the global mechanisms category, the JL kinetic model under-predicted the GRl LFS with an average of 87% and 28% at $\phi = 0.6$ and $\phi = 0.8$, respectively, while WO mechanism over-predicted GRl mechanism LFS with an average of 317% and 241% at $\phi = 0.6$ and $\phi = 0.8$, respectively.

Effect of Preheat Temperature

In many combustion systems, the reactants initial temperature is very important due to, for instance, compression in gas turbines or heat waste recovery. This will have effects on the combustion characteristics and emissions. Figure 4.10 shows the effect of preheat temperature on the predicted LFS for 50/50 H_2/CO syngas composition. Generally, increasing the preheat temperature increases the LFS due to the increased energy for flame propagation. This trend was confirmed by experimental results and the mechanisms understudy at $\phi = 0.6$ (Figure 4.10a) and $\phi = 0.9$ (Figure 4.10b). The GRI detailed mechanism and the reduced mechanism of PO resulted in good predictions up to 400 K preheat temperature with less than 5% error as compared to 5-10% error range for SL, DA, and NI mechanisms. C1 and BO mechanisms had up to 12% error at $\phi = 0.6$. As the temperature increases beyond 500 K, the discrepancy between the predicted and measured LFSs rises sharply with up to 35% error in GRI, PO, NI and SL mechanisms, and with 44-48% error ranges for C1 and DA mechanisms and about 53% error for BO mechanism. In the global mechanism category, JL consistently under-predicted the LFS for more than 50% at all temperatures while WO mechanism

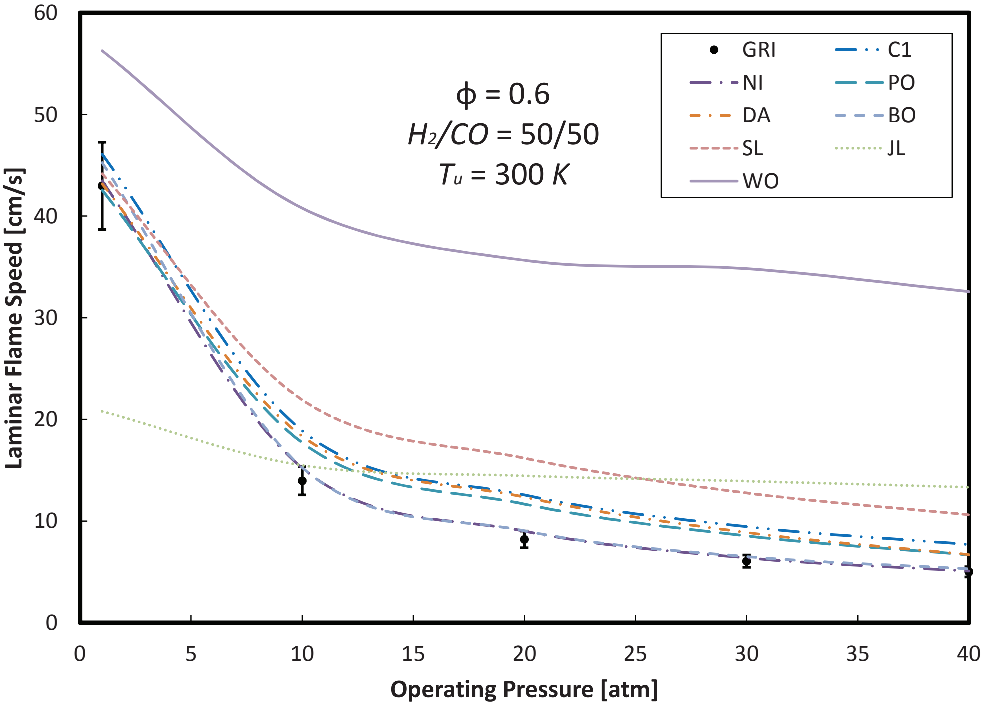

(a)

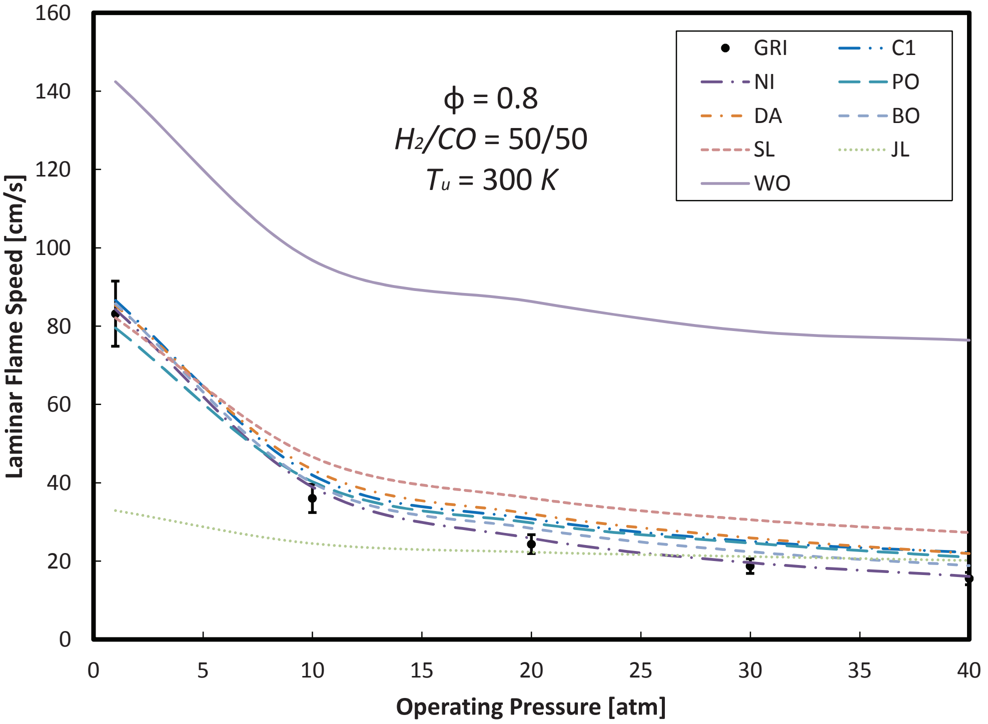

(b)

Figure 4.9: Predicted laminar flame speeds for varying operating pressure at (a) $\phi = 0.6$ and (b) $\phi = 0.8$. Reference mechanism: GRI Mech. 3.0. $H_2/CO = 50/50$ and $T_u = 300K$

over-predicted the LFS by 48% at 300 K and up to 64% at 700 K. As the fuel becomes richer ($\phi = 0.9$), the accuracy of the detailed and reduced mechanisms further reduces with GRI, NI, PO, and SL having 20-35% discrepancy while DA, C1, and BO having approximately 28-47% error. This shows that effect of high preheat temperature cannot be fully captured by the present mechanisms especially when coupled with rich mixtures. The discrepancy error, however, continues to increase in the global mechanisms with JL mechanism under-predicted the LFS up to 65% while WO over-predicted by more than 100% at 700 K.

The average error obtained for all mechanisms understudy is summarized in Figure 4.11. SL mechanism was observed to have an average error of less than 20% (except for varying preheat temperature at equivalence ratio of 0.9), which is comparable to the GRI mechanism, making it a promising mechanism. The global mechanisms have mostly average error of more than 40% and even up to 100% in WO mechanism. The observed high error in the global mechanisms will have substantial effect on the accuracy of the CFD simulation including NO_X formation. It may be concluded that the use of the two global mechanisms understudy (JL and WO) need further improvement (parameter optimization) to enhance its accuracy for possible use in the CFD modeling of lean premixed syngas combustion. Due to this requirement the global mechanism of JL and WO was not further studied in this work.

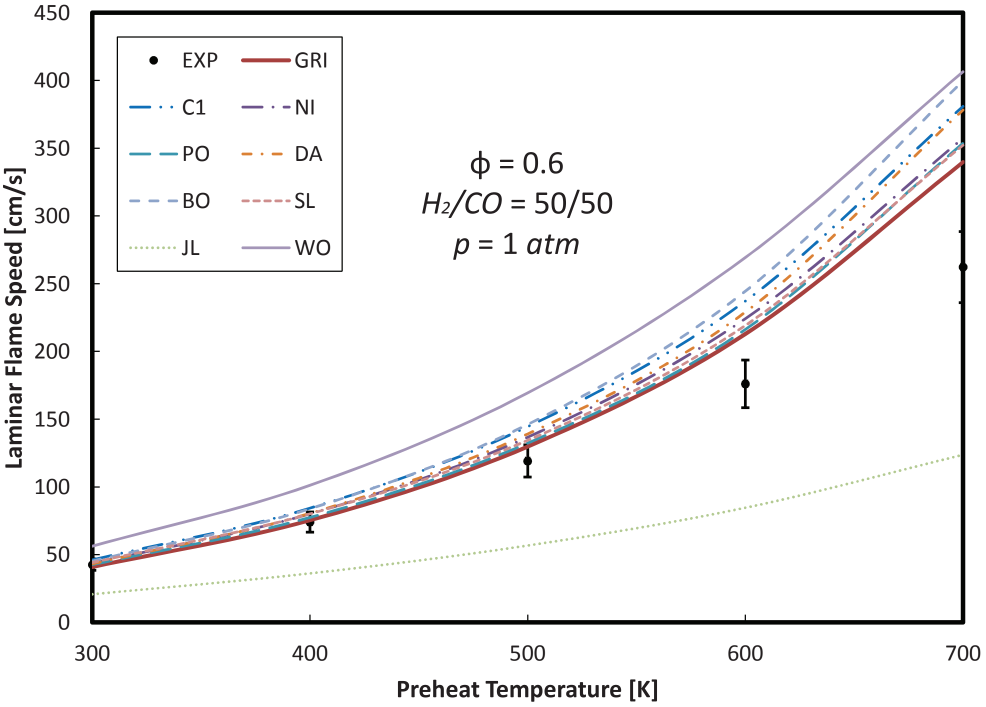

(a)

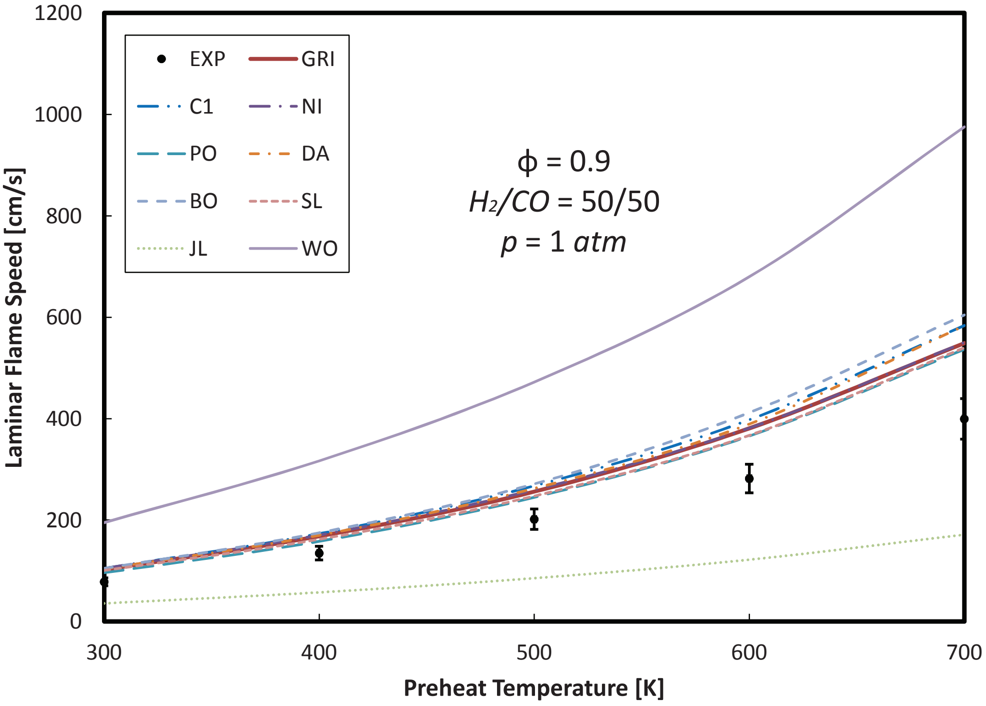

(b)

Figure 4.10: Experimental (symbols) and predicted (lines) laminar flame speeds for varying preheat temperature at (a) $\phi = 0.6$ and (b) $\phi = 0.9$. Experimental from Natarajan [32]. $H_2/CO = 50/50$ and $p = 1atm$

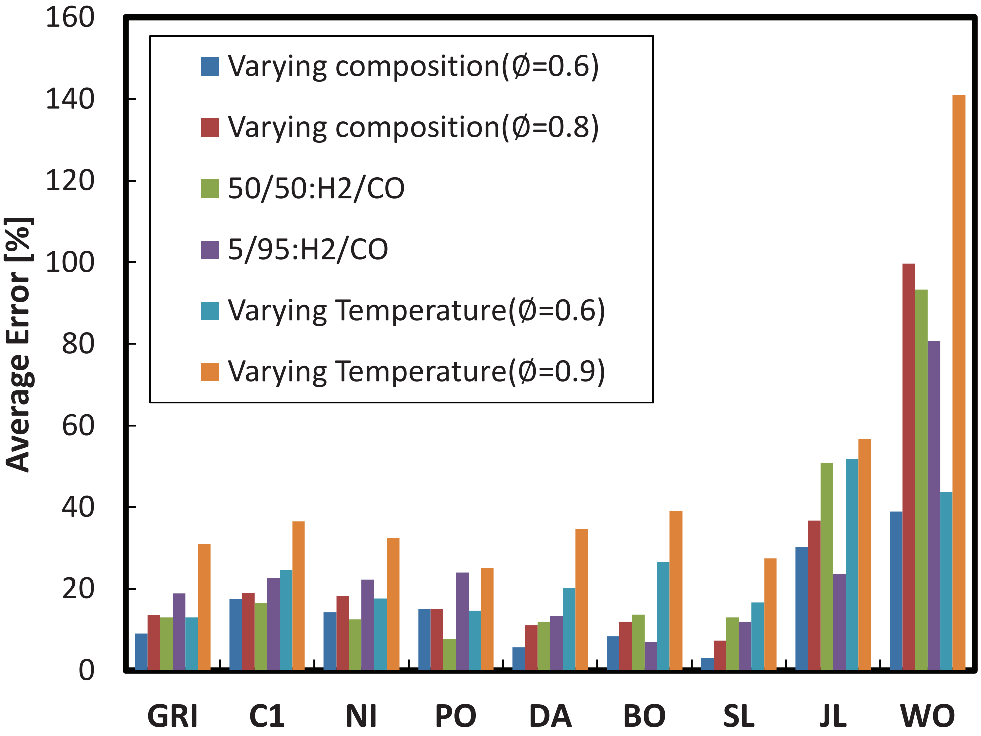

Figure 4.11: Laminar flame speed average error between experimental and calculated values for all kinetic models. Varied parameters are calculated at fixed $H_2/CO = 50/50$, $p = 1atm$, and $T_u = 300K$

4.3.3 NO Emissions

The NO_X chemistry used in the C1 model and the reduced mechanisms was based on the three-step *Zeldovich* mechanism that accounts basically for the thermal NO_X production while the GRI contains the detailed N chemistry that accounts for both the thermal and prompt NO_X. Figure 4.12a shows the NO estimates for 25/75 H_2/CO at lean conditions. As the equivalence ratio increases the NO concentration was also observed to increase due to presence of more fuel in the fuel-air mixture, which raises combustion temperature and hence increases the thermal NO formation. This trend was followed by the reduced and detail mechanisms understudy. The discrepancies in the NO prediction between GRI and other mechanisms was observed to increase as the mixture approached stoichiometry with a discrepancy of about 3% when compared to GRI for all mechanisms except SL with 6% discrepancy. Similar trend was observed for the 50/50 and 75/25 H_2/CO mixtures. At 75/25 H_2/CO composition, SL was observed to consistently over-predict NO as compared to GRI. The discrepancy was highest in SL mechanism with a difference of about 16% at $\phi = 0.9$. This is, however, not unusual since the GRI mechanism over-predicted the measured LFS by 19% as against 4% under-prediction by SL under similar conditions.

The effect of H_2 content in syngas on NO formation is presented in Figure 4.13. There is a significant difference between GRI predicted NO and other mechanisms at low hydrogen content and very lean conditions (Figure 4.13a). This is attributed to relative importance of prompt NO compared to thermal NO at low equivalence ratios which is accounted for by only the GRI mechanism. However, at higher equivalence ratio ($\phi = 0.9$) the thermal NO contribution becomes dominant and the NO prediction by all mechanisms is within 10% GRI base case prediction range, except for SL model. This is due to the amplification of the error in the predicted LFS of both GRI and SL, being connected with the LFS characteristic observed in Figure 4.8. For example, GRI over-predicted the LFS by 11% while SL under-predicted the LFS by 5% at 5% H_2. On the other hand at $\phi = 0.9$ the GRI under-predicted the LFS by about 4% and SL model over-predicted it by around 2%.

The effect of increasing the operating pressure on NO prediction by the reduced and detailed mechanisms at very lean condition ($\phi = 0.5$) and close to stoichiometry ($\phi = 0.9$) are summarized in Figure 4.14 along with the premixed mixture AFT predicted by the GRI mechanism. At $\phi = 0.5$, it can be observed that the increase in the operating pressure increases the AFT. The NO prediction, however, decreases with increasing pressure except in the case of Boivon mechanism. While the increased AFT favors the formation of the thermal NO, the dissociation of the NO formed into its original constituents at higher pressures outweigh the amount formed thereby leading to continuous decline in the NO formation. This effect is important at low equivalence ratios where thermal NO formation route is insignificant. This reason is also responsible for the remarkable difference observed in the NO prediction by the GRl and other mechanisms understudy. At higher equivalence ratio ($\phi = 0.9$), the thermal NO formation and

AFT followed the same trend. All the reduced mechanisms gave NO mole fractions within 10% prediction range of the GRI mechanism, except for the case of SL mechanism that increasingly under-predicted the NO formation with operating pressure.

Figure 4.15 shows the effect of preheat temperature on NO prediction. Increasing the preheat temperature was observed to increase the flame temperature which enhances the formation of thermal NO. At very lean condition ($\phi = 0.5$) (Figure 4.15a), the observed NO prediction by the reduced and detailed mechanisms is more than 50% prediction range of the GRI at low preheat temperature. This is due to the unaccounted prompt NO in the reduced mechanisms which have relative importance as compared to the thermal NO at very lean condition. Though the accuracy of the mechanisms improve with increasing preheat temperature, due to the increased contribution of the thermal NO formation, the NO prediction was generally more than 10% for all the reduced and detailed mechanisms, except the case of PO and NI with about 2% and 6% prediction range of the GRI, respectively. However, near stoichiometric condition ($\phi = 0.9$, Figure 4.15b), the reduced and detailed mechanisms have similar NO predictions within 10% prediction range of the GRI.

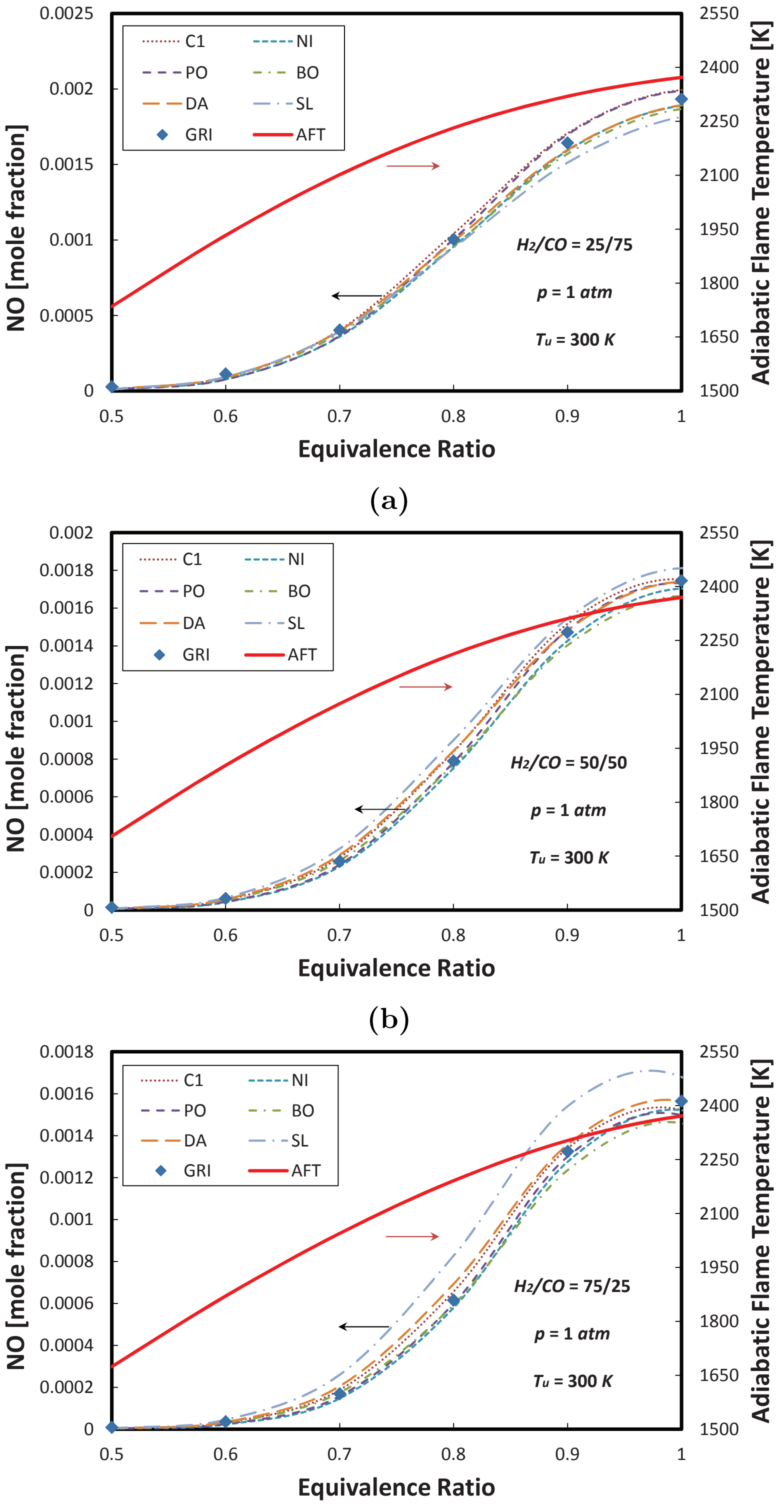

(a)

(b)

(c)

Figure 4.12: NO predictions of detailed and reduced kinetic models at varying equivalence ratio for (a) 50/50 (b) 25/75 and (c) 75/25 H_2/CO syngas compositions. $p = 1atm$ and $T_u = 300K$

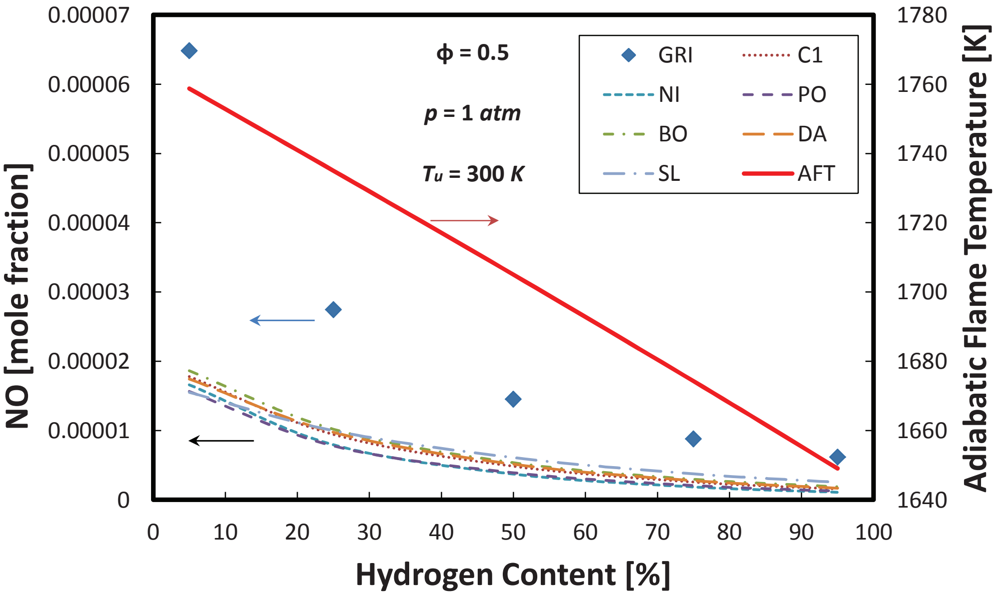

(a)

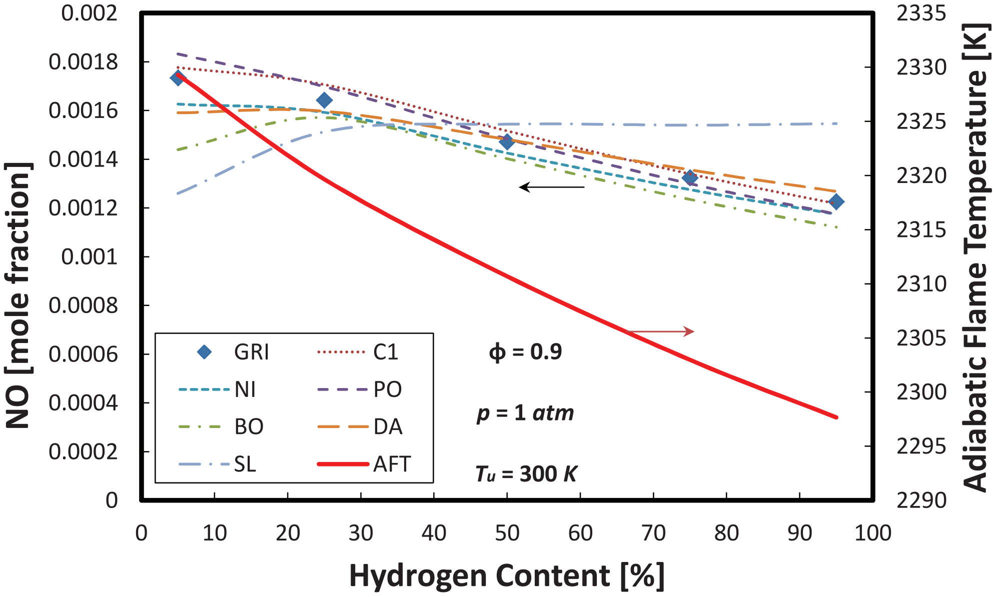

(b)

Figure 4.13: NO predictions of detailed and reduced kinetic models for varying syngas composition at (a) $\phi = 0.5$ and (b) $\phi = 0.9$. $p = 1atm$ and $T_u = 300K$

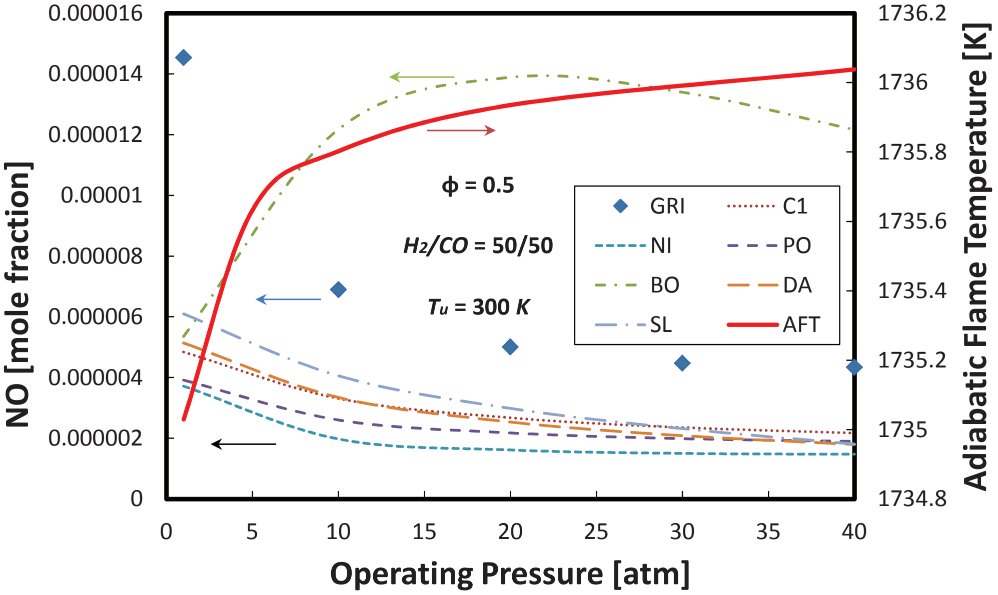

(a)

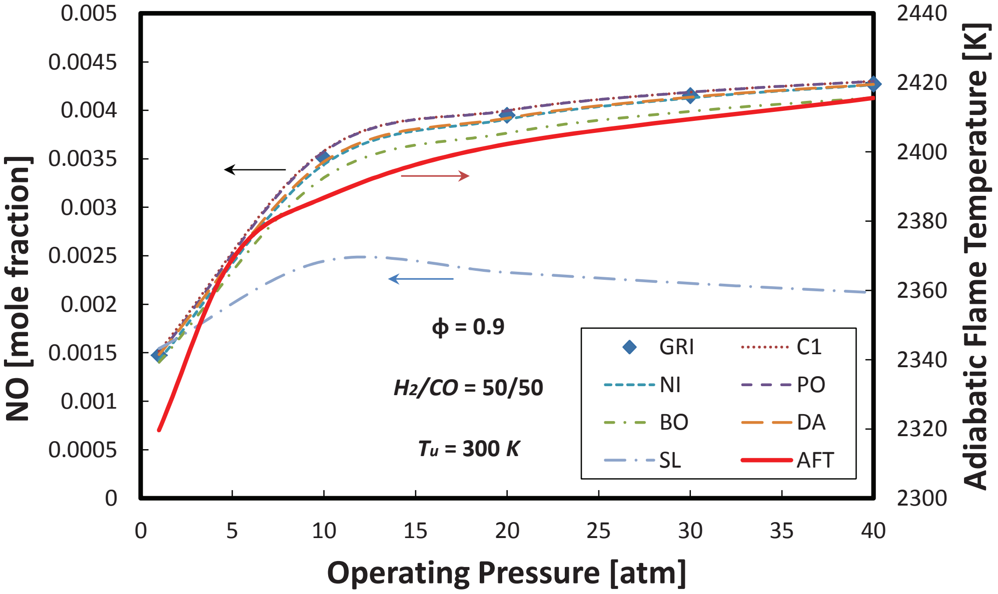

(b)

Figure 4.14: NO predictions of detailed and reduced kinetic models for varying operating pressure at (a) $\phi = 0.5$ and (b) $\phi = 0.9$. $H_2/CO = 50/50$ and $T_u = 300K$

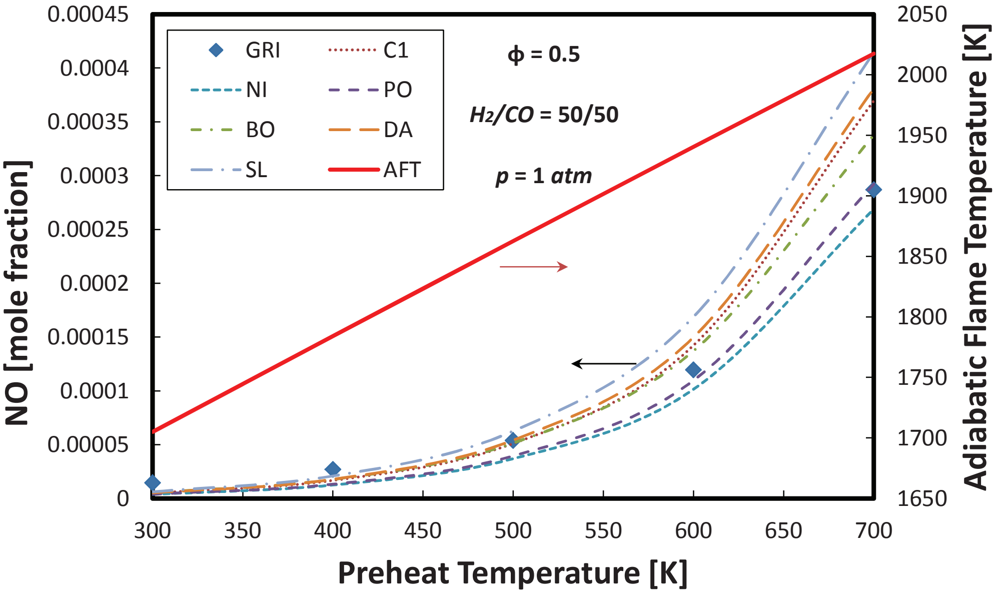

(a)

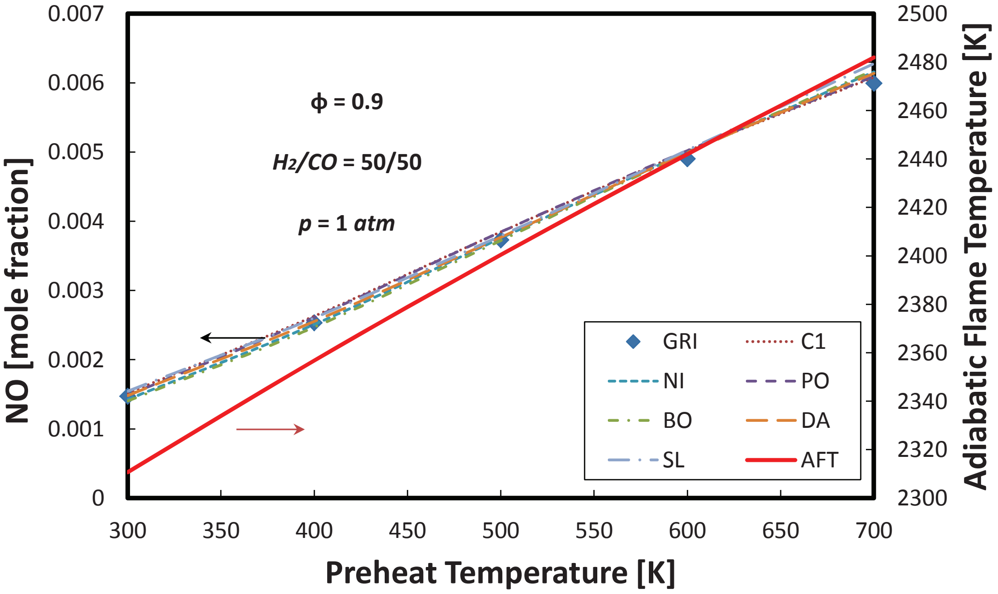

(b)

Figure 4.15: NO predictions of detailed and reduced kinetic models for varying preheat temperature at (a) $\phi = 0.5$ and (b) $\phi = 0.9$. $H_2/CO = 50/50$ and $p = 1atm$

CHAPTER 5

SIMULATION OF LPM SYNGAS COMBUSTION IN A SWIRL-STABILIZED COMBUSTOR

In this chapter, the simulation of LPM syngas combustion in a lab-scale swirl-stabilized combustor is presented. The simulation is intended to have an insight into the effect of swirl number, syngas composition, and equivalence ratio on the characteristics and emissions of LPM syngas turbulent flames. The geometry description and boundary conditions, computational details, solution procedure, models validation, and results and discussion are described in details.

5.1 Geometry Description and Boundary Conditions

The geometry of the swirl-stabilized combustor is represented in Figure 5.1 and Figure 5.2. The premixed syngas-air mixture enters the combustor at atmospheric pressure and temperature through a 38 mm diameter inlet pipe with a uniform velocity profile. 42.5 mm downstream the inlet section, the pipe expands into a 76 mm diameter pipe representing the combustion chamber diameter. The length of the chamber is 10 times its diameter i.e. 760 mm. The velocity condition at the chamber wall is zero following the no-slip condition. For the case of non-zero swirl number, a swirler is introduced in the inlet section, creating a tangential velocity component of the inlet jet. Different swirl numbers (S = 0, 0.3, 0.5, 0.7, and 1.0 corresponding to a swirl angle of 0^o, 25^o, 35^o, 45^o, and 55^o), syngas compositions (H_2/CO = 5/95, 25/75, 50/50, 75/25, and 95/5, % by volume), and equivalence ratios (ϕ = 0.4, 0.5, 0.6, 0.7, and 0.8) are implemented for the parametric study. The base case at which the parameters are varied at is $S = 0.7$, $H_2/CO = 50/50$, and $\phi = 0.6$. The simulations are conducted at a fixed Reynolds number ($Re = 20,000$) based on the inlet section pipe diameter. A pressure outlet boundary condition is imposed at the exit section, while the combustion chamber wall is maintained at a constant temperature of 600 K as an attempt to replicate the condition at an actual gas turbine combustor. Table 5.1 shows a description of the different cases simulated.

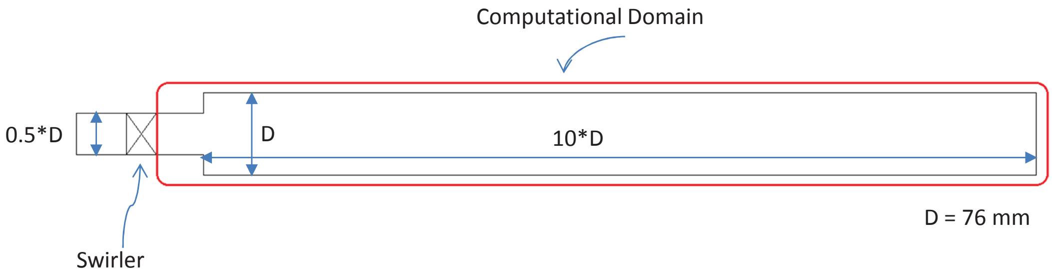

Figure 5.1: Two-dimensional view of the swirl-stabilized combustor

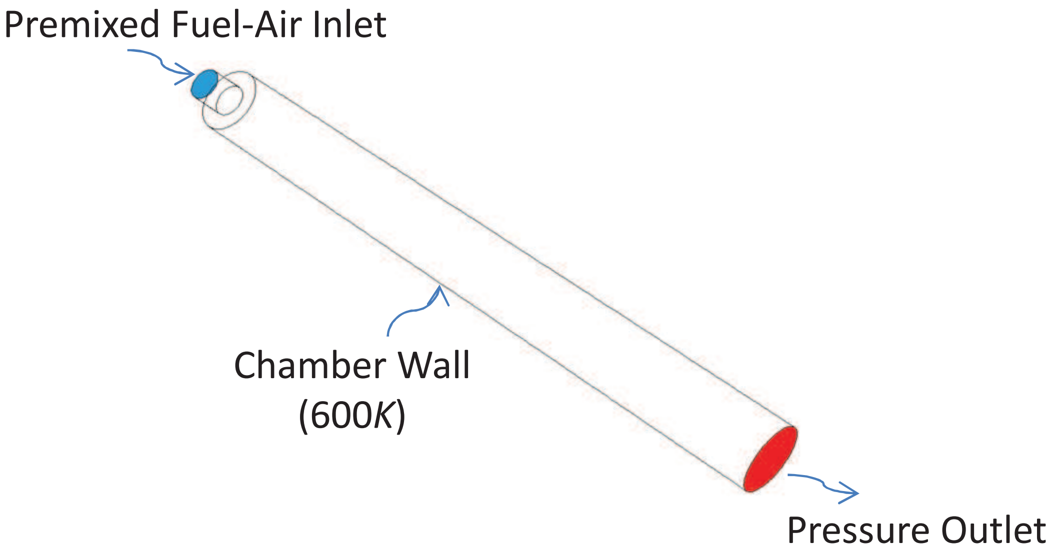

Figure 5.2: Three-dimensional view of the swirl-stabilized combustor along with the boundary conditions

Table 5.1: Cases used in the parametric study of LPM syngas combustion in the swirl-stabilized combustor. $Re = 20,000$

Case	S	H_2/CO [vol %]	ϕ	u [m/s]	w [m/s]	Power Input [kW]
1	0.0	50/50	0.6	21.710	0.000	55.29
2	0.3	50/50	0.6	19.834	8.830	55.29
3	0.5	50/50	0.6	17.339	13.066	55.29
4	0.7	50/50	0.6	15.352	15.352	55.29
5	1.0	50/50	0.6	12.140	17.999	55.29
6	0.7	05/95	0.6	4.9834	4.9834	19.24
7	0.7	25/75	0.6	5.1373	5.1373	19.24
8	0.5	50/50	0.6	5.3434	5.3434	19.24
9	0.7	75/25	0.6	5.5669	5.5669	19.24
10	0.7	95/05	0.6	5.7595	5.7595	19.24
11	0.7	50/50	0.4	13.589	13.589	34.95
12	0.7	50/50	0.5	14.559	14.559	45.21
13	0.5	50/50	0.6	17.339	13.066	55.29
14	0.7	50/50	0.7	16.012	16.012	65.10
15	0.7	50/50	0.8	16.572	16.572	74.57

5.2 Mathematical Models

The $k - \epsilon$ model for modeling turbulence has been used in this calculation. This model was selected in this case because historically it has been extensively used in modeling turbulence in industrial CFD applications [75]. The DO model was selected for modeling radiation since it is suitable for a wide range of optical thicknesses, covering many applications such as radiation exchange between gases and walls in combustion systems and surface-to-surface radiation. Moreover, the Weighted Sum of Gray Gas model (WSGGM) has been used to model absorption coefficient of the mixture. Furthermore, Eddy-Dissipation Concept (EDC) model for turbulence-chemistry interactions has been used since it is the appropriate model that allows the implementation of a detailed chemical mechanism.

In addition, this model is more suitable for modeling combustion that involves CO burning [76].

The steady state mathematical equations, in the Reynolds Averaging context, representing these models are described [77–79].

5.2.1 Continuity Equation

$$\frac{\partial \overline{\rho} \overline{u}_j}{\partial x_j} = 0 \tag{5.1}$$

5.2.2 Momentum Equation

$$\frac{\partial \overline{\rho u_i u_j}}{\partial x_i} = -\frac{\partial \overline{p}}{\partial x_i} + \frac{\partial \left(\overline{t}_{ij} + \overline{\tau}_{ij}\right)}{\partial x_j} \tag{5.2}$$

where $\overline{t}_{ij}$ is the viscous stress tensor, and $\overline{\tau}_{ij}$ is the average Reynolds stress tensor given in Eq. 5.3 and Eq. 5.4, respectively.

$$\overline{t}_{ij} = \mu \left[\left(\frac{\partial \overline{u_i}}{\partial x_j} + \frac{\partial \overline{u_j}}{\partial x_i} \right) - \frac{2}{3} \frac{\partial \overline{u_k}}{\partial x_k} \delta_{ij} \right] \tag{5.3}$$

$$\overline{\tau}_{ij} = -\overline{\rho u_i' u_j'} \tag{5.4}$$

$$\overline{\tau}_{ij} = \mu_t \left[\left(\frac{\partial \overline{u_i}}{\partial x_j} + \frac{\partial \overline{u_j}}{\partial x_i} \right) - \frac{2}{3} \frac{\partial \overline{u_k}}{\partial x_k} \delta_{ij} \right] - \frac{2}{3} \left(\overline{\rho k \delta_{ij}} \right) \tag{5.5}$$

where $\delta_{ij} = 1$ if $i = j$, and $\delta_{ij} = 0$ if $i \neq j$ k is the turbulent kinetic energy.

The Realizable $k - \epsilon$ model, which ensures positivity of normal stresses and Schwarz inequality for shear stresses, gives Eq. 5.6 and Eq. 5.7 for the turbulent kinetic energy and turbulent dissipation rate, respectively.

$$\frac{\partial \overline{\rho k u_j}}{\partial x_j} = \frac{\partial \left[\left(\mu + \frac{\mu_t}{\sigma_k} \right) \left(\frac{\partial \bar{k}}{\partial x_j} \right) \right]}{\partial x_j} + G_k - \overline{\rho \epsilon} \tag{5.6}$$

$$\frac{\partial \overline{\rho \epsilon u_j}}{\partial x_j} = \frac{\partial \left[\left(\mu + \frac{\mu_t}{\sigma_\epsilon} \right) \left(\frac{\partial \bar{\epsilon}}{\partial x_j} \right) \right]}{\partial x_j} + C_{1\epsilon} \frac{\bar{\epsilon}}{k} - C_{2\epsilon} \bar{\rho} \frac{\overline{\epsilon^2}}{k} \tag{5.7}$$

where G_k represents the production of turbulent kinetic energy and is defined by Eq. 5.8

$$G_k = \mu_t \left[\left(\frac{\partial \overline{u_i}}{\partial x_j} + \frac{\partial \overline{u_j}}{\partial x_i} \right) \right] \frac{\partial \overline{u_i}}{\partial x_j} - \frac{2}{3} \frac{\partial \overline{u_i}}{\partial x_i} \delta_{ij} \left[\mu_t \frac{\partial \overline{u_k}}{\partial x_k} + \overline{\rho k} \right] \tag{5.8}$$

$C_{1\epsilon}$, $C_{2\epsilon}$, σ_k, and σ_ϵ are constants given as 1.44, 1.9, 1.0, and 1.2, respectively. The standard wall function was used for near wall treatment.

Solving for k and ϵ, the turbulent viscosity, thus, is given by Eq. 5.9.

$$\mu_t = \rho C_\mu \frac{k^2}{\epsilon} \tag{5.9}$$

The standard $k - \epsilon$ model assumes C_μ to be constant at all times. This assumption, however, fails in ensuring positive values of the normal stresses when the strain rate in the flow is large. In order to fix this problem, the realizable $k - \epsilon$ model sensitizes C_μ to the mean flow and turbulence by making it variable, thus ensuring positivity of normal stresses as well as Schwarz inequality for shear stresses. For the realizable $k - \epsilon$ model, C_μ is given by Eq. 5.10.

$$C_\mu = \frac{1}{A_0 + A_S \frac{kU^\star}{\epsilon}} \tag{5.10}$$

where

$$U^\star \equiv \sqrt{S_{ij}S_{ij} + \widehat{\Omega_{ij}}\widehat{\Omega_{ij}}} \tag{5.11}$$

$$\widehat{\Omega_{ij}} = \overline{\Omega}_{ij} - 3\epsilon_{ijk}\omega_k \tag{5.12}$$

$$S_{ij} = \frac{1}{2}\left(\frac{\partial \overline{u_i}}{\partial x_j} + \frac{\partial \overline{u_j}}{\partial x_i}\right) \tag{5.13}$$

The model constants are given by Eq. 5.14.

$$A_0 = 4.04, \quad A_S = \sqrt{6}\cos\phi \tag{5.14}$$

where

$$\phi = \frac{1}{3}\cos^{-1}(\sqrt{6}W), \quad W = \frac{S_{ij}S_{jk}S_{ki}}{\overline{S}^3}, \quad \overline{S} = \sqrt{S_{ij}S_{ij}} \tag{5.15}$$

5.2.3 Energy Equation

The energy equation (Eq. 5.16) accounts for the heat transfer by conduction, convection, species diffusion, and viscous dissipation as well as any source of heat.

$$\frac{\partial}{\partial x_j}\overline{(\rho E + P)\, u_j} = \frac{\partial}{\partial x_j}\left[K_{eff}\left(\frac{\partial T}{\partial x_j}\right) - \sum_j h_j J_j + \tau_{eff} u_j\right] + S_h \tag{5.16}$$

where E is the total energy given by Eq. 5.17.

$$E = h - \frac{P}{\rho} + \frac{v_2}{2} \tag{5.17}$$

K_{eff} is the effective thermal conductivity given as $K_{eff} = k + k_t$, and S_h is the energy source term which includes the heat source due to chemical reactions as well as due to radiation heat transfer.

5.2.4 Radiation Equation

The DO radiation model has been used to solve the radiative heat transfer equation (Eq. 5.18) to obtain the radiation intensity over the distance s.

$$\frac{dI(r,s)}{ds} + (a + \sigma_s) I(r,s) = a n^2 \frac{\sigma T^4}{\pi} + \frac{\sigma_s}{4\pi}\int_0^{4\pi} I(r,s')\Phi(s \cdot s')d\Omega' \tag{5.18}$$

where r is the position vector, s is the direction vector, s' is the scattering direction vector, a is the absorption coefficient, n is the refractive index, σ_s is the scattering coefficient through the path length s, σ is the Stefan-Boltzmann constant ($5.669\times10^{-8}\ W/m^2{\cdot}K^4$), I is the radiation intensity which depends on both, position r and direction s, T is the local temperature, Φ is the phase function and

Ω' is the solid angle.

The weighted-sum-of-gray-gases model (WSGGM) was used for the computation of a variable absorption coefficient, a as given in the general form by Eq. 5.19.

$$a = -\frac{ln(1-\epsilon)}{s} \tag{5.19}$$

where ϵ is the total emissivity over the distance s (Eq. 5.20).

$$\epsilon = \sum_{i=0}^{N} a_{\epsilon,i}(T)\left(1 - e^{-\kappa_i ps}\right) \tag{5.20}$$

where $a_{\epsilon,i}$ is the emissivity weighting factor for the i^{th} fictitious gray gas, $(1 - e^{-\kappa_i ps})$ is the i^{th} fictitious gray gas emissivity, κ_i is the absorption coefficient of the i^{th} gray gas, and p is the sum of partial pressures of all absorbing gases.

5.2.5 Species Equation

The species mass fractions, Y_m are obtained by solving the convection-diffusion equation for the m^{th} species (Eq. 5.21).

$$\frac{\partial}{\partial x_i}(\rho \overline{u}_i Y_m) = -\frac{\partial J_{m,i}}{\partial x_i} + R_m \tag{5.21}$$

where $J_{m,i}$ is the diffusion flux of the m^{th} species resulting from the gradients of concentration and temperature and is given by Eq. 5.22.

$$J_{m,i} = -\left(\rho D_m + \frac{\mu_t}{Sc_t}\right)\frac{\partial Y_m}{\partial x_i} - D_T \frac{\partial T}{\partial x_i}\frac{1}{T} \tag{5.22}$$

where D_m is the mass diffusion coefficient for the m^{th} species, Sc_t is the turbulent Schmidt number, and D_T is the thermal diffusion coefficient.

R_m is the species source term that represents the rate of generation or destruction of the m^{th} species by chemical reactions. It is computed using the eddy-dissipation concept (EDC) model that allows the inclusion of detailed chemical mechanisms in turbulent flows where the reaction rate constant, k is calculated using the Arrhenius model (Eq. 5.23).

$$k = AT^n exp\left(\frac{-E_a}{RT}\right) \tag{5.23}$$

where A is the pre-exponential factor, n is the temperature exponent, and E_a is the activation energy.

5.3 Computational Details and Solution Methods

The governing equations describing the reacting flow are solved numerically using the steady state, pressure based solver in ANSYS FLUENT 14.5. A Finite volume method has been used for the spatial discretization, with Standard scheme for pressure, and Second Order Upwind for density, momentum, turbulent kinetic energy, turbulent dissipation rate, species, energy, and discrete ordinates. The

SIMPLE scheme has been used for the pressure-velocity coupling. The residuals representing the convergence criteria were set to 10^{-3} for continuity, momentum, turbulent kinetic energy, and turbulent dissipation rate; and 10^{-6} for energy, radiation, and species. The NO_X calculations were performed after the solution is converged in the post-processing stage. The convergence criteria for NO_X was set to 10^{-6}.

In order to validate our geometry, a grid independence test was conducted using the base case. Starting with a coarse mesh (330,000 cells), the mesh size was increased to 400,000 cells, 500,000 cells, 650,000 cells, and 850,000 cells. It is worth mentioning that more grids are used in high gradient regions such as inlet section, expansion plane, and vicinity of the wall. The influence of the mesh refinement on the axial velocity and temperature along the centerline of the combustion chamber is shown in Figure 5.3. The results indicated that the difference in the axial velocity and temperature across the centerline of the combustor between the 500,000 and 650,000 grid sizes was 2% and 0.5%, respectively. However, increasing the mesh size to 850,000 cells had a negligible impact on the results with difference of 0.4% in axial velocity and 0.07% in temperature. Therefore, the mesh with grid size of 650,000 cells was selected for performing the parametric study.

5.4 Models Validation

It is important to validate the models used in the simulation of LPM syngas combustion in the swril-stabilized combustor. For this purpose, two sets of ex-

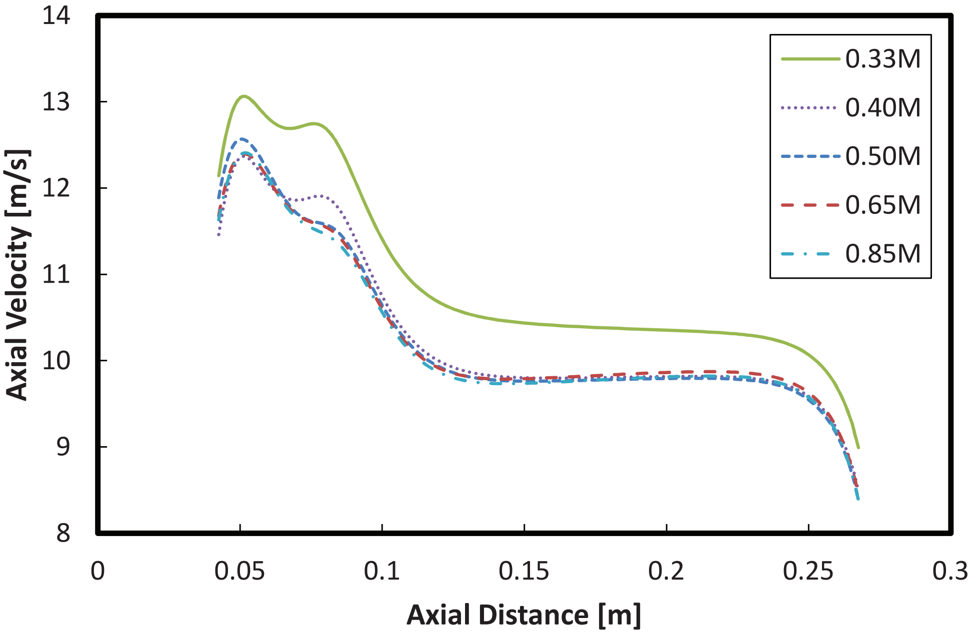

(a)

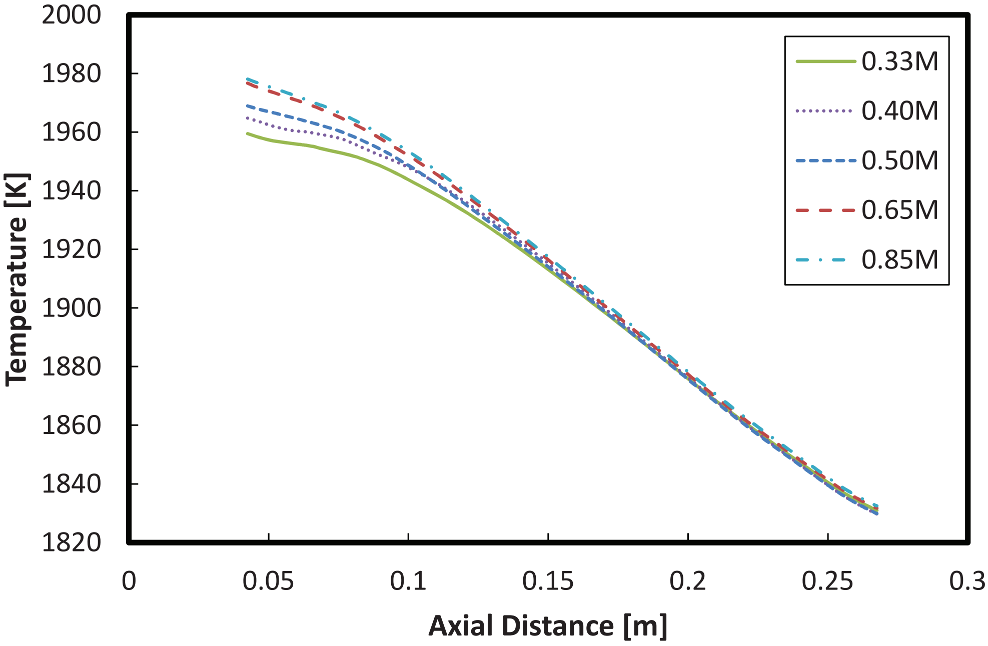

(b)

Figure 5.3: The influence of mesh refinement on (a) the axial velocity and (b) temperature along the centerline of the combustion chamber. $S = 0.7$, $H_2/CO = 50/50$, and $\phi = 0.6$

perimental data were used. The first one is from da Silva et al. [80] and was used in order to make a selection between different turbulence models (Standard $k-\epsilon$ model, Realizable $k-\epsilon$ model, RNG $k-\epsilon$ model, and transition SST model).

The second set of experimental data is from Louis et al. [81] and was used to validate the different models of turbulence, radiation, combustion, and chemistry. In addition, a number of kinetic models for syngas combustion were compared and a suitable chemistry model was selected to perform the parametric study of LPM syngas combustion in the swirl-stabilized combustor.

5.4.1 Choosing a Turbulence Model

Da Silva et al. [80] performed a numerical simulation of a non-premixed natural gas in a 600 kW axis-symmetrical cylindrical burner using a two-step mechanism for methane combustion. The burner supplied the fuel through a 6 cm central circular pipe, while the air was supplied through an annular section in the same plane as the fuel with a 2 cm difference between outer and inner diameters. The combustor had a length of 170 cm and a diameter of 50 cm. The combustion products left the chamber through a 25 cm exhaust pipe. The fuel composed of 90% methane and 10% nitrogen by volume, while the air had a composition of 76% nitrogen, 23% oxygen, and 1% water vaport by mass. Excess air of 5% was used, resulting in fuel and air supply of 0.0125 kg/s (7.76 m/s) at 313.15 K and 0.186 kg/s (36.29 m/s) at 323.15 K, respectively. Figure 5.4 shows the combustor geometry along with the boundary conditions.

The axial and radial distributions of temperature inside the combustion chamber is presented in Figure 5.5 for the four models investigated. For the axial distribution (Figure 5.5a), it can be seen that in the upstream region, all models, except the RNG, predicted the experimental data fairly well. Around the middle of the combustor, all models, except the RNG, under-predicted the experimental data. In the downstream region of the combustor, the Standard model over-predicted the experimental data, while the Realizable under-predicted it. The SST model, however, was the best to predict the data in this case. Looking at the radial distribution of temperature 1.326 m downstream the inlet section (Figure 5.5b), it can

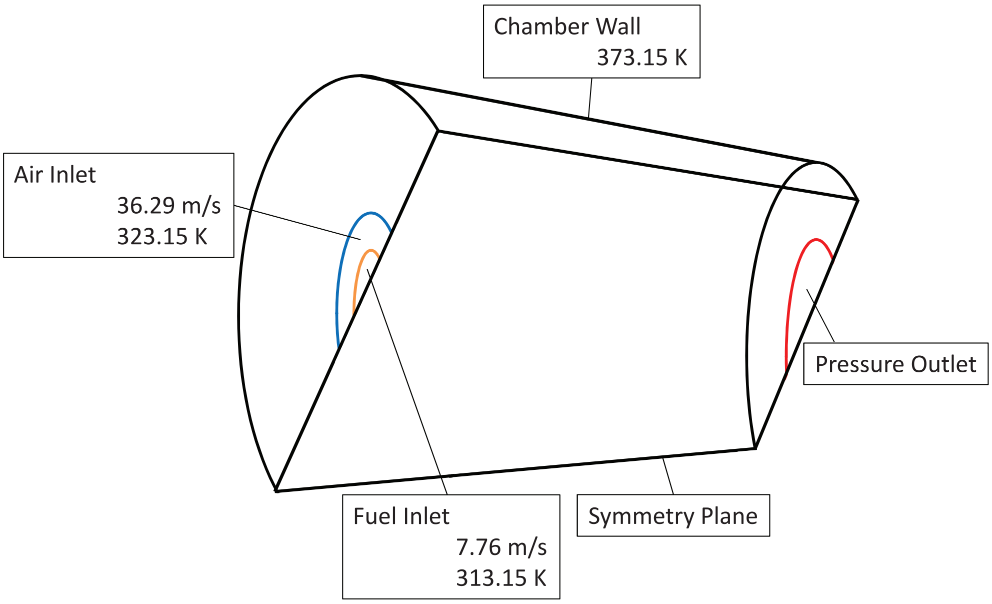

Figure 5.4: Geometry and boundary conditions used for the investigation of the different turbulence models

be seen that close to the centerline, the Realizable model was the best to predict the experimental data. The rest of the models gave bad predictions, with the RNG giving the worst among them. At a further distance from the centerline, the Standard and Realizable models were very good in predicting the experimental data, while the SST model under-predicted the data. The RNG model had high over-prediction in this case. To summarize, the Realizable model is considered most suitable compared to the other models in this case.

Figure 5.6 shows the axial distribution of O_2 and CO mass fractions along the centerline of the combustion chamber. It is shown that the O_2 mass fraction (Figure 5.6a) is worst predicted by the RNG model. In the region after the burner, the data is best predicted by the Standard, SST, and then the Realizable. However, close to the middle region of the combustor and the downstream region close to the exit, the Realizable model seems to be the best to predict the experimental data.

As for the axial distribution of CO mass fraction, again the RNG model gave the worst prediction. However, the rest of the models predicted the experimental data very well up to the middle region of the combustor, in which the models started deviating, except for the Realizable model which was the best in predicting the data in the downstream region. From the above comparison, the Realizable $k - \epsilon$ model was selected for the simulation of the LPM syngas combustion in the swirl stabilized combustor.

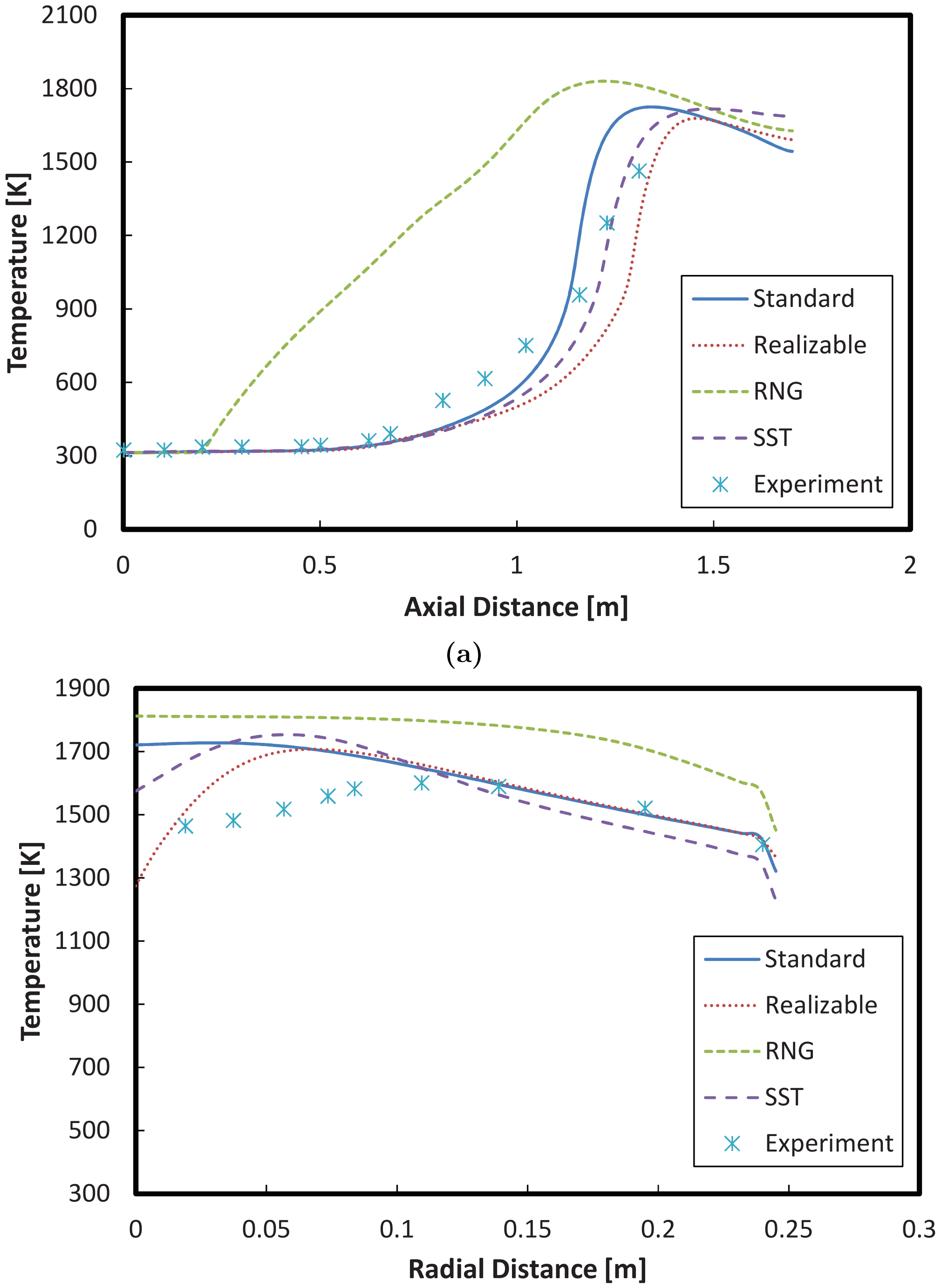

(a)

(b)

Figure 5.5: Temperature distribution predicted by the four turbulence models. (a) Axial distribution of temperature along the cenerline of the combustor. (b) Radial distribution of temperature along a section 1.326m downstream the burner

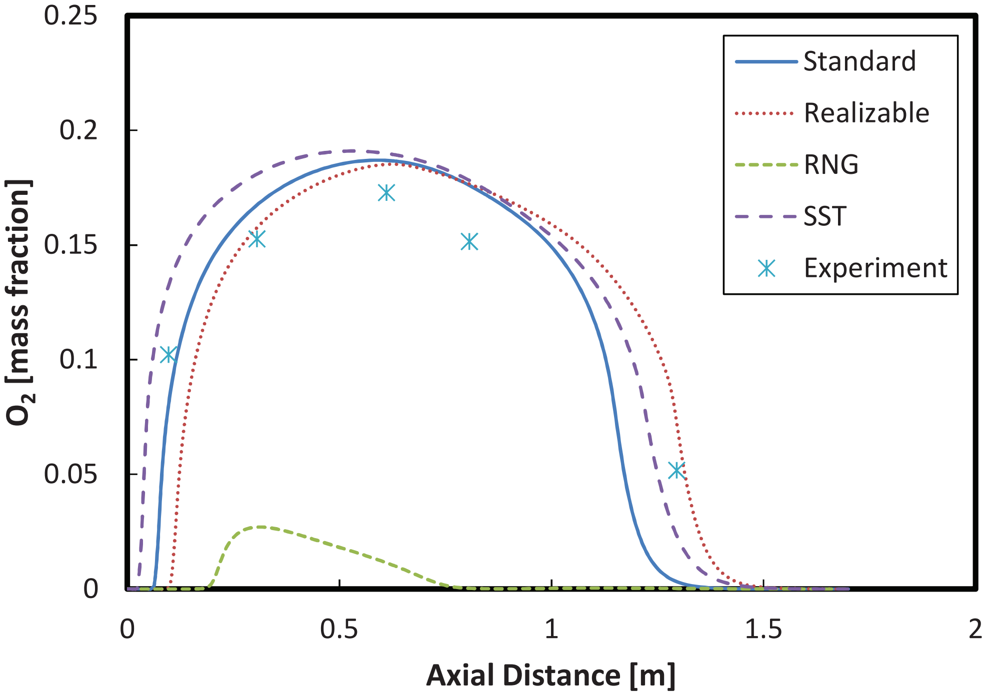

(a)

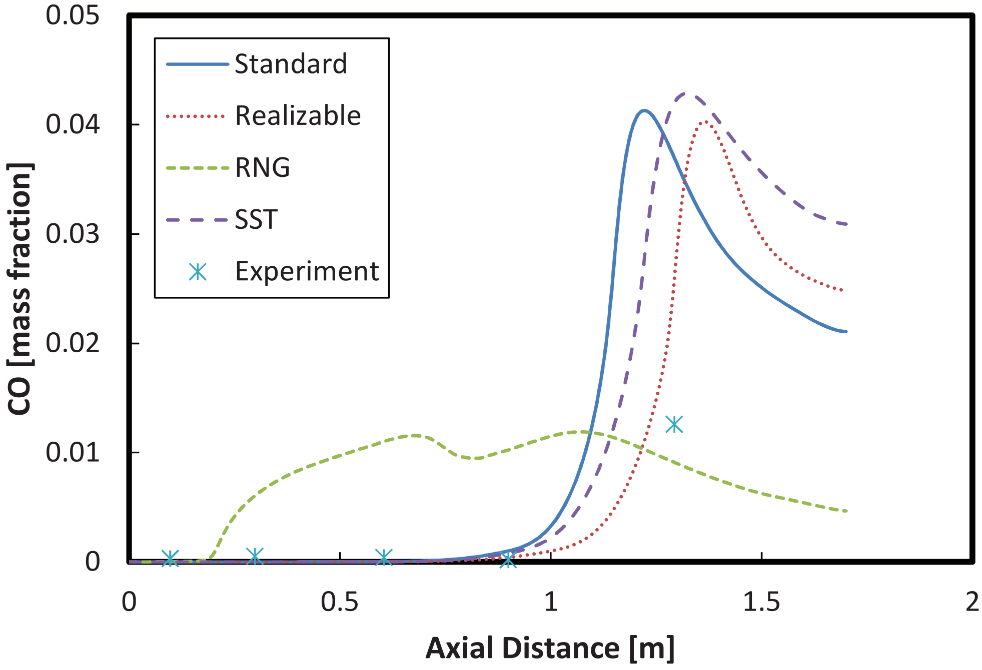

(b)

Figure 5.6: Axial distribution of species along the centerline of the combustor predicted by the four turbulence models. (a) Axial distribution of O_2. (b) Axial distribution of CO

5.4.2 Models Validation and Chemistry Model Selection

Louis et al. [81] conducted experimental and numerical investigations on the combustion of turbulent non-premixed syngas flame in a cooled cylindrical combustion chamber. The experimental data in their work consisted of species mole fractions measurements. These data were used to validate the different models of turbulence (Realizable $k - \epsilon$), radiation (DO), and combustion (EDC). In addition, since the chemistry model is a key element for accurate predictions of the different flame properties, such as flame temperature, species concentrations, etc, Boivin mechanism [19], Davis mechanism [9], Louis mechanism [81] and WO global mechanism [22] have been compared against the experimental and numerical data for the purpose of selecting the most suitable one for use in the simulation of LPM syngas combustion in the swirl-stabilized combustor. It is worth mentioning that the purpose of the numerical work conducted by Louis et al. [81] was to validate a combustion model developed by the authors. This model predicted the mixing, combustion, and heat loss using four independent scalar variables, namely mixture fraction, an enthalpy variable, and two reaction progress variables for hydrogen and carbon monoxide combustion. The turbulence-chemistry interactions were modeled using an assumed probability density function (PDF). Therefore, this validation work provided a comparison between the two combustion models as well.

The geometry of the combustion chamber along with the boundary conditions are shown in Figure 5.7. Syngas fuel, composed of 40% H_2, 40% CO, and 20%

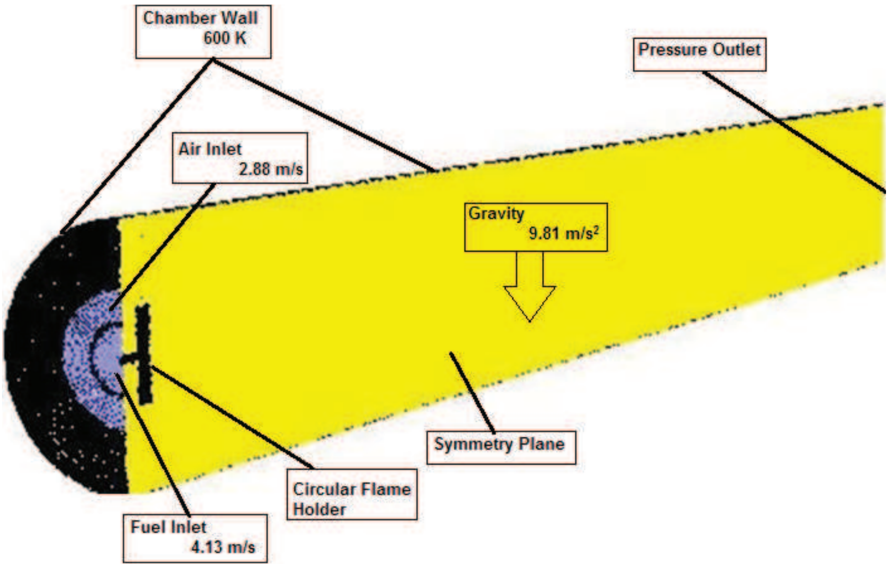

Figure 5.7: Geometry and boundary conditions used for the validation of the different models of turbulence, radiation, combustion, and chemistry

N_2 by volume enters the combustion chamber through a 24 mm diameter pipe, while the air enters through an external annular pipe with outer diameter of 50 mm. The chamber, which is 100 mm in diameter and 1 m long, includes a circular flame holder 36 mm in diameter and 10 mm thick, positioned 10 mm downstream the burner. The fuel and air were supplied at velocities of 4.13 m/s and 2.88 m/s, respectively, resulting in an HHV of 16 kW. To validate the geometry, a mesh independence test was performed on six different mesh sizes, namely 0.24 million cells, 0.31 million cells, 0.42 million cells, 0.57 million cells, 0.77 million cells, and 1.11 million cells. The difference in the species mole fractions between the last two grids was negligible, hence the 0.77 million cells grid was selected to perform the models validation investigation.

Figure 5.8 shows the radial distribution of CO concentration along two different cross sections in the combustion chamber. At $x = 0.065$ m (Figure 5.8a), all kinetic models, except WO, predicted the experimental data fairly well. It can also be seen that Boivin mechanism had the best prediction of experimental data around the centerline among the other mechanisms. On the other hand, WO mechanism had the worst prediction. It is also shown that the EDC model using Louis mechanism was better than the PDF based model (Louis_Num plot represents numerical results by Louis et al. [81]) in predicting the data. At $x = 0.300$ m (Figure 5.8b), the Boivin mechanism was closest in predicting the experimental data among all other kinetic models. As for the combustion models comparison, model by Louis et al. over-predicted the data in the lower part of the combustion chamber, while matching the data very well in the upper part. As for the EDC model, it well predicted the data in the lower part of the chamber, while under-predicting the data in the upper part.

Figure 5.9 presents the radial distribution of O_2 concentration along separate cross sections in the chamber. It was noticed that at $x = 0.065$ m (Figure 5.9a) Louis, Boivin, and Davis mechanisms had similar predictions, which were very well in the lower part of the chamber but with under-prediction in the upper part. WO under-predicted the data in both parts of the chamber. It can also be seen that the PDF based combustion model over-predicts the data in the lower part but with better predictions in the upper part, at least not close to the wall where under-predictions of the data were noticed. At $x = 0.300$ m (Figure 5.8b), the combustion model by Louis et al. had closer predictions of the experimental data, with some degree of under-prediction in the lower part and over-prediction in the upper part of the chamber. The EDC model had higher level of under-prediction in both part of the combustion chamber except for a small region in the upper part where all kinetic models had very good predictions of the experimental data.

The radial distribution of NO concentration along two different cross sections inside the combustion chamber is shown in Figure 5.10 for the different kinetic and combustion models. At $x = 0.065\ m$ (Figure 5.10a), significant under-prediction by all models understudy is noticed, except for the WO mechanism where it significantly over-predicted the data around the two peaks in the lower and upper parts of the chamber, while it under-predicted the data around the centerline. In addition, the PDF based model was better than the EDC in being closer the experimental data. Boivin mechanism predictions were higher than those of the other kinetic models. In a downstream section ($x = 0.150\ m$, Figure 5.10b), Boivin mechanism had the best prediction among all other chemical mechanisms, while WO had the worst prediction. As for the two combustion models, PDF based model had a better matching of the experimental data than the EDC model using Louis mechanism.

Based on the foregoing comparison, Boivin et al. mechanism [19] was considered to be the most suitable kinetic model to be used in LPM syngas combustion in the swirl-stabilized combustor.

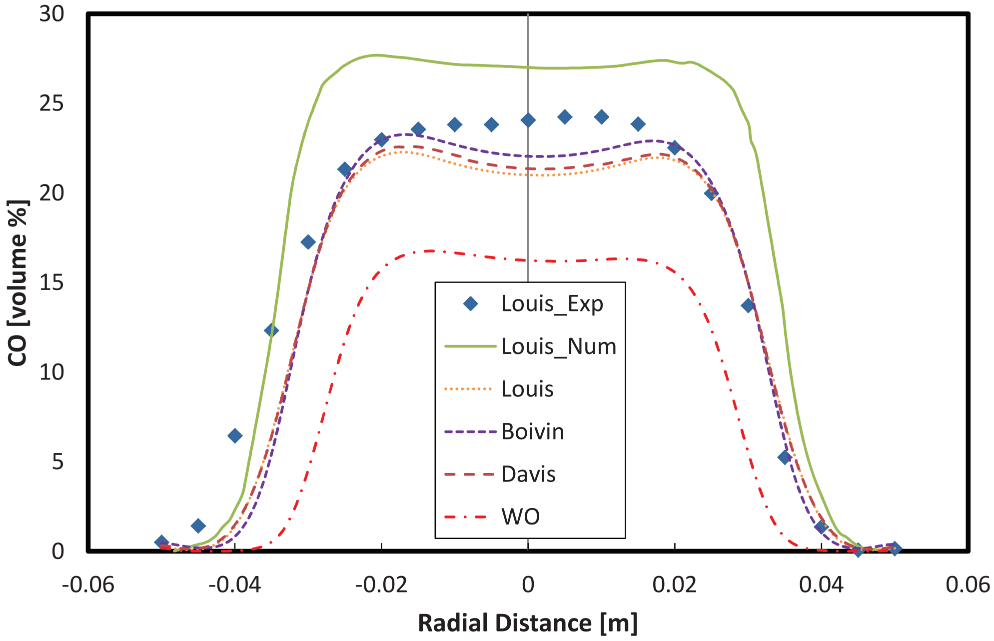

(a)

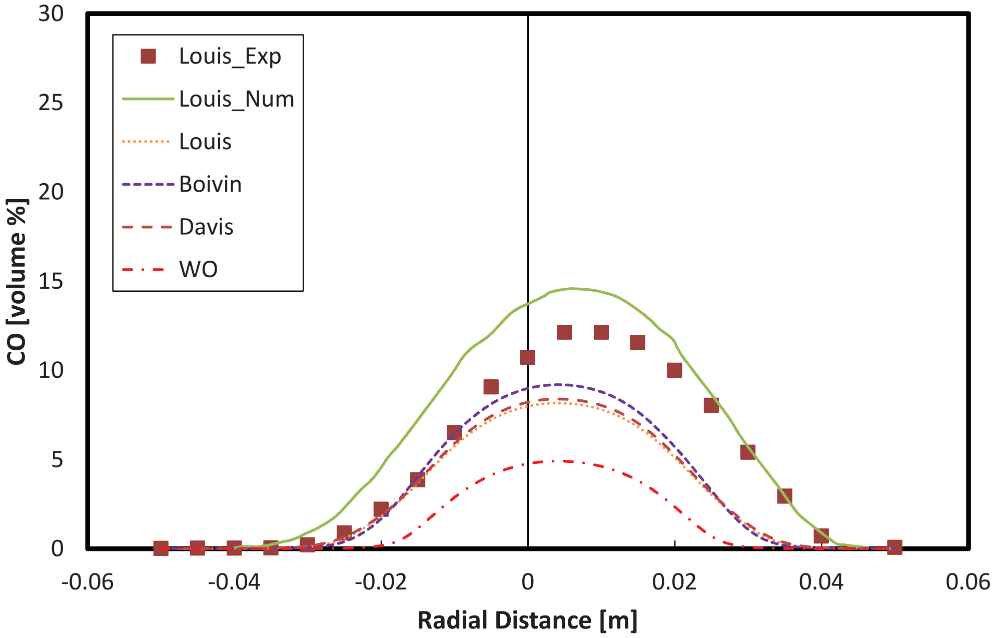

(b)

Figure 5.8: Radial distribution of CO concentration predicted by the Realizable $k-\epsilon$ model, DO model, EDC model and a number of kinetic models at (a) $x = 0.065m$ and (b) $x = 0.300m$

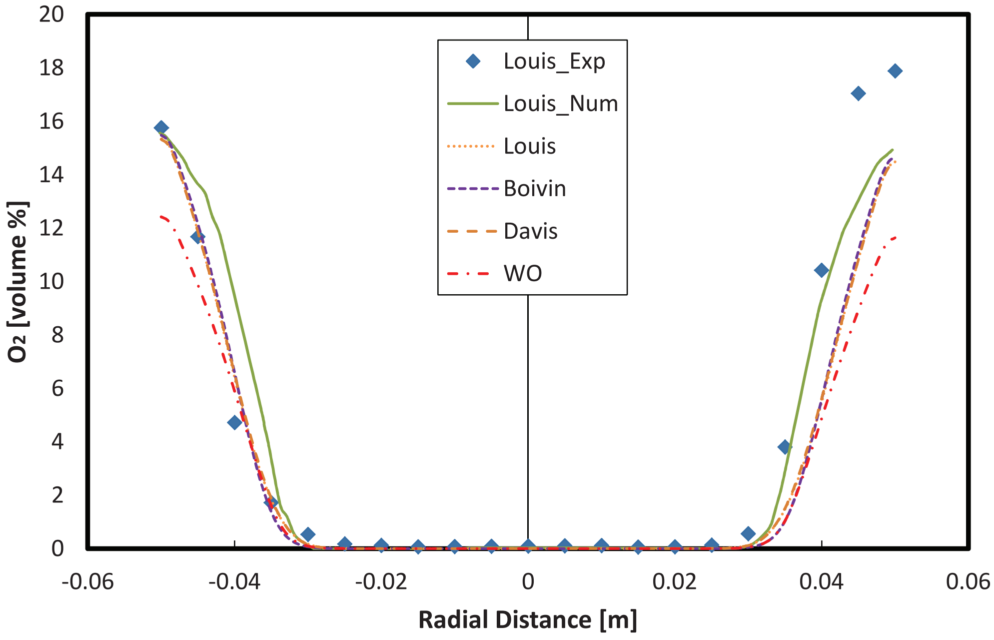

(a)

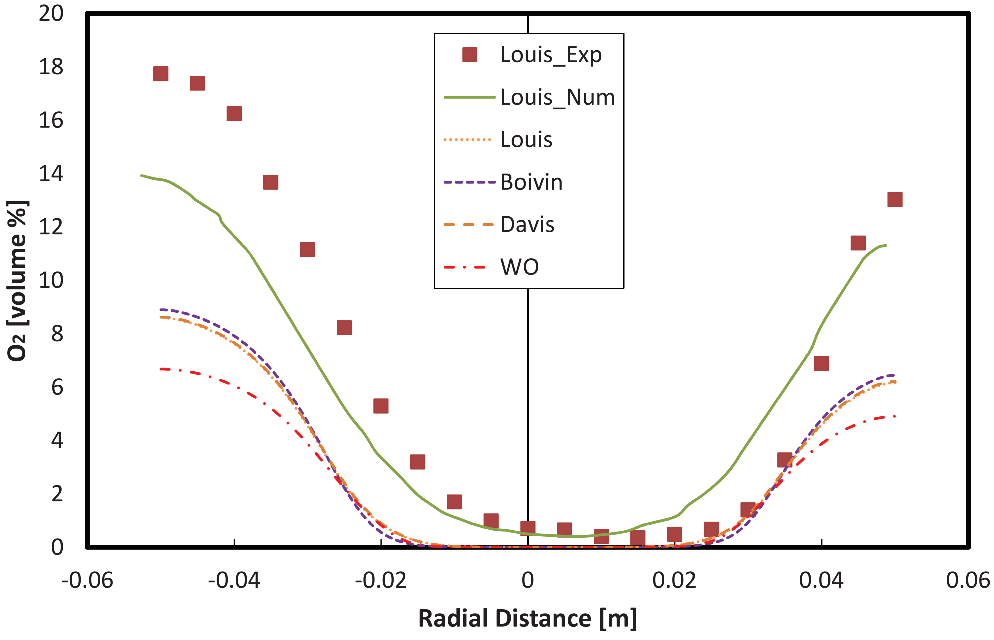

(b)

Figure 5.9: Radial distribution of O_2 concentration predicted by the Realizable $k - \epsilon$ model, DO model, EDC model and a number of kinetic models at (a) $x = 0.065m$ and (b) $x = 0.300m$

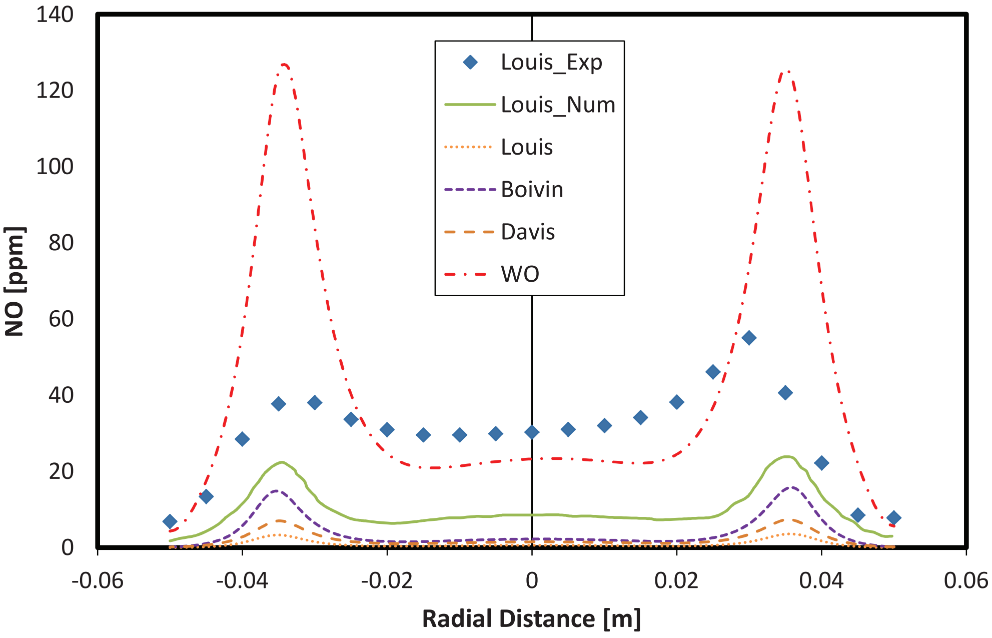

(a)

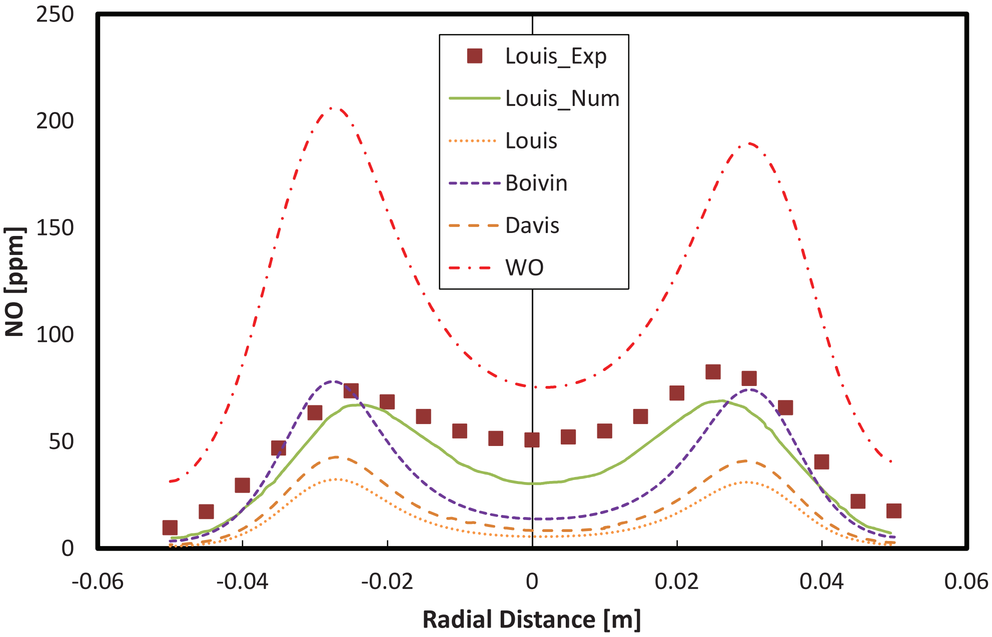

(b)

Figure 5.10: Radial distribution of NO concentration predicted by the Realizable $k-\epsilon$ model, DO model, EDC model and a number of kinetic models at (a) $x = 0.065m$ and (b) $x = 0.150m$. NO calculations were performed in the post-processing stage

5.5 Results and Discussion

5.5.1 Influence of Swirl Number

In this section, the effect of the swirl number on the flow field, flame structure, temperature field, fuel consumption, and emissions is discussed.

Effect of Swirl Number on Velocity Field

Contours of the axial velocity component are shown in Figure 5.11 for different swirl numbers. For the case of zero swirl number ($S = 0$), the axial velocity contour shows that there is a reverse flow upstream close to the wall, known as outer recirculation zone (ORZ), due to the sudden expansion. The size of this ORZ is observed to decrease with swirl number. This observation is consistent with the work of Huang et al. [82] that presented a similar study on the combustion dynamics in a swirl-stabilized combustor. Under low swirl condition ($S = 0.3$), there is a development of a low velocity region downstream the expansion plane in the center of the combustor. This low velocity region increases with the increase in the swilr number. However, for the case of $S = 0.5$, 0.7, and 1.0, there is a further development of an inner recirculation zone in the wake of the swirler (IRZ-W). The strength of the IRZ-W is observed to increase with increasing swirl number.

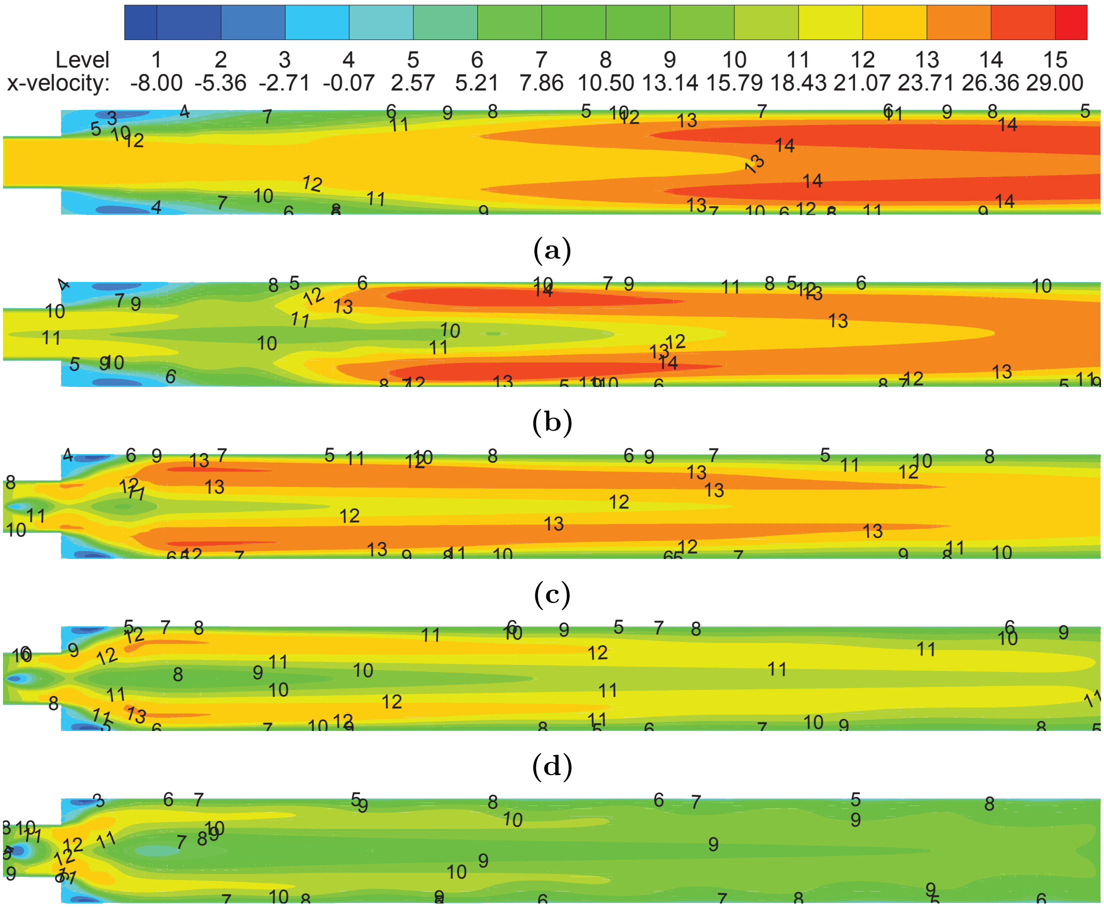

(a)

(b)

(c)

(d)

(e)

Figure 5.11: Axial velocity contours across a vertical-symmetrical plane for different swirl numbers. (a) $S = 0.0$, (b) $S = 0.3$, (c) $S = 0.5$, (d) $S = 0.7$, and (e) $S = 1.0$. $\phi = 0.6$ and $H_2/CO = 50/50$

The axial velocity profiles across the centerline of the combustion chamber are shown in Figure 5.12. In general, lower axial velocity is noticed for higher swirl numbers. This is attributed to the fact that incorporating a swirler creates a tangential component of the inlet jet velocity, and thus reducing the axial velocity component. On the other hand, for the swirl number cases, regions of low axial velocity can be observed after the sudden expansion. This is explained by the basic law of continuity where the velocity decreases with increase in the cross-sectional

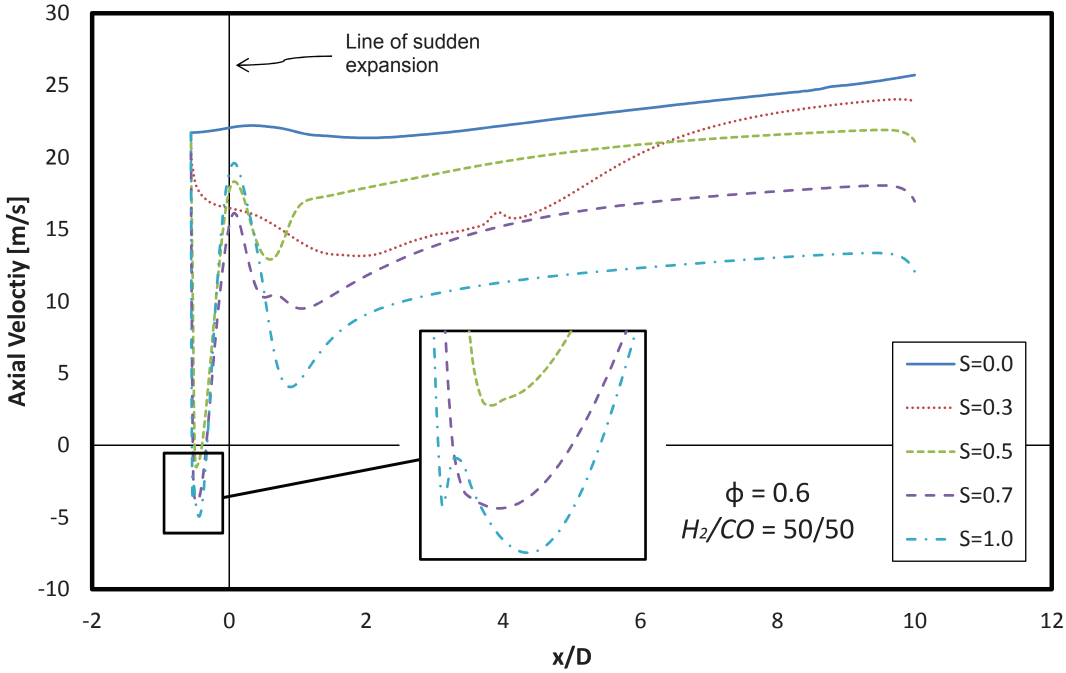

Figure 5.12: Axial velocity profiles across the centerline of combustion chamber for different swirl numbers. $\phi = 0.6$ and $H_2/CO = 50/50$

area. Beyond this region, the velocity starts increasing which is attributed to the expansion of the gases that resulted from the combustion process. The expansion of the gases increases the volume flow rate in the combustor which consequently increases the flow velocity. The negative velocity regions (IRZ-W) are observed for the case of $S = 0.5$, 0.7, and 1.0, as explained above.

The radial profiles of axial velocity at different cross-sections are shown in Figure 5.13 for different swirl numbers. Downstream the inlet section (Figure 5.13a), a uniform velocity is observed for the zero swirl number, while under swirl conditions, the IRZ-W is observed. The size of the IRZ-W decreases with increasing swirl number. The strength, however, increases with the swirl number. In a section after the sudden expansion (Figure 5.13b), the damping of the IRZ-W is observed with the development of an ORZ, which is larger in size for lower swirl numbers. Similarly, the strength of the ORZ increases with increasing swirl number. In a further downstream section (Figure 5.13c), no ORZ is observed. In addition, more uniform velocity is noticed for the case of no swirl ($S = 0$), while for the swirling flow cases, the peak of the axial velocity occurs further away from the centerline of the combustor.

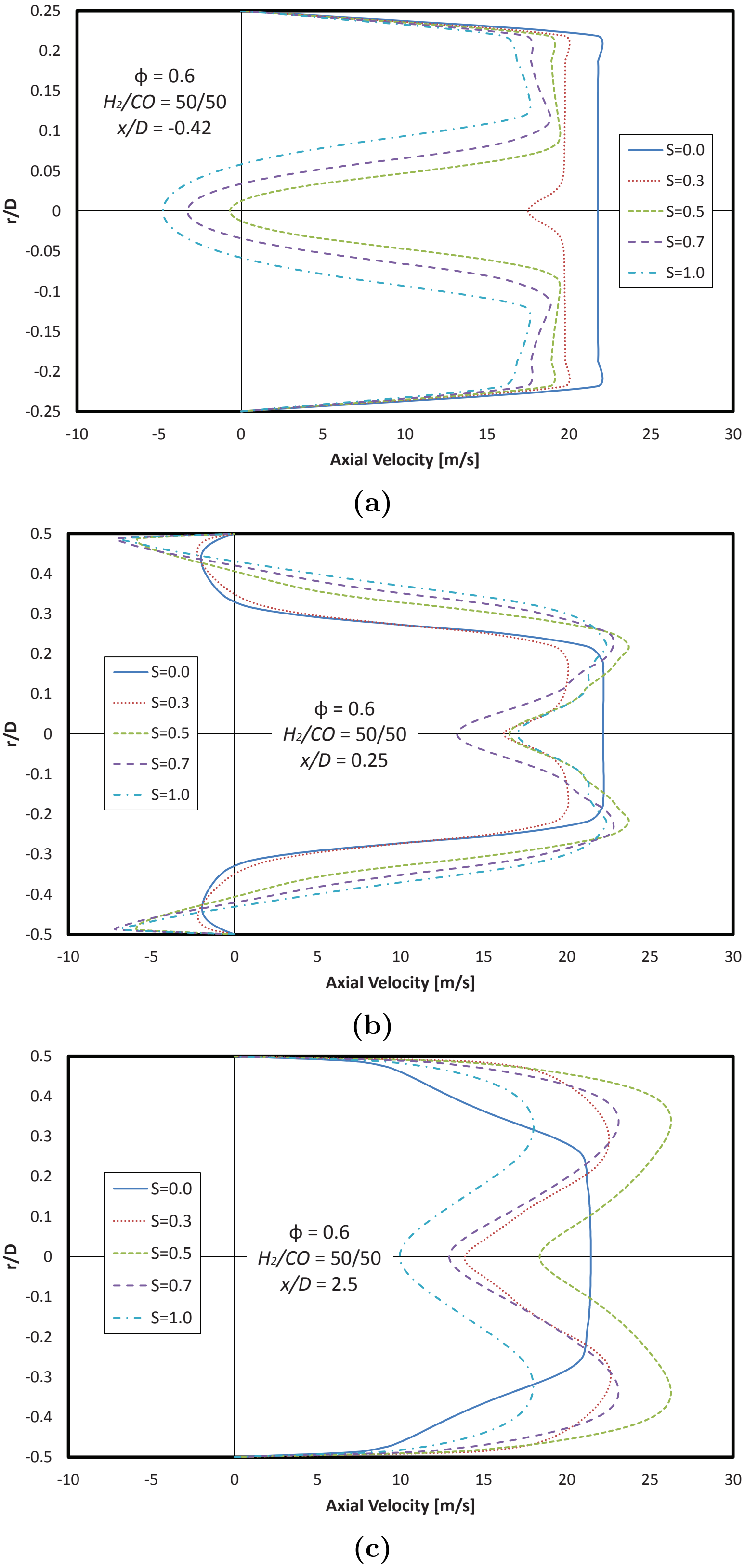

Figure 5.13: Radial profiles of axial velocity for different swirl numbers. (a) $x/D = -0.42$ (b) $x/D = 0.25$ and (c) $x/D = 2.5$. $x = 0$ is the line of sudden expansion. $\phi = 0.6$ and $H_2/CO = 50/50$

Effect of Swirl Number on Flame Structure and Temperature Field

Figure 5.14 presents contours of OH intermediate species, which is a marker for the flame, while Figure 5.15 presents temperature contours both shown at a symmetrical plane of the combustor for different swirl numbers. In the case of $S = 0$, the fuel-air mixture is ignited and sustained by the ORZ. The ensuing combustion in the ORZ gradually preheats the high velocity jet until the whole mixture is burned close to the exit of the combustor. Under low swirling flow ($S = 0.3$), a low velocity region is developed in the vicinity of the combustor centerline. This enhances the mixing between the combustion products and incoming reactants which facilitate earlier attainment of the ignition temperature. As the swirl number is increased, the formation of the IRZ-W shifts the reaction zone even farther upstream of the combustor. It is generally observed that increasing the swirl number leads to a more compact combustion. Similar conclusions have been drawn from the work of Huang et al. [82] and Kim et al. [83].

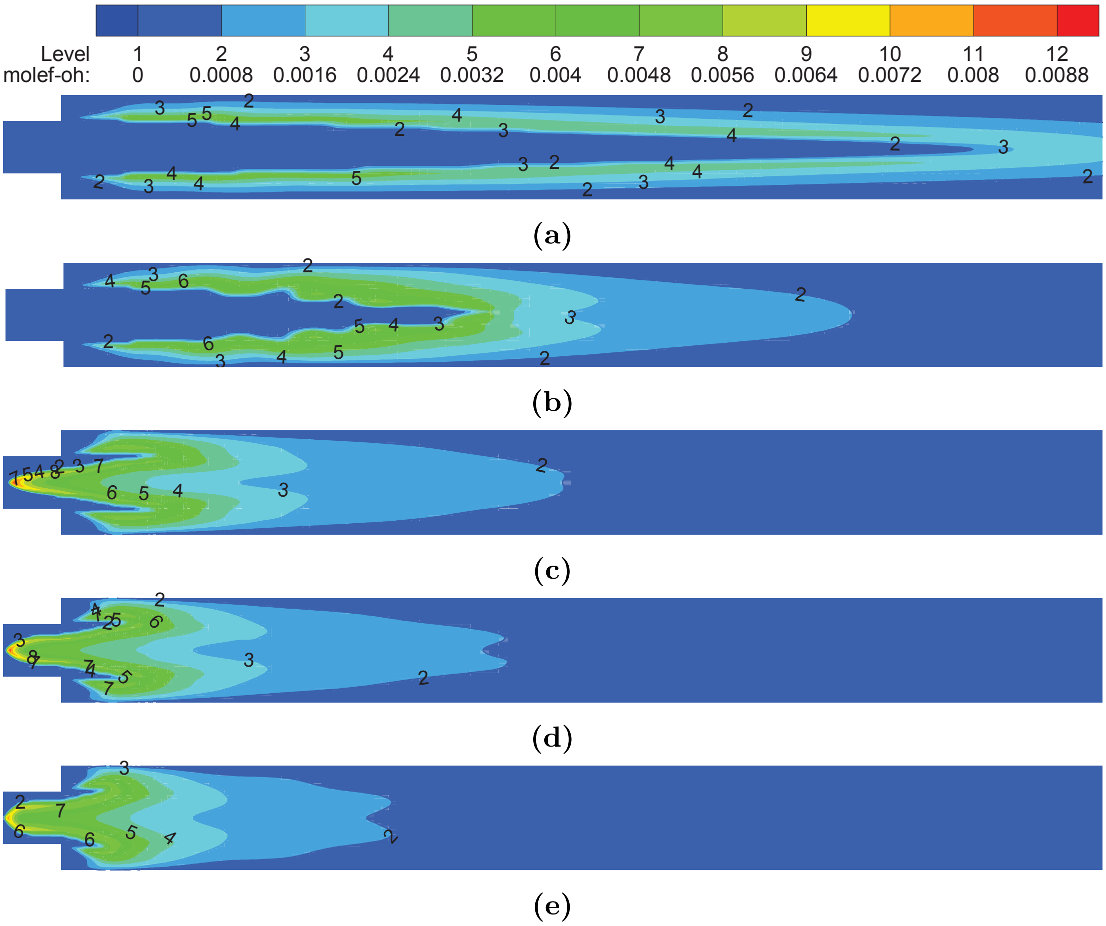

Figure 5.14: OH contours along a vertical-symmetrical plane across combustion chamber for different swirl numbers. (a) $S = 0.0$, (b) $S = 0.3$, (c) $S = 0.5$, (d) $S = 0.7$, and (e) $S = 1.0$. $\phi = 0.6$ and $H_2/CO = 50/50$

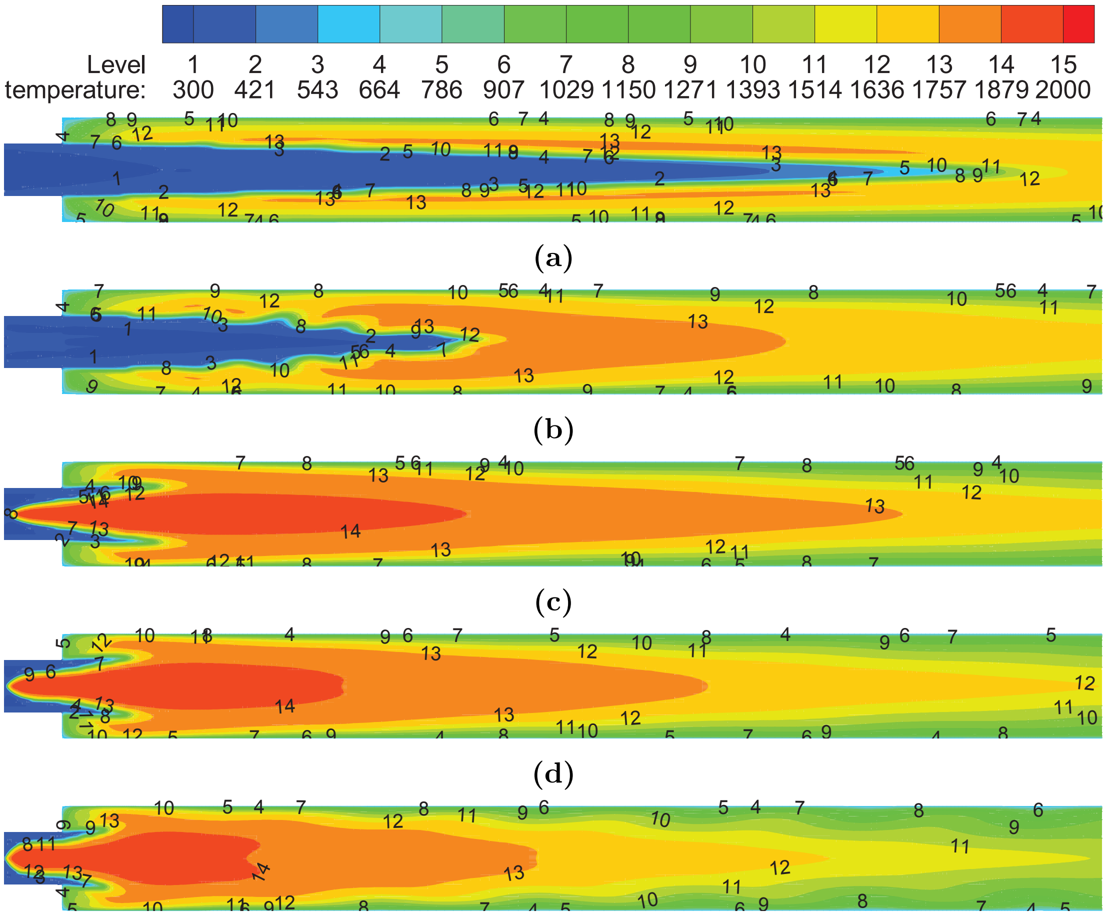

(a)

(b)

(c)

(d)

(e)

Figure 5.15: Temperature contours along a vertical-symmetrical plane across combustion chamber for different swirl numbers. (a) $S = 0.0$, (b) $S = 0.3$, (c) $S = 0.5$, (d) $S = 0.7$, and (e) $S = 1.0$. $\phi = 0.6$ and $H_2/CO = 50/50$

Axial profiles of temperature across the centerline of the combustor are given in Figure 5.16. It is clearly shown that the maximum temperature location is shifted upstream as the swirl number is increased. This is inline with what was earlier observed by the shifting of the reaction zone upstream of the combustor as the swirl number is increased. Beyond the maximum temperature location, the centerline temperature for swirling flows is observed to decrease as the length of the combustor increases. This is can be ascribed to the continuous heat exchange

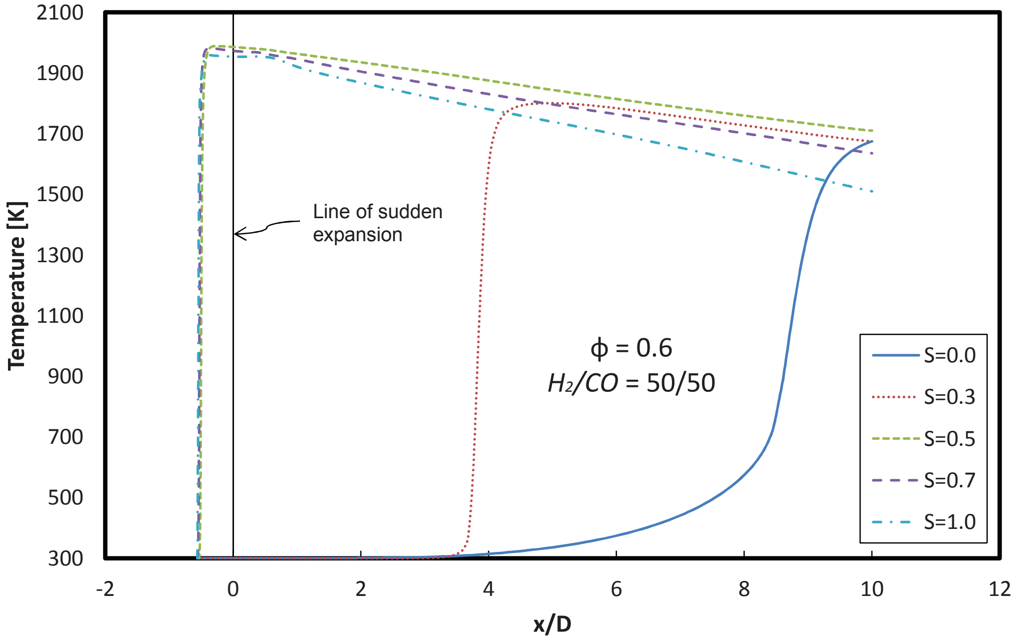

Figure 5.16: Axial profiles of temperature across combustor centerline for different swirl numbers. $\phi = 0.6$ and $H_2/CO = 50/50$

between the combustion products and the combustor wall, which is higher for higher swirl numbers.

A comparison between maximum, average, and exit temperatures is shown in Figure 5.17 for different swirl numbers. It is observed that the maximum temperature and the average temperature increase with increasing swirl number up to $S = 0.5$ and decreases thereafter. This is attributed to the fact that at no swirl, the combustion occurs in the vicinity of the wall. This leads to a higher heat loss to the combustor wall. As the swirl number increases ($S = 0.3$), the combustion zone shifts towards the vicinity of the centerline, thus reducing the heat transfer to the wall. At higher swirl number ($S = 0.5$), the development of the IRZ-W stabilizes the flame across the centerline of the combustor, and further reduces the heat transfer to the combustor wall. Further increase in the

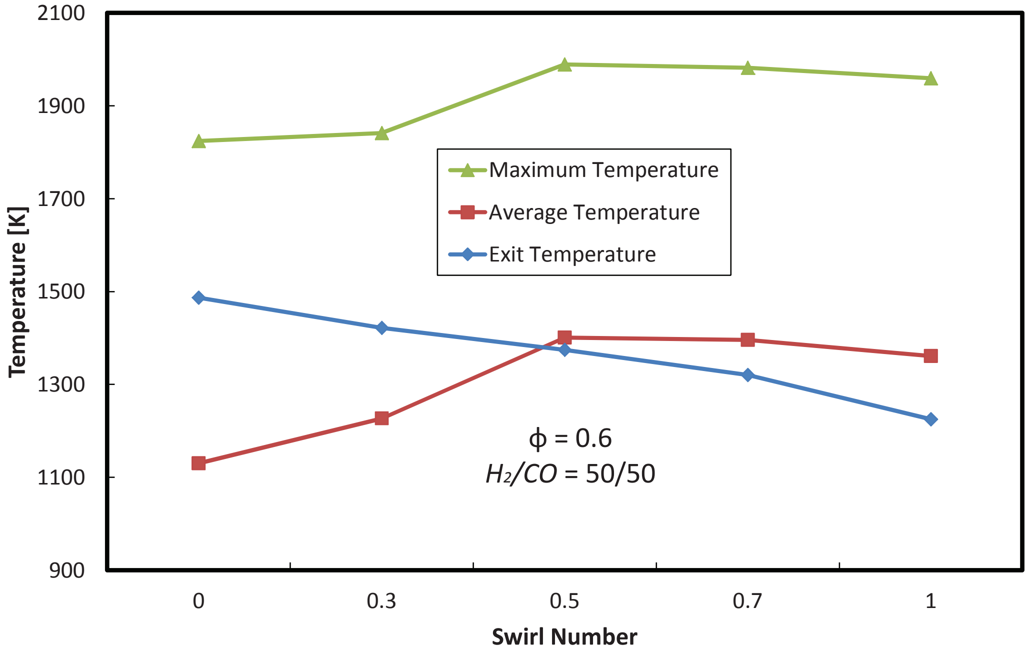

Figure 5.17: Comparison between maximum, average and exit temperatures for different swirl numbers. $\phi = 0.6$ and $H_2/CO = 50/50$

swirl number, however, decreases the maximum and average temperatures due to increased cold reactants recirculation. The exit temperature, on the other hand, is observed to decrease with increasing swirl number. This is attributed to the increased compactness of combustion zone, resulting in an increase in the residence time of the combustion products. The higher residence time leads to a more heat exchange between the combustion products and the wall of the combustor, thus reducing the products temperature.

Effect of Swirl Number on Fuel Consumption

Figure 5.18 shows the axial distribution of H_2 and CO concentrations in mole fraction along the centerline of the combustor for different swirl numbers. It is generally observed that the rate of burning of H_2 is higher than that of CO.

This is attributed to the higher diffusivity and lower ignition temperature of H_2 gas as compared to CO. For the cases of high swirl numbers, H_2 is depleted around the expansion plane ($x/D = 0$), while CO is depleted at a further location downstream of the expansion plane ($x/D \approx 2$). Similarly, for low swirl number cases, H_2 is depleted faster than CO.

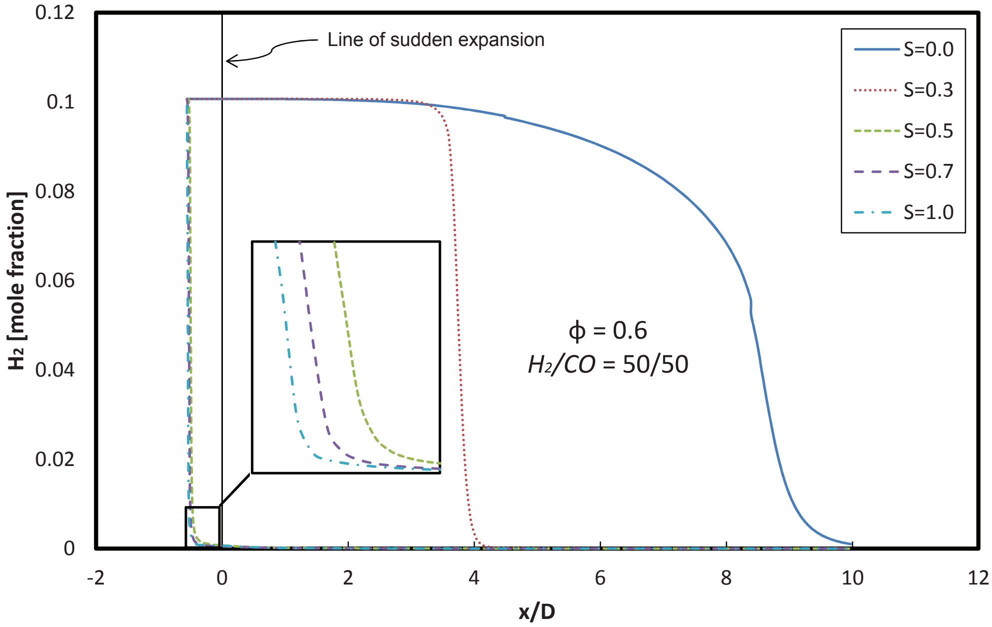

(a)

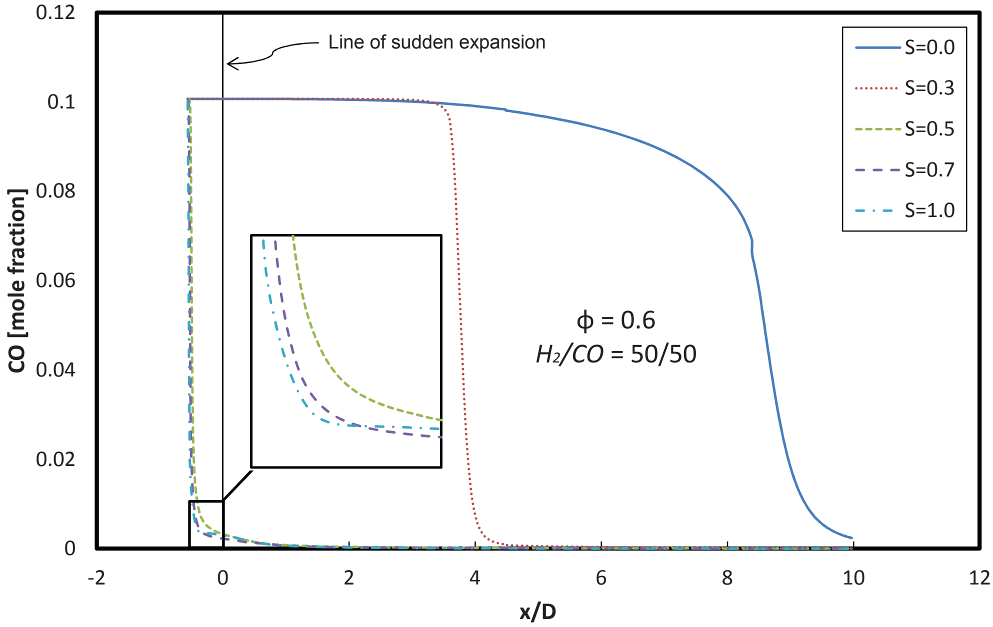

(b)

Figure 5.18: Axial profiles of (a) H_2 and (b) CO concentrations in the $H_2/CO/air$ mixture across combustor centerline for different swirl numbers. $\phi = 0.6$ and $H_2/CO = 50/50$

Effect of Swirl Number on Emissions

Figure 5.19 shows pollutant emissions at the exit of the combustor of NO and CO, while Figure 5.20 shows CO_2 emission at the exit of the combustor as well. For all cases, NO emission is observed to follow the trend of the maximum temperature. It can generally be observed that NO levels are ultra-low (less than 2 ppm). This is due to the fact that the excess air present in the LPM combustion of syngas act as heat sink, therefore limiting the formation of hot spots that are important for NO_X formation. CO emission, on the other hand, is observed to decrease with the increase in the swirl number. This is attributed to the improved mixing between the reactants and combustion products as the swirl number increases. The ensuing effect is a more compact combustion that enhances the residence time for CO burnout. Looking at CO_2 emission, which is the main cause for global warming, it is generally observed that increasing the swirl number results in increasing CO_2 emission as a result of the more efficient mixing that favors the complete combustion of CO to CO_2. However, this increase is gradual with a maximum increase of about 0.3% from $S = 0$ to $S = 0.3$.

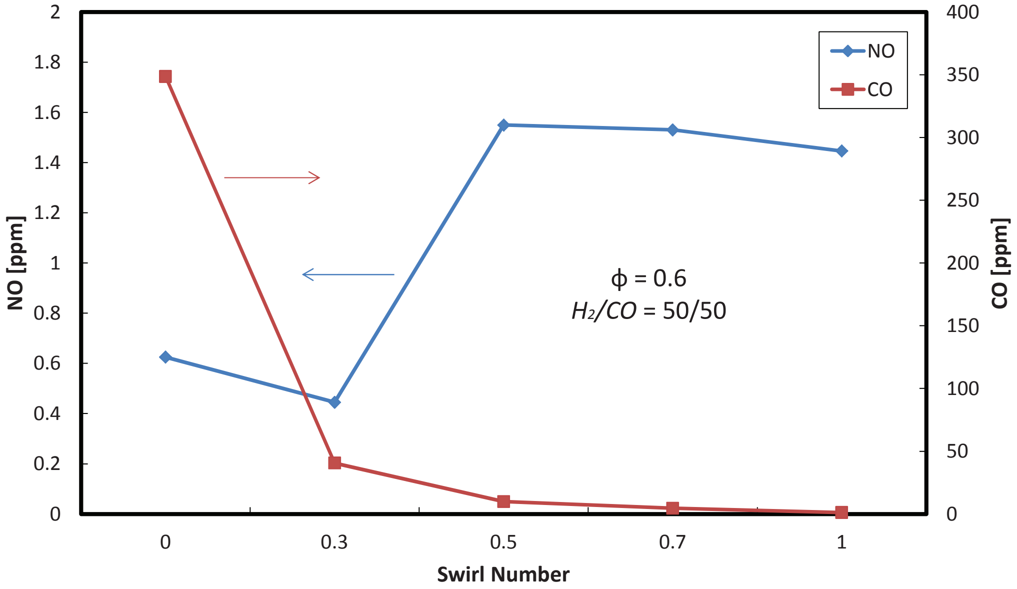

Figure 5.19: NO and CO emissions at the exit of the combustor for different swirl numbers. $\phi = 0.6$ and $H_2/CO = 50/50$

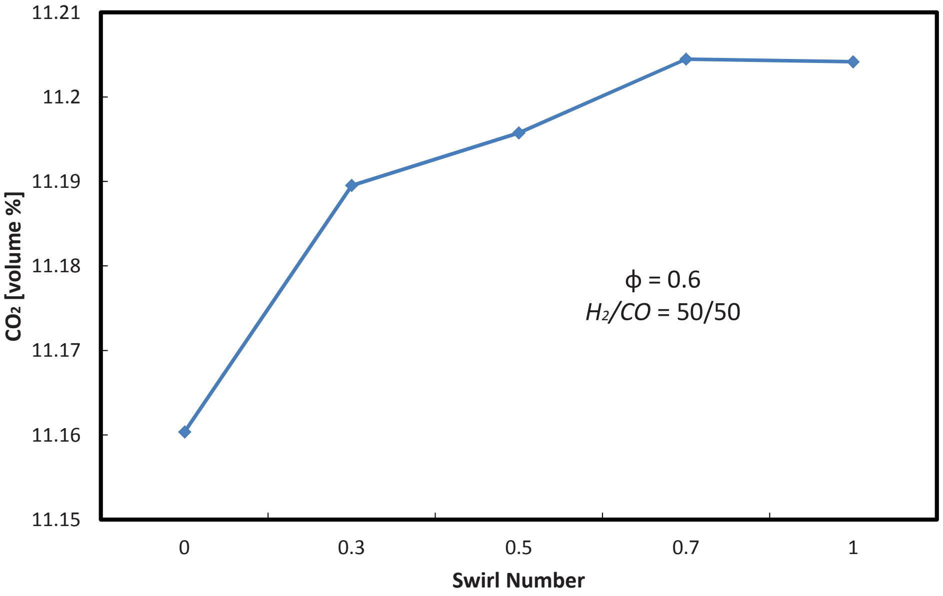

Figure 5.20: CO_2 emissions at the exit of the combustor for different swirl numbers. $\phi = 0.6$ and $H_2/CO = 50/50$

5.5.2 Influence of H_2/CO Ratio

Syngas composition can affect the combustion characteristics and emissions significantly. This section describes these effects on flow field, flame structure, temperature field, fuel consumption, and emissions.

Effect of H_2/CO Ratio on Velocity Field

Figure 5.21 shows contours of axial velocity for the different levels of hydrogen in syngas. For the low hydrogen content case ($H_2 = 5\%$), there exists three regions of reverse flow; an inner recirculation zone in the wake downstream of the swirler (IRZ-W), an inner recirculation zone after the sudden expansion in the vicinity of the centerline (IRZ-C), and an outer recirculation zone after the sudden expansion in the vicinity of the wall (ORZ). The figure shows that the size and strength of the IRZ-C reduce as the level of hydrogen in the fuel increases. The higher diffusivity and reactivity of hydrogen increase the amount of combustible gases. This reduces further the density of the hot gases, resulting in higher volume flow rates and and flow velocities. These conclusions agree well with the works in the literature by Kim et al. [60] and De et al. [68].

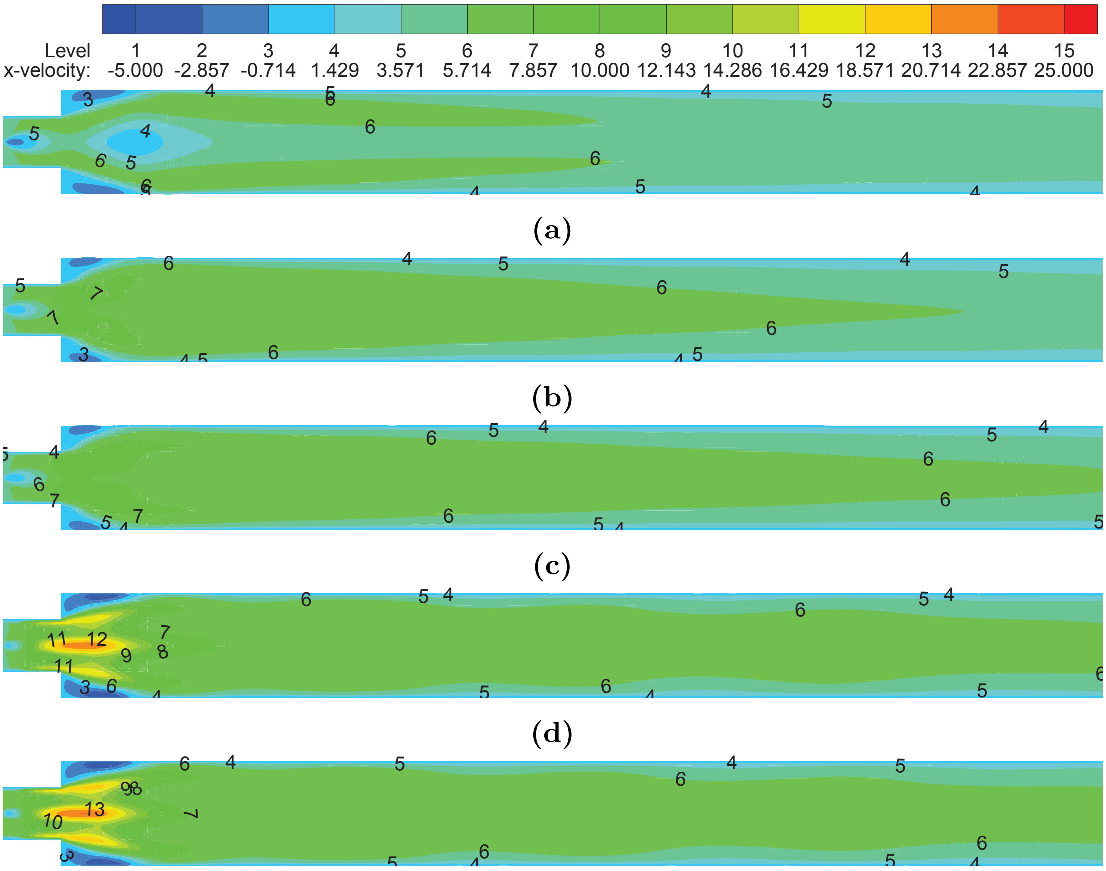

(a)

(b)

(c)

(d)

(e)

Figure 5.21: Axial velocity contours across a vertical-symmetrical plane for different hydrogen content. (a) $H_2 = 5\%$, (b) $H_2 = 25\%$, (c) $H_2 = 50\%$, (d) $H_2 = 75\%$, and (e) $H_2 = 95\%$. $\phi = 0.6$ and $S = 0.7$

Figure 5.22 shows the axial velocity profiles along the centerline of the combustion chamber for different volume percent of hydrogen in syngas. It is generally observed that the axial velocity increases and the IRZ-W is reduced in strength as the hydrogen content increases. This is due to the higher volume flow rates associated with higher expansion of the hot gasses as a result of the presence of more reactive hydrogen content.

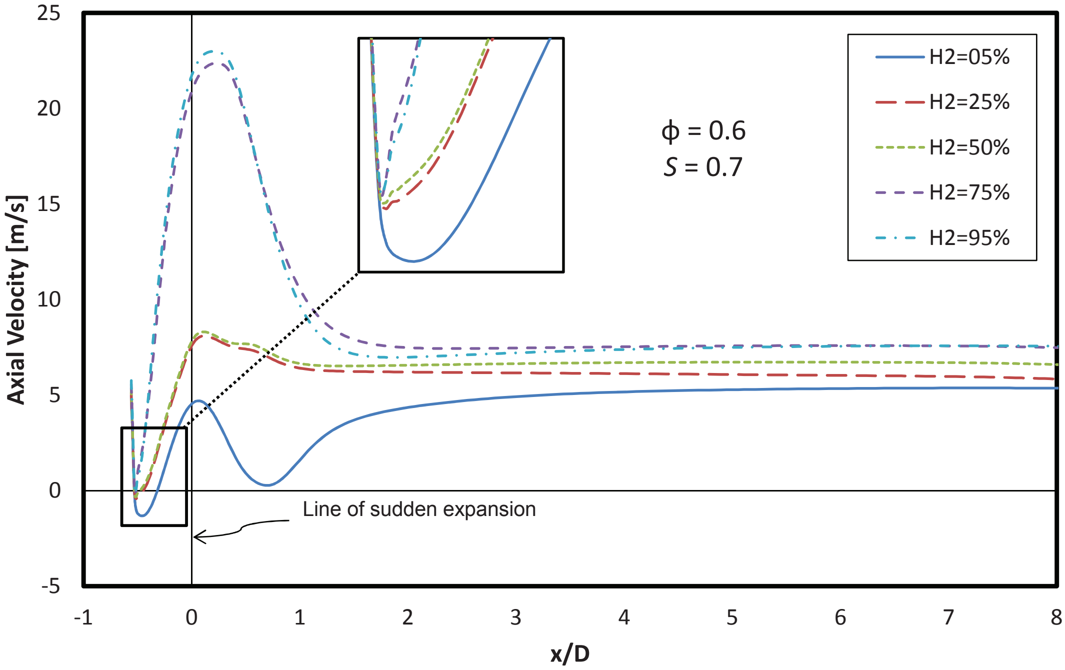

Figure 5.22: Axial velocity profiles along the centerline of the combustor for different hydrogen content in syngas. $\phi = 0.6$ and $S = 0.7$

Figure 5.23 shows the radial profiles of axial velocity at different cross-sections. In general, it is observed that the axial velocity increases with increasing hydrogen content in the fuel. At a section downstream of the swirler, it is indicated that the strength of the IRZ-W reduces as the level of hydrogen content in syngas increases. At a section downstream of the expansion plane, it can also be inferred that the strength of the ORZ increases with increasing hydrogen level. At a further downstream section, the ORZ is damped with the peak axial velocity shifted to the vicinity of the wall and a more uniform velocity profile for the higher hydrogen content cases ($H_2 = 75\%$ and $H_2 = 95\%$). It is generally observed that buoyancy effects on the flow field are negligible.

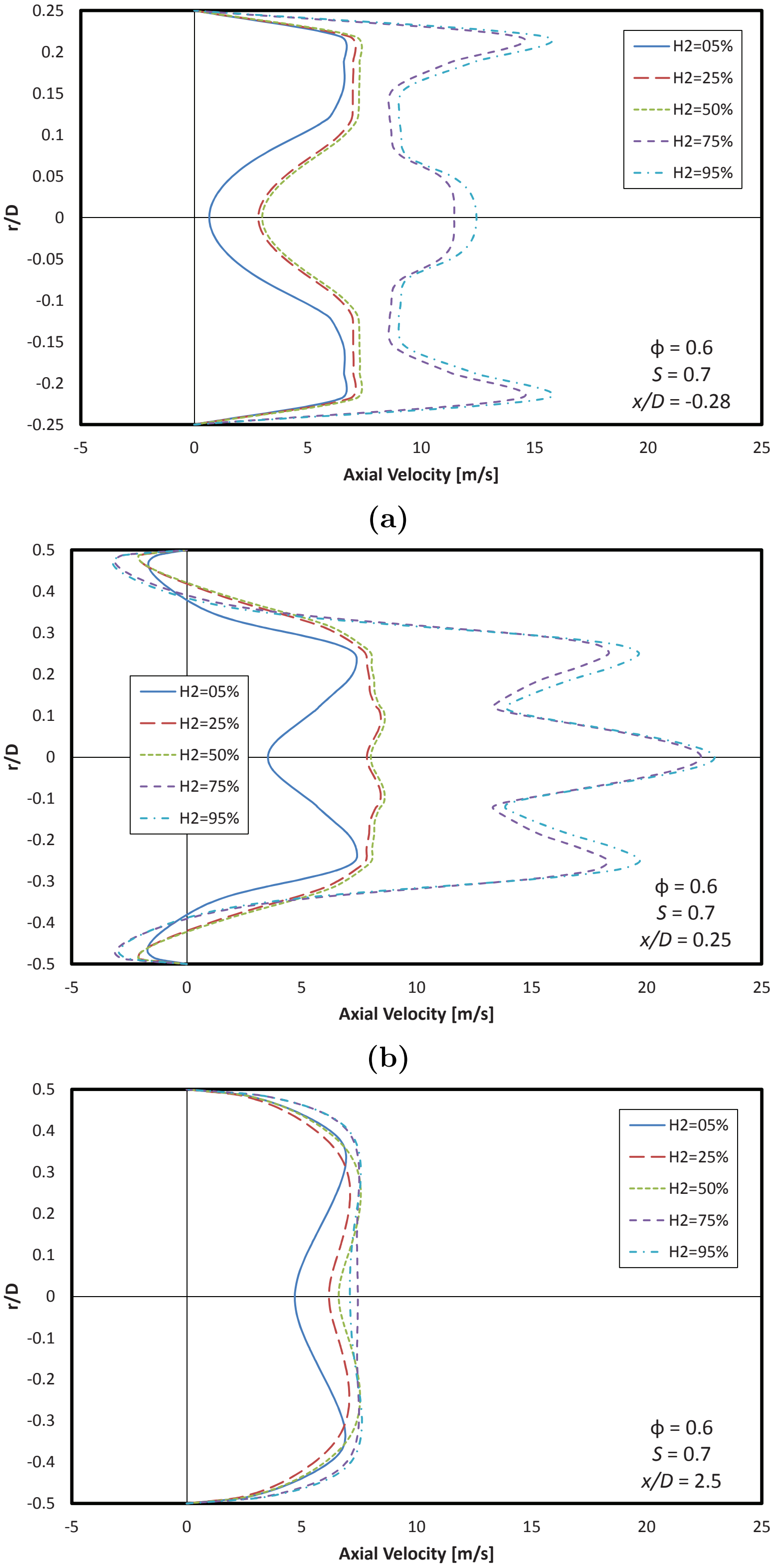

(a)

(b)

(c)

Figure 5.23: Radial profiles of axial velocity at different cross-sections for different hydrogen content in syngas. (a) $x/D = -0.42$ (b) $x/D = 0.25$ and (c) $x/D = 2.5$. $x = 0$ is the line of sudden expansion. $\phi = 0.6$ and $S = 0.7$

Effect of H_2/CO Ratio on Flame Structure and Temperature Field

Figure 5.24 and Figure 5.25 show OH and temperature contours, respectively, at a symmetrical plane of the combustor for different syngas compositions. In qualitative terms, higher temperatures and shorter flames are observed for higher hydrogen content in syngas. This is attributed to the higher reactivity and flame speeds of hydrogen. For the cases of $H_2 = 75\%$ and $H_2 = 95\%$, it is observed that there exists a sustained flame in the inlet pipe upstream of the expansion plane. This indicates a flashback behavior (a boundary layer type), which occurs when the higher flame speeds of hydrogen causes the flame to travel upstream of the combustor into its inlet sections. These conclusions are similar to the work of De et al. [68].

Quantitatively, the axial profiles of temperature across the centerline of the combustor are presented in Figure 5.26. It is generally observed that increasing the volume percent of hydrogen in syngas causes the centerline temperature to increase. This is attributed to the higher reactivity of hydrogen which enhances more heat release. For a given hydrogen content, however, the centerline temperature decreases along the length of the combustor due to the heat loss to the combustor's wall.

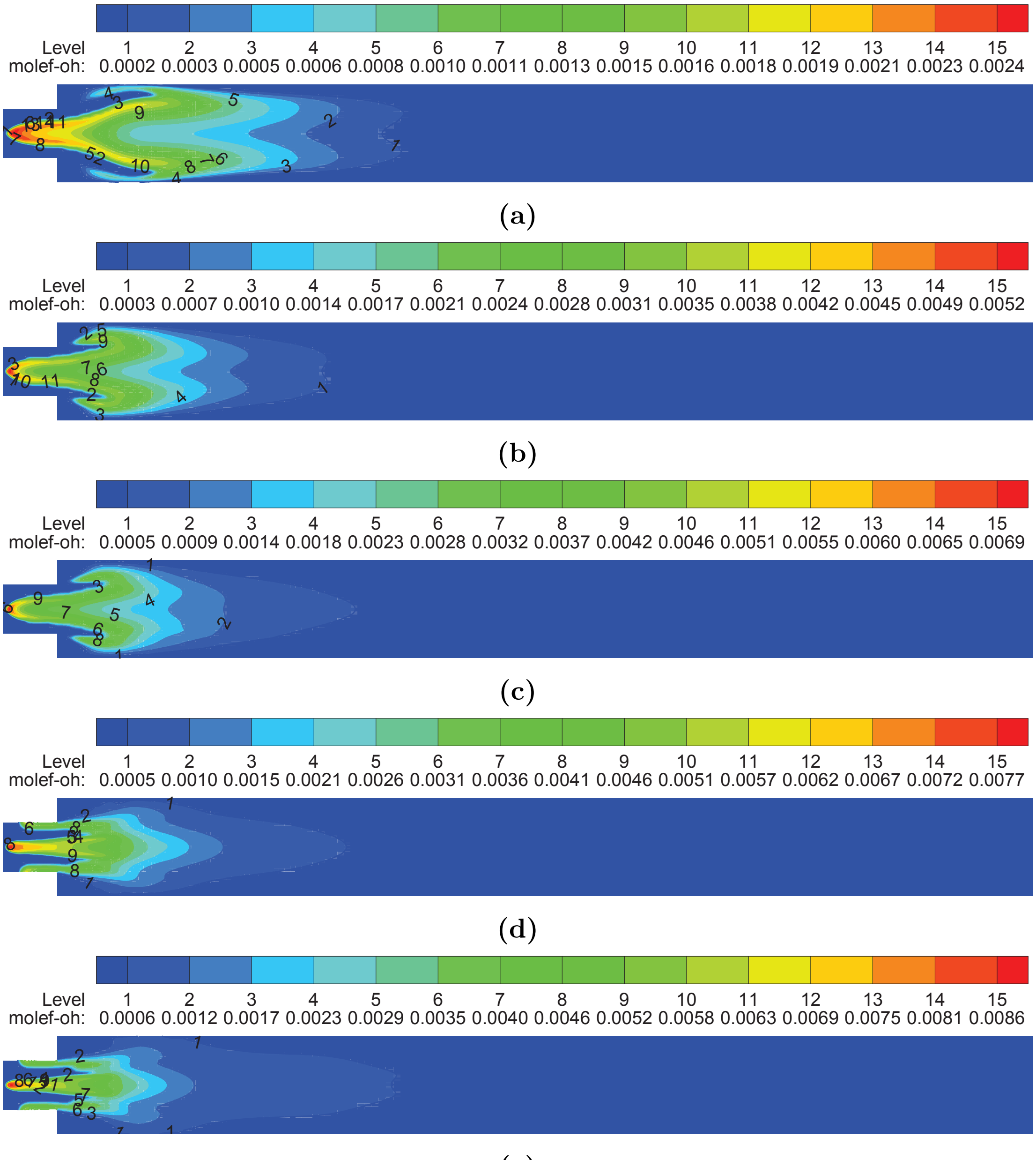

(a)

(b)

(c)

(d)

(e)

Figure 5.24: OH contours along a vertical-symmetrical plane across combustion chamber for different hydrogen content in syngas. (a) $H_2 = 5\%$, (b) $H_2 = 25\%$, (c) $H_2 = 50\%$, (d) $H_2 = 75\%$, and (e) $H_2 = 95\%$. $\phi = 0.6$ and $S = 0.7$

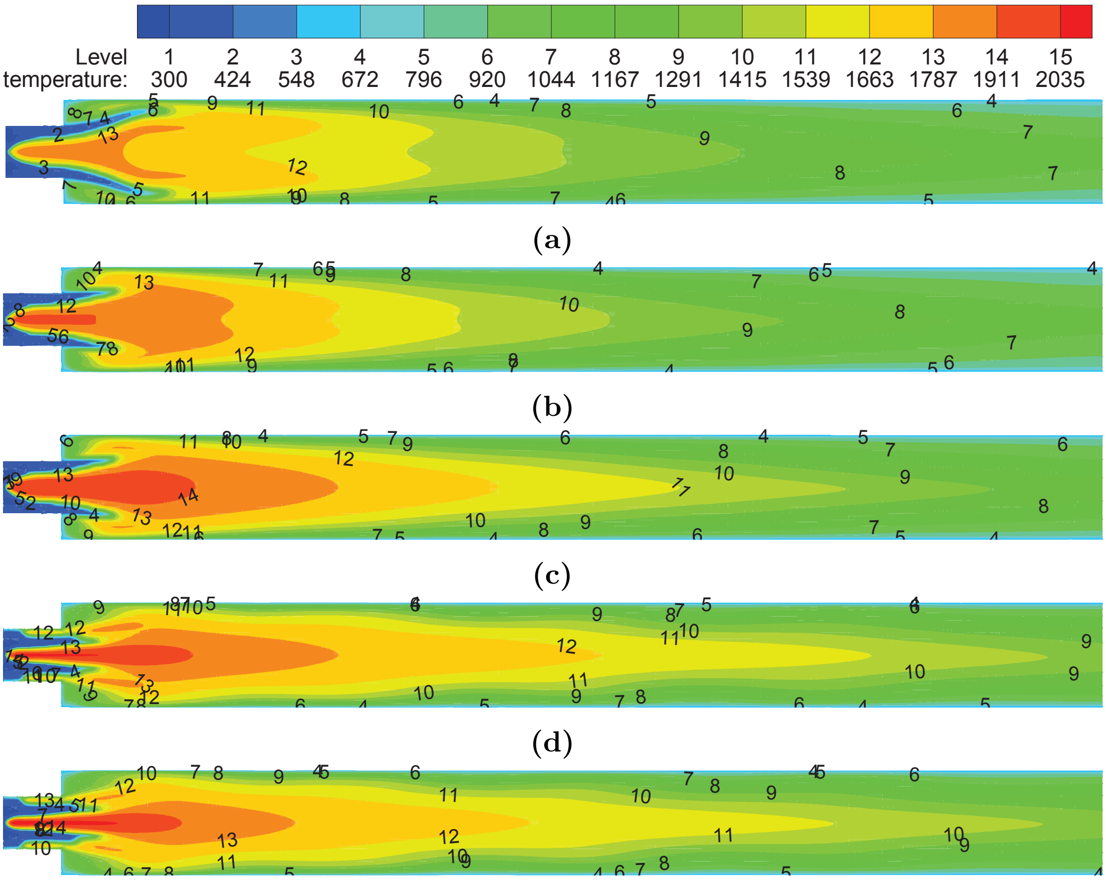

(a)

(b)

(c)

(d)

(e)

Figure 5.25: Temperature contours along a vertical-symmetrical plane across combustion chamber for different hydrogen content in syngas. (a) $H_2 = 5\%$, (b) $H_2 = 25\%$, (c) $H_2 = 50\%$, (d) $H_2 = 75\%$, and (e) $H_2 = 95\%$. $\phi = 0.6$ and $S = 0.7$

A comparison between maximum, average and exit temperatures are given in Figure 5.27 for different syngas compositions. The maximum temperature is observed to increase with hydrogen volume percent. This is due to the hydrogen reactivity which enhances more heat release raising the maximum temperature locally. On the other hand, the average and exit temperatures are almost constant. This can be explained by the energy input which is fixed for all cases of varying hydrogen content (Table 5.1).

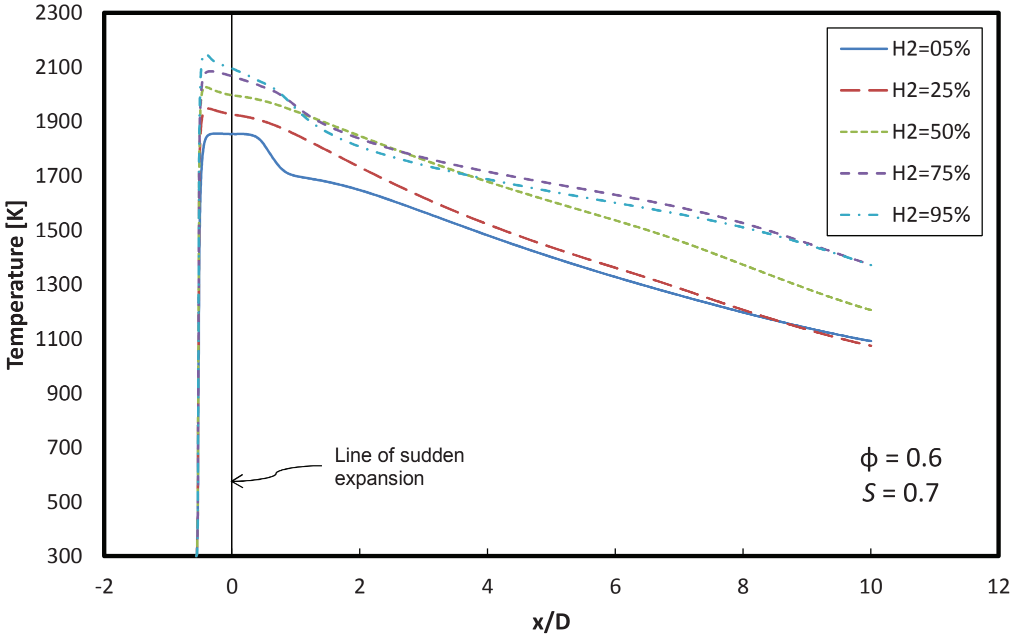

Figure 5.26: Axial profiles of temperature along the centerline of the combustion chamber for different hydrogen content in syngas. $\phi = 0.6$ and $S = 0.7$

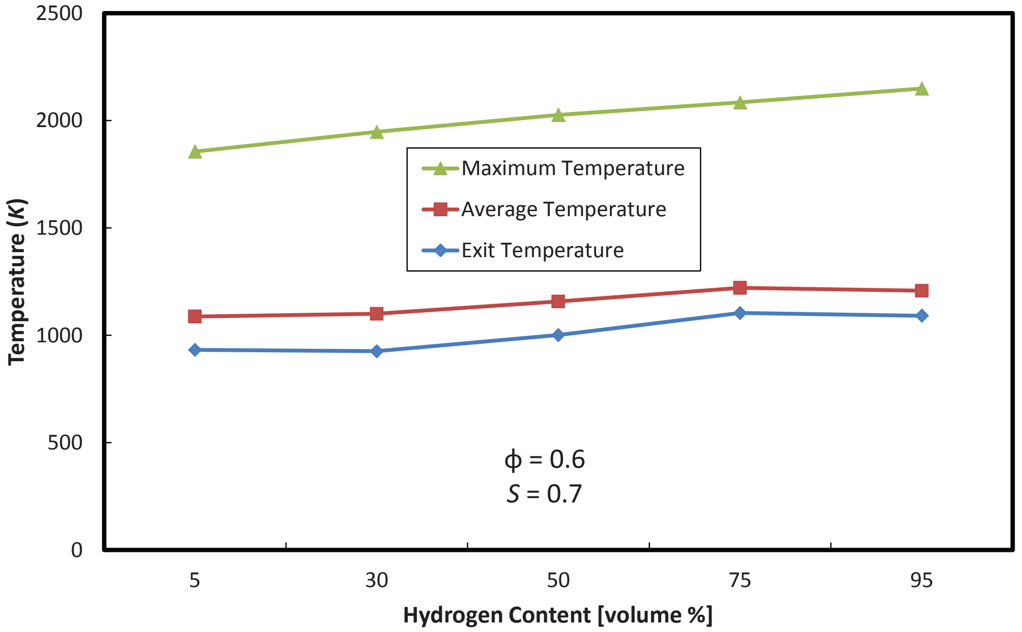

Figure 5.27: Comparison between maximum, average and exit temperatures for different syngas compositions. $\phi = 0.6$ and $S = 0.7$

Effect of H_2/CO Ratio on Fuel Consumption

Figure 5.28 shows the axial distribution of hydrogen and carbon monoxide concentrations along the centerline of the combustor for the different syngas compositions. Figure 5.28a show that hydrogen is rapidly depleted before the sudden expansion. It can also be seen that concentration gradients are higher for higher hydrogen content in syngas. On the other hand, Figure 5.28b shows that there is a delay in CO burnout especially for the low hydrogen case ($H_2 = 5\%$). This is attributed to the high ignition temperature of CO as compared to H_2. At low hydrogen content, low energy is available for ignition. As hydrogen level in syngas increases, more energy is available to achieve ignition temperature of CO. This, combined with lower CO concentrations, will make the depletion rate of CO faster for higher levels of H_2.

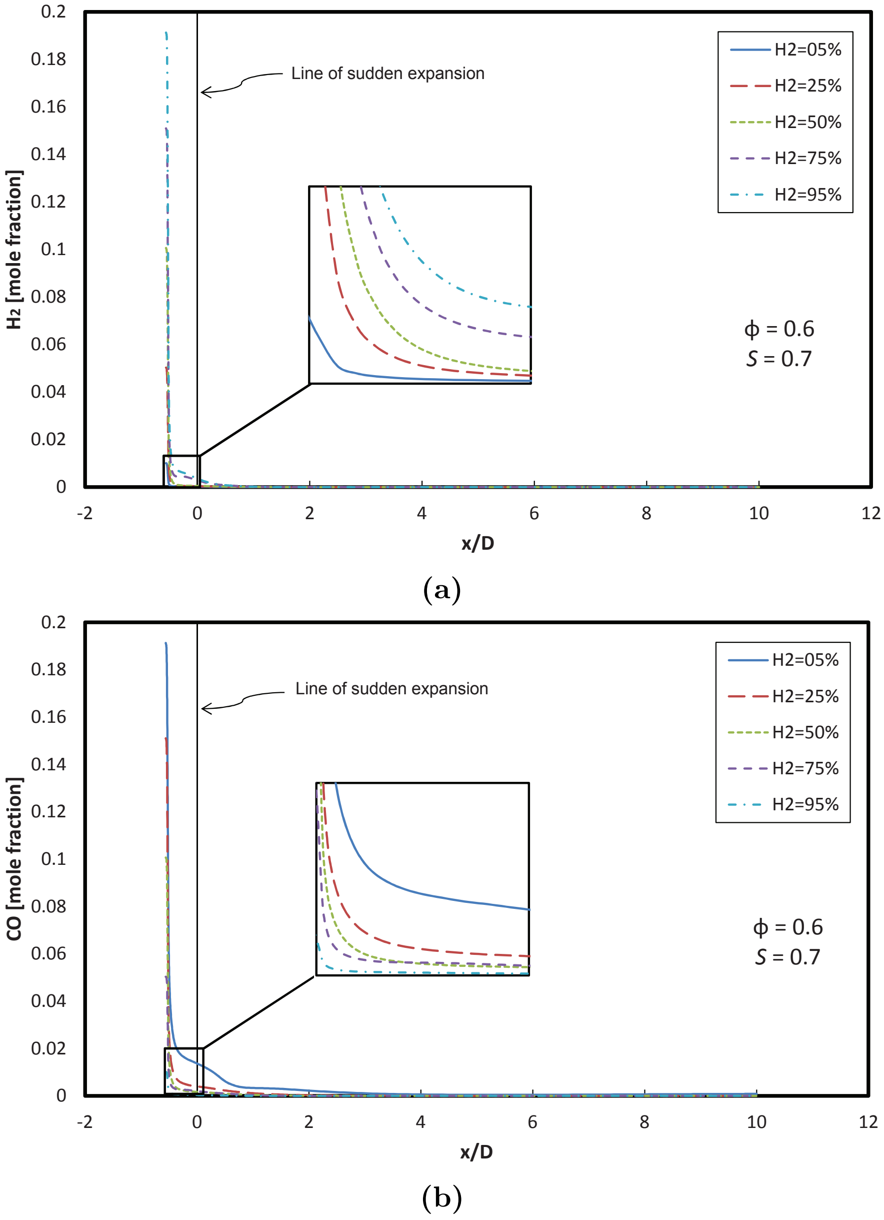

Figure 5.28: Axial profiles of (a) H_2 and (b) CO concentrations in the $H_2/CO/air$ mixture across combustor centerline for different syngas compositions. $x/D = 0$ is the line of sudden expansion. $\phi = 0.6$ and $S = 0.7$

Effect of H_2/CO Ratio on Emissions

Figure 5.29 presents NO and CO pollutants emission at the exit of the combustor for the different hydrogen contents. It is shown that NO emission follows the maximum temperature trend. It is generally observed that NO emission is below

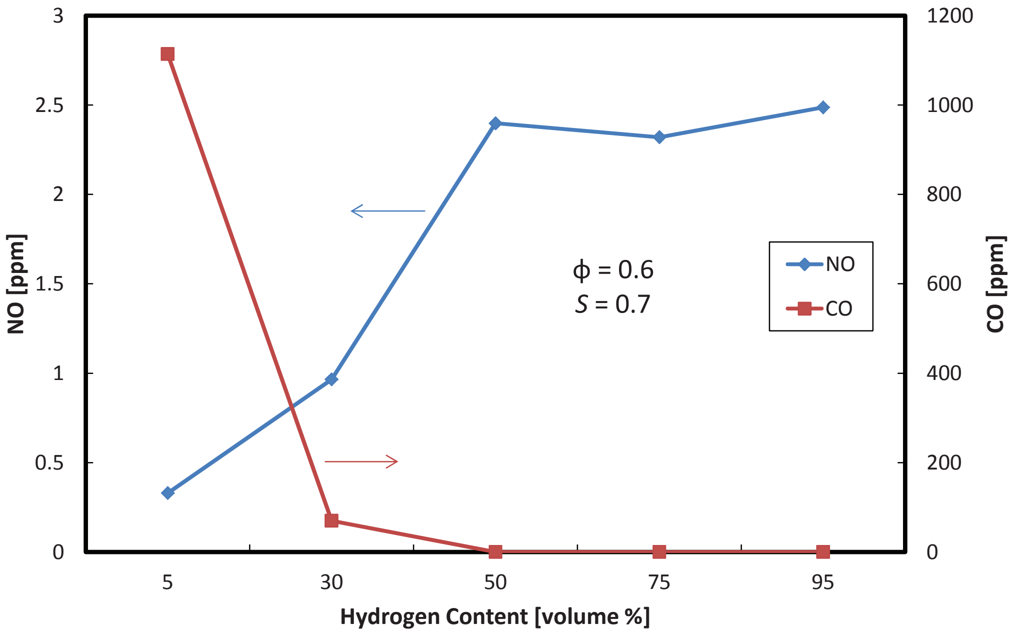

Figure 5.29: NO and CO emissions at the exit of combustor for different syngas compositions. $\phi = 0.6$ and $S = 0.7$

2.5 *ppm* for all cases. In a different manner, exit CO emission is observed to decrease with hydrogen content. This is attributed to the increased residence time of the products that stem from increasing hydrogen level in syngas. On the other hand, Figure 5.30 shows CO_2 emission decreases as the volume percent of H_2 increases. This is due to the fact that the increase in H_2 volume percent decreases the amount of conversion from CO to CO_2 in the combustion process.

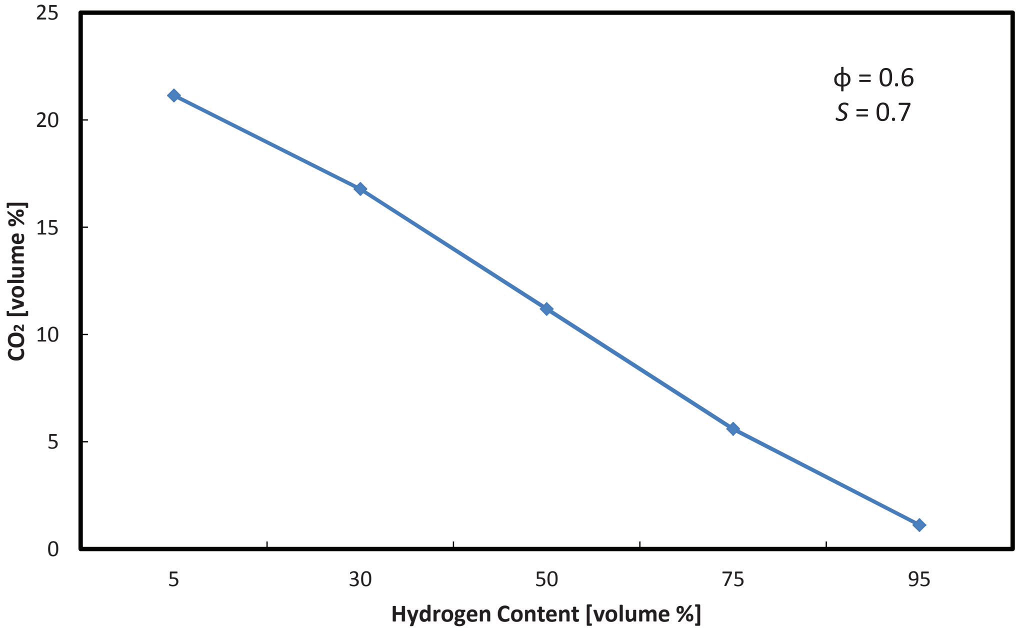

Figure 5.30: CO_2 emissions at the exit of combustor for different syngas compositions. $\phi = 0.6$ and $S = 0.7$

5.5.3 Influence of Equivalence Ratio

The variation in equivalence ratio can effect the different combustion characteristics. In this section, the equivalence ratio influence on flow field, flame structure, temperature field, fuel consumption, and emissions will be described.

Effect of Equivalence Ratio on Velocity Field

Figure 5.31 shows the axial velocity contours along a vertical-symmetrical plane of the combustor for different equivalence ratios. For the low equivalence ratio cases ($\phi = 0.4$ and $\phi = 0.5$), there exists IRZ-W, IRZ-C, and ORZ. The size of these recirculation zones is relatively larger for the case $\phi = 0.4$. As the equivalence ratio increases, the IRZ-C is damped and the IRZ-W is reduced in strength. This is due to the fact that as the equivalence ratio increases, the amount of air dilution decreases. This promotes higher expansion of the gases which increases the volume flow rate, and consequently the flow velocity. This can be clearly observed in Figure 5.32, which shows the axial velocity profiles along the centerline of the combustor for the different equivalence ratios. It is generally observed that increasing the equivalence ratio causes the axial velocity to increase.

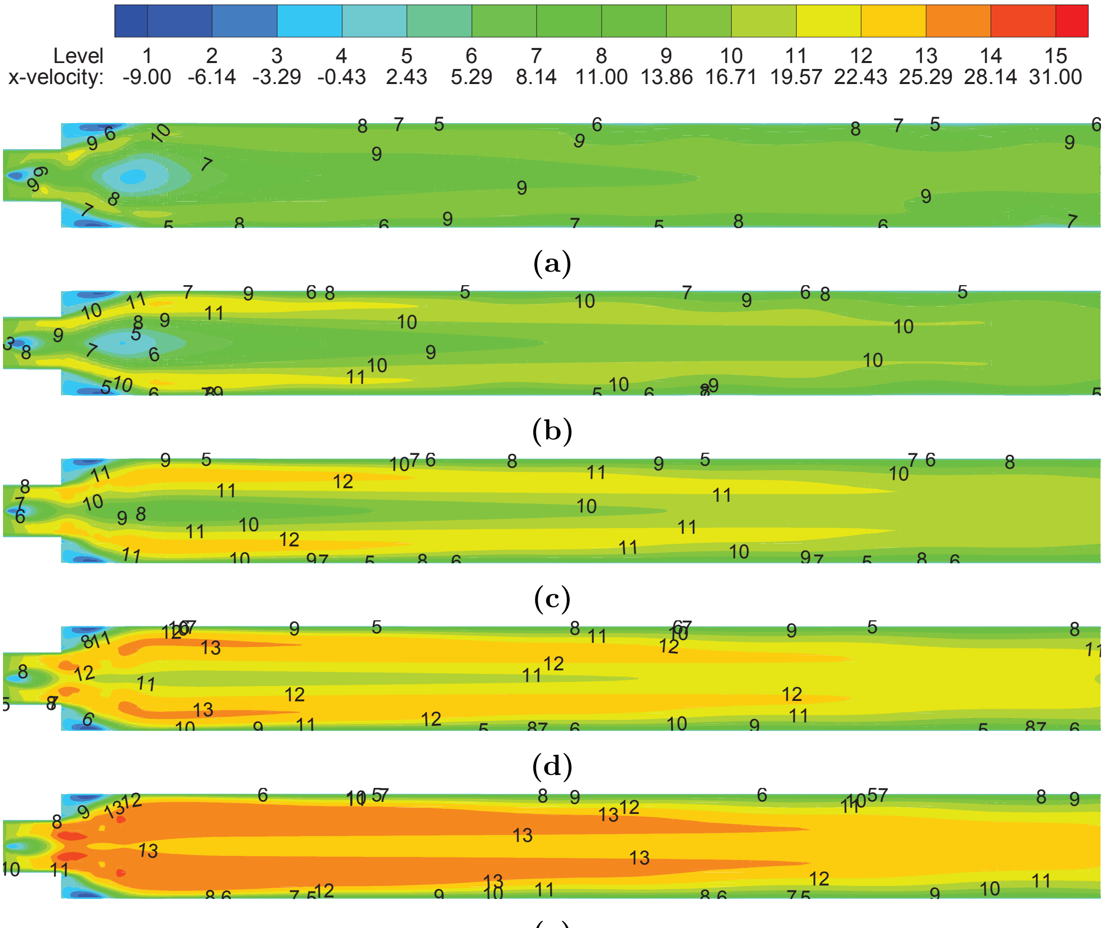

Figure 5.31: Axial velocity contours across a vertical-symmetrical plane for different equivalence ratios. (a) $\phi = 0.4$, (b) $\phi = 0.5$, (c) $\phi = 0.6$, (d) $\phi = 0.7$, and (e) $\phi = 0.8$. $H_2/CO = 50/50$ and $S = 0.7$

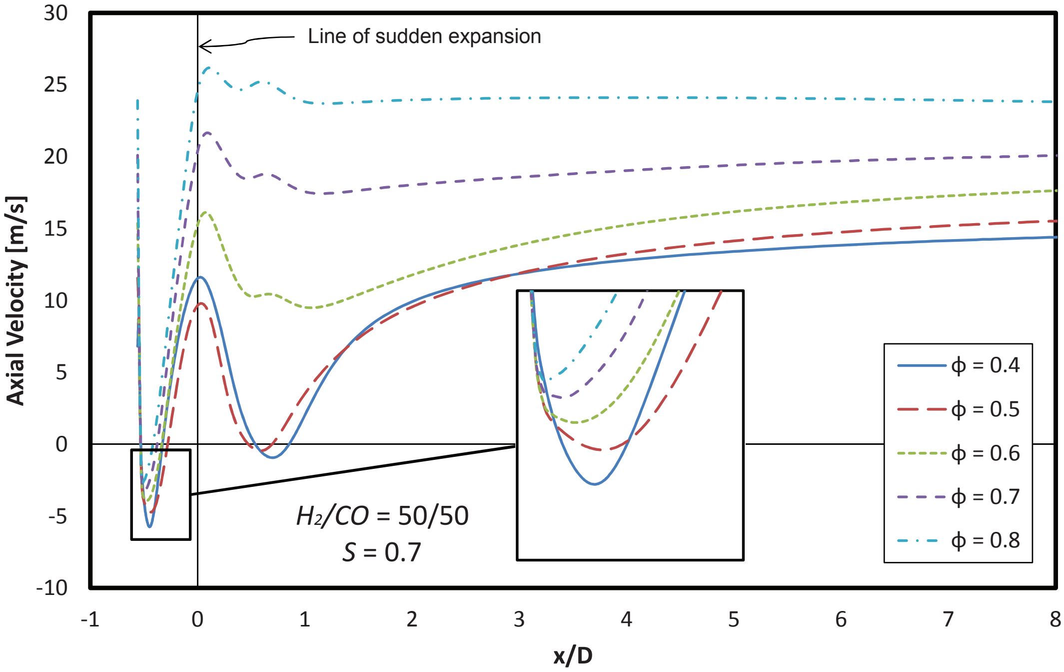

Figure 5.32: Axial velocity profiles across the centerline of combustion chamber for different equivalence ratios. $H_2/CO = 50/50$ and $S = 0.7$

The radial profiles of axial velocity at different cross-sections are shown in Figure 5.33 for different equivalence ratios. In general, axial velocity increases as the equivalence ratio increases due to the corresponding increase in volume flow rates resulting from the combustion process. In a section downstream of the swirler, the strength of the IRZ-W decreases with equivalence ratio. The opposite occurs to the ORZ downstream of the expansion plane, where its strength increases with increasing the equivalence ratio. In a further downstream section, damping of the ORZ takes place. Peak velocities, on the other hand, occur in the vicinity of the wall instead of the centerline. For the case of $\phi = 0.4$, buoyancy forces tend to have a small effect on the flow distribution.

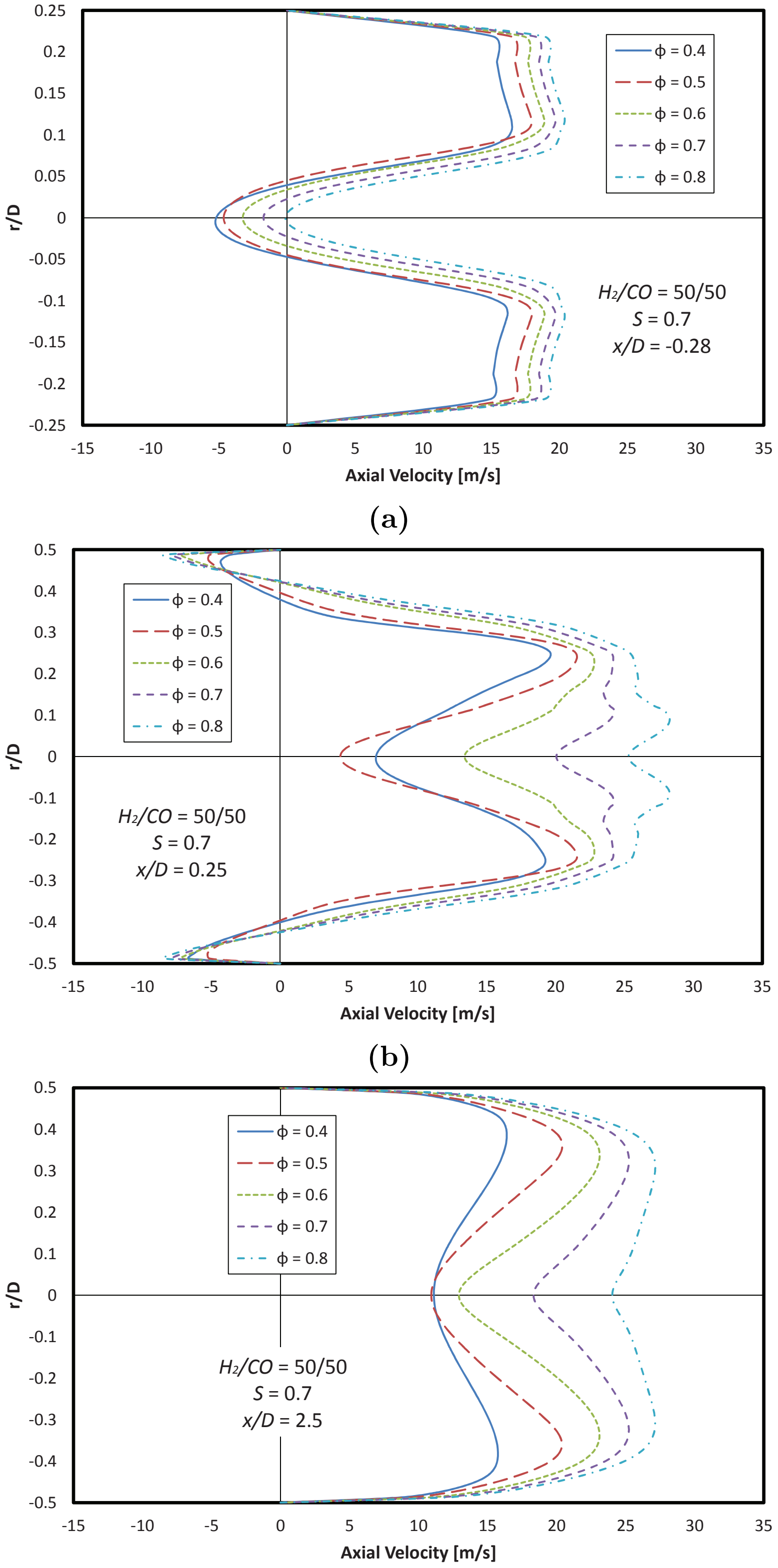

(a)

(b)

(c)

Figure 5.33: Radial profiles of axial velocity at different cross-sections for different equivalence ratios. (a) $x/D = -0.42$ (b) $x/D = 0.25$ and (c) $x/D = 2.5$. $x = 0$ is the line of sudden expansion. $H_2/CO = 50/50$ and $S = 0.7$

Effect of Equivalence Ratio on Flame Structure and Temperature Field

Qualitative OH radical and temperature contours are shown in Figure 5.34 and Figure 5.35, respectively, for the different equivalence ratio cases. It can be seen that as the equivalence ratio increases, the flame length and flame temperature increase. This is attributed to the fact that at higher equivalence ratios, the fuel is burned with less excess of air, thus burning more fuel and releasing higher energy increasing the flame temperature and length. This conclusion was also reported by Zheng et al. [69] who studied the effect of equivalence ratio on LPM syngas flame characteristics at fixed composition and Reynolds number.

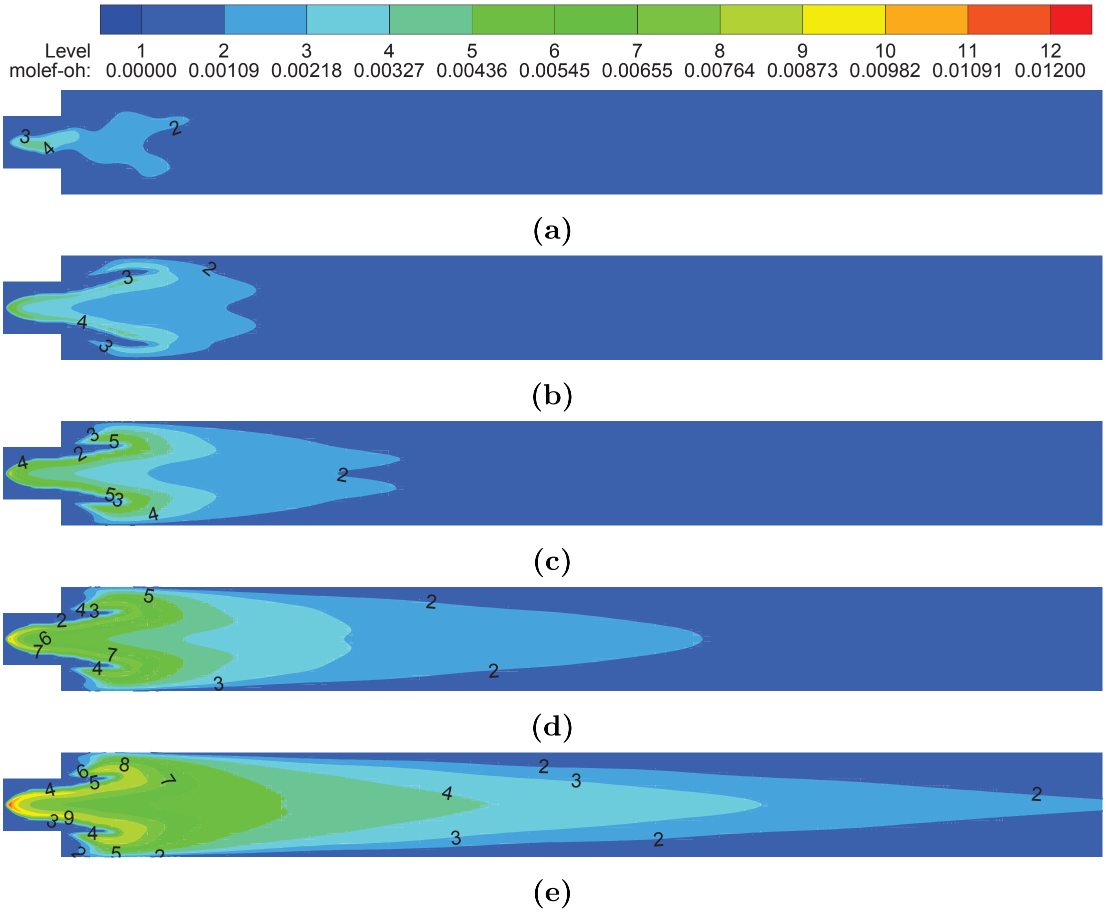

Figure 5.34: OH contours along a vertical-symmetrical plane across combustion chamber for different equivalence ratios. (a) $\phi = 0.4$, (b) $\phi = 0.5$, (c) $\phi = 0.6$, (d) $\phi = 0.7$, and (e) $\phi = 0.8$. $H_2/CO = 50/50$ and $S = 0.7$

The axial profiles of temperature along the centerline of the combustion chamber are given in Figure 5.36 for different equivalence ratios. The profiles show that increasing the equivalence ratio increases the centerline temperature. For the case $\phi = 0.4$, there is a slight drop in the centerline temperature upstream of the expansion plane. This is attributed to the higher recirculated cold reactants by the IRZ-W which is largest in this case.

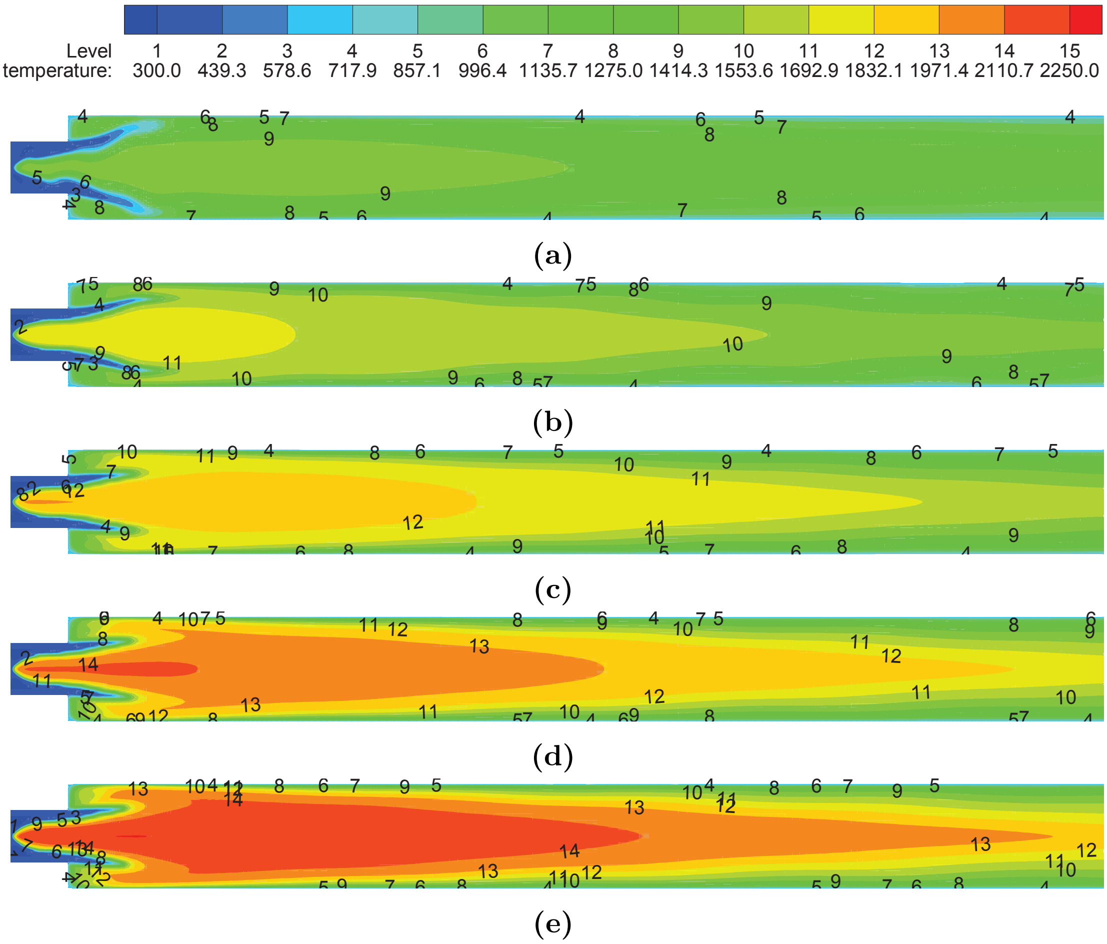

Figure 5.35: Temperature contours along a vertical-symmetrical plane across combustion chamber for different equivalence ratios. (a) $\phi = 0.4$, (b) $\phi = 0.5$, (c) $\phi = 0.6$, (d) $\phi = 0.7$, and (e) $\phi = 0.8$. $H_2/CO = 50/50$ and $S = 0.7$

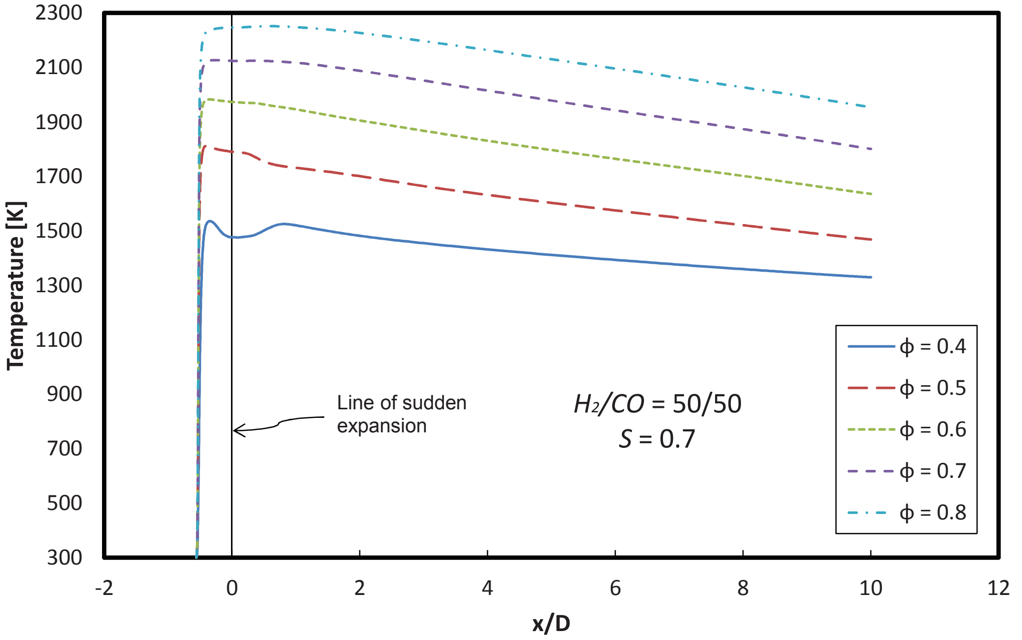

Figure 5.36: Axial profiles of temperature along the centerline of the combustion chamber for different equivalence ratios. $H_2/CO = 50/50$ and $S = 0.7$

A comparison between the maximum, average and exit temperatures for the different equivalence ratio cases is given in Figure 5.37. The figure clearly shows that all temperatures increase with increasing the equivalence ratio. This is due to the increased thermal power as the fuel to air ratio increases.

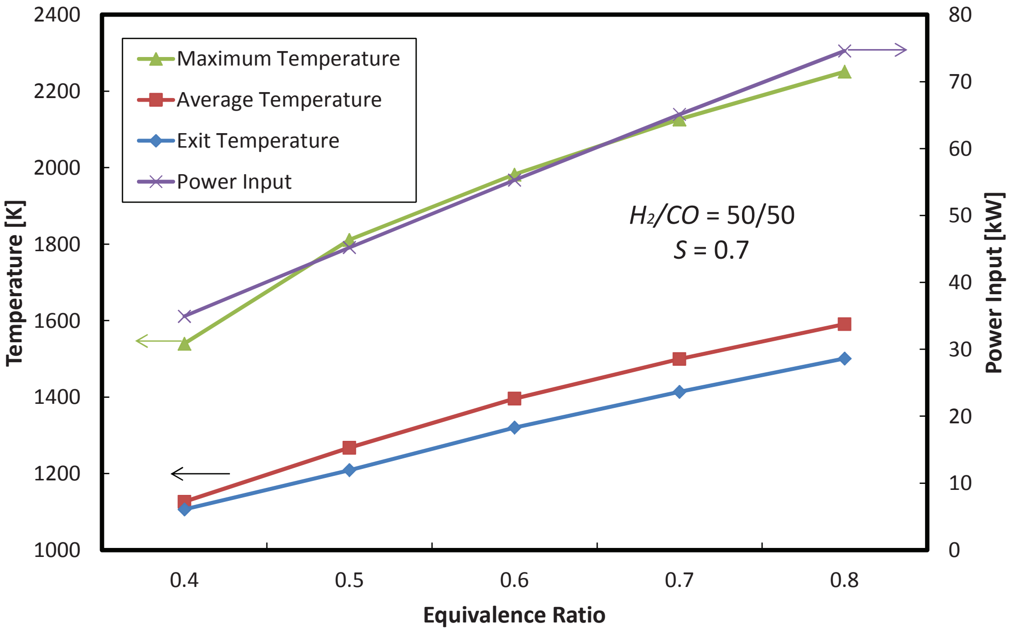

Figure 5.37: Comparison between maximum, average and exit temperatures for different equivalence ratios. $H_2/CO = 50/50$ and $S = 0.7$

Effect of Equivalence Ratio on Fuel Consumption

Figure 5.38 presents the axial distribution of hydrogen and carbon monoxide concentrations along the centerline of the combustor for different equivalence ratios. Hydrogen is depleted completely before the sudden expansion. For the very low equivalence ratio case ($\phi = 0.4$), there is a delay in the burnout of H_2 compared to all other cases. This is mainly due to the high amount of excess air which acts as a heat sink, reducing the energy required for ignition. CO, on the other hand, is depleted slower than H_2. This is due to the higher autoignition temperature of

CO as compared to H_2. It is generally observed that the rate of burning of CO is faster for low equivalence ratios. This is owing to the less amount of CO present in the fuel-air mixture, which requires less energy for ignition. However, for the case of $\phi = 0.4$, the higher amount of excess air as well as cold reactants recirculation are responsible for the delay in CO depletion downstream of the swirler.

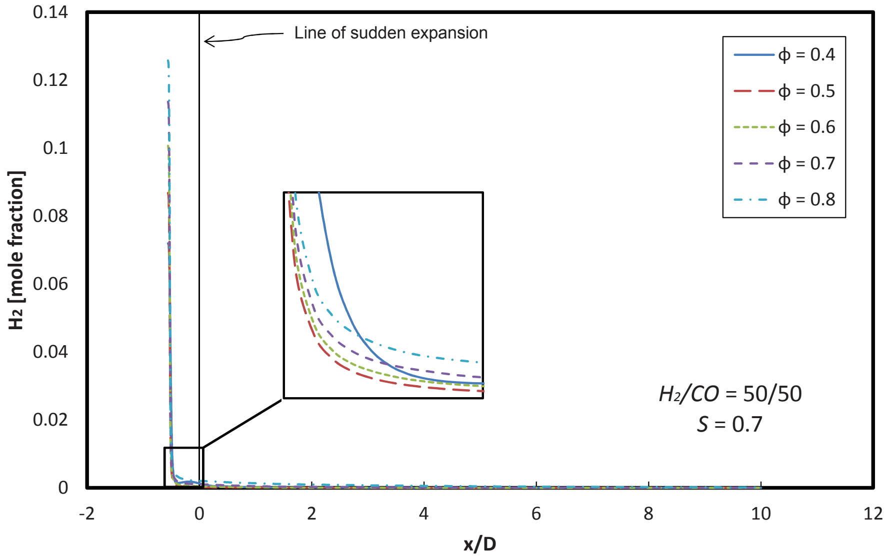

(a)

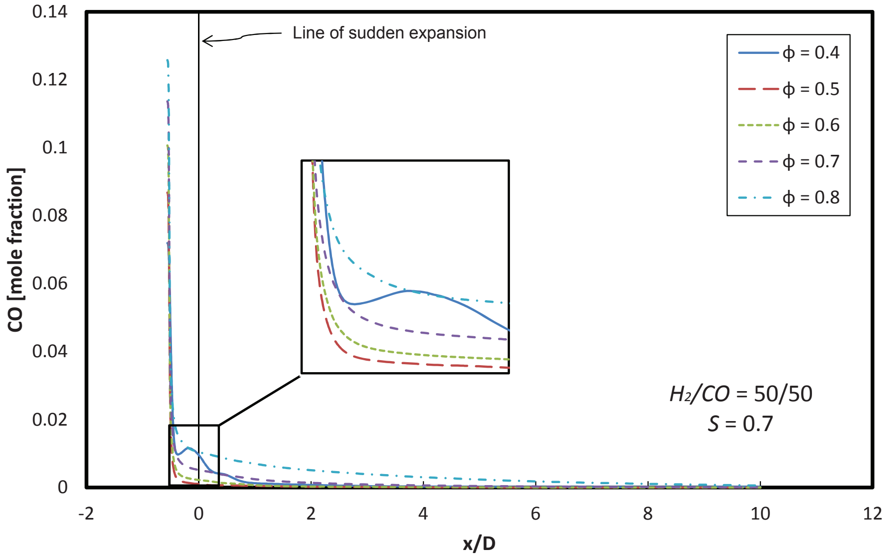

(b)

Figure 5.38: Axial profiles of (a) H_2 and (b) CO concentrations in the $H_2/CO/air$ mixture across combustor centerline for different equivalence ratios. $x/D = 0$ is the line of sudden expansion. $H_2/CO = 50/50$ and $S = 0.7$

Effect of Equivalence Ratio on Emissions

Pollutant Emissions of NO, CO, and CO_2 at the exit of the combustion chamber are given in Figure 5.39 and Figure 5.40 for different equivalence ratios. It is

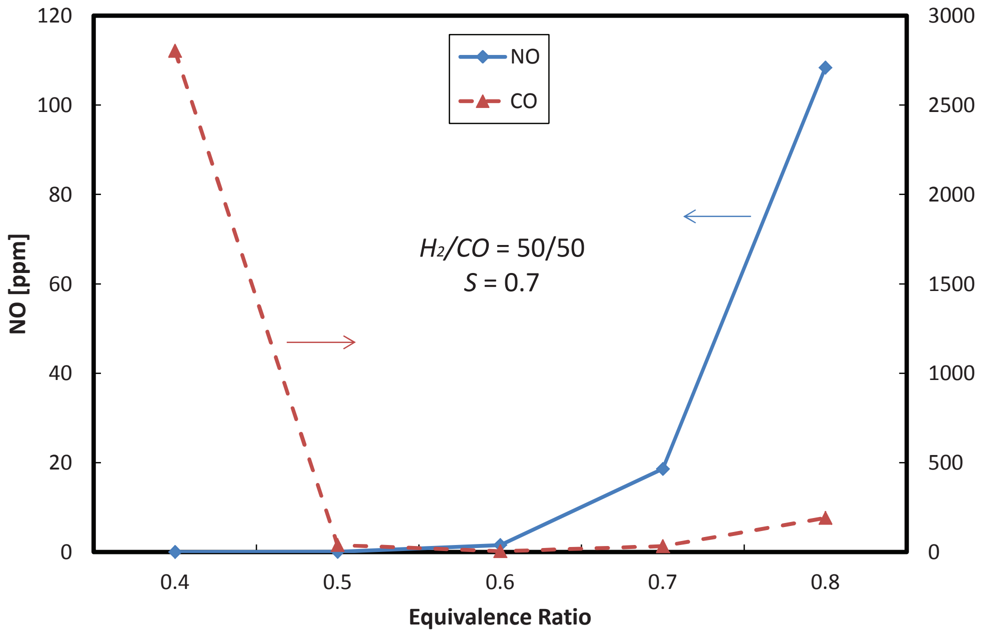

Figure 5.39: NO and CO emissions (in ppm) at the exit of combustor for different equivalence ratios. $H_2/CO = 50/50$ and $S = 0.7$

generally observed that lower equivalence ratios decrease the level of NO emissions due to the reduced flame temperature. Similar conclusions were described by Zheng et al. [69]. CO emissions, on the other hand, are observed to decrease up to equivalence ratio of 0.6, with a significant decrease from 2800 ppm at $\phi = 0.4$ to 40 ppm at $\phi = 0.5$. This represents a 98.5% decrease in CO emissions. This is attributed to the fact that at $\phi = 0.4$, energy required for complete oxidation of CO is scarce due to the excessive cooling air that serves as a heat sink. Beyond $\phi = 0.6$, CO emissions are observed to increase with equivalence ratio. This can be ascribed to the richer levels of the fuel as the equivalence ratio increases, which cause incomplete combustion of the reactants. CO_2 emissions are observed to increase with equivalence ratio due to the reduced level of cooling air, which favors the complete combustion of CO to CO_2.

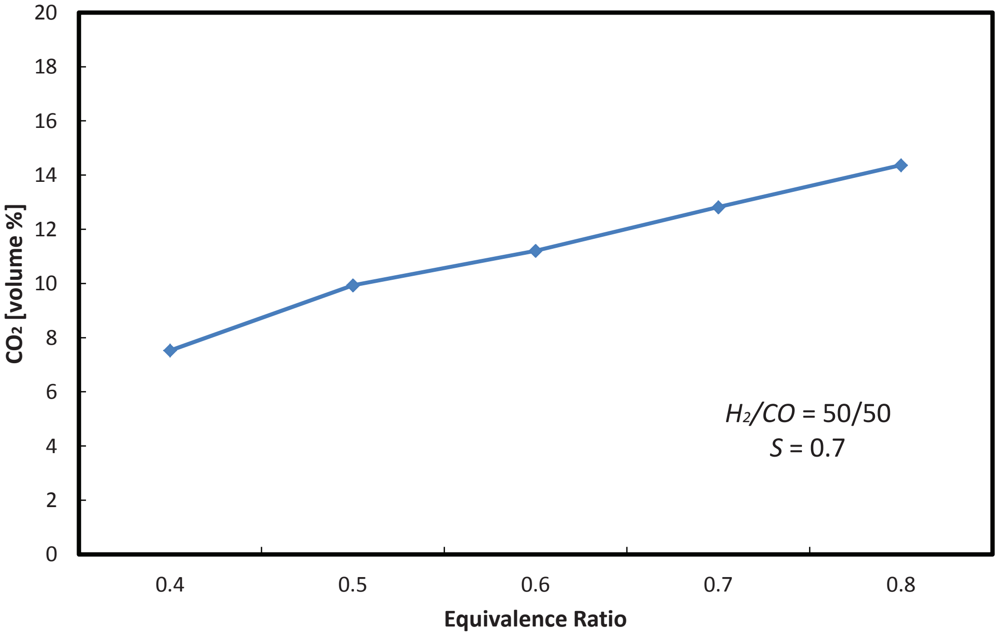

Figure 5.40: CO_2 emissions at the exit of combustor for different equivalence ratios. $H_2/CO = 50/50$ and $S = 0.7$

CHAPTER 6

CONCLUSIONS

The following conclusions and recommendations can be drawn from the current thesis work.

1. The adiabatic flame temperature increased with increasing equivalence ratio for all syngas compositions, operating pressures, and preheat temperatures.
2. For a fixed equivalence ratio, the preheat temperature had the most significant effect on the adiabatic flame temperature.
3. The operating pressure had a negligible effect on the adiabatic flame temperature at very lean conditions. However, this effect was more pronounced at higher equivalence ratios.
4. The adiabatic flame temperature prediction of all mechanisms understudy was within 10% prediction range of the GRI-Mech. 3.0.
5. The laminar flame speed increased with equivalence ratio for all conditions. However, this increase was more significant with increasing hydrogen volume

percent in syngas than with preheat temperature.

6. The flame speed decreased with increasing operating pressure for all conditions.
7. The NO production increased with increasing equivalence ratio and preheat temperature. However, it decreased with increasing hydrogen in the syngas.
8. There is a need to develop kinetic models for syngas (H_2+CO) that accurately predict the laminar flame speed at high pressures and preheat temperatures, these conditions being relevant to gas turbine combustion.
9. There is a lack in experimental data for laminar flame speed at high pressurs with air as the oxidizer, which will help in validating the developed models.
10. The global mechanisms for syngas show high deviation from experiments and results from detailed chemistry. However, their small number of reaction equations and species make it attractive for turbulent reacting flow simulations and will be mechanisms of choice if optimized to improve their accuracy to an acceptable level.
11. The swirl-stabilized geometry affected the different flame properties.
12. As the swirl number increased, the inner recirculation zones broadened, the turbulent intensity, hence the flame speed, increased, and the premixed flame length decreased.
13. The lack in internal source of ignition by hot gases recirculation in the case

of $S = 0$ was made up for by introducing a swirl motion ($S = 0.3$), which shifted the reaction zone away from the wall, reducing the heat loss and increasing the maximum flame temperature and NO_X levels.

14. Levels of NO_X were below 2 *ppm* for all swirl number cases.

15. CO emission decreased with increasing swirl number.

16. Increasing the swirl number resulted in increasing CO_2 emission.

17. Increasing H_2/CO ratio resulted in higher flame temperatures, shorter flame lengths, and weaker reverse flow associated with the inner recirculation zones.

18. Upstream flame propagation (flashback phenomenon) occurred beyond $H_2 =$ 50% by volume.

19. Higher NO_X emissions and lower CO and CO_2 emissions resulted from increasing H_2/CO ratio.

20. The equivalence ratio had the most significant effect of flame characteristics and emissions.

21. Undesirable levels of NO_X were observed beyond $\phi = 0.6$, while undesirbale levels of CO were indicated below $\phi = 0.6$.

22. CO_2 emissions increased with increasing equivalence ratio.

APPENDICES

APPENDIX A

SYNGAS REACTION MECHANISMS

This Appendix represents the elemntary reactions and their Arrhnius rate parameters used in the analysis in chapter 4. The units are $(cm^3/mol)^{r-1}s^{-1}$ for the pre-exponetial factor, A and (cal/mol) for the activation energy, E_a.

Table A.1: GRI reaction mechanism

No.	Reaction	A	n	E_a
1	$O + H_2 \leftrightarrow H + OH$	3.87E+04	2.7	6260
2	$O + HO_2 \leftrightarrow OH + O_2$	2.00E+13	0	0
3	$O + H_2O_2 \leftrightarrow OH + HO_2$	9.63E+06	2	4000
4	$O + CH \leftrightarrow H + CO$	5.70E+13	0	0
5	$O + CH_2 \leftrightarrow H + HCO$	8.00E+13	0	0
6	$O + CH_2(S) \leftrightarrow H_2 + CO$	1.50E+13	0	0
7	$O + CH_2(S) \leftrightarrow H + HCO$	1.50E+13	0	0
8	$O + CH_3 \leftrightarrow H + CH_2O$	5.06E+13	0	0
9	$O + CH_4 \leftrightarrow OH + CH_3$	1.02E+09	1.5	8600
10	$O + HCO \leftrightarrow OH + CO$	3.00E+13	0	0

Continued on next page

No.	Reaction	A	n	E_a
11	$O + HCO \leftrightarrow H + CO_2$	3.00E+13	0	0
12	$O + CH_2O \leftrightarrow OH + HCO$	3.90E+13	0	3540
13	$O + CH_2OH \leftrightarrow OH + CH_2O$	1.00E+13	0	0
14	$O + CH_3O \leftrightarrow OH + CH_2O$	1.00E+13	0	0
15	$O + CH_3OH \leftrightarrow OH + CH_2OH$	3.88E+05	2.5	3100
16	$O + CH_3OH \leftrightarrow OH + CH_3O$	1.30E+05	2.5	5000
17	$O + C_2H \leftrightarrow CH + CO$	5.00E+13	0	0
18	$O + C_2H_2 \leftrightarrow H + HCCO$	1.35E+07	2	1900
19	$O + C_2H_2 \leftrightarrow OH + C_2H$	4.60E+19	-1.41	28950
20	$O + C_2H_2 \leftrightarrow CO + CH_2$	6.94E+06	2	1900
21	$O + C_2H3 \leftrightarrow H + CH_2CO$	3.00E+13	0	0
22	$O + C_2H_4 \leftrightarrow CH_3 + HCO$	1.25E+07	1.83	220
23	$O + C_2H_5 \leftrightarrow CH_3 + CH_2O$	2.24E+13	0	0
24	$O + C_2H_6 \leftrightarrow OH + C_2H_5$	8.98E+07	1.92	5690
25	$O + HCCO \leftrightarrow H + 2CO$	1.00E+14	0	0
26	$O + CH_2CO \leftrightarrow OH + HCCO$	1.00E+13	0	8000
27	$O + CH_2CO \leftrightarrow CH_2 + CO_2$	1.75E+12	0	1350
28	$O_2 + CO \leftrightarrow O + CO_2$	2.50E+12	0	47800
29	$O_2 + CH_2O \leftrightarrow HO_2 + HCO$	1.00E+14	0	40000
30	$H + 2O_2 \leftrightarrow HO_2 + O_2$	2.08E+19	-1.24	0
31	$H + O_2 + H_2O \leftrightarrow HO_2 + H_2O$	1.13E+19	-0.76	0
32	$H + O_2 + N_2 \leftrightarrow HO_2 + N_2$	2.60E+19	-1.24	0
33	$H + O_2 + AR \leftrightarrow HO_2 + AR$	7.00E+17	-0.8	0
34	$H + O_2 \leftrightarrow O + OH$	2.65E+16	-0.6707	17041
35	$2H + H_2 \leftrightarrow 2H_2$	9.00E+16	-0.6	0
36	$2H + H_2O \leftrightarrow H_2 + H_2O$	6.00E+19	-1.25	0
37	$2H + CO_2 \leftrightarrow H_2 + CO_2$	5.50E+20	-2	0
38	$H + HO_2 \leftrightarrow O + H_2O$	3.97E+12	0	671
39	$H + HO_2 \leftrightarrow O_2 + H_2$	4.48E+13	0	1068
40	$H + HO_2 \leftrightarrow 2OH$	8.40E+13	0	635
41	$H + H_2O_2 \leftrightarrow HO_2 + H_2$	1.21E+07	2	5200
42	$H + H_2O_2 \leftrightarrow OH + H_2O$	1.00E+13	0	3600

Continued on next page

No.	Reaction	A	n	E_a
43	$H + CH \leftrightarrow C + H_2$	1.65E+14	0	0
44	$H + CH_2(S) \leftrightarrow CH + H_2$	3.00E+13	0	0
45	$H + CH_4 \leftrightarrow CH_3 + H_2$	6.60E+08	1.62	10840
46	$H + HCO \leftrightarrow H_2 + CO$	7.34E+13	0	0
47	$H + CH_2O \leftrightarrow HCO + H_2$	5.74E+07	1.9	2742
48	$H + CH_2OH \leftrightarrow H_2 + CH_2O$	2.00E+13	0	0
49	$H + CH_2OH \leftrightarrow OH + CH_3$	1.65E+11	0.65	-284
50	$H + CH_2OH \leftrightarrow CH_2(S) + H_2O$	3.28E+13	-0.09	610
51	$H + CH_3O \leftrightarrow H + CH_2OH$	4.15E+07	1.63	1924
52	$H + CH_3O \leftrightarrow H_2 + CH_2O$	2.00E+13	0	0
53	$H + CH_3O \leftrightarrow OH + CH_3$	1.50E+12	0.5	-110
54	$H + CH_3O \leftrightarrow CH_2(S) + H_2O$	2.62E+14	-0.23	1070
55	$H + CH_3OH \leftrightarrow CH_2OH + H_2$	1.70E+07	2.1	4870
56	$H + CH_3OH \leftrightarrow CH_3O + H_2$	4.20E+06	2.1	4870
57	$H + C_2H3 \leftrightarrow H_2 + C_2H_2$	3.00E+13	0	0
58	$H + C_2H_4 \leftrightarrow C_2H3 + H_2$	1.33E+06	2.53	12240
59	$H + C_2H_5 \leftrightarrow H_2 + C_2H_4$	2.00E+12	0	0
60	$H + C_2H_6 \leftrightarrow C_2H_5 + H_2$	1.15E+08	1.9	7530
61	$H + HCCO \leftrightarrow CH_2(S) + CO$	1.00E+14	0	0
62	$H + CH_2CO \leftrightarrow HCCO + H_2$	5.00E+13	0	8000
63	$H + CH_2CO \leftrightarrow CH_3 + CO$	1.13E+13	0	3428
64	$H + HCCOH \leftrightarrow H + CH_2CO$	1.00E+13	0	0
65	$OH + H_2 \leftrightarrow H + H_2O$	2.16E+08	1.51	3430
66	$2OH \leftrightarrow O + H_2O$	3.57E+04	2.4	-2110
67	$OH + HO_2 \leftrightarrow O_2 + H_2O$	1.45E+13	0	-500
68	$OH + H_2O_2 \leftrightarrow HO_2 + H_2O$	2.00E+12	0	427
69	$OH + H_2O_2 \leftrightarrow HO_2 + H_2O$	1.70E+18	0	29410
70	$OH + C \leftrightarrow H + CO$	5.00E+13	0	0
71	$OH + CH \leftrightarrow H + HCO$	3.00E+13	0	0
72	$OH + CH_2 \leftrightarrow H + CH_2O$	2.00E+13	0	0
73	$OH + CH_2 \leftrightarrow CH + H_2O$	1.13E+07	2	3000
74	$OH + CH_2(S) \leftrightarrow H + CH_2O$	3.00E+13	0	0

Continued on next page

No.	Reaction	A	n	E_a
75	$OH + CH_3 \leftrightarrow CH_2 + H_2O$	5.60E+07	1.6	5420
76	$OH + CH_3 \leftrightarrow CH_2(S) + H_2O$	6.44E+17	-1.34	1417
77	$OH + CH_4 \leftrightarrow CH_3 + H_2O$	1.00E+08	1.6	3120
78	$OH + CO \leftrightarrow H + CO_2$	4.76E+07	1.228	70
79	$OH + HCO \leftrightarrow H_2O + CO$	5.00E+13	0	0
80	$OH + CH_2O \leftrightarrow HCO + H_2O$	3.43E+09	1.18	-447
81	$OH + CH_2OH \leftrightarrow H_2O + CH_2O$	5.00E+12	0	0
82	$OH + CH_3O \leftrightarrow H_2O + CH_2O$	5.00E+12	0	0
83	$OH + CH_3OH \leftrightarrow CH_2OH + H_2O$	1.44E+06	2	-840
84	$OH + CH_3OH \leftrightarrow CH_3O + H_2O$	6.30E+06	2	1500
85	$OH + C_2H \leftrightarrow H + HCCO$	2.00E+13	0	0
86	$OH + C_2H_2 \leftrightarrow H + CH_2CO$	2.18E-04	4.5	-1000
87	$OH + C_2H_2 \leftrightarrow H + HCCOH$	5.04E+05	2.3	13500
88	$OH + C_2H_2 \leftrightarrow C_2H + H_2O$	3.37E+07	2	14000
89	$OH + C_2H_2 \leftrightarrow CH_3 + CO$	4.83E-04	4	-2000
90	$OH + C_2H3 \leftrightarrow H_2O + C_2H_2$	5.00E+12	0	0
91	$OH + C_2H_4 \leftrightarrow C_2H3 + H_2O$	3.60E+06	2	2500
92	$OH + C_2H_6 \leftrightarrow C_2H_5 + H_2O$	3.54E+06	2.12	870
93	$OH + CH_2CO \leftrightarrow HCCO + H_2O$	7.50E+12	0	2000
94	$2HO_2 \leftrightarrow O_2 + H_2O_2$	1.30E+11	0	-1630
95	$2HO_2 \leftrightarrow O_2 + H_2O_2$	4.20E+14	0	12000
96	$HO_2 + CH_2 \leftrightarrow OH + CH_2O$	2.00E+13	0	0
97	$HO_2 + CH_3 \leftrightarrow O_2 + CH_4$	1.00E+12	0	0
98	$HO_2 + CH_3 \leftrightarrow OH + CH_3O$	3.78E+13	0	0
99	$HO_2 + CO \leftrightarrow OH + CO_2$	1.50E+14	0	23600
100	$HO_2 + CH_2O \leftrightarrow HCO + H_2O_2$	5.60E+06	2	12000
101	$C + O_2 \leftrightarrow O + CO$	5.80E+13	0	576
102	$C + CH_2 \leftrightarrow H + C_2H$	5.00E+13	0	0
103	$C + CH_3 \leftrightarrow H + C_2H_2$	5.00E+13	0	0
104	$CH + O_2 \leftrightarrow O + HCO$	6.71E+13	0	0
105	$CH + H_2 \leftrightarrow H + CH_2$	1.08E+14	0	3110
106	$CH + H_2O \leftrightarrow H + CH_2O$	5.71E+12	0	-755

Continued on next page

No.	Reaction	A	n	E_a
107	$CH + CH_2 \leftrightarrow H + C_2H_2$	4.00E+13	0	0
108	$CH + CH_3 \leftrightarrow H + C_2H3$	3.00E+13	0	0
109	$CH + CH_4 \leftrightarrow H + C_2H_4$	6.00E+13	0	0
110	$CH + CO_2 \leftrightarrow HCO + CO$	1.90E+14	0	15792
111	$CH + CH_2O \leftrightarrow H + CH_2CO$	9.46E+13	0	-515
112	$CH + HCCO \leftrightarrow CO + C_2H_2$	5.00E+13	0	0
113	$CH_2 + O_2 \rightarrow OH + H + CO$	5.00E+12	0	1500
114	$CH_2 + H_2 \leftrightarrow H + CH_3$	5.00E+05	2	7230
115	$2CH_2 \leftrightarrow H_2 + C_2H_2$	1.60E+15	0	11944
116	$CH_2 + CH_3 \leftrightarrow H + C_2H_4$	4.00E+13	0	0
117	$CH_2 + CH_4 \leftrightarrow 2CH_3$	2.46E+06	2	8270
118	$CH_2 + HCCO \leftrightarrow C_2H3 + CO$	3.00E+13	0	0
119	$CH_2(S) + N_2 \leftrightarrow CH_2 + N_2$	1.50E+13	0	600
120	$CH_2(S) + AR \leftrightarrow CH_2 + AR$	9.00E+12	0	600
121	$CH_2(S) + O_2 \leftrightarrow H + OH + CO$	2.80E+13	0	0
122	$CH_2(S) + O_2 \leftrightarrow CO + H_2O$	1.20E+13	0	0
123	$CH_2(S) + H_2 \leftrightarrow CH_3 + H$	7.00E+13	0	0
124	$CH_2(S) + H_2O \leftrightarrow CH_2 + H_2O$	3.00E+13	0	0
125	$CH_2(S) + CH_3 \leftrightarrow H + C_2H_4$	1.20E+13	0	-570
126	$CH_2(S) + CH_4 \leftrightarrow 2CH_3$	1.60E+13	0	-570
127	$CH_2(S) + CO \leftrightarrow CH_2 + CO$	9.00E+12	0	0
128	$CH_2(S) + CO_2 \leftrightarrow CH_2 + CO_2$	7.00E+12	0	0
129	$CH_2(S) + CO_2 \leftrightarrow CO + CH_2O$	1.40E+13	0	0
130	$CH_2(S) + C_2H_6 \leftrightarrow CH_3 + C_2H_5$	4.00E+13	0	-550
131	$CH_3 + O_2 \leftrightarrow O + CH_3O$	3.56E+13	0	30480
132	$CH_3 + O_2 \leftrightarrow OH + CH_2O$	2.31E+12	0	20315
133	$CH_3 + H_2O_2 \leftrightarrow HO_2 + CH_4$	2.45E+04	2.47	5180
134	$2CH_3 \leftrightarrow H + C_2H_5$	6.84E+12	0.1	10600
135	$CH_3 + HCO \leftrightarrow CH_4 + CO$	2.65E+13	0	0
136	$CH_3 + CH_2O \leftrightarrow HCO + CH_4$	3.32E+03	2.81	5860
137	$CH_3 + CH_3OH \leftrightarrow CH_2OH + CH_4$	3.00E+07	1.5	9940
138	$CH_3 + CH_3OH \leftrightarrow CH_3O + CH_4$	1.00E+07	1.5	9940

Continued on next page

No.	Reaction	A	n	E_a
139	$CH_3 + C_2H_4 \leftrightarrow C_2H3 + CH_4$	2.27E+05	2	9200
140	$CH_3 + C_2H_6 \leftrightarrow C_2H_5 + CH_4$	6.14E+06	1.74	10450
141	$HCO + H_2O \leftrightarrow H + CO + H_2O$	1.50E+18	-1	17000
142	$HCO + O_2 \leftrightarrow HO_2 + CO$	1.35E+13	0	400
143	$CH_2OH + O_2 \leftrightarrow HO_2 + CH_2O$	1.80E+13	0	900
144	$CH_3O + O_2 \leftrightarrow HO_2 + CH_2O$	4.28E-13	7.6	-3530
145	$C_2H + O_2 \leftrightarrow HCO + CO$	1.00E+13	0	-755
146	$C_2H + H_2 \leftrightarrow H + C_2H_2$	5.68E+10	0.9	1993
147	$C_2H3 + O_2 \leftrightarrow HCO + CH_2O$	4.58E+16	-1.39	1015
148	$C_2H_5 + O_2 \leftrightarrow HO_2 + C_2H_4$	8.40E+11	0	3875
149	$HCCO + O_2 \leftrightarrow OH + 2CO$	3.20E+12	0	854
150	$2HCCO \leftrightarrow 2CO + C_2H_2$	1.00E+13	0	0
151	$N + NO \leftrightarrow N_2 + O$	2.70E+13	0	355
152	$N + O_2 \leftrightarrow NO + O$	9.00E+09	1	6500
153	$N + OH \leftrightarrow NO + H$	3.36E+13	0	385
154	$N_2O + O \leftrightarrow N_2 + O_2$	1.40E+12	0	10810
155	$N_2O + O \leftrightarrow 2NO$	2.90E+13	0	23150
156	$N_2O + H \leftrightarrow N_2 + OH$	3.87E+14	0	18880
157	$N_2O + OH \leftrightarrow N_2 + HO_2$	2.00E+12	0	21060
158	$HO_2 + NO \leftrightarrow NO_2 + OH$	2.11E+12	0	-480
159	$NO_2 + O \leftrightarrow NO + O_2$	3.90E+12	0	-240
160	$NO_2 + H \leftrightarrow NO + OH$	1.32E+14	0	360
161	$NH + O \leftrightarrow NO + H$	4.00E+13	0	0
162	$NH + H \leftrightarrow N + H_2$	3.20E+13	0	330
163	$NH + OH \leftrightarrow HNO + H$	2.00E+13	0	0
164	$NH + OH \leftrightarrow N + H_2O$	2.00E+09	1.2	0
165	$NH + O_2 \leftrightarrow HNO + O$	4.61E+05	2	6500
166	$NH + O_2 \leftrightarrow NO + OH$	1.28E+06	1.5	100
167	$NH + N \leftrightarrow N_2 + H$	1.50E+13	0	0
168	$NH + H_2O \leftrightarrow HNO + H_2$	2.00E+13	0	13850
169	$NH + NO \leftrightarrow N_2 + OH$	2.16E+13	-0.23	0
170	$NH + NO \leftrightarrow N_2O + H$	3.65E+14	-0.45	0

Continued on next page

No.	Reaction	A	n	E_a
171	$NH_2 + O \leftrightarrow OH + NH$	3.00E+12	0	0
172	$NH_2 + O \leftrightarrow H + HNO$	3.90E+13	0	0
173	$NH_2 + H \leftrightarrow NH + H_2$	4.00E+13	0	3650
174	$NH_2 + OH \leftrightarrow NH + H_2O$	9.00E+07	1.5	-460
175	$NNH \leftrightarrow N_2 + H$	3.30E+08	0	0
176	$NNH + O_2 \leftrightarrow HO_2 + N_2$	5.00E+12	0	0
177	$NNH + O \leftrightarrow OH + N_2$	2.50E+13	0	0
178	$NNH + O \leftrightarrow NH + NO$	7.00E+13	0	0
179	$NNH + H \leftrightarrow H_2 + N_2$	5.00E+13	0	0
180	$NNH + OH \leftrightarrow H_2O + N_2$	2.00E+13	0	0
181	$NNH + CH_3 \leftrightarrow CH_4 + N_2$	2.50E+13	0	0
182	$HNO + O \leftrightarrow NO + OH$	2.50E+13	0	0
183	$HNO + H \leftrightarrow H_2 + NO$	9.00E+11	0.72	660
184	$HNO + OH \leftrightarrow NO + H_2O$	1.30E+07	1.9	-950
185	$HNO + O_2 \leftrightarrow HO_2 + NO$	1.00E+13	0	13000
186	$CN + O \leftrightarrow CO + N$	7.70E+13	0	0
187	$CN + OH \leftrightarrow NCO + H$	4.00E+13	0	0
188	$CN + H_2O \leftrightarrow HCN + OH$	8.00E+12	0	7460
189	$CN + O_2 \leftrightarrow NCO + O$	6.14E+12	0	-440
190	$CN + H_2 \leftrightarrow HCN + H$	2.95E+05	2.45	2240
191	$NCO + O \leftrightarrow NO + CO$	2.35E+13	0	0
192	$NCO + H \leftrightarrow NH + CO$	5.40E+13	0	0
193	$NCO + OH \leftrightarrow NO + H + CO$	2.50E+12	0	0
194	$NCO + N \leftrightarrow N_2 + CO$	2.00E+13	0	0
195	$NCO + O_2 \leftrightarrow NO + CO_2$	2.00E+12	0	20000
196	$NCO + NO \leftrightarrow N_2O + CO$	1.90E+17	-1.52	740
197	$NCO + NO \leftrightarrow N_2 + CO_2$	3.80E+18	-2	800
198	$HCN + O \leftrightarrow NCO + H$	2.03E+04	2.64	4980
199	$HCN + O \leftrightarrow NH + CO$	5.07E+03	2.64	4980
200	$HCN + O \leftrightarrow CN + OH$	3.91E+09	1.58	26600
201	$HCN + OH \leftrightarrow HOCN + H$	1.10E+06	2.03	13370
202	$HCN + OH \leftrightarrow HNCO + H$	4.40E+03	2.26	6400

Continued on next page

No.	Reaction	A	n	E_a
203	$HCN + OH \leftrightarrow NH_2 + CO$	1.60E+02	2.56	9000
204	$H_2CN + N \leftrightarrow N_2 + CH_2$	6.00E+13	0	400
205	$C + N_2 \leftrightarrow CN + N$	6.30E+13	0	46020
206	$CH + N_2 \leftrightarrow HCN + N$	3.12E+09	0.88	20130
207	$CH_2 + N_2 \leftrightarrow HCN + NH$	1.00E+13	0	74000
208	$CH_2(S) + N_2 \leftrightarrow NH + HCN$	1.00E+11	0	65000
209	$C + NO \leftrightarrow CN + O$	1.90E+13	0	0
210	$C + NO \leftrightarrow CO + N$	2.90E+13	0	0
211	$CH + NO \leftrightarrow HCN + O$	4.10E+13	0	0
212	$CH + NO \leftrightarrow H + NCO$	1.62E+13	0	0
213	$CH + NO \leftrightarrow N + HCO$	2.46E+13	0	0
214	$CH_2 + NO \leftrightarrow H + HNCO$	3.10E+17	-1.38	1270
215	$CH_2 + NO \leftrightarrow OH + HCN$	2.90E+14	-0.69	760
216	$CH_2 + NO \leftrightarrow H + HCNO$	3.80E+13	-0.36	580
217	$CH_2(S) + NO \leftrightarrow H + HNCO$	3.10E+17	-1.38	1270
218	$CH_2(S) + NO \leftrightarrow OH + HCN$	2.90E+14	-0.69	760
219	$CH_2(S) + NO \leftrightarrow H + HCNO$	3.80E+13	-0.36	580
220	$CH_3 + NO \leftrightarrow HCN + H_2O$	9.60E+13	0	28800
221	$CH_3 + NO \leftrightarrow H_2CN + OH$	1.00E+12	0	21750
222	$HCNN + O \leftrightarrow CO + H + N_2$	2.20E+13	0	0
223	$HCNN + O \leftrightarrow HCN + NO$	2.00E+12	0	0
224	$HCNN + O_2 \leftrightarrow O + HCO + N_2$	1.20E+13	0	0
225	$HCNN + OH \leftrightarrow H + HCO + N_2$	1.20E+13	0	0
226	$HCNN + H \leftrightarrow CH_2 + N_2$	1.00E+14	0	0
227	$HNCO + O \leftrightarrow NH + CO_2$	9.80E+07	1.41	8500
228	$HNCO + O \leftrightarrow HNO + CO$	1.50E+08	1.57	44000
229	$HNCO + O \leftrightarrow NCO + OH$	2.20E+06	2.11	11400
230	$HNCO + H \leftrightarrow NH_2 + CO$	2.25E+07	1.7	3800
231	$HNCO + H \leftrightarrow H_2 + NCO$	1.05E+05	2.5	13300
232	$HNCO + OH \leftrightarrow NCO + H_2O$	3.30E+07	1.5	3600
233	$HNCO + OH \leftrightarrow NH_2 + CO_2$	3.30E+06	1.5	3600
234	$HCNO + H \leftrightarrow H + HNCO$	2.10E+15	-0.69	2850

Continued on next page

No.	Reaction	A	n	E_a
235	$HCNO + H \leftrightarrow OH + HCN$	2.70E+11	0.18	2120
236	$HCNO + H \leftrightarrow NH_2 + CO$	1.70E+14	-0.75	2890
237	$HOCN + H \leftrightarrow H + HNCO$	2.00E+07	2	2000
238	$HCCO + NO \leftrightarrow HCNO + CO$	9.00E+12	0	0
239	$CH_3 + N \leftrightarrow H_2CN + H$	6.10E+14	-0.31	290
240	$CH_3 + N \leftrightarrow HCN + H_2$	3.70E+12	0.15	-90
241	$NH3 + H \leftrightarrow NH_2 + H_2$	5.40E+05	2.4	9915
242	$NH3 + OH \leftrightarrow NH_2 + H_2O$	5.00E+07	1.6	955
243	$NH3 + O \leftrightarrow NH_2 + OH$	9.40E+06	1.94	6460
244	$NH + CO_2 \leftrightarrow HNO + CO$	1.00E+13	0	14350
245	$CN + NO_2 \leftrightarrow NCO + NO$	6.16E+15	-0.752	345
246	$NCO + NO_2 \leftrightarrow N_2O + CO_2$	3.25E+12	0	-705
247	$N + CO_2 \leftrightarrow NO + CO$	3.00E+12	0	11300
248	$O + CH_3 \rightarrow H + H_2 + CO$	3.37E+13	0	0
249	$O + C_2H_4 \leftrightarrow H + CH_2CHO$	6.70E+06	1.83	220
250	$O + C_2H_5 \leftrightarrow H + CH_3CHO$	1.10E+14	0	0
251	$OH + HO_2 \leftrightarrow O_2 + H_2O$	5.00E+15	0	17330
252	$OH + CH_3 \rightarrow H_2 + CH_2O$	8.00E+09	0.5	-1755
253	$CH_2 + O_2 \rightarrow 2H + CO_2$	5.80E+12	0	1500
254	$CH_2 + O_2 \leftrightarrow O + CH_2O$	2.40E+12	0	1500
255	$CH_2 + CH_2 \rightarrow 2H + C_2H_2$	2.00E+14	0	10989
256	$CH_2(S) + H_2O \rightarrow H_2 + CH_2O$	6.82E+10	0.25	-935
257	$C_2H3 + O_2 \leftrightarrow O + CH_2CHO$	3.03E+11	0.29	11
258	$C_2H3 + O_2 \leftrightarrow HO_2 + C_2H_2$	1.34E+06	1.61	-384
259	$O + CH_3CHO \leftrightarrow OH + CH_2CHO$	2.92E+12	0	1808
260	$O + CH_3CHO \rightarrow OH + CH_3 + CO$	2.92E+12	0	1808
261	$O_2 + CH_3CHO \rightarrow HO_2 + CH_3 + CO$	3.01E+13	0	39150
262	$H + CH_3CHO \leftrightarrow CH_2CHO + H_2$	2.05E+09	1.16	2405
263	$H + CH_3CHO \rightarrow CH_3 + H_2 + CO$	2.05E+09	1.16	2405
264	$OH + CH_3CHO \rightarrow CH_3 + H_2O + CO$	2.34E+10	0.73	-1113
265	$HO_2 + CH_3CHO \rightarrow CH_3 + H_2O_2 + CO$	3.01E+12	0	11923
266	$CH_3 + CH_3CHO \rightarrow CH_3 + CH_4 + CO$	2.72E+06	1.77	5920

Continued on next page

No.	Reaction	A	n	E_a
267	$O + CH_2CHO \rightarrow H + CH_2 + CO_2$	1.50E+14	0	0
268	$O_2 + CH_2CHO \rightarrow OH + CO + CH_2O$	1.81E+10	0	0
269	$O_2 + CH_2CHO \rightarrow OH + 2HCO$	2.35E+10	0	0
270	$H + CH_2CHO \leftrightarrow CH_3 + HCO$	2.20E+13	0	0
271	$H + CH_2CHO \leftrightarrow CH_2CO + H_2$	1.10E+13	0	0
272	$OH + CH_2CHO \leftrightarrow H_2O + CH_2CO$	1.20E+13	0	0
273	$OH + CH_2CHO \leftrightarrow HCO + CH_2OH$	3.01E+13	0	0
274	$O + C3H_8 \leftrightarrow OH + C_3H_7$	1.93E+05	2.68	3716
275	$H + C3H_8 \leftrightarrow C_3H_7 + H_2$	1.32E+06	2.54	6756
276	$OH + C3H_8 \leftrightarrow C_3H_7 + H_2O$	3.16E+07	1.8	934
277	$C_3H_7 + H_2O_2 \leftrightarrow HO_2 + C3H_8$	3.78E+02	2.72	1500
278	$CH_3 + C3H_8 \leftrightarrow C_3H_7 + CH_4$	9.03E-01	3.65	7154
279	$O + C_3H_7 \leftrightarrow C_2H_5 + CH_2O$	9.64E+13	0	0
280	$H + C_3H_7 \leftrightarrow CH_3 + C_2H_5$	4.06E+06	2.19	890
281	$OH + C_3H_7 \leftrightarrow C_2H_5 + CH_2OH$	2.41E+13	0	0
282	$HO_2 + C_3H_7 \leftrightarrow O_2 + C3H_8$	2.55E+10	0.255	-943
283	$HO_2 + C_3H_7 \rightarrow OH + C_2H_5 + CH_2O$	2.41E+13	0	0
284	$CH_3 + C_3H_7 \leftrightarrow 2C_2H_5$	1.93E+13	-0.32	0
285	$2O + M \leftrightarrow O_2 + M$	1.20E+17	-1	0
	$H_2/2.40/H_2O/15.40/CH_4/2.00/CO/1.75/CO_2/3.60/C_2H_6/3.00/AR/0.83/$			
286	$O + H + M \leftrightarrow OH + M$	5.00E+17	-1	0
	$H_2/2.00/H_2O/6.00/CH_4/2.00/CO/1.50/CO_2/2.00/C_2H_6/3.00/AR/0.70/$			
287	$H + O_2 + M \leftrightarrow HO_2 + M$	2.80E+18	-0.86	0
	$O_2/0.00/H_2O/0.00/CO/0.75/CO_2/1.50/C_2H_6/1.50/N_2/0.00/AR/0.00/$			
288	$2H + M \leftrightarrow H_2 + M$	1.00E+18	-1	0
	$H_2/0.00/H_2O/0.00/CH_4/2.00/CO_2/0.00/C_2H_6/3.00/AR/0.63/$			
289	$H + OH + M \leftrightarrow H_2O + M$	2.20E+22	-2	0
	$H_2/0.73/H_2O/3.65/CH_4/2.00/C_2H_6/3.00/AR/0.38/$			
290	$HCO + M \leftrightarrow H + CO + M$	1.87E+17	-1	17000
	$H_2/2.00/H_2O/0.00/CH_4/2.00/CO/1.50/CO_2/2.00/C_2H_6/3.00/$			
291	$NO + O + M \leftrightarrow NO_2 + M$	1.06E+20	-1.41	0
	$H_2/2.00/H_2O/6.00/CH_4/2.00/CO/1.50/CO_2/2.00/C_2H_6/3.00/AR/0.70/$			

Continued on next page

No.	Reaction	A	n	E_a
292	$NNH + M \leftrightarrow N_2 + H + M$	1.30E+14	-0.11	4980
	$H_2/2.00/H_2O/6.00/CH_4/2.00/CO/1.50/CO_2/2.00/C_2H_6/3.00/AR/0.70/$			
293	$H + NO + M \leftrightarrow HNO + M$	4.48E+19	-1.32	740
	$H_2/2.00/H_2O/6.00/CH_4/2.00/CO/1.50/CO_2/2.00/C_2H_6/3.00/AR/0.70/$			
294	$NCO + M \leftrightarrow N + CO + M$	3.10E+14	0	54050
	$H_2/2.00/H_2O/6.00/CH_4/2.00/CO/1.50/CO_2/2.00/C_2H_6/3.00/AR/0.70/$			
295	$HCN + M \leftrightarrow H + CN + M$	1.04E+29	-3.3	126600
	$H_2/2.00/H_2O/6.00/CH_4/2.00/CO/1.50/CO_2/2.00/C_2H_6/3.00/AR/0.70/$			
296	$HNCO + M \leftrightarrow NH + CO + M$	1.18E+16	0	84720
	$H_2/2.00/H_2O/6.00/CH_4/2.00/CO/1.50/CO_2/2.00/C_2H_6/3.00/AR/.70/$			
297	$O + CO(+M) \leftrightarrow CO_2(+M)$	1.80E+10	0	2385
	$LOW/$	6.02E+14	0	3000
	$H_2/2.00/O_2/6.00/H_2O/6.00/CH_4/2.00/CO/1.50/CO_2/3.50/C_2H_6/3.00/AR/.50/$			
298	$H + CH_2(+M) \leftrightarrow CH_3(+M)$	6.00E+14	0	0
	$LOW/$	1.04E+26	-2.76	1600
	$TROE/0.5620/91.00/5836.00/8552.00/$			
	$H_2/2.00/H_2O/6.00/CH_4/2.00/CO/1.50/CO_2/2.00/C_2H_6/3.00/AR/.70/$			
299	$H + CH_3(+M) \leftrightarrow CH_4(+M)$	1.39E+16	-0.534	536
	$LOW/$	2.62E+33	-4.76	2440
	$TROE/0.7830/74.00/2941.00/6964.00/$			
	$H_2/2.00/H_2O/6.00/CH_4/3.00/CO/1.50/CO_2/2.00/C_2H_6/3.00/AR/.70/$			
300	$H + HCO(+M) \leftrightarrow CH_2O(+M)$	1.09E+12	0.48	-260
	$LOW/$	2.47E+24	-2.57	425
	$TROE/0.7824/271.00/2755.00/6570.00/$			
	$H_2/2.00/H_2O/6.00/CH_4/2.00/CO/1.50/CO_2/2.00/C_2H_6/3.00/AR/.70/$			
301	$H + CH_2O(+M) \leftrightarrow CH_2OH(+M)$	5.40E+11	0.454	3600
	$LOW/$	1.27E+32	-4.82	6530
	$TROE/0.7187/103.00/1291.00/4160.00/$			
	$H_2/2.00/H_2O/6.00/CH_4/2.00/CO/1.50/CO_2/2.00/C_2H_6/3.00/$			
302	$H + CH_2OH(+M) \leftrightarrow CH_3OH(+M)$	1.06E+12	0.5	86
	$LOW/$	4.36E+31	-4.65	5080
	$TROE/0.600/100.00/90000.0/10000.0/$			

Continued on next page

No.	Reaction	A	n	E_a
	$H_2/2.00/H_2O/6.00/CH_4/2.00/CO/1.50/CO_2/2.00/C_2H_6/3.00/$			
303	$H + CH_3O(+M) \leftrightarrow CH_3OH(+M)$	2.43E+12	0.515	50
	$LOW/$	4.66E+41	-7.44	14080
	$TROE/0.700/100.00/90000.0/10000.00/$			
	$H_2/2.00/H_2O/6.00/CH_4/2.00/CO/1.50/CO_2/2.00/C_2H_6/3.00/$			
304	$H + C_2H(+M) \leftrightarrow C_2H_2(+M)$	1.00E+17	-1	0
	$LOW/$	3.75E+33	-4.8	1900
	$TROE/0.6464/132.00/1315.00/5566.00/$			
	$H_2/2.00/H_2O/6.00/CH_4/2.00/CO/1.50/CO_2/2.00/C_2H_6/3.00/AR/.70/$			
305	$H + C_2H_2(+M) \leftrightarrow C_2H3(+M)$	5.60E+12	0	2400
	$LOW/$	3.80E+40	-7.27	7220
	$TROE/0.7507/98.50/1302.00/4167.00/$			
	$H_2/2.00/H_2O/6.00/CH_4/2.00/CO/1.50/CO_2/2.00/C_2H_6/3.00/AR/.70/$			
306	$H + C_2H3(+M) \leftrightarrow C_2H_4(+M)$	6.08E+12	0.27	280
	$LOW/$	1.40E+30	-3.86	3320
	$TROE/0.7820/207.50/2663.00/6095.00/$			
	$H_2/2.00/H_2O/6.00/CH_4/2.00/CO/1.50/CO_2/2.00/C_2H_6/3.00/AR/.70/$			
307	$H + C_2H_4(+M) \leftrightarrow C_2H_5(+M)$	5.40E+11	0.454	1820
	$LOW/$	6.00E+41	-7.62	6970
	$TROE/0.9753/210.00/984.00/4374.00/$			
	$H_2/2.00/H_2O/6.00/CH_4/2.00/CO/1.50/CO_2/2.00/C_2H_6/3.00/AR/.70/$			
308	$H + C_2H_5(+M) \leftrightarrow C_2H_6(+M)$	5.21E+17	-0.99	1580
	$LOW/$	1.99E+41	-7.08	6685
	$TROE/0.8422/125.00/2219.00/6882.00/$			
	$H_2/2.00/H_2O/6.00/CH_4/2.00/CO/1.50/CO_2/2.00/C_2H_6/3.00/AR/.70/$			
309	$H_2 + CO(+M) \leftrightarrow CH_2O(+M)$	4.30E+07	1.5	79600
	$LOW/$	5.07E+27	-3.42	84350
	$TROE/0.9320/197.00/1540.00/10300.00/$			
	$H_2/2.00/H_2O/6.00/CH_4/2.00/CO/1.50/CO_2/2.00/C_2H_6/3.00/AR/.70/$			
310	$2OH(+M) \leftrightarrow H_2O_2(+M)$	7.40E+13	-0.37	0
	$LOW/$	2.30E+18	-0.9	-1700
	$TROE/0.7346/94.00/1756.00/5182.00/$			

Continued on next page

No.	Reaction	A	n	E_a
	$H_2/2.00/H_2O/6.00/CH_4/2.00/CO/1.50/CO_2/2.00/C_2H_6/3.00/AR/.70/$			
311	$OH + CH_3(+M) \leftrightarrow CH_3OH(+M)$	2.79E+18	-1.43	1330
	$LOW/$	4.00E+36	-5.92	3140
	$TROE/0.4120/195.0/5900.00/6394.00/$			
	$H_2/2.00/H_2O/6.00/CH_4/2.00/CO/1.50/CO_2/2.00/C_2H_6/3.00/$			
312	$CH + CO(+M) \leftrightarrow HCCO(+M)$	5.00E+13	0	0
	$LOW/$	2.69E+28	-3.74	1936
	$TROE/0.5757/237.00/1652.00/5069.00/$			
	$H_2/2.00/H_2O/6.00/CH_4/2.00/CO/1.50/CO_2/2.00/C_2H_6/3.00/AR/.70/$			
313	$CH_2 + CO(+M) \leftrightarrow CH_2CO(+M)$	8.10E+11	0.5	4510
	$LOW/$	2.69E+33	-5.11	7095
	$TROE/0.5907/275.00/1226.00/5185.00/$			
	$H_2/2.00/H_2O/6.00/CH_4/2.00/CO/1.50/CO_2/2.00/C_2H_6/3.00/AR/.70/$			
314	$CH_2(S) + H_2O(+M) \leftrightarrow CH_3OH(+M)$	4.82E+17	-1.16	1145
	$LOW/$	1.88E+38	-6.36	5040
	$TROE/0.6027/208.00/3922.00/10180.0/$			
	$H_2/2.00/H_2O/6.00/CH_4/2.00/CO/1.50/CO_2/2.00/C_2H_6/3.00/$			
315	$2CH_3(+M) \leftrightarrow C_2H_6(+M)$	6.77E+16	-1.18	654
	$LOW/$	3.40E+41	-7.03	2762
	$TROE/0.6190/73.20/1180.00/9999.00/$			
	$H_2/2.00/H_2O/6.00/CH_4/2.00/CO/1.50/CO_2/2.00/C_2H_6/3.00/AR/.70/$			
316	$C_2H_4(+M) \leftrightarrow H_2 + C_2H_2(+M)$	8.00E+12	0.44	86770
	$LOW/$	1.58E+51	-9.3	97800
	$TROE/0.7345/180.00/1035.00/5417.00/$			
	$H_2/2.00/H_2O/6.00/CH_4/2.00/CO/1.50/CO_2/2.00/C_2H_6/3.00/AR/.70/$			
317	$N_2O(+M) \leftrightarrow N_2 + O(+M)$	7.91E+10	0	56020
	$LOW/$	6.37E+14	0	56640
	$H_2/2.00/H_2O/6.00/CH_4/2.00/CO/1.50/CO_2/2.00/C_2H_6/3.00/AR/.625/$			
318	$H + HCN(+M) \leftrightarrow H_2CN(+M)$	3.30E+13	0	0
	$LOW/$	1.40E+26	-3.4	1900
	$H_2/2.00/H_2O/6.00/CH_4/2.00/CO/1.50/CO_2/2.00/C_2H_6/3.00/AR/.70/$			
319	$CH + N_2(+M) \leftrightarrow HCNN(+M)$	3.10E+12	0.15	0

Continued on next page

No.	Reaction	A	n	E_a
	$LOW/$	1.30E+25	-3.16	740
	$TROE/0.6670/235.00/2117.00/4536.00/$			
	$H_2/2.00/H_2O/6.00/CH_4/2.00/CO/1.50/CO_2/2.00/C_2H_6/3.00/AR/1.0/$			
320	$CH + H_2(+M) \leftrightarrow CH_3(+M)$	1.97E+12	0.43	-370
	$LOW/$	4.82E+25	-2.8	590
	$TROE/0.578/122.0/2535.0/9365.0/$			
	$H_2/2.00/H_2O/6.00/CH_4/2.00/CO/1.50/CO_2/2.00/C_2H_6/3.00/AR/.70/$			
321	$H + CH_2CO(+M) \leftrightarrow CH_2CHO(+M)$	4.87E+11	0.422	-1755
	$LOW/$	1.01E+42	-7.63	3854
	$TROE/0.465/201.0/1773.0/5333.0/$			
	$H_2/2.00/H_2O/6.00/CH_4/2.00/CO/1.50/CO_2/2.00/C_2H_6/3.00/AR/.70/$			
322	$CH_3 + C_2H_5(+M) \leftrightarrow C3H_8(+M)$	9.43E+12	0	0
	$LOW/$	2.71E+74	-16.82	13065
	$TROE/0.1527/291.0/2742.0/7748.0/$			
	$H_2/2.00/H_2O/6.00/CH_4/2.00/CO/1.50/CO_2/2.00/C_2H_6/3.00/AR/.70/$			
323	$CH_3 + C_2H_4(+M) \leftrightarrow C_3H_7(+M)$	2.55E+06	1.6	5700
	$LOW/$	3.00E+63	-14.6	18170
	$TROE/0.1894/277.0/8748.0/7891.0/$			
	$H_2/2.00/H_2O/6.00/CH_4/2.00/CO/1.50/CO_2/2.00/C_2H_6/3.00/AR/.70/$			
324	$H + C_3H_7(+M) \leftrightarrow C3H_8(+M)$	3.61E+13	0	0
	$LOW/$	4.42E+61	-13.545	11357
	$TROE/0.315/369.0/3285.0/6667.0/$			
	$H_2/2.00/H_2O/6.00/CH_4/2.00/CO/1.50/CO_2/2.00/C_2H_6/3.00/AR/.70/$			
325	$H + CH_2O(+M) \leftrightarrow CH_3O(+M)$	5.40E+11	0.454	2600
	$LOW/$	2.20E+30	-4.8	5560
	$TROE/0.7580/94.00/1555.00/4200.00/$			
	$H_2/2.00/H_2O/6.00/CH_4/2.00/CO/1.50/CO_2/2.00/C_2H_6/3.00$			

Table A.2: C1 reaction mechanism

No.	Reaction	A	n	E_a
1	$H + O_2 = O + OH$	3.55E+15	-0.46	1.66E+04
2	$O + H_2 = H + OH$	5.08E+04	2.67	6.29E+03
3	$H_2 + OH = H_2O + H$	2.16E+08	1.51	3.43E+03
4	$O + H_2O = OH + OH$	2.97E+06	2.02	1.34E+04
5	$H_2 + M = H + H + M$	4.58E+19	-1.4	1.04E+05
	$H_2/2.5/H_2O/12/CO/1.9/CO_2/3.8/AR/0.0/HE/0.0/$			
7	$H_2 + AR = H + H + AR$	5.84E+18	-1.1	1.04E+05
8	$H_2 + HE = H + H + HE$	5.84E+18	-1.1	1.04E+05
9	$O + O + M = O_2 + M$	6.17E+15	-0.5	0.00E+00
	$H_2/2.5/H_2O/12/AR/0.0/HE/0.0/CO/1.9/CO_2/3.8/$			
10	$O + O + AR = O_2 + AR$	1.89E+13	0	-1.79E+03
11	$O + O + HE = O_2 + HE$	1.89E+13	0	-1.79E+03
12	$O + H + M = OH + M$	4.71E+18	-1	0.00E+00
	$H_2/2.5/H_2O/12/AR/0.75/HE/0.75/CO/1.9/CO_2/3.8/$			
13	$H + OH + M = H_2O + M$	3.80E+22	-2	0.00E+00
	$H_2/2.5/H_2O/12/AR/0.38/HE/0.38/CO/1.9/CO_2/3.8/$			
14	$H + O_2(+M) = HO_2(+M)$	1.48E+12	0.6	0.00E+00
	$LOW/$	6.37E+20	-1.72	5.25E+02
	$TROE/0.8/1E-30/1E+30/$			
	$H_2/2.0/H_2O/11./O_2/0.78/CO/1.9/CO_2/3.8/$			
15	$HO_2 + H = H_2 + O_2$	1.66E+13	0	8.23E+02
16	$HO_2 + H = OH + OH$	7.08E+13	0	2.95E+02
17	$HO_2 + O = O_2 + OH$	3.25E+13	0	0.00E+00
18	$HO_2 + OH = H_2O + O_2$	2.89E+13	0	-4.97E+02
19	$HO_2 + HO_2 = H_2O_2 + O_2$	4.20E+14	0	1.20E+04
20	$HO_2 + HO_2 = H_2O_2 + O_2$	1.30E+11	0	-1.63E+03
21	$H_2O_2(+M) = OH + OH(+M)$	2.95E+14	0	4.84E+04
	$LOW/$	1.20E+17	0	4.55E+04
	$TROE/0.5/1E-30/1E+30/$			
	$H_2/2.5/H_2O/12/CO/1.9/CO_2/3.8/AR/0.64/HE/0.64/$			

Continued on next page

No.	Reaction	A	n	E_a
22	$H_2O_2 + H = H_2O + OH$	2.41E+13	0	3.97E+03
23	$H_2O_2 + H = HO_2 + H_2$	4.82E+13	0	7.95E+03
24	$H_2O_2 + O = OH + HO_2$	9.55E+06	2	3.97E+03
25	$H_2O_2 + OH = HO_2 + H_2O$	1.00E+12	0	0.00E+00
26	$H_2O_2 + OH = HO_2 + H_2O$	5.80E+14	0	9.56E+03
27	$CO + O(+M) = CO_2(+M)$	1.80E+10	0	2.38E+03
	$LOW/$	1.55E+24	-2.79	4.19E+03
	$H_2/2.5/H_2O/12/CO/1.9/CO_2/3.8/AR/0.87/$			
28	$CO + O_2 = CO_2 + O$	2.53E+12	0	4.77E+04
29	$CO + HO_2 = CO_2 + OH$	1.57E+05	2.18	1.79E+04
30	$CO + OH = CO_2 + H$	2.23E+05	1.89	-1.16E+03
31	$HCO + M = H + CO + M$	4.75E+11	0.659	1.49E+04
	$H_2/2.5/H_2O/12/CO/1.9/CO_2/3.8/$			
32	$HCO + O_2 = CO + HO_2$	7.58E+12	0	4.10E+02
33	$HCO + H = CO + H_2$	7.23E+13	0	0.00E+00
34	$HCO + O = CO + OH$	3.02E+13	0	0.00E+00
35	$HCO + OH = CO + H_2O$	3.02E+13	0	0.00E+00
36	$HCO + O = CO_2 + H$	3.00E+13	0	0.00E+00
37	$HCO + HO_2 = CO_2 + OH + H$	3.00E+13	0	0.00E+00
38	$HCO + HCO = H_2 + CO + CO$	3.00E+12	0	0.00E+00
39	$HCO + CH_3 = CO + CH_4$	1.20E+14	0	0.00E+00
40	$HCO + HCO = CH_2O + CO$	3.00E+13	0	0.00E+00
41	$CH_2O + M = HCO + H + M$	3.30E+39	-6.3	9.99E+04
	$H_2/2.5/H_2O/12.0/CO/1.9/CO_2/3.8/AR/0.7/$			
42	$CH_2O + M = CO + H_2 + M$	3.10E+45	-8	9.75E+04
	$H_2/2.5/H_2O/12.0/CO/1.9/CO_2/3.8/AR/0.7/$			
43	$CH_2O + H = HCO + H_2$	5.74E+07	1.9	2.75E+03
44	$CH_2O + O = HCO + OH$	1.81E+13	0	3.08E+03
45	$CH_2O + OH = HCO + H_2O$	3.43E+09	1.18	-4.47E+02
46	$CH_2O + O_2 = HCO + HO_2$	1.23E+06	3	5.20E+04
47	$CH_2O + HO_2 = HCO + H_2O_2$	4.11E+04	2.5	1.02E+04
48	$CH_2O + CH_3 = HCO + CH_4$	3.64E-06	5.42	9.98E+02

Continued on next page

No.	Reaction	A	n	E_a
49	$CH_3 + O = CH_2O + H$	8.43E+13	0	0.00E+00
50	$CH_3 + O_2 = CH_3O + O$	1.99E+18	-1.57	2.92E+04
51	$CH_3 + O_2 = CH_2O + OH$	3.74E+11	0	1.46E+04
52	$CH_3 + HO_2 = CH_3O + OH$	2.41E+10	0.76	-2.33E+03
53	$CH_3 + CH_3(+M) = C_2H_6(+M)$	9.21E+16	-1.17	6.36E+02
	$LOW/$	1.14E+36	-5.246	1.71E+03
	$TROE/0.405/1120/69.6/1.E+15/$			
	$H_2/2/H_2O/5/CO/2/CO_2/3/$			
54	$CH_3 + H(+M) = CH_4(+M)$	1.27E+16	-0.63	3.83E+02
	$LOW/$	2.48E+33	-4.76	2.44E+03
	$TROE/0.7830/74.00/2941.00/6964/$			
	$H_2/2.0/H_2O/6.0/CH_4/2.0/CO/1.5/CO_2/2.0/C_2H_6/3.0/AR/0.7/$			
55	$CH_4 + H = CH_3 + H_2$	5.47E+07	1.97	1.12E+04
56	$CH_4 + O = CH_3 + OH$	3.15E+12	0.5	1.03E+04
57	$CH_4 + OH = CH_3 + H_2O$	5.72E+06	1.96	2.64E+03
58	$CH_3 + HO_2 = CH_4 + O_2$	3.16E+12	0	0.00E+00
59	$CH_4 + HO_2 = CH_3 + H_2O_2$	1.81E+11	0	1.86E+04
60	$CH_2OH + M = CH_2O + H + M$	1.00E+14	0	2.51E+04
61	$CH_2OH + H = CH_2O + H_2$	6.00E+12	0	0.00E+00
62	$CH_2OH + H = CH_3 + OH$	9.64E+13	0	0.00E+00
63	$CH_2OH + O = CH_2O + OH$	4.20E+13	0	0.00E+00
64	$CH_2OH + OH = CH_2O + H_2O$	2.40E+13	0	0.00E+00
65	$CH_2OH + O_2 = CH_2O + HO_2$	2.41E+14	0	5.02E+03
66	$CH_2OH + O_2 = CH_2O + HO_2$	1.51E+15	-1	0.00E+00
67	$CH_2OH + HO_2 = CH_2O + H_2O_2$	1.20E+13	0	0.00E+00
68	$CH_2OH + HCO = CH_3OH + CO$	1.00E+13	0	0.00E+00
69	$CH_2OH + HCO = CH_2O + CH_2O$	1.50E+13	0	0.00E+00
70	$2CH_2OH = CH_3OH + CH_2O$	3.00E+12	0	0.00E+00
71	$CH_2OH + CH_3O = CH_3OH + CH_2O$	2.40E+13	0	0.00E+00
72	$CH_3O + M = CH_2O + H + M$	8.30E+17	-1.2	1.55E+04
73	$CH_3O + H = CH_3 + OH$	3.20E+13	0	0.00E+00
74	$CH_3O + O = CH_2O + OH$	6.00E+12	0	0.00E+00

Continued on next page

No.	Reaction	A	n	E_a
75	$CH_3O + OH = CH_2O + H_2O$	1.80E+13	0	0.00E+00
76	$CH_3O + O_2 = CH_2O + HO_2$	9.03E+13	0	1.20E+04
77	$CH_3O + O_2 = CH_2O + HO_2$	2.20E+10	0	1.75E+03
78	$CH_3O + HO_2 = CH_2O + H_2O_2$	3.00E+11	0	0.00E+00
79	$CH_3O + CO = CH_3 + CO_2$	1.60E+13	0	1.18E+04
80	$CH_3O + HCO = CH_3OH + CO$	9.00E+13	0	0.00E+00
81	$2CH_3O = CH_3OH + CH_2O$	6.00E+13	0	0.00E+00
82	$OH + CH_3(+M) = CH_3OH(+M)$	2.79E+18	-1.43	1.33E+03
	$LOW/$	4.00E+36	-5.92	3140
	$TROE/$0.4120/195.0/5900.00/6394.00/			
	$H_2/2.00/H_2O/6.00/CH_4/2.00/CO/1.50/CO_2/2.00/C_2H_6/3.00/$			
83	$H + CH_2OH(+M) = CH_3OH(+M)$	1.06E+12	0.5	8.60E+01
	$LOW/$	4.36E+31	-4.65	5080
	$TROE/$0.600/100.00/90000.0/10000.0/			
	$H_2/2.00/H_2O/6.00/CH_4/2.00/CO/1.50/CO_2/2.00/C_2H_6/3.00/$			
84	$H + CH_3O(+M) = CH_3OH(+M)$	2.43E+12	0.515	5.00E+01
	$LOW/$	4.66E+41	-7.44	14080
	$TROE/$0.700/100.00/90000.0/10000.00/			
	$H_2/2.00/H_2O/6.00/CH_4/2.00/CO/1.50/CO_2/2.00/C_2H_6/3.00/$			
85	$CH_3OH + H = CH_2OH + H_2$	3.20E+13	0	6.10E+03
86	$CH_3OH + H = CH_3O + H_2$	8.00E+12	0	6.10E+03
87	$CH_3OH + O = CH_2OH + OH$	3.88E+05	2.5	3.08E+03
88	$CH_3OH + OH = CH_3O + H_2O$	1.00E+06	2.1	4.97E+02
89	$CH_3OH + OH = CH_2OH + H_2O$	7.10E+06	1.8	-5.96E+02
90	$CH_3OH + O_2 = CH_2OH + HO_2$	2.05E+13	0	4.49E+04
91	$CH_3OH + HCO = CH_2OH + CH_2O$	9.64E+03	2.9	1.31E+04
92	$CH_3OH + HO_2 = CH_2OH + H_2O_2$	3.98E+13	0	1.94E+04
93	$CH_3OH + CH_3 = CH_2OH + CH_4$	3.19E+01	3.17	7.17E+03
94	$CH_3O + CH_3OH = CH_3OH + CH_2OH$	3.00E+11	0	4.06E+03

Table A.3: NI reaction mechanism

No.	Reaction	A	n	E_a
1	$H + O_2 \leftrightarrow O + OH$	2.65E+16	-0.6707	17041
2	$O + H_2 \leftrightarrow H + OH$	3.87E+04	2.7	6260
3	$OH + H_2 \leftrightarrow H + H_2O$	2.16E+08	1.51	3430
4	$OH + OH \leftrightarrow O + H_2O$	3.57E+04	2.4	-2110
5	$H + O_2 + M \leftrightarrow HO_2 + M$	2.80E+18	-0.86	0
	$O_2/.0/H_2O/.0/CO/.75/CO_2/1.50/N_2/.0/AR/.0/HE/.0/$			
6	$H + O_2 + H_2O \leftrightarrow HO_2 + H_2O$	1.13E+19	-0.76	0
7	$H + O_2 + N_2 \leftrightarrow HO_2 + N_2$	2.54E+19	-1.3392	0
8	$H + O_2 + HE \rightarrow HO_2 + HE$	7.00E+17	-0.8	0
9	$H + O_2 + AR \rightarrow HO_2 + AR$	7.00E+17	-0.8	0
10	$H + O_2 + O_2 \leftrightarrow HO_2 + O_2$	2.08E+19	-1.24	0
11	$H + HO_2 \leftrightarrow OH + OH$	8.32E+13	0	635
12	$H + HO_2 \leftrightarrow O_2 + H_2$	4.48E+13	0	1068
13	$OH + HO_2 \leftrightarrow O_2 + H_2O$	1.45E+13	0	-500
14	$OH + HO_2 \leftrightarrow O_2 + H_2O$	5.00E+15	0	17330
15	$H + HO_2 \leftrightarrow O + H_2O$	3.97E+12	0	671
16	$O + HO_2 \leftrightarrow OH + O_2$	2.00E+13	0	0
17	$HO_2 + HO_2 \leftrightarrow O_2 + H_2O_2$	1.30E+11	0	-1630
18	$HO_2 + HO_2 \leftrightarrow O_2 + H_2O_2$	4.20E+14	0	12000
19	$OH + OH(+M) \leftrightarrow H_2O_2(+M)$	7.40E+13	-0.37	0
	$LOW/$	2.30E+18	-0.9	-1700
	$TROE/0.7346/94.00/1756./5182./$			
	$H_2/2.00/H_2O/6.00/CH_4/2.0/CO/1.5/CO_2/2.0/AR/.70/HE/.70/$			
20	$H + H_2O_2 \leftrightarrow OH + H_2O$	1.00E+13	0	3600
21	$OH + H_2O_2 \leftrightarrow HO_2 + H_2O$	1.70E+18	0	29410
22	$OH + H_2O_2 \leftrightarrow HO_2 + H_2O$	2.00E+12	0	427
23	$H + H_2O_2 \leftrightarrow HO_2 + H_2$	1.21E+07	2	5200
24	$O + H_2O_2 \leftrightarrow OH + HO_2$	9.63E+06	2	4000
25	$H + H + M \leftrightarrow H_2 + M$	1.00E+18	-1	0
	$H_2/.0/H_2O/.0/CH_4/2.0/CO_2/.0/AR/.63/HE/.63/$			

Continued on next page

No.	Reaction	A	n	E_a
26	$H + H + H_2 \leftrightarrow H_2 + H_2$	9.00E+16	-0.6	0
27	$H + H + CO_2 \leftrightarrow H_2 + CO_2$	5.50E+20	-2	0
28	$H + H + H_2O \leftrightarrow H_2 + H_2O$	6.00E+19	-1.25	0
29	$H + OH + M \leftrightarrow H_2O + M$	2.20E+22	-2	0
	$H_2/.73/H_2O/3.65/CH_4/2.0/AR/0.38/HE/0.38/$			
30	$O + O + M \leftrightarrow O_2 + M$	1.20E+17	-1	0
	$H_2/2.4/H_2O/15.4/CH_4/2.0/CO/1.75/CO_2/3.6/AR/0.83/HE/0.83/$			
31	$O + H + M \leftrightarrow OH + M$	5.00E+17	-1	0
	$H_2/2.0/H_2O/6.0/CH_4/2.0/CO/1.5/CO_2/2.0/AR/0.7/HE/0.7/$			
32	$OH + CO \leftrightarrow H + CO_2$	4.69E+07	1.228	70
33	$HO_2 + CO \leftrightarrow OH + CO_2$	1.50E+14	0	24544
34	$O + CO(+M) \leftrightarrow CO_2(+M)$	1.80E+10	0	2385
	$LOW/$	6.02E+14	0	3000
	$H_2/2.0/O_2/6.0/H_2O/6.0/CH_4/2./CO/1.5/CO_2/3.5/AR/.5/HE/.5/$			
35	$H + HCO \leftrightarrow H_2 + CO$	7.34E+13	0	0
36	$OH + HCO \leftrightarrow H_2O + CO$	5.00E+13	0	0
37	$HCO + O_2 \leftrightarrow HO_2 + CO$	1.35E+13	0	400
38	$HCO + M \leftrightarrow H + CO + M$	1.87E+17	-1	17000
	$H_2/2.0/H_2O/.0/CH_4/2.0/CO/1.5/CO_2/2.0/$			
39	$HCO + H_2O \leftrightarrow H + CO + H_2O$	1.50E+18	-1	17000
40	$O + HCO \leftrightarrow H + CO_2$	3.00E+13	0	0
41	$O + CH_4 \leftrightarrow OH + CH_3$	1.02E+09	1.5	8600
42	$OH + CH_4 \leftrightarrow CH_3 + H_2O$	1.00E+08	1.6	3120
43	$O + CH_3 \leftrightarrow H + CH_2O$	5.06E+13	0	0
44	$O + CH_3 \rightarrow H + H_2 + CO$	3.37E+13	0	0
45	$O + CH_2O \leftrightarrow OH + HCO$	3.90E+13	0	3540
46	$H + CH_3(+M) \leftrightarrow CH_4(+M)$	1.39E+16	-0.534	536
	$LOW/$	2.62E+33	-4.76	2440
	$TROE/7830.0/74.00/2941.00/6964.00/$			
	$H_2/2.0/H_2O/6.0/CH_4/3.0/CO/1.5/CO_2/2.0/AR/.7/HE/.7/$			
47	$H + CH_4 \leftrightarrow CH_3 + H_2$	6.60E+08	1.62	10840
48	$H + CH_2O \leftrightarrow HCO + H_2$	5.74E+07	1.9	2742

Continued on next page

No.	Reaction	A	n	E_a
49	$OH + CH_2O \leftrightarrow HCO + H_2O$	3.43E+09	1.18	-447

Table A.4: PO reaction mechanism

No.	Reaction	A	n	E_a
1	$H + O_2 \leftrightarrow OH + O$	2.21E+14	0	16650
2	$O + H_2 \leftrightarrow OH + H$	4.33E+13	0	10000
3	$H + O_2(+M) \leftrightarrow HO_2(+M)$	4.65E+12	0.4	0
	$LOW/$	7.00E+17	-0.8	0
	$TROE/0.5000/0.1000E-29/0.1000E+31/$			
	$H_2O/18.00/H_2/2.50/N_2/1.26/AR/.80/HE/.80/O_2/.00/CO/1.20/CO_2/2.40/$			
4	$H + O_2 + O_2 \leftrightarrow HO_2 + O_2$	8.90E+14	0	-2822
5	$OH + HO_2 \leftrightarrow H_2O + O_2$	5.00E+13	0	1000
6	$H + HO_2 \leftrightarrow OH + OH$	2.50E+14	0	1900
7	$O + HO_2 \leftrightarrow O_2 + OH$	3.25E+13	0	0
8	$OH + OH \leftrightarrow O + H_2O$	3.57E+04	2.4	-2110
9	$H_2 + M \leftrightarrow H + H + M$	2.23E+14	0	96081
	$H_2/2.50/H_2O/12.00/AR/.50/HE/.50/CO/1.90/CO_2/3.80/$			
10	$O_2 + M \leftrightarrow O + O + M$	1.55E+14	0	115120
	$H_2/2.50/H_2O/12.00/AR/.20/HE/.20/CO/1.90/CO_2/3.80/$			
11	$H + OH + M \leftrightarrow H_2O + M$	4.50E+22	-2	0
	$H_2O/16.00/H_2/2.00/CO_2/1.90/$			
12	$H + HO_2 \leftrightarrow H_2 + O_2$	2.50E+13	0	700
13	$HO_2 + HO_2 \leftrightarrow H_2O_2 + O_2$	2.11E+12	0	0
14	$OH + OH(+M) \leftrightarrow H_2O_2(+M)$	7.40E+13	-0.37	0
	$LOW/$	2.30E+18	-0.9	-1700
	$TROE/.7346/94.00/1756./5182./$			
	$H_2/2.00/H_2O/6.00/CO/1.50/CO_2/2.00/AR/.70/HE/.70/$			
15	$O + OH + M \leftrightarrow HO_2 + M$	1.00E+16	0	0
16	$O_2 + CO \leftrightarrow CO_2 + O$	2.53E+12	0	47700
17	$O_2 + HCO \leftrightarrow HO_2 + CO$	1.00E+12	0	0
18	$CO + O(+M) \leftrightarrow CO_2(+M)$	9.64E+10	0	3800
	$LOW/$	2.07E+26	-3.34	7610
	$H_2O/12.00/H_2/2.00/CO/1.50/CO_2/2.00/AR/.50/$			
19	$CO + OH \leftrightarrow CO_2 + H$	9.60E+11	0.14	7352

Continued on next page

No.	Reaction	A	n	E_a
20	$CO + OH \leftrightarrow CO_2 + H$	7.32E+10	0.03	-16
21	$CO + HO_2 \leftrightarrow CO_2 + OH$	3.00E+13	0	23000
22	$CO + H_2O \leftrightarrow CO_2 + H_2$	2.00E+11	0	38000
23	$HCO + M \leftrightarrow CO + H + M$	1.20E+17	-1	17000
	$H_2O/5.00/CO_2/3.00/H_2/1.90/CO/1.90/$			
24	$HCO + O \leftrightarrow CO_2 + H$	3.00E+13	0	0
25	$HCO + H \leftrightarrow H_2 + CO$	1.00E+14	0	0
26	$HCO + OH \leftrightarrow H_2O + CO$	5.00E+13	0	0
27	$HCO + HO_2 \leftrightarrow H_2O_2 + CO$	4.00E+11	0	0
28	$HCO + HO_2 \rightarrow H + OH + CO_2$	3.00E+13	0	0
29	$H + H_2O \leftrightarrow H_2 + OH$	4.00E+10	1	19000
30	$H_2O_2 + H \leftrightarrow H_2O + OH$	2.41E+13	0	3970
31	$H_2O_2 + H \leftrightarrow H_2 + HO_2$	6.03E+13	0	7950
32	$HO_2 + H_2O \rightarrow H_2O_2 + OH$	5.39E+05	2	28780.05
33	$OH + H_2O_2 \rightarrow H_2O + HO_2$	3.20E+05	2	-4169.95
34	$O + H_2O_2 \rightarrow OH + HO_2$	1.08E+06	2	-1657.32

Table A.5: DA reaction mechanism

No.	Reaction	A	n	E_a
1	$H + O_2 \leftrightarrow O + OH$	2.65E+16	-0.671	17041
2	$O + H_2 \leftrightarrow H + OH$	3.87E+04	2.7	6260
3	$OH + H_2 \leftrightarrow H + H_2O$	2.16E+08	1.51	3430
4	$OH + OH \leftrightarrow O + H_2O$	3.57E+04	2.4	-2110
5	$H + H + M \leftrightarrow H_2 + M$	1.00E+18	-1	0
	$H_2O/.0/H_2/.0/CO_2/.0/AR/.63/HE/.63/$			
6	$H + H + H_2O \leftrightarrow H_2 + H_2O$	6.00E+19	-1.25	0
7	$H + H + H_2 \leftrightarrow H_2 + H_2$	5.06E+16	-0.6	0
8	$H + H + CO_2 \leftrightarrow H_2 + CO_2$	3.09E+20	-2	0
9	$H + OH + M \leftrightarrow H_2O + M$	2.20E+22	-2	0
	$H_2/2./H_2O/6.3/CO/1.75/CO_2/3.6/AR/0.38/HE/0.38/$			
10	$O + H + M \leftrightarrow OH + M$	4.71E+18	-1	0
	$H_2/2.0/H_2O/12.0/CO/1.75/CO_2/3.6/AR/0.7/HE/0.7/$			
11	$O + O + M \leftrightarrow O_2 + M$	1.20E+17	-1	0
	$H_2/2.4/H_2O/15.4/CO/1.75/CO_2/3.6/AR/0.83/HE/0.83/$			
12	$H + O_2(+M) \leftrightarrow HO_2(+M)$	4.65E+12	0.44	0
	$LOW/$	5.75E+19	-1.4	0
	$TROE/0.5/1E-30/1E+30/$			
	$AR/.53/HE/.53/O_2/.75/H_2O/12.0/CO/1.2/CO_2/2.4/$			
13	$H_2 + O_2 \leftrightarrow HO_2 + H$	7.40E+05	2.433	53502
14	$OH + OH(+M) \leftrightarrow H_2O_2(+M)$	7.40E+13	-0.37	0
	$LOW/$	1.34E+17	-0.584	-2293
	$TROE/0.7346/1756/5182/$			
	$H_2/2.0/H_2O/6.0/CO/1.75/CO_2/3.6/AR/.70/HE/.70/$			
15	$HO_2 + H \leftrightarrow O + H_2O$	3.97E+12	0	671
16	$HO_2 + H \leftrightarrow OH + OH$	7.08E+13	0	295
17	$HO_2 + O \leftrightarrow OH + O_2$	2.00E+13	0	0
18	$HO_2 + OH \leftrightarrow O_2 + H_2O$	2.90E+13	0	-500
19	$HO_2 + OH \leftrightarrow O_2 + H_2O$	1.00E+16	0	17330
20	$HO_2 + HO_2 \leftrightarrow O_2 + H_2O_2$	1.30E+11	0	-1630

Continued on next page

No.	Reaction	A	n	E_a
21	$HO_2 + HO_2 \leftrightarrow O_2 + H_2O_2$	4.20E+14	0	12000
22	$H_2O_2 + H \leftrightarrow HO_2 + H_2$	1.21E+07	0	25200
23	$H_2O_2 + H \leftrightarrow OH + H_2O$	2.41E+13	0	3970
24	$H_2O_2 + O \leftrightarrow OH + HO_2$	9.63E+06	0	23970
25	$H_2O_2 + OH \leftrightarrow HO_2 + H_2O$	2.00E+12	0	427
26	$H_2O_2 + OH \leftrightarrow HO_2 + H_2O$	2.67E+41	0	-737600
27	$CO + O(+M) \leftrightarrow CO_2(+M)$	1.80E+10	0	2384
	$LOW/$	1.55E+24	-2.79	4191
	$TROE/1.0/1E-30/1E+30/$			
	$H_2/2.0/H_2O/12.0/CO/1.75/CO_2/3.6/AR/.7/HE/.7/$			
28	$CO + OH \leftrightarrow CO_2 + H$	9.60E+11	0.14	7352
29	$CO + OH \leftrightarrow CO_2 + H$	7.32E+10	0.03	-16
30	$CO + O_2 \leftrightarrow CO_2 + O$	2.53E+12	0	47700
31	$CO + HO_2 \leftrightarrow CO_2 + OH$	3.01E+13	0	23000
32	$HCO + H \leftrightarrow CO + H_2$	1.20E+14	0	0
33	$HCO + O \leftrightarrow CO + OH$	3.00E+13	0	0
34	$HCO + O \leftrightarrow CO_2 + H$	3.00E+13	0	0
35	$HCO + OH \leftrightarrow CO + H_2O$	3.02E+13	0	0
36	$HCO + M \leftrightarrow CO + H + M$	9.35E+16	-1	17000
	$H_2O/12.0/H_2/2.0/CO/1.75/CO_2/3.6/$			
37	$HCO + O_2 \leftrightarrow CO + HO_2$	1.20E+10	0.807	-727

Table A.6: BO reaction mechanism

No.	Reaction	A	n	E_a
1	$H + O_2 \rightarrow OH + O$	3.52E+16	-0.7	17058
2	$OH + O \rightarrow H + O_2$	7.04E+13	-0.26	143.3
3	$O + H_2 \rightarrow OH + H$	5.06E+04	2.67	6286.4
4	$OH + H \rightarrow O + H_2$	3.03E+04	2.63	4831.9
5	$H_2 + OH \rightarrow H + H_2O$	1.17E+09	1.3	3632.8
6	$H + H_2O \rightarrow H_2 + OH$	1.28E+10	1.19	18689.7
7	$H + O_2(+M) \rightarrow HO_2(+M)$	4.65E+12	0.44	0
	$LOW/$	5.75E+19	-1.4	0
	$TROE/0.5/1E-30/1E+30/$			
	$H_2O/16.00/H_2/2.50/AR/.70/HE/.70/CO/1.20/CO_2/2.40/$			
8	$HO_2 + H \rightarrow OH + OH$	7.08E+13	0	293.78
9	$HO_2 + H \rightarrow H_2 + O_2$	1.66E+13	0	821.63
10	$H_2 + O_2 \rightarrow HO_2 + H$	2.69E+12	0.36	55378.8
11	$OH + HO_2 \rightarrow H_2O + O_2$	2.89E+13	0	-496.8
12	$H + OH + M \rightarrow H_2O + M$	4.00E+22	-2	0
	$H_2O/12.00/H_2/2.50/CO_2/3.80/CO/1.90/AR/0.38/HE/0.38/$			
13	$H_2O + M \rightarrow H + OH + M$	1.03E+23	-1.75	118501
	$H_2O/12.00/H_2/2.50/CO_2/3.80/CO/1.90/AR/0.38/HE/0.38/$			
14	$H + H + M \rightarrow H_2 + M$	1.30E+18	-1	0
	$H_2/2.50/H_2O/12.00/AR/.50/HE/.50/CO/1.90/CO_2/3.80/$			
15	$H_2 + M \rightarrow H + H + M$	3.04E+17	-0.65	103441.8
	$H_2/2.50/H_2O/12.00/AR/.50/HE/.50/CO/1.90/CO_2/3.80/$			
16	$HO_2 + HO_2 \rightarrow H_2O_2 + O_2$	3.02E+12	0	1385.3
	$HO_2 + H_2 \rightarrow H_2O_2 + H$	1.62E+11	0.61	23918
17	$H_2O_2(+M) \rightarrow OH + OH(+M)$	2.62E+19	-1.39	51289.8
	$LOW/$	8.15E+23	-1.9	49589.2
	$TROE/0.735/94/1756/5182/$			
	$H_2/2.00/H_2O/6.00/CO/1.50/CO_2/2.00/AR/.40/HE/.40/$			
18	$CO + OH \rightarrow CO_2 + H$	4.40E+06	1.5	-740.42
19	$CO_2 + H \rightarrow CO + OH$	2.41E+13	0.22	24983.3/

Continued on next page

No.	Reaction	A	n	E_a
20	$CO + HO_2 \rightarrow CO_2 + OH$	6.03E+13	0	22929.2
21	$HCO + M \rightarrow CO + H + M$	1.86E+17	-1	16989.1
22	$H_2O/12.00/CO_2/2.50/H_2/1.90/CO/2.50/$			
23	$CO + H + M \rightarrow HCO + M$	3.51E+16	-0.77	1277.83/
	$H_2O/12.00/CO_2/2.50/H_2/1.90/CO/2.50/$			
24	$HCO + H \rightarrow CO + H_2$	5.00E+13	0	0

Table A.7: SL reaction mechanism

No.	Reaction	A	n	E_a
1	$O + H_2 \rightarrow H + OH$	3.87E+04	2.7	6302
2	$H + OH \rightarrow O + H_2$	2.91E+04	2.64	4472
3	$O + HO_2 \rightarrow OH + O_2$	2.00E+13	0	0
4	$H + O_2 + M \rightarrow HO_2 + M$	3.50E+16	-0.41	-1116
5	$H + O_2 \rightarrow O + OH$	2.65E+16	-0.67	17152
6	$O + OH \rightarrow H + O_2$	6.96E+13	-0.27	-216
7	$H + H + H_2O \rightarrow H_2 + H_2O$	6.00E+19	-1.25	0
8	$H + OH + M \rightarrow H_2O + M$	2.20E+22	-1.95	0
	$H_2O/3.5/CO/.75/CO_2/2.5/O_2/.5/$			
9	$H + HO_2 \rightarrow O + H_2O$	3.97E+12	0	676
10	$H + HO_2 \rightarrow O_2 + H_2$	4.48E+13	0	1076
11	$H + HO_2 \rightarrow OH + OH$	8.40E+13	0	640
12	$H + HCO \rightarrow H_2 + CO$	7.34E+13	0	0
13	$OH + H_2 \rightarrow H + H_2O$	2.16E+08	1.51	3452
14	$OH + OH \rightarrow O + H_2O$	3.57E+04	2.4	-2124
15	$O + H_2O \rightarrow OH + OH$	4.49E+06	2.1	15954
16	$OH + CO \rightarrow H + CO_2$	1.30E+07	1.3	-760
17	$H + CO_2 \rightarrow OH + CO$	8.38E+13	0.02	25562
18	$HCO + M \rightarrow H + CO + M$	1.87E+17	-1	17112
	$H_2O/3.5/CO/.75/CO_2/2.5/O_2/.5/$			
19	$H + CO + M \rightarrow HCO + M$	1.18E+15	-0.35	254
	$H_2O/3.5/CO/.75/CO_2/2.5/O_2/.5/$			
20	$HCO + O_2 \rightarrow HO_2 + CO$	1.35E+13	0	402

Table A.8: JL reaction mechanism

No.	Reaction	A	n	E_a
1	$CO + H_2O \leftrightarrow CO_2 + H_2$	2.63E+13	0	18500
2	$H_2 + 0.5O_2 \rightarrow H_2O$	1.05E+17	-1	37700
	$FORD/H_2/.33/$			
	$FORD/O_2/1.4/$			
3	$H_2O + H_2 + O_2 \rightarrow 2H_2 + 1.5O_2$	1.90E+23	-0.877	94000
	$FORD/H_2O/1/$			
	$FORD/H_2/.75/$			
	$FORD/O_2/1/$			

Table A.9: WO reaction mechanism

No.	Reaction	A	n	E_a
1	$H_2 + 0.5O_2 \leftrightarrow H_2O$	1.21E+18	-1	40000
2	$H_2O + CO + 0.5O_2 \rightarrow H_2O + CO_2$	3.98E+14	0	40000
	$FORD/H_2O/0.5/$			
	$FORD/O_2/0.25/$			
	$FORD/CO/1.0/$			
3	$CO + H_2O \leftrightarrow CO_2 + H_2$	2.75E+12	0	20000

APPENDIX B

CANTERA CODES

B.1 Adiabatic Flame Temperature

The following MATLAB script gives an example for the calculation and plotting of the adiabatic flame temperature as a function of equivalence ratio.

```
% SYNGAS - Adiabatic Flame Temperature

% This script simulates the adiabatic flame temperature for

% syngas-air mixture


help syngasTad


clear all;

clc;

clf;
```

```
figure(1)

alph = [0.05 0.25 0.5 0.75 0.95];

phi = 0.5:0.1:2.0;


gas = IdealGasMix('Syngas_JL_Glob_Opt.cti');

kH2 = speciesIndex(gas, 'H2');

kCO = speciesIndex(gas, 'CO');

kO2 = speciesIndex(gas, 'O2');

kN2 = speciesIndex(gas, 'N2');

X = zeros(nSpecies(gas),1);

Tad = zeros(size(phi'));


for i=1:length(alph)

    X(kH2) = alph(i);

    X(kCO) = 1-alph(i);

    for j=1:length(phi)

        a = 1/(2*phi(j));

        X(kO2)= 1/(2*phi(j));

        X(kN2)= (1/(2*phi(j)))*3.76;

        set(gas, 'T', 300, 'P', 30*oneatm, 'X', X);

        equilibrate(gas, 'HP');

        Tad(j) = temperature(gas);

    end
```

```
        if i==1, color='k';
        xlswrite('JL_Tad_95CO_30atm_300K',Tad);
        end;
    if i==2, color='b';
        xlswrite('JL_Tad_75CO_30atm_300K' ,Tad);
        end;
    if i==3, color='r';
        xlswrite('JL_Tad_50CO_30atm_300K' ,Tad);
        end;
    if i==4, color='y';
        xlswrite('JL_Tad_25CO_30atm_300K' ,Tad);
        end;
    if i==5, color='g';
        xlswrite('JL_Tad_5CO_30atm_300K'  ,Tad);
        end;

    plot(phi, Tad, color, 'linewidth', 0.5);
    grid on
    hold on
end

legend('95% CO','75% CO', '50% CO','25% CO', '5% CO');
```

B.2 Laminar Flame Speed

The following PYTHON script gives an example for the calculation of the laminar flame speed.

```python
# ADIABATIC_FLAME - A freely-propagating, premixed syngas/air
#    flat flame with mixture-averaged transport properties

from Cantera import *
from Cantera.OneD import *
from Cantera.OneD.FreeFlame import FreeFlame

##############################################################
#
# parameter values
#
p          =   OneAtm               # pressure
tin        =   300.0                # unburned gas temperature
mdot       =   0.04                 # kg/m^2/s

comp       =  'H2:0.001, CO:0.999, O2:0.5, N2:1.88'
# premixed gas composition

initial_grid = [0.0, 0.001, 0.01, 0.02, 0.029, 0.03]
```

```
tol_ss    = [1.0e-5, 1.0e-9]  # [rtol atol] for steady-state
                              # problem
tol_ts    = [1.0e-5, 1.0e-9]  # [rtol atol] for time stepping

loglevel  = 1                 # amount of diagnostic output (0
                              # to 5)

refine_grid = 1               # 1 to enable refinement, 0 to
                              # disable


gas = IdealGasMix('c1.cti')

# set its state to that of the unburned gas
gas.setState_TPX(tin, p, comp)

f = FreeFlame(gas = gas, grid = initial_grid, tfix = 600.0)

# set the upstream properties
f.inlet.set(mole_fractions = comp, temperature = tin)

f.set(tol = tol_ss, tol_time = tol_ts)
f.showSolution()
```

```
f.set(energy = 'off')
f.setRefineCriteria(ratio = 10.0, slope = 1, curve = 1)
f.setMaxJacAge(50, 50)
f.setTimeStep(1.0e-5, [1, 2, 5, 10, 20])

f.solve(loglevel, refine_grid)
f.save('adiabatic_flame.xml','no_energy',
       'solution with the energy equation disabled')

f.set(energy = 'on')
f.setRefineCriteria(ratio = 3.0, slope = 0.1, curve = 0.2)
f.solve(loglevel, refine_grid)
f.save('adiabatic_flame.xml','energy',
       'solution with the energy equation enabled')
print 'mixture-averaged flamespeed = ',f.u()[0]*100

# write the velocity, temperature, density, and mole fractions
# to a CSV file
z = f.flame.grid()
T = f.T()
u = f.u()
V = f.V()
fcsv = open('C1_syngas_0.5_300K_40atm_75-25_H2-CO_FS.csv','w')
```

```
writeCSV(fcsv, ['z (m)', 'u (m/s)', 'V (1/s)', 'T (K)',
 'rho (kg/m3)']
             + list(gas.speciesNames()))
for n in range(f.flame.nPoints()):
    f.setGasState(n)
    writeCSV(fcsv, [z[n], u[n], V[n], T[n], gas.density()]
             +list(gas.moleFractions()))
fcsv.close()

print 'solution saved to adiabatic_flame.csv'

f.showStats()
```

B.3 NO Emissions

The following MATLAB script gives an example for the calculation and plotting of the NO mole fraction as a function of equivalence ratio.

```
% SYNGAS - NOx Emissions
% This script simulates the NOx emissions for syngas-air
% mixture in a well stirred reactor


help NO_Emissions_WSR


clear all;
clc;


r = 25e-2;
vol_d = 4/3*pi*r^3;
alpha = 0.95;


%Initilization
gas1 = IdealGasMix('Syngas_Slavinskaya_NO.cti');
gas2 = IdealGasMix('Syngas_Slavinskaya_NO.cti');
gas3 = IdealGasMix('Syngas_Slavinskaya_NO.cti');
gas4 = IdealGasMix('Syngas_Slavinskaya_NO.cti');
kO2 = speciesIndex(gas3,'O2');
```

```
kCO = speciesIndex(gas3,'CO');

kH2 = speciesIndex(gas3,'H2');

kCO2 = speciesIndex(gas3,'CO2');

kN2 = speciesIndex(gas3,'N2');

kNO = speciesIndex(gas3,'NO');


phi = 0.5:0.1:2.0;


for i=1:length(phi)


X3 = zeros(nSpecies(gas3),1);

X3(kO2) = 0.5;

X3(kN2) = 0.5*3.76;

X3(kCO) = (1-alpha)*phi(i);

X3(kH2) = alpha*phi(i);


set(gas1,'T',300,'P',1*oneatm,'X',X3);

set(gas2,'T',300,'P',1*oneatm,'X',X3);

set(gas3,'T',300,'P',1*oneatm,'X',X3);


equilibrate(gas2,'HP');

equilibrate(gas3,'HP');


for vol = 5*vol_d:-vol_d:vol_d;
```

```
R = 8.314;

Tres=20;

density = pressure(gas1)*meanMolecularWeight(gas1)*10^-3/

        (R*temperature(gas1));

mdot=100*density*vol/Tres;


inlet = Reservoir(gas1);

outlet = Reservoir(gas3);

r1 = Reactor(gas2);

setInitialVolume(r1, vol);

mfc = MassFlowController(inlet, r1);

setMassFlowRate(mfc, mdot);

v = Valve(r1, outlet);

setValveCoeff(v, 10);


T = []; Y = []; X = [];

n = ReactorNet({inlet,r1,outlet});

setMaxTimeStep(n,1000);

setTolerances(n, 1e-11, 1e-22);


meanMolecularWeight(gas1);


advance(n, Tres);
```

```
T = temperature(r1);
Y = massFractions(r1);
set(gas4,'Y',Y);
X = moleFractions(gas4);

end

figure(1)
plot(phi(i),T,'-ro')
xlabel('Eq Ratio','FontSize',16)
ylabel('Temperature (K)','FontSize',16)
hold on;

figure(2)
plot(phi(i),X([kNO],:),'-r*','linewidth',2)
names = speciesNames(gas4);
legend(names([kNO]))
xlabel('Eq Ratio','FontSize',16)
ylabel('Mole Fraction','FontSize',16)
hold on;

if i==1,
xlswrite('Slavinskaya_NO_95H2_1atm_300K',X([kNO]),'A1:A1');
end
```

```
if i==2,
xlswrite('Slavinskaya_NO_95H2_1atm_300K',X([kNO]),'A2:A2');
end
if i==3,
xlswrite('Slavinskaya_NO_95H2_1atm_300K',X([kNO]),'A3:A3');
end
if i==4,
xlswrite('Slavinskaya_NO_95H2_1atm_300K',X([kNO]),'A4:A4');
end
if i==5,
xlswrite('Slavinskaya_NO_95H2_1atm_300K',X([kNO]),'A5:A5');
end
if i==6,
xlswrite('Slavinskaya_NO_95H2_1atm_300K',X([kNO]),'A6:A6');
end
if i==7,
xlswrite('Slavinskaya_NO_95H2_1atm_300K',X([kNO]),'A7:A7');
end
if i==8,
xlswrite('Slavinskaya_NO_95H2_1atm_300K',X([kNO]),'A8:A8');
end
if i==9,
xlswrite('Slavinskaya_NO_95H2_1atm_300K',X([kNO]),'A9:A9');
end
```

```
if i==10,
xlswrite('Slavinskaya_NO_95H2_1atm_300K',X([kNO]),'A10:A10');
end
if i==11,
xlswrite('Slavinskaya_NO_95H2_1atm_300K',X([kNO]),'A11:A11');
end
if i==12,
xlswrite('Slavinskaya_NO_95H2_1atm_300K',X([kNO]),'A12:A12');
end
if i==13,
xlswrite('Slavinskaya_NO_95H2_1atm_300K',X([kNO]),'A13:A13');
end
if i==14,
xlswrite('Slavinskaya_NO_95H2_1atm_300K',X([kNO]),'A14:A14');
end
if i==15,
xlswrite('Slavinskaya_NO_95H2_1atm_300K',X([kNO]),'A15:A15');
end
if i==16,
xlswrite('Slavinskaya_NO_95H2_1atm_300K',X([kNO]),'A16:A16');
end

figure(3)
plot(phi(i),X([kCO],:),'-r*','linewidth',2)
```

```
names = speciesNames(gas4);

legend(names([kCO]))

xlabel('Eq Ratio','FontSize',16)

ylabel('Mole Fraction','FontSize',16)

hold on;


end
```

REFERENCES

[1] M. Escudero, A. Jimenez, C. Gonzalez, and I. Lopez. “Quantitative analysis of potential power production and environmental benefits of Biomass Integrated Gasification Combined Cycles in the European Union”. In: *Energy Policy* 53.0 (2013), pp. 63 –75.

[2] A. Rovira, M.J. Montes, F. Varela, and M. Gil. “Comparison of Heat Transfer Fluid and Direct Steam Generation technologies for Integrated Solar Combined Cycles”. In: *Applied Thermal Engineering* 52.2 (2013), pp. 264 –274.

[3] A.A. Eter, E.J. Sheu, A. Mitsos, E.M. Mokheimer, M.A. Habib, and A. Al-Qutub. “A Review of Hybrid Solar-Fossil Fuel Power Generation Systems and Performance Metircs”. In: *Journal of Solar Energy Engineering* 134 (2012).

[4] L.J. Shadle, D.A. Berry, and M. Syamlal. “Coal Conversion Processes, Gasification”. In: *Kirk-Othmer Encyclopedia of Chemical Technology.* John Wiley & Sons, Inc., 2000.

[5] G.A. Richards and K.H. Casleton. “Gasification technology to produce synthesis gas”. In: *Synthesis Gas Combustion Fundamentals and Applications.* Ed. by T. Lieuwen, V. Yang, and R. Yetter. 2010.

[6] S. Lee. “Concepts in Syngas Manufacture. By Jens Rostrup-Nielsen and Lars J. Christiansen”. In: *Energy Technology* 1.7 (2013), pp. 419–420.

[7] R.A. Yetter, F.L. Dryer, and H. Rabitz. “A Comprehensive Reaction Mechanism For Carbon Monoxide/Hydrogen/Oxygen Kinetics”. In: *Combustion Science and Technology* 79.1-3 (1991a), pp. 97–128.

[8] F.L. Dryer, M. Chaos, M.P. Burke, and Y. Ju. “Syngas Chemical Kinetics And Reaction Mechanisms”. In: *Synthesis Gas Combustion.* CRC Press, Sept. 2009, pp. 29 –70.

[9] S.G. Davis, A.V. Joshi, H. Wang, and F. Egolfopoulos. “An optimized kinetic model of $H_2/COcombustion$”. In: *Proceedings of the Combustion Institute* 30.1 (2005), pp. 1283 –1292.

[10] P. Saxena and F.A. Williams. “Testing a small detailed chemical-kinetic mechanism for the combustion of hydrogen and carbon monoxide”. In: *Combustion and Flame* 145 (2006), pp. 316 –323.

[11] H. Sun, S.I. Yang, G. Jomaas, and C.K. Law. “High-pressure laminar flame speeds and kinetic modeling of carbon monoxide/hydrogen combustion”. In: *Proceedings of the Combustion Institute* 31.1 (2007), pp. 439 –446.

[12] J. Li, Z. Zhao, A. Kazakov, M. Chaos, F.L. Dryer, and J.J. Scire. "A comprehensive kinetic mechanism for CO, CH2O, and CH3OH combustion". In: *International Journal of Chemical Kinetics* 39.3 (2007), pp. 109–136.

[13] A. Frassoldati, T. Faravelli, and E. Ranzi. "The ignition, combustion and flame structure of carbon monoxide/hydrogen mixtures. Note 1: Detailed kinetic modeling of syngas combustion also in presence of nitrogen compounds". In: *International Journal of Hydrogen Energy* 32.15 (2007). International Symposium on Solar-Hydrogen-Fuel Cells 2005, pp. 3471 –3485.

[14] O. Skreiberg, P. Kilpinen, and P. Glarborg. "Ammonia chemistry below 1400K under fuel-rich conditions in a flow reactor". In: *Combustion and Flame* 136.4 (2004), pp. 501 –518.

[15] A. Cuoci, A. Frassoldati, G.B. Ferraris, T. Faravelli, and E. Ranzi. "The ignition, combustion and flame structure of carbon monoxide/hydrogen mixtures. Note 2: Fluid dynamics and kinetic aspects of syngas combustion". In: *International Journal of Hydrogen Energy* 32.15 (2007). International Symposium on Solar-Hydrogen-Fuel Cells 2005, pp. 3486 –3500.

[16] N. Slavinskaya, M. Braun-Unkhoff, and P. Frank. "Reduced Reaction Mechanisms for Methane and Syngas Combustion in Gas Turbines". In: *Journal of Engineering for Gas Turbines and Power* 130.2 (2008), pp. 021504 –021509.

[17] A. Cuoci, A. Frassoldati, T. Faravelli, and E. Ranzi. "Accuracy and Flexibility of Simplified Kinetic Models for cfd applications". In: *Combustion*

Colloquia, Universitadegli Studi di Napoli Federico II, April. 2009, pp. 26–28.

[18] A.M. Starik, N.S. Titova, A.S. Sharipov, and V.E. Kozlov. “Syngas Oxidation Mechanism”. English. In: *Combustion, Explosion, and Shock Waves* 46.5 (2010), pp. 491 –506.

[19] P. Boivin, C. Jimenez, A.L. Sanchez, and F.A. Williams. “A four-step reduced mechanism for syngas combustion”. In: *Combustion and Flame* 158.6 (2011), pp. 1059 –1063.

[20] Z.M. Nikolaou, J.Y. Chen, and N. Swaminathan. “A 5-step reduced mechanism for combustion of $CO/H_2/H_2O/CH_4/CO_2$ mixtures with low hydrogen/methane and high H_2O content”. In: *Combustion and Flame* 160.1 (2013), pp. 56 –75.

[21] G.P. Smith, D.M. Golden, M. Frenklach, N.W. Moriarty, B. Eiteneer, M. Goldenberg, C.T. Bowman, R.K. Hanson, S. Song, W.C. Gardiner, V.V. Lissianski, and Z. Qin. URL: `http://www.me.berkeley.edu/gri_mech/`.

[22] O. Marzouk and E. Huckaby. “A Comparitive Study of Eight Finite-Rate Chemistry Kinetics for CO/$\mathrm{H_2}$*Combustion*”. In: *Engineering Applications of Computational Fluid Mechanics* 4.3 (2010), pp. 331 –356.

[23] J. Natarajan, Y. Kochar, T. Lieuwen, and J. Seitzman. “Laminar Flame Speeds of $H_2/CO/O_2/He$ Mixtures at Elevated Pressure and Preheat Temperature”. In: *2007 Technical Meeting.* Eastern States Section of the Combustion Institute. University of Virginia.

[24] C. Dong, Q. Zhou, Q. Zhao, Y. Zhang, T. Xu, and S. Hui. "Experimental study on the laminar flame speed of hydrogen/carbon monoxide/air mixtures". In: *Fuel* 88.10 (2009), pp. 1858 –1863.

[25] C. Prathap, A. Ray, and M.R. Ravi. "Effects of dilution with carbon dioxide on the laminar burning velocity and flame stability of $H_2 - CO$ mixtures at atmospheric condition". In: *Combustion and Flame* 159.2 (2012), pp. 482 –492.

[26] S. Yousefian, A. Ghafourian, and M. Darbandi. "Numerical Study Of Syngas Premixed Flame Structure and Extinction". In: *Proceedings - Combustion Institute* (2011).

[27] N. Bouvet, C. Chauveau, I. Gokalp, and F. Halter. "Experimental studies of the fundamental flame speeds of syngas (H2/CO)/air mixtures". In: *Proceedings of the Combustion Institute* 33.1 (2011), pp. 913 –920.

[28] I.C. McLean, D.B. Smith, and S.C. Taylor. "The use of carbon monoxide/hydrogen burning velocities to examine the rate of the CO+OH reaction". In: *Symposium (International) on Combustion* 25.1 (1994). Twenty-Fifth Symposium (International) on Combustion, pp. 749 –757.

[29] C. Sung and C.K. Law. "Fundamental Combustion Properties of H2/CO Mixtures: Ignition and Flame Propagation at Elevated Pressures". In: *Combustion Science and Technology* 180.6 (2008), pp. 1097–1116.

[30] N. Bouvet, S.-Y. Lee, I. Gokalp, and R.J. Santoro. “Flame Speed Characteristics of Syngas ($H_2 - CO$) with Straight Burners for Laminar Premixed Flames”. In: Third European Combustion Meeting, 2007.

[31] H.A. Yepes and A.A. Amell. “Laminar burning velocity with oxygen-enriched air of syngas produced from biomass gasification”. In: *International Journal of Hydrogen Energy* 38.18 (2013), pp. 7519 –7527.

[32] J. Natarajan, T. Lieuwen, and J. Seitzman. “Laminar flame speeds of H2/CO mixtures: Effect of {CO2} dilution, preheat temperature, and pressure”. In: *Combustion and Flame* 151 (2007), pp. 104 –119.

[33] E. Monteiro and A. Rouboa. “Measurements of the Laminar Burning Velocities for Typical Syngas-Air Mixtures at Elevated Pressures”. In: *Journal of Energy Resources Technology* 133.3 (Sept. 2011), pp. 031002 –031007.

[34] J. Fu, C. Tang, W. Jin, L.D. Thi, Z. Huang, and Y. Zhang. “Study on laminar flame speed and flame structure of syngas with varied compositions using OH-PLIF and spectrograph”. In: *International Journal of Hydrogen Energy* 38.3 (2013). 2011 Zing International Hydrogen and Fuel Cells Conference: from Nanomaterials to Demonstrators, pp. 1636 –1643.

[35] V. Iyer, J. Haynes, P. May, and A. Anand. “Evaluation of Emissions Performance of Existing Combustion Technologies for Syngas Combustion”. In: vol. 2. International Gas Turbine Institute. ASME Proceedings - Combustion Fuels, 2005.

[36] K.W. Chun, H.-J. Chung, S.H. Chung, and J.H. Choi. “A numerical study on extinction and NOx formation in nonpremixed flames with syngas fuel”. English. In: *Journal of Mechanical Science and Technology* 25.11 (2011), pp. 2943–2949.

[37] D.E. Giles, S. Som, and S.K. Aggarwal. “NOx emission characteristics of counterflow syngas diffusion flames with airstream dilution”. In: *Fuel* 85 (2006), pp. 1729 –1742.

[38] N. Ding, R. Arora, M. Norconk, and S.-Y. Lee. “Numerical investigation of diluent influence on flame extinction limits and emission characteristic of lean-premixed $H_2 - CO$ (syngas) flames”. In: *International Journal of Hydrogen Energy* 36.4 (2011), pp. 3222 –3231.

[39] G.J. Rortveit, J.E. Hustad, S.-C. Li, and F.A. Williams. “Effects of diluents on NOx formation in hydrogen counterflow flames”. In: *Combustion and Flame* 130 (2002), pp. 48 –61.

[40] J.M. Seitzman and J. Natarajan. “Laminar Flame Properties Of H2/ CO Mixtures”. In: *Synthesis Gas Combustion*. CRC Press, Sept. 2009, pp. 71 –98.

[41] R.A. Yetter, G. Ribert, V. Yang, Z. Wang, and P. Thakre. “Fundamental Combustion Characteristics Of Syngas”. In: *Synthesis Gas Combustion*. CRC Press, Sept. 2009, pp. 99 –128.

[42] R.L. Speth and A.F. Ghoniem. “Using a strained flame model to collapse dynamic mode data in a swirl-stabilized syngas combustor”. In: *Proceedings of the Combustion Institute* 32.2 (2009), pp. 2993 –3000.

[43] S.R. Turns. *An Introduction to Combustion: Concepts and Applications.* Second Edition, 2000. McGraw-Hill, New York, 1996.

[44] C.K. Law and C.J. Sung. “Structure, aerodynamics, and geometry of premixed flamelets”. In: *Progress in Energy and Combustion Science* 26 (2000), pp. 459 –505.

[45] *Premix: A program for modeling steady, laminar, one-dimensional premixed flames.* Chemkin. Release 3.6 September 2000. URL: `http://www.cvd.louisville.edu/Course/.../chemkin7premix.pdf`.

[46] C.M. Vagelopoulos and F.N. Egolfopoulos. “Laminar flame speeds and extinction strain rates of mixtures of carbon monoxide with hydrogen, methane, and air”. In: *Symposium (International) on Combustion* 25.1 (1994). Twenty-Fifth Symposium (International) on Combustion, pp. 1317 –1323.

[47] J.B. Heywood. *Internal Combustion Engine Fundamentals.* Print. McGraw-Hill, 1988.

[48] G.A. Karim, I. Wierzba, and S. Boon. “Some considerations of the lean flammability limits of mixtures involving hydrogen”. In: *International Journal of Hydrogen Energy* 10.2 (1985), pp. 117 –123.

[49] I. Wierzba and V. Kilchyk. “Flammability limits of hydrogencarbon monoxide mixtures at moderately elevated temperatures”. In: *International Journal of Hydrogen Energy* 26.6 (2001), pp. 639 –643.

[50] H.F. Coward and G.W. Jones. *Limits of Flammability of Gases and Vapors*. USBM. U.S. Bureau of Mines, 1952.

[51] D. Charlston-Goch, B.L. Chadwick, R.J.S. Morrison, A. Campisi, D.D. Thomsen, and N.M. Laurendeau. “Laser-Induced fluorescence measurements and modeling of nitric oxide in premixed flames of CO+H2+CH4 and air at high pressures: I. Nitrogen fixation”. In: *Combustion and Flame* 125 (2001), pp. 729 –743.

[52] N.A. Chigier and J.M. Beer. “Velocity and Static-Pressure Distributions in Swirling Air Jets Issuing From Annular and Divergent Nozzles”. In: *Journal of Fluids Engineering* 86.4 (Dec. 1964), pp. 788 –796.

[53] H.J. Sheen, W.J. Chen, S.Y. Jeng, and T.L. Huang. “Correlation of swirl number for a radial-type swirl generator”. In: *Experimental Thermal and Fluid Science* 12.4 (1996), pp. 444 –451.

[54] P. Sayad, A. Schonborn, and J. Klingmann. “Experimental Investigations of the Lean Blowout Limit of Different Syngas Mixtures in an Atmospheric, Premixed, Variable-Swirl Burner”. In: *Energy & Fuels* 27.5 (2013), pp. 2783 –2793. eprint: `http://pubs.acs.org/doi/pdf/10.1021/ef301825t`.

[55] N. Syred, M. Abdulsada, A. Griffiths, T. ODoherty, and P. Bowen. “The effect of hydrogen containing fuel blends upon flashback in swirl burners”. In:

Applied Energy 89.1 (2012). Special issue on Thermal Energy Management in the Process Industries, pp. 106 –110.

[56] N. Shelil, A. Bagdanavicius, N. Syred, A. Griffiths, and P. Bowen. “Premixed swirl combustion and flash back analysis with hydrogen/methane mixture”. In: *48th AIAA Aerospace Sciences Meeting, Orlando, USA, ref. AIAA-2010-1169*. 2010.

[57] W. Shao, Y. Xiong, K. Mu, Z. Zhang, Y. Wang, and Y. Xiao. “The influence of fuel-air swirl intensity on flame structures of syngas swirl-stabilized diffusion flame”. English. In: *Journal of Thermal Science* 19.3 (2010), pp. 276 –283.

[58] P. Kutne, R. Sadanandan, and W. Meier. “Experimental analysis of the combustion behaviour of syngas mixtures in a gas turbine model combustor under elevated pressure”. In: *Proceedings of the European Combustion Meeting*. 2009.

[59] H.S. Kim, V.K. Arghode, and A.K. Gupta. “Flame characteristics of hydrogen-enriched methaneair premixed swirling flames”. In: *International Journal of Hydrogen Energy* 34.2 (2009), pp. 1063 –1073.

[60] H.S. Kim, V.K. Arghode, M.B. Linck, and A.K. Gupta. “Hydrogen addition effects in a confined swirl-stabilized methane-air flame”. In: *International Journal of Hydrogen Energy* 34.2 (2009), pp. 1054 –1062.

[61] S. Daniele, P. Jansohn, and K. Boulouchos. “Experimental investigation of lean premixed syngas combustion at gas turbine relevant conditions: lean

blow out limits, emissions and turbulent flame speed". In: *Proceedings of 32nd Annual Meeting of the Italian Section on the Combustion Colloquia.* 2009.

[62] R.W. Schefer, D.M. Wicksall, and A.K. Agrawal. "Combustion of hydrogen-enriched methane in a lean premixed swirl-stabilized burner". In: *Proceedings of the Combustion Institute* 29.1 (2002). Proceedings of the Combustion Institute, pp. 843 –851.

[63] C. Ghenai. "Combustion of syngas fuel in gas turbine can combustor". In: *Advances in Mechanical Engineering* (2010).

[64] S. Navarro-Martinez and A. Kronenburg. "Flame Stabilization Mechanisms in Lifted Flames". English. In: *Flow, Turbulence and Combustion* 87.2-3 (2011), pp. 377 –406.

[65] E. Giacomazzi, D. Cecerel, F. Donato, et al. "LES Analysis of a Syngas Turbulent Premixed Dump-Combustor at 5 Bar". In: *Int. Conf. on Processes and Technologies for a Sustainable Energy, Ischia, June 27.* Vol. 30. 2010.

[66] Y.J. Chen. "Development of reduced mechanisms for numerical modelling of turbulent combustion". In: *Workshop on Numerical Aspects of Reduction in Chemical Kinetics, CERMICS-ENPC, Cite Descartes, Champus sur Marne, France.* 1997.

[67] A. De and S. Acharya. "Parametric study of upstream flame propagation in hydrogen-enriched premixed combustion: Effects of swirl, geometry and premixedness". In: *International Journal of Hydrogen Energy* 37.19 (2012).

{HYFUSEN} Special Issue for the 4th National - 3rd Latin American Conference on Hydrogen and Sustainable Energy Sources (HYFUSEN), 6-9 June 2011, Mar Del Plata, Argentina, pp. 14649 –14668.

[68] A. De and S. Acharya. "Dynamics of upstream flame propagation in a hydrogen-enriched premixed flame". In: *International Journal of Hydrogen Energy* 37.22 (2012). HySafe 1, pp. 17294 –17309.

[69] Y. Zheng, M. Zhu, D.M. Martinez, and X. Jiang. "Large-eddy simulation of mixing and combustion in a premixed swirling combustor with synthesis gases". In: *Computers & Fluids* 88.0 (2013), pp. 702 –714.

[70] D. Goodwin. *Cantera: An object-oriented software toolkit for chemical kinetics, thermodynamics, and transport processes.* Caltech, Pasadena. 2009. URL: `http://code.google.com/p/cantera`.

[71] W.R. Smith and R.W. Missen. *Chemical reaction equilibrium analysis: theory and algorithms.* Wiley New York, 1982.

[72] B. Bunkute and J.B. Moss. "Laminar Burning Velocities of Carbon Monoxide/Hydrogen Air Mixtures at High Temperatures and Pressures". In: Third European Combustion Meeting, 2007.

[73] M.I. Hassan, K.T. Aung, and G.M. Faeth. "Properties of Laminar Premixed CO/H_2/Air Flames at Various Pressures". In: *Journal of Propulsion and Power* 13.2 (Mar. 1997), pp. 239 –245.

[74] M.P. Burke, X. Qin, Y. Ju, and F.L. Dryer. “Measurements of hydrogen syngas flame speeds at elevated pressures”. In: *5th US Combustion Meeting.* Vol. 25. 2007.

[75] *ANSYS FLUENT User Guide.* Release 14.0. ANSYS, Inc. 2011.

[76] *ANSYS FLUENT Theory Guide.* Release 14.0. ANSYS, Inc. 2011.

[77] W.C. Reynolds and STANFORD UNIV CA DEPT OF MECHANICAL ENGINEERING. *Fundamentals of Turbulence for Turbulence Modeling and Simulation.* Defense Technical Information Center, 1987.

[78] T.-H. Shih, W.W. Liou, A. Shabbir, Z. Yang, and J. Zhu. “A new $k-\epsilon$ eddy viscosity model for high reynolds number turbulent flows”. In: *Computers & Fluids* 24.3 (1995), pp. 227 –238.

[79] M.A. Habib, R. Ben-Mansour, H.M. Badr, S.F. Ahmed, and A.F. Ghoniem. “Computational fluid dynamic simulation of oxyfuel combustion in gas-fired water tube boilers”. In: *Computers & Fluids* 56.0 (2012), pp. 152 –165.

[80] C.V. da Silva, H.A. Vielmo, and F.H.R. Franca. “Numerical Simulation of the Combustion of Methane and Air in a Cylindrical Chamber”. In: *Thermal Engineering* 5.1 (2006), pp. 13 –21.

[81] J.J.J. Louis, J.B.W. Kok, and S.A. Klein. “Modeling and measurements of a 16-kW turbulent nonadiabatic syngas diffusion flame in a cooled cylindrical combustion chamber”. In: *Combustion and Flame* 125 (2001), pp. 1012 – 1031.

[82] Y. Huang and V. Yang. “Effect of swirl on combustion dynamics in a lean-premixed swirl-stabilized combustor”. In: *Proceedings of the Combustion Institute* 30.2 (2005), pp. 1775 –1782.

[83] T.J. Kim, R.A. Yetter, and F.L. Dryer. “New results on moist CO oxidation: high pressure, high temperature experiments and comprehensive kinetic modeling”. In: *Symposium (International) on Combustion* 25.1 (1994). Twenty-Fifth Symposium (International) on Combustion, pp. 759 –766.

Vitae

- Name: Fahad Mohammed Majhoud Alzahrani
- Nationality: Saudi Arabia
- Date of Birth: 18 March 1987
- Email: *falkhazmari@gmail.com*
- Permenant Address: P.O. Box 197

  King Fahd University of Petroleum & Minerals

  Dhahran 31261, the Kingdom of Saudi Arabia
- Education:

  - MS in Mechanical Engineering, KFUPM, Dhahran, KSA

  - BS in Applied Mechanical Engineering, KFUPM, Dhahran, KSA
- Presentations:

  - A.F. Ghoniem, S. Shanbhogue, K. Vogiatzaki, S. Taamallah, G. Kewlani, E. Sheu, A. Mitsos, F.M. Alzahrani. "Hybrid Concentrated Solar-Natural Gas for Power Generation Plant". *Energy Night*, Cambridge, MA. 2012

  - F.M. Alzahrani, M.A.M. Habib, E.M.A. Mokheimer. "Effect of Swirl Number on Combustion Characteristics and Emissions of $H_2/CO/air$ Premixed Flame in a Swirl-Stabilized Combustor". 4^{th} *SAS-Combustion Institute Annual Meeting.* April 29^{th}, 2014: KAUST, Thuwal, KSA. p. 38